PhD Thesis

Ludovic
GUILLAUME
September 2017

LIÈGE
université

On the design of waste heat recovery organic Rankine cycle systems for engines of long-haul trucks

PhD Thesis
submitted the 29th of September 2017
and defended the 8th of November 2017
at the
UNIVERSITY OF LIEGE

for the degree of Doctor of Philosophy

by
Ludovic Guillaume

under suggestion of:
Professor Vincent Lemort (ULg), supervisor

and under recommendation of the members of the jury:
Professor David Chalet (School of Central Nantes), examiner
Professor Roberto Cipollone (University of L'Aquila), examiner
Professor Michel De Paepe (University of Ghent), examiner
Professor Pierre Dewallef (University of Liège), examiner
Lecturer Sylvain Quoilin (University of Liège), examiner

On the design of waste heat recovery organic Rankine cycle systems for engines of long-haul trucks

To my wife and son

It is good to have an end to journey toward;
but it is the journey that matters, in the end.

— Ursula K. Le Guin

Preface

The present thesis was prepared at the Thermodynamics laboratory, Department of Aerospace and Mechanical Engineering, University of Liege (ULg). It is submitted as a partial fulfillment of the requirements for the degree of Doctor of Philosophy and is written as a monograph.

The work was carried out for 6 years, from October 2011 to September 2017, under supervision of Professor Vincent Lemort (ULg).

Liege, 29th September 2017   Ludovic Guillaume

Acknowledgements

The completion of this dissertation has been an enriching experience that could not have been achieved alone. First I would like to thank Professor Vincent Lemort for giving me the opportunity to make this thesis and to work on multiple interesting projects in the last 6 years. I also thank the technicians José Concha, Richard Labenda, Bernard Loly for their advice and the numerous hours they spent on the construction of test benches for this thesis. I would also like to thank all the colleagues I have worked with during those six years spent in the Thermodynamics Laboratory. Finally, I thank Amanda Stroobants and my family for their support during all these years.

Abstract

This thesis contributes to the characterization and the design of Waste Heat Recovery (WHR) Organic Rankince Cycle (ORC) system for engine of long haul trucks. It is based on experimental studies and simulation models.

A methodology is proposed for the working fluid selection. A data base containing the relevant characteristics of various substances is constituted. Those characteristics are the thermophysical properties of the fluid but also the environmental impact if the substance is released, its price and its 'dangerousness level' (toxicity, etc). The properties are used as selection criteria to identify the fluid candidates for the application. In addition, the heat sources and sinks to consider for the application are identified.

A small scale ORC test rig, integrating a radial-inflow turbine, is built and operated to characterize the ORC components. A major attention is devoted to the turbine-generator set, the pump and the brazed-plate type condenser. The performance of those devices are compared for two low critical temperature working fluids. In particular, a 3-step method is proposed to compare the performance of the turbine-generator set achieved with both fluids. Uncertainty propagation analysis are also performed to check the validity of the measurements.

A mean-line model of the turbine is developed and the gathered experimental data is exploited to validate this model. Various volumetric expansion machine and pump technologies as well as a heat exchanger designed for waste heat recovery from engine exhaust gases are also experimentally investigated. The gathered data is used to validate model of the components.

All the proposed models are physic based tools, which once validated, are used to extrapolate the performance of the components outside their validation region (e.g. for another component size or using another working fluid). To this end, methods based on similarity relations are proposed. The resulting component models are devoted to be used in both the design and the simulation phase of the ORC system. Based on the investigated heat sources and sinks, and the considered ORC components, various architectures of ORC candidates are identified and modeled. Those models are built interconnecting the component models together. A 3-step optimization process is then proposed. The first step consists in the identification of the design conditions for the ORC systems based on the investigated heat sources, working fluid and system architecture. Then, because in addition to the maximization of the performance of the system, the minimization of the cost should be kept in mind, a thermo-economic optimization phase is achieved during the design phase of the ORC systems for the identified design conditions previously identified. Finally, the performance of the systems are maximized in off-design conditions for various operating conditions. In addition

to the comparison of the system performance, economic indicators are defined to compare the profitability of the developed systems.

Because of the transient nature of the heat sources, dynamic models of the system are also developed and simulations are performed along driving cycles of the truck. To this end, a control strategy is developed to optimize the performance and ensure a safe operation of the systems but also to observe the constraints inherent to the integration of the ORC technology in the truck. The value of the system performance and economic indicators is finally updated compared to the steady-state simulations results.

Keywords. Thermo-economic optimization, waste heat recovery, Heavy duty trucks, Organic Rankine cycles.

Resumé

Cette thèse contribue à la caractérisation et à la conception de système de type Cycle de Rankine Organique (ORC) dédiés à la récupération de chaleur initialement perdue (WHR) sur les moteur des camions long-courriers. Elle est basé sur des études expérimentales et des modèles de simulation.

Une méthodologie est proposée pour la sélection du fluide de travail. Une base de données contenant les caractéristiques pertinentes de diverses substances est constituée. Ces caractéristiques sont les propriétés thermodynamiques du fluide, mais aussi l'impact environnemental si la substance est relâchée, son prix et 'son niveau de danger' (toxicité, etc.). Ces propriétés sont utilisées comme critères de sélection pour identifier les fluides potentiellement candidats pour l'application. En outre, les sources et puits de chaleur à considérer pour l'application sont identifiés.

Un banc d'essais ORC de petite échelle, intégrant une turbine de type radial-inflow, est construit et exploité pour caractériser les composants du système ORC. Une attention majeure est accordée au groupe turbine-générateur, à la pompe et au condenseur à plaques brasées. Les performances de ces composants sont comparées pour deux fluides de travail à faible température critique. En particulier, une comparaison en 3 étapes est proposée concernant les performances du groupe turbine-générateur obtenues avec les deux fluides. Des analyses de propagation d' incertitude sont également effectuées pour vérifier la validité des mesures.

Un modèle au rayon moyen de la turbine est développé et les données expérimentales collectées sont exploitées pour valider ce modèle. Diverses technologies de machines de détente et pompes volumétrique, ainsi qu'un échangeur de chaleur conçu pour la récupération de chaleur des gaz moteur, sont également étudiés expérimentalement. Les données collectées sont utilisées pour valider les modèles des composants.

Tous les modèles proposés sont des outils basés sur la physique qui, une fois validés, servent à extrapoler les performances des composants en dehors de leur région de validation (par exemple pour une autre taille de composant ou en utilisant un autre fluide de travail). À cette fin, des méthodes basées sur des relations de similitudes sont proposées. Les modèles de composants résultants sont destinés à être utilisés tant dans la conception que dans la phase de simulation du système ORC. Sur la base des sources et puits de chaleur étudiés, et des composants du system ORC considérés, diverses architectures de candidats ORC sont identifiées et modélisées. Ces modèles sont construits en interconnectnant les modèles de composants. Un processus d'optimisation en 3 étapes est alors proposé. La première étape consiste à identifier les conditions de dimensionnement des systèmes ORC en fonction des

sources de chaleur étudiées, du fluide de travail et de l'architecture du système. Ensuite, car en plus de la maximisation des performances du système, il faut tenir compte de la minimisation du coût, une optimisation thermoéconomique est réalisée au cours du dimensionnement des systèmes ORC pour les conditions de conception préalablement identifiées. Enfin, les performances des systèmes sont maximisées en condition off-design pour diverses conditions de fonctionnement. En plus de la comparaison des performances du système, des indicateurs économiques sont définis pour comparer la rentabilité des systèmes développés.

En raison de la nature transitoire des sources de chaleur, des modèles dynamiques du système sont également construits et des simulations sont effectuées le long de cycles de conduite du camion. A cette fin, ne stratégie de contrôle est développée pour optimiser les performances et assurer un fonctionnement sûr des systèmes, mais aussi pour respecter les contraintes inhérentes à l'intégration de la technologie ORC dans le camion. La valeur des performances du système et des indicateurs économiques est finalement mise à jour par rapport aux résultats de simulation en régime permanent.

Mots clés. Optimisation thermo-économique, Récupération de chaleur fatale, Camions long routiers, Cycle de Rankine organiques.

Papers and Presentations

Part of the work performed during the PhD project resulted in peer-reviewed publications and presentations, which are listed hereafter in the order of acceptance and by category. They are directly or indirectly related to the main topics of this thesis.

Peer-review publications

- Guillaume L., Legros A., Desideri A., Lemort V., Performance of a radial-inflow turbine integrated in an ORC system and designed for a WHR on truck application: An experimental comparison between R245fa and R1233zd, in Applied Energy, Volume 186, Part 3, Pages 408–422, 2017.

- Legros A., Guillaume L., Diny M., Zaïdi H., Lemort V., Comparison and impact of waste heat recovery technologies on passenger car fuel consumption on a normalized driving cycle, in Energies, Volume 7, Pages 5273-5290, 2014.

- Declaye S., Quoilin S., Guillaume L., Lemort V., Experimental study on an open-drive scroll expander integrated into an ORC (Organic Rankine Cycle) system with R245fa as working fluid, in Energy, Volume 55, Pages 173–183, 2013.

- Oudkerk J.F., Quoilin S., Declaye S., Guillaume L., Winandy E., Lemort V., Evaluation of the Energy Performance of an Organic Rankine Cycle-Based Micro Combined Heat and Power System Involving a Hermetic Scroll Expander, in Journal of Engineering for Gas Turbines and Power, Volume 135 / 042306-1, 2013.

Peer-review presentations

- Gendebien S, Guillaume L, Bellolio S, Francois P, Dechesnes B, Dubois S, Lemort V, Etude expérimentale et numérique d'un échangeur destiné à la récupération de chaleur fatale sur bancs d'essais de moteurs aéronautiques, CIFQ 2017; Saint-Lô, France.

- Guillaume L., Legros A., Lemort V., Thermo-economic optimization of organic Rankine cycle systems for waste heat recovery from exhaust and recirculated gases of heavy duty trucks, in proceedings of the engine organic Rankine cycle consortium, 2016.

- Guillaume L., Ameel B., Criens C., Siera I., Hernandez A., De Paepe M., Lemort V., Dynamic modeling of waste heat recovery organic Rankine cycle systems in the AMESim platform, in proceedings of the engine organic Rankine cycle consortium, 2016.

- Bettoja F., Perosino A., Lemort V., Guillaume L., Reiche T., NoWaste: waste heat re-use for greener truck, Proceedings of 6th Transport Research Arena, 2016.

- Vodicka V., Guillaume L., Mascuch J, Lemort V.,Testing and modeling a vane expander used in an orc working with hexamethyldisiloxane (MM), in proceedings of the ASME ORC third international seminar on ORC power systems, 2015.

- Guillaume L., Legros A., Lemort V., Experimental comparison of the performance of a Waste Heat Recovery Organic Rankine Cycle system for truck application using R245fa and R1233zd, in proceedings of the Sustem International Conference, 2015.

- Legros A., Guillaume L., Diny M., Zaïdi H., Lemort V., Experimental investigations of the valorization of the exhaust waste heat of a gasoline engine based on a Rankine cycle, in 35th FISITA world automotive congress, 2014.

- Grelet, V., Reiche, T., Guillaume, L., Lemort, V., Optimal waste heat recovery Rankine based for heavy duty applications, in 35th FISITA world automotive congress, 2014.

- Guillaume L., Legros A., Quoilin S., Declaye S., Lemort V., Sizing models and performance analysis of waste heat recovery organic Rankine cycles for heavy duty trucks, in proceedings of the ASME ORC second international seminar on ORC power systems, 2013.

- Guillaume L., Legros A., Quoilin S., Declaye S., Lemort V., Sizing models and performance analysis of volumetric expansion machines for waste heat recovery through organic Rankine cycles on passenger cars, in proceedings of the International conference on compressors and their systems, 2013.

- Legros A., Guillaume L., Lemort V., Diny M., Bell I., Quoilin S., Investigation on a scroll expander for waste heat recovery on internal combustion engines, in proceedings of the International conference on compressors and their systems, 2013.

- Lemort V., Guillaume L., Legros A., Declaye S., Quoilin S., A comparison of piston, screw and scroll expanders for small scale Rankine cycle systems, in Proceedings of the 3rd International Conference on Microgeneration and Related Technologies, 2013.

- Quoilin S., Declaye S., Legros A., Guillaume L., Lemort V., Working fluid selection and operating maps for Organic Rankine Cycle expansion machines, in Proceedings of the 21st International Compressor Conference at Purdue, 2012.

Contents

Nomenclature

Abbreviations

AC   Alternative Current

APS   Absolute Pressure Sensor

CFM   Coriolis Flow Meter

GHG   Green House Gases

GWP   Global Warming Potential

ODP   Ozone Depletion Potential

ORC   Organic Rankine Cycle

PP   Pinch Point

REB   Rolling Element Bearings

SISO   Single Input Single Output

TIT   Turbine Inlet Temperature

WHR   Waste Heat Recovery

Greek letters

α Mass fraction $[-]$

β Chevron angle $[rad]$

ϵ Efficiency $[-]$

η Effectiveness $[-]$

ρ Density $[kg/m^3]$

Symbols

$\dot{H}$ Enthalpy flow rate variation $[W]$

Nomenclature

$\dot{M}$ Mass flow rate $[kg/s]$

$\dot{Q}$ Heat flow rate $[W]$

$\dot{W}$ Mechanical or electrical power $[W]$

A Area $[m^2]$

Bo Boiling number $[-]$

C Empiric coefficient $[-]$ or Cost $[\text{£}]$ or Velocity $[m/s]$

D Diameter $[m]$

DC Direct cost $[\text{€}]$

e Plate thickness $[m]$

F Coefficients in Martin's correlation $[-]$

f Fanning friction factor $[-]$

G Mass velocity $[kg/s.m^2]$

h Specific enthalpy $[J/kg]$ or heat transfer coefficient $[W/m^2.K]$

IC Indirect cost $[\text{€}]$

k Thermal conductivity $[W/m.K]$

L Plate length $[m]$

M Mach number $[-]$

m Empiric coefficient $[-]$

mu Dynamic viscosity $[Pa.s]$

N Rotational speed $[RPM]$

n Empiric coefficient $[-]$

Nu Nusselt number $[-]$

P Pressure $[Pa]$

p Pitch $[m]$

Pr Prandtl number $[-]$

Re Reynolds number $[-]$

SIC Specific investment cost $[\text{€}]$

T	Temperature [$°C$ or K]
TIC	Total investment cost [€]
U	Global heat transfer coefficient [$W/m^2.K$]
V	Volume [m^3]
x	Vapor mass fraction [$-$]

Subscripts

air	Air
c	Compressor
cd	Condenser
cf	Cold Fluid
co	Corrugation
cond	Conduction
conv	Convection
crit	Critical
ctrl	Control
EG	Exhaust Gases
EGR	Exhaust Gas Recirculation
el	Electrical
Eng	Engine
eq	Equivalent
ev	Evaporator
ex	Exhaust
exp	Expander
h	Hydraulic
hf	Hot Fluid
HP	High Pressure
HT	High Temperature

instl	Installation
is	Isentropic
l	Saturated liquid
liq	Liquid
LP	Low Pressure
LT	Low Temperature
lub	Lubrication
p	Piping
pp	Pump
rot	rotational
s	Swept
sh	Shaft
su	Supply
syst	System
tgs	Turbo Generator Set
thr	Throat
tp	Two-phase
v	Saturated vapor
vap	Vapor
wf	Working fluid

Superscripts

0	Reference

1 Introduction

It is now accepted that emissions of greenhouse gases (GHG) from human activities are enhancing the global warming effect keeping the earth at a temperature higher than it would otherwise be [2]. In the last twenty years, the world energy use has increased by more than 30% [3] despite the adoption by the United Nations on Climate Change of various Protocols (Kyoto 1992 [4], Copenhague 2009, Doha 2012, Paris 2015).

Alone, the EU is responsible for around 10 % of the global emissions of greenhouse gases. Nearly 80 % of those emissions come from the production and use of energy and transport [5]. Looking at the situation as it was in 2015 in Europe in terms of GHG emissions (Figure 1.1), it can be seen that the transport sector is responsible of about one quarter of these emissions. It is also pointed out by the European Commission that "*Heavy-Duty Vehicles (HDV) represent about a quarter of EU road transport CO_2 emissions and some 6% of the total EU emissions* [6]". For a long time, the EU has stressed the need to limit the global warming to $2°C$ maximum in
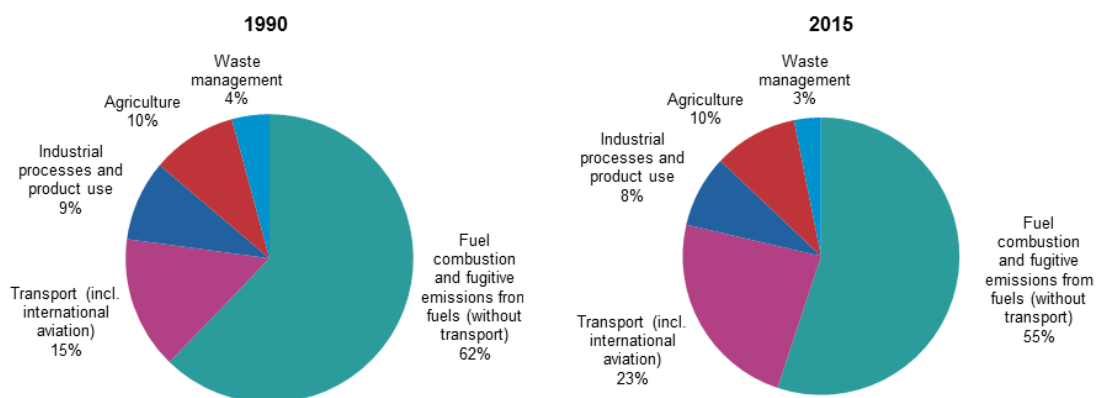

Figure 1.1 – European GHG emissions by sector in 1990 and 2015. [7]

2100 compared to the level of 1900 while the current projections forecast a minimum of 3.5 to $4°C$ of temperature increase. This $2°C$ target resulted from one of the various prediction

scenarios emitted by the IPCC on climate change (AR1 to AR6) [8] and was identified as the limit in order to avoid the potential catastrophic consequences of the global warming due to anthropogenic emissions. This limit has recently been updated to $1.5°C$ by the IPCC (SR15) while the symbolic level of $1°C$ increase was reached in 2015 [9]. *The likely range of global temperature increase is 2.0-4.9°C , with median 3.2°C and a 5% (1%) chance that it will be less than 2°C (1.5°C) [10].* The recent withdraw of the United States from the Paris climate accord will not improve the chance to reach the target.

In 2007 were established the horizon 2020 objectives of the EU, which aimed at reducing the green houses gazes emission by 20 % compared to the emission level of 1990, increasing the renewable share of the global consumption to 20 % and increasing the energy efficiency of the processes by 20 %. Those objectives are part of a low-carbon economy road-map aiming at reducing the greenhouse gas emissions to 80 % below 1990 levels by 2050. This strategy is split into milestones (20 % in 2020, 40 % in 2030 and 60 % in 2040) and suggests all sectors (power generation and distribution, transport, buildings, industry and agriculture) need to contribute.
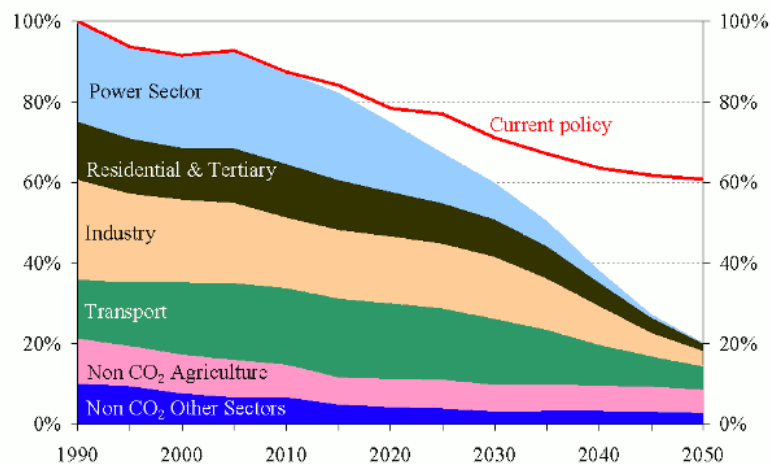
Figure 1.2 – Targeted greenhouse gases emissions in 2050 compared to 1990 (100 %) [11]

Concerning the transport sector, the objectives imply an emission reduction of 60 % thanks to, among others, more fuel-efficient diesel engine in the short-term and bio-fuels and hybridization in the mid-to-long term. However, despite the improvements in fuel consumption efficiency, HDV emissions are still rising, mainly because of the increasing number of vehicles in traffic. Nowadays, HDV are the second-biggest source of CO_2 emissions within the transport sector, i.e. larger than both international aviation and shipping. As a result, the reduction of the CO_2 emissions from HDV has become a strategic goal of the EU. "*As part of the EU's future strategy to address HDV fuel consumption and CO_2 emissions, a number of actions can be considered that will result in:*

- *improved vehicle efficiency through new engines, materials and design,*

- ***cleaner energy use through new fuels and propulsion systems,***

- ***better use of networks and more efficient fleet operation, with the support of information and communication systems.***

[6]"

A very promising solution is the re-use of the waste heat, which is about 60% of the combustion energy. Transforming this thermal energy in mechanical or electrical energy will enable to increase the overall energy efficiency of the vehicle. Consequently, the fuel consumption and the CO_2 emissions will be reduced.

The heat recovery can be performed by means of a thermodynamic cycle (e.g. organic or non-organic Rankine cycles) using the waste heat as energy source as it is being adopted for large stationary applications.

However the adoption of such technology in the automotive domain requires specific R&D activities to identify the most appropriate system architecture and integration level so to achieve sustainable cost and the reliability requirements. Among others, the transient behavior of the engine, the selection of the heat sources, the limited additional heat rejection capacity of the truck, the use of the energy produced by the expansion machine and the impact on the engine back pressure caused by the evaporator [12] are as many challenges to overcome during the design of the WHR system.

1.1 Brief history

Year 2020 also corresponds to the bicentenary of the birth of William John Macquorn Rankine (1820-1872). As one of the founding contributors of thermodynamics, the mechanical engineer developed and published, among others, the theory of the steam engine, which is now known under is name. The principle is relatively simple and is the foundation of our current power plants. Water is evaporated at a high constant pressure level and the resulting saturated vapor is expanded through an expansion machine until a low pressure level. The energy content of the fluid is converted by the expander into mechanical energy and further into electricity by means of a generator. The expanded steam is condensed at the low constant pressure level and returned to its initial saturated-liquid state, from where it is pumped to the high pressure line.

It was not long before the apparition of the first experiments replacing water by non-conventional working fluids and the birth of the Organic Rankine Cycle (ORC) systems. The ORC system is constituted of the same basic components as those of the steam engine except organic fluids (in this work defined as all fluids but water), whose thermo-physical characteristics are suited for efficiently exploiting low grade thermal energy sources, are used. At the beginning, the technology was designed to be used as a bottoming system of Rankine engines. According to Macchi et al. [13], the first commercial application was developed in 1853 by Du Tremblay, a

french engineer, in a combined cycle. A secondary organic fluid was evaporated by condensing the steam of a primary Rankine system. Nonetheless, the most well-known historic example is probably the development of naphta engines to propel small pleasure boats by Frank Oefeldt [14]. Those boats were quite popular until around 1900 when the Internal Combustion Engine (ICE) became a true alternative. From that time, only few applications of ORC have been recorded, all using solar energy rather than fossil fuels [13].

A new rise of the technology was observed in Italy around the thirties with the work of 2 pioneers Mario Dornig and Luigi D'Amelio [15] who exploited solar energy at low temperature using fluids other than water. In 1961, Tabor and Bronicki proposed a new architecture using a recuperator [13]. In 1967 was installed the first geothermal binary ORC power plant in the Kamchatka peninsula of the Soviet Union [15]. To the author knowledge, the first attempts of compounding a truck diesel engine with an ORC were achieved in 1976 by Patel and Doyle [16] and in 1979 by Doyle et al. [17]. The working fluid was a mixture of water and trifluoroethanol (50 % molar) and the expander was a three-stage axial turbine. Results from tests conducted with a Mack 676 diesel engine and a bottoming ORC system were presented and showed a gain of 13 % in power without additional fuel at the peak power condition. On the other hand, the Kitson-Still locomotive [18] was probably the first land vehicle to embark on an energy recovery system. Built in 1926, the evaporator was attached to the exhaust line of a diesel engine. An additional power of 15 to 30 % could be produced. Between 1976 and 1984, Gianfranco Angelino, Mario Gaia and Ennio Macchi designed and contributed to the realization of fourteen ORC power plants, spanning the power range from 3 to 500 kW, and for the conversion of various thermal energy sources (solar energy, geothermal fluids, industrial waste heat).

In the last decades, the needs in increased energy efficiency have led to a renewed interest in both research and industrial levels, in particular in the transport sector in which many prototypes have emerged. In 1993, Oomori et al. were pioneers integrating an ORC unit instead of the cooling system. Fluid R123 and a scroll expander were used while the cycle efficiency reached 3 %. In 2005, BMW innovated with the Turbosteamer to recover the heat from the exhaust gases and the engine coolant of gasoline passenger cars. Two versions of the prototypes were presented and an increase of the engine efficiency above 10 % was announced [19] [20]. In 2007, Honda also investigated the Rankine cycle on passenger car and reached a 3.8 % of engine thermal efficiency improvement [21]. Renault Trucks has investigated waste heat recovery both through Organic Rankine Cycle systems and thermo-electricity [22]. The new target of the group is a demonstration vehicle that consumes 13 % less fuel through the new program named Falcon [23]. Since 2011, Cummins has been developing an organic Rankine cycle working with refrigerant R245fa for a heavy duty application recovering heat from the EGR, the exhaust gas and the charged air in the latest configuration [24]. The study led to the development of a demonstrator within the Supertruck program. A fuel economy greater than 7.4 % was measured.

1.2 Objectives

The ORC technology can play a significant role in reducing the fuel consumption and resulting emissions of heavy duty trucks. The Supertruck proposed by Cummins and the Falcon project initiated by Volvo are examples among others. On the other hand, the truck industry can also be the driver of the future development of the ORC technology. For years, ORC power systems have been successfully adopted to convert thermal energy into power in solar, geothermal, biomass combustion, industrial waste heat recovery processes, proving the technology to be a mature, flexible and commercially viable. However those are niche markets while the integration of the ORC technology in mobile applications such as heavy duty trucks might well lead, thanks to supply chain production, to an exploding number of devices, thus attracting both industrial and academic research to continuously improve the technology. Nonetheless, the introduction of the technology in mobile applications will result mainly from economic considerations. The reduction of the pollutants emission by the engine is not a sufficient reason to drive investments in the field. The system has to be profitable for both the truck manufacturer and the future truck owner. In this regards, there is a need to evaluate accurately the fuel economy and the costs linked to the on board system.

In this design study, an economic model is thus proposed to be overlapped to a thermodynamic model. First, the boundaries of the study are defined in terms of investigated working fluids, heat sources and sinks and ORC components. The number of publications devoted to the working fluid selection is remarkable ([25],[26],[27]) and is a consequence of high number of available organic fluids in the industry. Up to now no universal fluid selection technique has been identified while the most recent publications covering this subject present methodologies based on molecular design-technique [28]. Moreover, on a truck multiple heat sources and sinks are available, leading to a high number of possible combinations. The technologies of the ORC components are also various. Expanders are generally split into turbo and positive displacement machines but the subcategories are numerous. Different heat exchanger technologies are compatible with the truck application. In an ORC power system, the evaporator heat transfer is a key element and accurate evaporating heat transfer correlations are necessary to obtain an accurate estimation of the system performance. In this regard, there is a need to experimentally characterize the evaporation of working fluids for ORC power units in conditions similar to the final application, in order to validate existing correlations or derive new ones. Pumps are more rarely experimentally investigated while performance of those components are often limited, in particular when the driving chain is composed of an electrical motor regulated by a frequency drive. Once the boundaries of the study are defined, a model-based design methodology is developed. To the author opinion, the only reliable way to achieve an accurate performance prediction is to use experimentally validated models. To this end, in the frame of this thesis, various test rigs have been built and many ORC components, including pumps, heat exchangers and expanders have been experimentally investigated in laboratory. The results are used to develop and validate the simulation models. Obviously only a few number representatives of each component technol-

ogy could be investigated, with a limited number of working fluids, while the larger the base of experimental data, the more reliable the extrapolation results. A major part of this work is dedicated to the study of a radial-inflow turbine, the number of publications regarding experimental investigations of small-scale turbomachines integrated in ORC systems being limited. Interconnecting the component models and taking their operating limits into account, various ORC configurations are optimized during the design phase, depending on the considered heat sources, component technologies and the working fluid used. Including the economical considerations, the objective is the minimization of the specific investment cost of the systems. The main geometric characteristics of the ORC components being defined, the performance of the most promising systems for the application are then evaluated in off-design conditions through steady-state simulations. A first attempt is made to evaluate economical indicators, such as payback time and net present value, but due to the highly transient nature of the considered energy sources, steady-state simulations often overestimate the performance of the waste heat recovery unit. Dedicated control strategies ensuring safe and optimal operation of the ORC system during its operation are also required. In this regard dynamic modeling and simulation play a major role. Among others, they are useful to evaluate and optimize the response time of a system under transient boundary conditions, to develop and test control strategies and support the tuning of the controllers. In addition the thermal management has to be investigated since part of the heat recovered has to be rejected at the condenser of the ORC system. The impact on the activation of the truck cooling fan has to be quantified in order to avoid to consume a part of the power produced with the waste heat recovery system. Dynamic simulations are performed considering the most promising typologies and at the end of the process, a better estimation of the fuel savings, payback time and expected benefits for both the truck manufacturer and the truck owner is provided.

1.3   Thesis outline

Chapter 2 sets the boundaries of this study. The drivers for the fuel consumption of heavy duty trucks are presented as well as the existing possibilities to achieve this target. The working fluid selection process is presented and the heat sources and sinks used by the waste heat recovery system are identified. The investigated technologies of heat exchangers, expanders and pumps as well as their operating limits are described.

Chapter 3 presents the experimental campaign carried out on a radial-inflow turbine integrated in a small scale organic Rankine cycle power unit for low grade waste heat recovery application built at the Thermodynamics Laboratory of the University of Liege. The performance of the different components is analyzed in a wide range of working conditions for two low critical temperature organic fluids.

Chapter 4 describes the development of a mean-line model of the radial-inflow turbine investigated in Chapter 3. Modeling techniques of turbomachines are first reviewed as well as the main physical phenomena to take into account. The model is then confronted to the

available experimental data and the possibilities to extrapolate the model are discussed.

Chapter 5 is dedicated to the design of the ORC system architectures. The experimental studies achieved on the heat exchangers, volumetric expanders and pumps are first presented. The models of those components are then described and confronted to experimental data. The methodology to identify the most suitable design conditions is exhibited. A thermo-economic optimization is then achieved in order to minimize the specific investment cost of the ORC systems varying according to considered heat sources, ORC components and working fluid used. The performance is finally evaluated for several off-design operating conditions representative of the truck driving cycle and a first estimation of economical indicators (payback period, Net Present Value, etc) is provided based on the resulting fuel economy.

Chapter 6 deals with the dynamic modeling and simulations of the most promising ORC systems, identified in Chapter 5, for the current application and the given heat sources and sink conditions. A control strategy is developed and the performance of the units are evaluated over various driving cycles representative of the actual pathway of the considered truck. Based on those results, a new estimation of the fuel economy, payback period and net present value is proposed.

Chapter 7 finally summarizes the work achieved in the previous chapters. Conclusion and perspectives are drawn.

2 State of the art and field of investigation

Abstract

This study attempts to address this problematic of selecting the architecture, the expander technology, and the working fluid for a waste heat recovery organic (or non-organic) Rankine cycle system devoted to be coupled to a truck engine. In a first step, the main drivers leading to improve the engine thermal efficiency and the existing solutions are presented. Focus is then shifted to waste heat recovery technologies and in particular to the organic Rankine cycle systems. The boundaries of the study are defined in terms of considered heat sources and heat sinks and working fluid candidates. The constraints inherent to the integration of organic Rankine cycle unit on the truck are also discussed as well as the usage of the power produced by the waste heat recovery system. Finally, the investigated technologies of the organic Rankine cycle components are described and their operating limits are identified.

Keyword

State of the art, Boundaries, Truck efficiency, Waste Heat recovery, Organic Rankine Cycle

2.1 Introduction

In general, vehicles are responsible for 2 distinct types of emissions into the atmosphere: the emissions of GHG (including CO_2) contributing to climate change of the planet and the emissions of gases harmful to health. In the pursuit of a sustainable development approach, road transport has been engaged for several years in actions to reduce both the polluting emissions of vehicles through CO_2 objectives and Euro Standards. CO_2 objectives have already been briefly introduced. On the other hand, in order to limit harmful gas emissions, European regulations have been adopted since the beginning of the 1970s. They have been called Euro standards since 1990 and impose emission limits for Nitrogen Oxides (NOx), Carbon Monoxide (CO), Hydrocarbons (HC) and Particulate Matter (PM). In addition, since the first oil crisis in

1973, oil prices have been on the rise. This trend is reflected on the price of fuel, along with the policy of the governments, which makes it one of the most taxed products. From 1990 up to 2015, the general trend is strongly on the rise, based on records on fuel prices in France, with an increase of about 5 % per year [29]. However, large variations in the price of oil generate a significant dispersion around this trend. This continuous growth of the oil price coupled to the severity increase of the automotive emission standards along the years and the need for sustainability have led manufacturers to identify innovative solutions in order to improve the engine thermal efficiency and more generally the overall vehicle efficiency. Modern diesel engines dominate the commercial trucking industry with engine efficiency reaching, in 2015, around 43% [30]. Cummins [31] also indicated their engines can achieve a 9-15% fuel use reduction compared to established 2017-2018 standards, within the 2020-2030 time frame. This Figures rely, among other, on the integration of WHR ORC system alone responsible for 4-5% of the fuel economy. Because an important share of the combustion energy is lost in heat, it is convenient to recover and convert part of this thermal energy into useful energy and thus increase the vehicle efficiency. Various waste heat recovery technologies have been investigated during the past decades but thermodynamic cycle systems such as the Rankine cycle (Organic or not) are probably the most promising solutions. However, the key features to achieve more efficient engines are numerous and concern, among other, the improvement of the combustion process, air handling and friction reduction, turbocharging improvement, accessories electrification, tractor and trailer aerodynamics, tractor and trailer tires, etc.

2.2 Context

The main drivers for thermal efficiency improvements of internal combustion engines are environmental, regulation and economical. Environmental drivers have already been briefly introduced. The global warming due to anthropogenic activities is a fact and modifications in our lifestyle have to be achieved in order to limit the temperature increase to 1.5 to 2 $^{\circ}C$ in 2100 compare to 1900 emission levels and avoid the potential catastrophic consequence of the resulting climate change. In this direction, the European Commission has developed a strategy aimed at reaching this target. Various milestones have been established and include, among other, a reduction of the GHG emissions and an increase of the energy efficiency of 20 % in 2020 compared to 1990 levels. In 2050, the targeted emission reduction is of 80 % for which all sectors have to contribute. In particular, in the transport sector, the reduction could reach 60 %.

2.2.1 Regulation

The pollutant emissions from vehicles with a growth vehicle weight rating higher than 3.5 tonnes are governed by increasingly restrictive European standards. From the first of January 2014, a new Euro standard has been effective. This is the sixth standard on pollutant emissions for trucks and tractors since 1990. Those standards require truck manufacturers to regularly

review their engines. All new vehicles must now comply with the Euro VI standard, pursuant to Regulation No 595/2009 of the European Parliament and of the Council of 18 June 2009.

The European Union aims to implement these Euro standards in order to reduce emissions of polluting gases. These Euro standards are not intended to reduce CO_2 emissions but focus on four types of emissions:

- Unburned hydrocarbons (HC)

- Nitrogen oxides (NO_2 and NO_3)

- Carbon monoxide (CO)

- Particulate matters (PM)

Between the implementation of the Euro 0 and Euro 3 standards, pollutant emissions have been reduced by 70 %. The European Commission is also working to ensure that NOx emissions of vehicles are measured in real driving conditions using an on-board measurement device.

2.2.2 Economy

Despite recent improvements in diesel engine thermal efficiency, a considerable amount of energy is still rejected as heat both in the exhaust gases and the engine cooling system. The amount of waste energy is in the order of 60 % of the combustion energy. This energy, even if it is in form of high, medium and low temperature heat could be recovered and transformed into more useful forms so to increase the overall vehicle energy efficiency and consequently reduce the corresponding gas emissions, fuel consumption and cost. As an example, one can consider
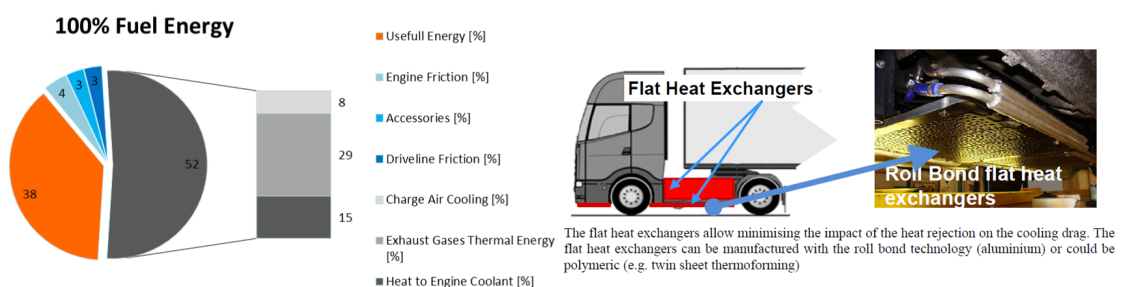
Figure 2.1 – Distribution of the energy consumption on a typical truck and representation of the integration of additional heat exchangers in the vehicle body panel [32]

a truck traveling 150000 km per year and consuming 35 l/100km with a fuel price of 1.1 €/l, an average fuel reduction of 4% provided by the waste heat recovery system would already provide a reduction of the fuel expenses of around 2300 €per year. This is encouraging since

11

the cost of the system is currently expected around 3200 €[33]. The payback period is then be below 1.5 year. Obviously the estimation of the savings resulting from the introduction of the WHR system is not that straightforward. Additional expenses such as the annual maintenance cost of the system have to be taken into account. On the other hand, the drawbacks linked to the integration of the WHR system on the truck have also to be considered. The ORC unit corresponds to an additional weight on the truck axles which thus results in an increase of the fuel consumption of the engine or a reduction of the load carried in the trailer. In addition, because only a part of the recovered waste heat can be converted into useful energy by the ORC unit, the remaining energy has to be rejected. This can be achieved through innovative but nonetheless costly strategies such as active shutters on the front end of the truck or additional innovative heat exchangers integrated in the vehicle body panels. The thermal energy can also be directly rejected at the front end radiator through the engine coolant but it then also increases the rejection needs of the truck and potentially the activation frequency (and power consumption) of the cooling fan. Finally, when the engines gases are considered as heat source, the integration of additional components on the exhaust line result in pressure drops that increase the engine back pressure and potentially reduce the engine efficiency.

2.3   Improving the truck efficiency

The improvement possibilities of the engine thermal efficiency are multiple. A non exhaustive list of the existing potential solutions is drawn in this section. According to Cummins [30], the largest contribution to the engine efficiency will result from improving the combustion process. Advanced combustion strategies can be implemented to optimize the heat release while keeping reduced the combustion temperature and the NOx emissions. In particular, the duration of the combustion could be reduced and the cylinder insulated to minimize the heat loss. Engine pumping losses can be partly addressed with an Exhaust Gases Recirculation (EGR) process also contributing to reduce NOx emissions. The diesel cycle efficiency can be improved increasing the compression ratio of the engine. New fuel-injection techniques involving higher injection pressure, finer spray-control and multiple injection are, among other possibilities, investigated [30]. Improving turbochargers can also help in this regard. Smaller leakage path reached based on new CFD and simulation techniques will improve the efficiency of both the turbocharger and the engine. Friction losses inherent to the engine can be reduced based on special coating techniques. Parasitic losses could also be reduced and the accessories electrified. For instance, the coolant pump losses could partly be addressed based on variable speed pumps. In the same way, the breathing of the engine could be enhanced based on flexible valve control instead of throttling system. Smart thermal management is also investigated. In this regards, energy storage and adequate heating techniques might help to keep the coolant and lubricating oil at acceptable temperature level, reducing the fuel consumption during start-up phases of the engine [34]. Electric hybridization could also investigated in order to keep the downsized ICE operating conditions in the maximal efficiency region. A lot of attention is also paid to the aerodynamics of the vehicles since the drag reduc-

tion could be a major contributor to fuel savings [35], [36]. Aerodynamic improvements can be made to all parts of the truck: the front, the side and the back. Generally, aerodynamics improvements are seen as one of the most cost-effective ways to reduce truck fuel consumption and carbon emissions. Low rolling resistance tires play a major role in reducing fuel use from trucks. Keeping the tires well inflated is extremely important. Monitoring the tire pressure can help to keep track of this. Fuel consumption does not only result from the on board technology but also from the driver behavior. Around 15 % of fuel could be saved with proper driving techniques. Therefore companies started training their drivers and rewarding the latter according to the money they save for the company. Predictive cruise control and autonomous vehicle might also make the difference. Waste Heat Recovery systems are suited to convert the energy initially lost whether in the gases or the coolant. After treatment improvements can be achieved through a lower back pressure and a closer coupling of the system with the engine in order to avoid undesirable heat losses. Insulation of the exhaust line could also results in a higher efficiency of the waste heat recovery system. It is probably worth noting that none of the solution is sufficient by itself. The different possibilities of improvement should be combined and the interactions of the various systems involved should be taken into account during the optimization stage. For instance, a better engine efficiency might also mean less energy available for the waste heat recovery system. Obviously, the described improvement are costly and there is probably an interest in introducing improvement progressively according the benefits they provide and the complexity and cost of their implementation. In this regards, enhance the driving techniques is probably the simplest solution to achieve a significant fuel economy with a reduced investment. Today state of the art of combining innovative techniques in trucking technology is probably the Daimler's Freightliner supertruck. The hybrid, diesel-electric, vehicle is equipped with a solar roof, smart aerodynamic features, a waste heat recovery system, and many other improvement ([37]) reducing the fuel consumption to 19 l/100 km, compared to 33 l/100 km in average in Europe.

2.4 Waste heat recovery technologies

Engine turbocompound consists in 1 (or more) turbine(s) converting the kinetic energy of the exhaust gases into mechanical energy. It is usually placed downstream of the turbine of the turbocharger, which can be considered as a waste heat recovery system. Air-craft engines were already equipped with the technology during the World War II. Scania Company has been producing trucks equipped with turbocompound engines since 1991 and Volvo since 2001. The current trend, in both turbocompound and turbochargers is the electrification of the systems in order to, among others, avoid the drawback of mechanical coupling due to the high speed of the turbine, remove the delay in the boost of the turbocharger, and enable the use of the latter in situations where the drive energy in the exhaust gases is not sufficient. The drawbacks of these technologies is the need of high efficiency high speed generator and a resulting significant back-pressure.

The Brayton cycle, first patented by John Barber in 1791, and then developed by George

Brayton in 1872 is a thermodynamic cycle mainly used in gas turbine power plants and jet engines. Few studies have been conducted to evaluate the benefit of waste heat recovery through a Brayton cycle for a mobile application. Pattersson et al. [38] showed by simulation an improvement in engine efficiency of approximately 7 %. However Heat2Power [39] propose Brayton solutions for automotive, truck, marine, railway and solar applications, promoting low cost, small footprint and high relative engine efficiency increase (25 %) [40].

The Thermoelectric generator (TEG) principle was discovered in 1821 by Thomas Johann Seebeck. It was observed few materials can generate electric power from heat, and use electricity to function as heat pumps providing active cooling or heating: such materials are said to be thermoelectric. Small pieces of thermoelectric material (TE elements) are connected alternating p-type and n-type elements. They are connected in series electrically, but thermally in parallel. A multitude of couples forms a TE-module and when a heat source is applied to the hot plate, and the cold plate is maintained at a cold temperature, a voltage difference is created between the cold and hot plates, that can induce a current in an external circuit. The efficiency of a TEG depends on the material as well as on the temperature drop across the device. An application on board a vehicle described in the literature is the Hi-Z/Mack Truck Generator. This system uses the waste heat of a class 8 Diesel Truck to produce about 1 kW electric power.

The Rankine cycle is a thermodynamic cycle which converts heat into work. The heat is supplied externally to a closed loop, which usually uses water or an organic fluid as the working fluid. The basic system is composed of 4 main components: Exhaust gas heat exchanger, expander (+generator), pump, and the condenser.

It is of course a non exhaustive list and other waste heat recovery technologies could be considered. For instance, in his review, Legros [41] investigated thermo-acoustic generators, 6-stroke engines, Stirling engines and thermo-photovoltaic generators. He also compared the different technologies in terms of gain in engine efficiency, cost, technical maturity, packaging and weigth to power ratios. He concluded that turbocompound and ORC technology remain the most likely solution to recover the waste heat on mobile applications.

2.5 Organic Rankine cycle system

During the past few years, the interest in ORC systems for waste heat recovery led to numerous works in the subject. In 2008, Lemort [42] investigated the integration of a scroll expander in ORC using R123 and recovering the heat from compressed hot air. The expander was a modified open-drive air scroll compressor. The thermal power at the boiler was ranging from 10 to 20 kW and the expander power reached 1.4 kW with an isentropic effiency of 68 %. In 2011, Quoilin [43] proposed solutions to improve the performance of the test-rig. The fluid R123 was replaced by R245fa and a liquid receiver was introduced. Work was also performed to reduce the leakage path of the new, smaller, expander and on the heat source configuration. The net output power has been increased by 25 % on the new test rig and slightly higher

expander efficiency values were obtained, above 70 %. In 2014, new improvements were proposed by Declaye [44]. The major drawback of air-scroll compressor is the tightness, requiring specific containment solutions when refrigerants are used. A magnetic coupling was used to link the shafts of the expander and asynchronous generator. Measured performance of the prototype was very promising in a wide range of operating conditions. The maximum shaft power was 2.1 kW and the maximum achieved isentropic efficiency was 75.7 %. In the same time, Legros [41], instead of using retrofitted compressor, designed a scroll expander. The target was to introduce the prototype in a new Rankine cycle system, using water and devoted the recover the heat from exhaust gases of a gasoline engine. The performance achieved with this first prototype was however limited. The low isentropic efficiency, around 12% and high filling factor values above 6 suggested high internal leakage flow rate. In 2016, Oudkerk [45] investigated a 5 cylinders swash plate piston expander integrated in small scale ORC unit recovering the heat from thermal oil and using R245fa as working fluid. Isentropic efficiency values between 30 and 53 % were achieved. Those values were justified by under expansion, internal leakages and mechanical losses.

Numerous works are also specifically dedicated to truck applications. In 2011, Espinosa [22] investigated ORC and TEG technologies as potential candidates as waste heat recovery systems on a heavy duty truck. Different architectures of ORC systems were compared and constraints resulting from the coupling of an ORC to an engine were partly discussed (heat rejection, energy usage and packaging). Fluids R245fa and water were identified as suited fluid candidates for experimental investigations. In 2016, Gunnar [46] designed and built a demonstrator of ORC unit recovering the heat from the recirculated gases of a 12.8 l diesel engine. The system was using a reciprocating expander and water as working fluid. An expander power around 3 kW could be reached for a thermal power of 30 kW with an isentropic efficiency around 50 %. The same year, Daimler [47] proposed a comparison of cooling system designs for a WHR ORC on a HDT. Two architectures were compared in terms of fuel economy. The base ORC design, using directly the engine coolant and radiator to cool down the condenser, revealed a fuel efficiency benefit of 2.6 %, while a more complicated design, including dedicated additional radiator in the front end of the truck, led to 3.1 % of fuel economy. Cippollone [48] designed and experimentally investigated an ORC for WHR in a Compression Ignition (CI) Internal Combustion Engine (ICE), a IVECO F1C engine, using fluid R236fa and sliding vane machines as pump and expander. A methodology in order to map the engine operating point in terms of exhaust gases mass flow rate and temperature was first proposed. Mechanical power recovered ranged from 0.7 kW up to 1.9 kW, with an overall cycle efficiency from 3.8 % up to 4.8 % respectively while the maximal overall expander efficiency values were ranging between 47.5 % and 53.3 %. In 2017, Pascual [49] modeled and experimentally investigated an ORC unit using ethanol as working fluid and a swash plate expander to recover the heat from a gasoline engine. Among other a economic evaluation of the system was proposed and the impact of increased cooling load, weight and engine pumping loss resulting from the ORC coupling were investigated. An increase of engine efficiency up to 4 % was announced. Di Battista [50] tested a single stage impulse axial turbine

driving an electric variable speed generator and an AC/DC converter. The overall net efficiency of the power unit was around 2-3 %, with a mechanical power production equal to 2.5 kW, when the thermal power transferred from the ICE exhaust gases was 55 kW.

The fluctuating nature of the waste heat source makes waste heat recovery on truck a challenging task. For this reason, many authors focused on dynamic modeling and/or control of ORC units devoted to recover the wasted heat on mobile applications. Among other, Peralez [51], Feru [52], Grelet [53] and Hernandez [54] investigated and implemented different control strategies of the ORC units.

2.5.1 Heat recovery potential

Multiple heat sources can be considered to recover the thermal energy wasted by the engine. A list of the potential heat sources available on a truck equipped with an Exhaust Gas Recirculation (EGR) system is given in Table 2.1. In this table, the temperature levels of the heat sources and the corresponding capacity flow rates are compared. Because increasing the number of sources will increase the level of complexity in terms of packaging and control and the cost of the system, it is proposed, in this study, to investigate only two heat sources. In [53], a second law analysis is performed and shows, based on the work performed in [55] and [56], that the most interesting sources are the exhaust gases, and the recirculated gases, to which correspond the highest temperature levels. The charged air is not considered because a modification of its temperature level might largely affects the performance of the engine. Ram

Table 2.1 – Description of the heat sources available on the investigated truck (US10 11l 320 kW)

Heat source	Temperature [$^\circ C$]	Capacity flow rate [kW/K]
Exhaust gases	Mid to high (310)	High (0.16)
Recirculated gases	High (450)	Low (0.04)
Charged air	Low (95)	High (0.2)
Engine coolant	Low (90)	High (4)
Oil	Low (90)	Low (N.A.)

air resulting from the vehicle motion (and eventually the fan) is the only heat sink available on a truck. This air is used as a secondary fluid to cool down the different heat exchangers of the cooling module, which typically includes the engine radiator, the charge air cooler, the air-conditioning radiator and the cooling fan. Adding a new heat exchanger (a direct condenser or the radiator of an indirect condenser) in the front end of the truck is challenging because of the limited free space. Moreover, the limited heat rejection capacity margin of the cooling module is constraining the heat recovery and might lead to more frequent engagements of the fan, which consumes a lot of energy. A configuration without excessive fan power consumption due to the ORC system is the use of the engine coolant in order to feed an indirect condenser as studied in [56]. Innovative solutions such as the increase of the heat rejection capacity

using part of the body panels as heat exchangers (flat heat exchangers) functionalizing the aerodynamic under-body or parts of the side body panels were nonetheless proposed [32] but might be more complex to implement. Finally, another possibility, the one retained in this study, is the use of a low temperature radiator dedicated to the Rankine condenser and placed between the charge air cooler and the engine radiator. This configuration has been shown to lead to an increase in net output power of the WHR system of about 11 % compared to the use of the engine coolant [53]. Combining the 2 investigated sources and the single heat sink, 6 possible topologies are identified for this study. They are shown in Figure 2.2. Only the 5 first architectures are considered in this work.
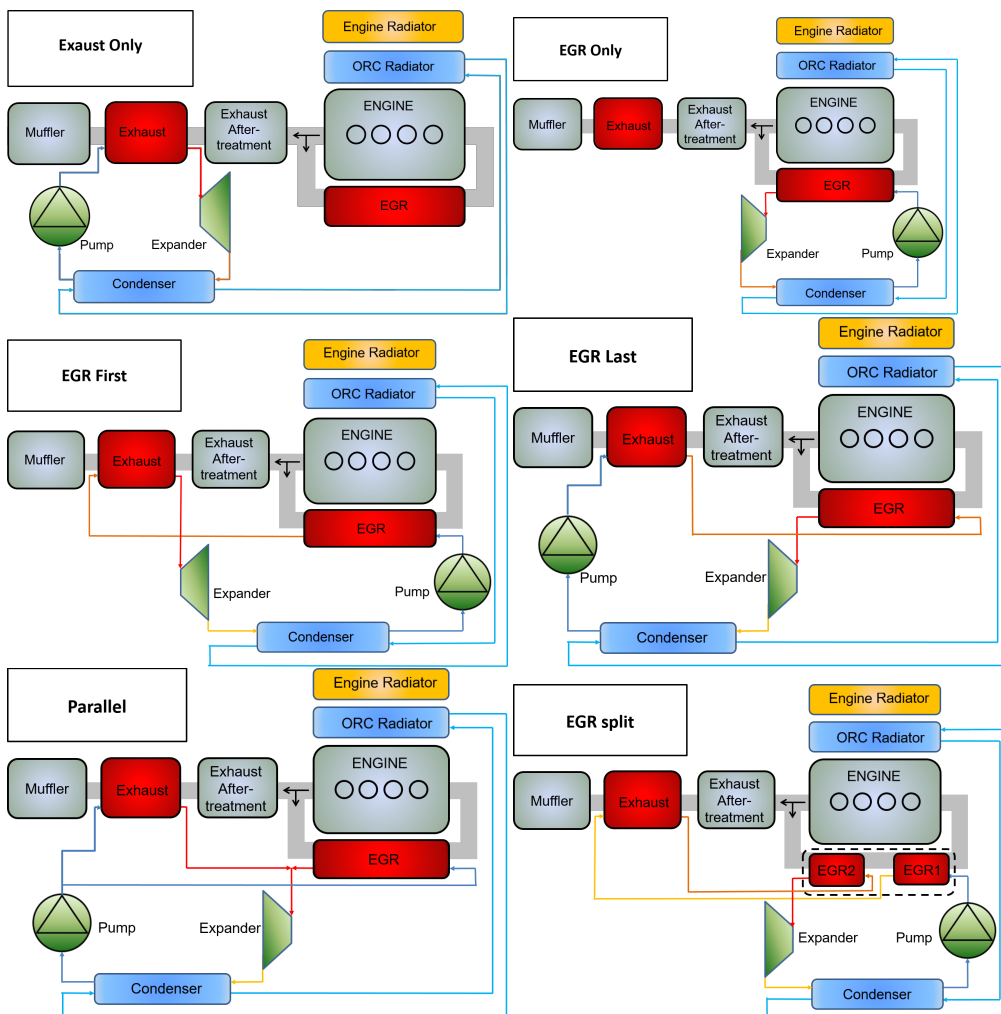

Figure 2.2 – Description of the investigated ORC system topologies depending on the considered heat sources and their combinations.

2.5.2 Working fluid selection

A major part of the research activities concerning the adoption of the Rankine technology in the automotive domain is dedicated to the selection of the working fluid and of the expansion machine. Numerous substances are available on the market and the selection of working fluids has been treated widely in scientific publications. Most of the time, a comparison between a set of fluid candidates in terms of thermodynamic performance and based on a thermodynamic model of the cycle is proposed. Quoilin [43] proposed some guidelines and indicators (thermophysical properties, thermodynamic performance, environmental impact, etc) when selecting the most appropriate working fluid. He also showed that very few studies include additional parameters considering the practical design of the ORC system, mainly because of the difficulty to define a proper function for a multi-objective optimization of the cycle, and he concluded that economic considerations should drive the final choice. Typically, the three working fluids, which are currently the most frequently investigated ([57], [58], [59], [60], [61], [62]) are HFC-R245fa, water and ethanol.

In this study, it is proposed to identify the suited medium for the application through a screening method starting with a wide range of working fluids. In the industry, the proprietary software Refprop [63] is the reference for the evaluation of the thermophysical properties of fluids, compressible or not, and mixtures. In this work the open-source CoolProp [64] has been selected as fluid library and only pure and pseudo-pure fluids are investigated. A set of 122 possible substances, which are listed in appendix A, is thus identified as starting point. Criteria are then defined to identify the most suited fluids and try to reduce the list if possible. *The first established criterion* is the environmental impact. Thus fluids with non-zero Ozone Depletion Potential (ODP) have been eliminated. Indeed those fluids were phased out through directives initiated by the Montreal Protocol. In the same way, fluids characterized by a Global Warming Potential (GWP) above 150 (based on the GWP 100y definition of the AR4 report emitted by IPCC) are also taken off the list. This excludes fluid R245fa (GWP 1030) because it is still frequently used while possible alternatives (HFO) have already been proposed by fluid manufacturers. At this stage, 82 fluids are remaining. *The second proposed criterion* concerns safety. Based of the safety data sheet of each fluid, substances that may be harmful to human health (e.g. fatal if swallowed or enter airways, toxic in contact with skin, suspected of causing cancer, etc) are not considered as possible candidates for the ORC system. There remain 60 potential fluid candidates. *The third criterion* deals with thermophysical characteristics of the fluid. Fluid characterized with a boiling and critical temperature respectively above and below 150 $°C$ have been taken off the list. This temperature limit is selected according to the temperature of the investigated heat source (above 200 $°C$) and the limited temperature of the coolant heat sink (around 60 $°C$). At the end, 13 potential candidates working fluids are identified and presented in table 2.2, in descending order of critical temperature.

Table 2.2 – Potential fluid candidates resulting from the proposed selection method

Water (R718)
DimethylCarbonate
Ethanol
Cyclopentane
Acetone
Isopentane (R601a)
SES36
R1233zd(E)
cis-2-Butene
trans-2-Butene
R245fa
n-Butane (R600)
R1234ze(Z)

2.5.3 Constraints

The integration of the ORC technology in the automotive domain generally implies interactions between the system with the truck components and constraints to be observed.

Position of the evaporator on the exhaust line

In conservative designs of mobile Rankine cycles recovering waste heat recovery from the exhaust line, the evaporator is mostly situated behind the Exhaust After Treatment System (EATS) of the exhaust gas. This configuration has the advantage that the after treatment of the exhaust gas is not disturbed. On the other hand the exhaust gas temperature decreases by 50 K to around 100 K in the after treatment system. The EATS thus limits the efficiency of the waste heat recovery. Another disadvantage of the conventional configuration is the possible corrosion and damage of the Rankine evaporator due to soot and ammonia from a possible SCR system. Research might focus on the possibility of an EATS adapted to lower exhaust gas temperatures. The advantage of this configuration would be founded in better heat exchanger efficiency due to higher heat source temperatures, which leads to reduced packaging needs. A good adaptation of the EATS configuration to low exhaust temperature could lead to a higher heat recovery efficiency but also in a gain of the after treatment efficiency since the after treatment system inlet temperatures could be controlled.

Heat rejection

Recovering the waste heat from an engine also implies to reject a part of the thermal energy through a condenser. The basic solution consists in an additional heat exchanger placed in the front end of the truck. The working fluid might then be cooled directly by the fresh air coming through the calender or by a coolant. However, this results in an additional heat rejection for

the cooling package of the truck, which has to be limited in order not to decrease the engine performance, ensure a proper cooling of the engine and avoid additional fan activation. The additional heat exchanger will also impact the cooling drag of the truck. Solutions exist in order to reduce the heat rejection added to the cooling package and the cooling drag. Most of them consist in additional innovative heat exchangers integrated in vehicle body panels. On the other hand, the vehicle heat rejection system is normally designed to comply with severe conditions (high thermal load, low vehicle speed, high external temperature, etc). In other words, in most of the operating conditions there is a heat capacity margin. Typically, the additional heat rejection is limited to 30 to 40 kW according to truck manufacturers. However, for full charge engine working points the cooling capacity of the vehicle might not be sufficient to cool the engine and the ORC condenser which leads to a necessary, but energy costly, fan engagement. An indirect heat transfer, using a caloric fluid to recover heat from the exhaust gas and transfers the heat to the Rankine cycle, present advantages but also increases the complexity of the overall waste heat recovery system, an additional weight and a loss in waste heat recovery efficiency. Nevertheless such a heat storage would enable to decouple the Rankine cycle from the internal combustion engine and to produce energy when the vehicle thermal management permits it. Another advantage of an independent Rankine cycle is the possibility to develop an independent control strategy for the waste heat recovery cycle.

Power use

The use of the net power produced is key element in designing the WHR system. Typically 2 possibilities are distinguished: the production of electrical power through a generator and the mechanical coupling of the expander and engine shafts. The main advantage of an electrical power production concerns control and power optimization since it allows to control the rotational speed of the expander and then, if a volumetric expander is used, the evaporating pressure. Whether turbines or volumetric machines are considered, the control of the expander rotational speed enables to optimize the power production and adapt it to the vehicle electrical consumption. However, the latter can hardly be predicted and is today too low (around 1.5 kW [53]) to absorb the production of an ORC system which could be up to 10 kW depending on the engine operating point. Therefore electrical power production is usually paired with accessories electrification. Espinosa [22] investigated the electrification of accessories increasing the power demand up to 4.5 kW in peak conditions, which does not meet the ORC system production. An alternative retained in this work is to couple the ORC generator to an electric motor through batteries but it would also increase the system cost, weight and complexity. Coupling the expander and engine shafts mechanically appears as simplest solution for a WHRS. However, it also implies the loss of a degree of freedom for the optimization and control the WHRS: the regulation of the evaporating pressure through the rotational speed of the (volumetric) expander is no more possible.

Other considerations

Concerns are also related to the gases temperature. The NOx reduction strategy through the EGR system should not be disturbed by the WHR system so the same temperature level should be achieved for the gases at the outlet of the EGR cooler. On the other hand, the temperature level of the exhaust gases should be kept above a minimum to avoid the condensation of eventual acids and the corrosion of the tail pipe. As for turbocompound and turbochargers, the addition of an element in the tail pipe, here a heat exchanger, is a source of pressure drop increasing the back pressure of the engine. This increase in back pressure should be considered and minimized during the design process of an WHR ORC system. Espinosa [22], performed simulations to characterize the increase in back pressure on the engine performance. The impact was shown negative on fuel consumption (around 1 % for 50 mbar) but positive on NOx reduction. The weight is generally another key element in mobile applications. Increasing the weight on the axles of the truck will lead to an increase in fuel consumption. A possibility could be to reduce the load embedded in the trailer to compensate the weight increase on the axles but it would thus reduced the efficiency of the transport vehicle. Therefore the additional weight corresponding to the introduction of a WHRS in the truck should be minimized. In addition, free space is usually rare in vehicles. This means that weight is not the only concern but the volume and probably the shape of the components should also be taken into account in order to avoid packaging issues. The cost is probably the factor that will determine if the WHR technology will be developed until chain production or if it will be forsaken. Obviously the cost linked to the additional system should be minimized and benefits ensured for both the manufacturer and truck owner based on the fuel consumption reduction. A step forward could be that the actors involved (OEM, tear 1 and 2 suppliers) agree on the selection of a single working fluid, which would facilitate the mass production of the ORC components thus reducing their cost.

2.6 Heat exchanger technologies

The heat exchangers are other important components of the Rankine system. Their thermal and hydraulic performance affects directly the performance of the Rankine system but it is also directly linked to their size and therefore their weight. In automotive applications, tube and fins and shell and tubes heat exchangers are used most of the time. In waste heat recovery applications, plate heat exchangers are often investigated. In this study a shell and plate heat exchanger designed to recover the heat from a gasoline automotive engine is experimentally investigated. This technology is thus retained for the high pressure heat exchangers of the Rankine systems. On the other hands, a brazed-plate type condenser was tested in laboratory and therefore considered for the low pressure heat exchanger of the ORC unit.

2.7 Expansion devices

From the selected working fluid results the optimal working conditions in terms of pressure ratio, temperatures and mass flow rate that enable the Rankine system to produce the maximal power. In other words, the optimal working conditions of the expansion machines are closely linked to the selected working fluid. On the other hand, numerous expander technologies are available on the market. Typically a distinction is made between positive displacement machines, decreasing the working fluid pressure by increasing the volume of the chambers containing the fluid, from turbo-expanders converting the energy content of the fluid into kinetic energy and then in mechanical energy through different blade rows. Positive displacement machines are generally categorized according to the type of motion of the rotor. This motion can be orbital such as in scroll machines. In rotary machines, the rotor(s) rotate(s) around its (their) axis, such as in screw, vane or roots expanders. In reciprocating machines, the axial motion of the piston is often converted into rotation of the shaft, for instance through a swash-plate or a cranck. In turbomachinary, the technologies are generally distinguished according to the direction of the flow (axial, radial-inflow, radial-outflow) at the inlet and outlet of the device and according to the degree of reaction (action or impulse vs reaction). In this study, several expander technologies, including volumetric machines and a turbine, could be investigated experimentally. Those are briefly described here but additional information about each technology can be found in [13]. Then their limitations are compared in terms of pressure ratio, inlet temperature, rotational speed and built-in volume ratio, etc through a literature review.

2.7.1 Scroll expander

Scroll expanders are orbiting machines composed of two involutes, one being the central symmetry of the other. Generally, one involute is fixed while the other one shows an orbiting movement. Their relative position defines a series of chambers acting as suction, expansion or discharge chambers.

The expansion of the fluid drives the orbital motion of the moving involute. Scroll expanders can be compliant or kinematically rigid. Compliance allows the scroll expander to adapt itself to the operating conditions with a degree of freedom along the radial, the axial, or both direction, leading to an increased efficiency. Kinematically rigid expanders cannot adapt to transient conditions, especially in the presence of liquid fluid or debris, which can cause damage when they are trapped between the involutes.

The scroll machine was patented by the French Léon Creux as an engine in 1905. But it is only after the 1980s that the technology has been used as a compressor in the refrigeration sector. The first publications on the machine operating in expander were released only in 1994 [65]. Today, the scroll machine is part of the dominant compressor technologies in air conditioning while it is only proposed by few companies as expansion machine (among which, Eneftech and Air Squared). Nevertheless, its high performance, combined with a reduced number of

moving parts, high reliability, broad power range and high availability [65] make the scroll expander a good candidate in ORC designed for small scale heat recovery.

The scroll technology can be classified into 2 categories. The first category, called here hermetic type, generally consists in lubricated machines used in refrigeration systems. Those machines accept high inlet pressure levels (up to 30 bar) and enables to avoid external leakage. However a constant lubrication is required. The second category, called here open-drive type, typically concerns scroll devices in air compression applications and which can also operate without the use of a lubricant. Beside the absence of oil, those machines are generally characterized by a higher built-in volume ratio (around 4), a higher temperature limit (up to $200\,^\circ C$) and are also easier to convert from compressor to expander. However, the absence of tightness, leading to external leakages of working fluid, is a major drawback and implies to set up containment solutions.

2.7.2 Screw expander

Currently, most of the screw expanders are twin-screw machines made up of two inter-meshing rotors, a male and a female, helically toothed and housed in a casing. Working chambers are delimited by both the casing and the rotors and evolve from an extremity of the rotors to the other where are located respectively the suction and exhaust port. Thus, the same chamber becomes, successively, a suction, an expansion, and finally a discharge chamber. For this technology, the volume ratio is not only a function of the geometry of the rotors but also depends on the angular position of the high-pressure control edge. The lower the angular position of the control edge the larger the built-in volume ratio but the smaller the swept volume. Hence, for given rotor dimensions, a trade-off has to be found between increasing the swept volume or the built-in volume ratio.

The early developments of the screw machine were made in 1930 by Alf Lysholm. Initially, the screw compressor was used as an air compressor and enabled to cover a range of power few covered so far (between reciprocating compressors and centrifugal compressors in terms of flow and pressure ratio). In the 1950s, the invention of the flooded compression enabled to produce machines at a lower cost (without timing gears and gaskets) and more effective. The screw compressor then became popular in refrigeration. But it is not before the 1970s that major developments have been made on screw compressors (evidenced by the large number of patent filed in the last 40 years on this technology, including patents on screws profiles). These developments can be explained by the arrival of performing tool machines (to achieve good tolerances) and the development of numerical simulation tools. It is also in 1970 that the screw machine was used for the first time in expander mode by Hydrothermal Power Co. It was in geothermal applications designed to produce a power of the order of 1 MWe.

Twin screw expanders can be split into 2 categories: synchronized through timing gears (oil-free) and unsynchronized (oil flooded). The timing gears prevent any contact between the rotors so the machine can be run without lubricating oil. However, it results a larger

internal leakage path and flow rate, which can be reduced by an increased rotational speed of the machine. In unsynchronized machines, a hydrodynamic contact between the rotors is ensured by a lubricant. The maximal circumferential speed is reduced in order to limit the hydrodynamic losses.

2.7.3 Piston expander

A reciprocating (or piston) expander is composed of one or several cylinders in each of which moves a piston in a reciprocating fashion from the Top Dead Center (TDC) to the Bottom Dead Center (BDC) [13]. Fluid goes in and out the cylinders through orifices equipped with valves. The most used types of valve are poppet valves, sleeve valves, and rotary valves. Both supply and exhaust valves can be actuated in order to control the volume at the end of the supply process and at the end of the discharge process. Piston expanders can be categorized according to the fluid flow inside the cylinder. In uniflow expanders the supply port is located close to the cylinder head while the exhaust port is located at the opposite cylinder extremity. Those ports generally consist in sleeve valves. In this configuration, the cylinder head is not cooled down during the exhaust process which result in lower heat losses during the suction phase. However, the compression starts earlier during the upward stroke resulting in a higher compression work and requiring a higher clearance volume in order to prevent over-compression [66]. In crossflow expanders both the supply and exhaust ports are located close to the cylinder head and consist in poppet valves or rotary valves. The compression work and clearance volume are lower than in uniflow expanders. For same stroke and displacement, the machine can admit a larger flow rate and lead to larger power production but the theoretical isentropic efficiency of the machine is lower because of the larger under-compression loss. Multiflow expanders are based on a combination of the two previous configurations [13].

A distinction can also be achieved according to the mechanisms used to transform the reciprocating motion of the piston(s) into a rotational motion of the shaft. In radial piston expanders, the crank mechanism is similar to the one used in internal combustion engines and relies on the use of a crankshaft connected to the piston. In axial piston expanders where several pistons are typically placed in parallel to the machine shaft are used swash and wobble plate mechanisms . Axial piston expanders, which are similar to mobile air conditioning piston compressors, are more compact than expanders with crank train mechanisms. For this reason, they present a large interest for ORC systems used for waste heat recovery from trucks engines. The tilt angle could also be adjusted in order to modify the piston stroke and hence the expander displacement [13].

The main developments of the piston were made during the industrial revolution. Few studies have been carried out between 1920 and 1960, but a renewed interest for this expander appeared in the 1970s. For example, research has been conducted on its use as a steam engine for passenger car [67]. Finally, since 2000, researches on piston expanders have focused, among other, on heat recovery from internal combustion engines [68], [69]. Today, few companies are

active in the field of small scale power production: Amovis, Exoes, Ranator, etc

2.7.4   Vane expander

A vane expander generally consists in a cylindrical rotor in rotation in a cylindrical stator housing. The rotation axis of the rotor is offset from the axis of the housing and vanes are inserted in slots that are spread out on the rotor periphery. The vanes are pushed out by a spring or other mechanisms (e.g. working fluid pressure) and pressed against the stator, thus delimiting chambers. Vane expanders using springs enable better volumetric performance, the vanes being pushed against the housing, but lead to higher friction losses compared to the system using the working fluid pressure. Therefore, the latter achieves better isentropic efficiency [70].

The rotary vane pump was invented and patented by Charles C. Barnes in 1874. Those devices are now commonly used in the automotive industry as, among other, supercharging, power-steering and automatic-transmission pumps. According to Mattei, the first use of a rotary vane compressor with an electric motor was in 1958. The first version of the turbosteamer [19] used 2 vane expanders for the dual loop system. Water was used in the high temperature loop while ethanol was used in the low temperature loop of a waste heat recovery system devoted to recover the heat from a 4 cylinder spark ignition engine. No record was provided regarding the performance of the machines. However, all the components of the turbosteamer were tested separately and because "*the tests on the vane-cell expanders were disappointing*", they were replaced by axial-piston expanders. Then in the second version of the turbosteamer, the architecture was simplified and reduced to a single loop using an axial impulse turbine as expander.

2.7.5   Root expander

Roots expanders often consist in two meshing male rotors comparable to a twin-screw expander. The rotors can be twisted, or not, along the axial direction. The main difference with screw expander results in the built-in volume ratio, which is in theory equal to 1. For this reason, roots machines are often refereed as blowers instead of compressors. The fluid enters the machine, then is trapped in a suction chamber comprised between the housing and the rotors and moved to the exhaust port where the fluid is released to the exhaust line. To the author knowledge, the only publication dedicated to the experimental study of a roots expander integrated in a small scale ORC is [71].

2.7.6   Radial-Inflow turbine

The radial-inflow turbine (RIT) often consists in 4 main elements. The flow enters the turbine stage through a single duct in an inlet volute (or scroll), which accelerate and distribute the fluid uniformly around the turbine periphery. The cross-sectional area of the scroll generally

decreases around the circumference [72]. The flow then passes through a nozzles blade row, in which is provided further acceleration and an increase in circumferential component of velocity [73]. The fluid goes through a vaneless passage before it enters the rotor row, in which the kinetic energy of the fluid, as it expands, is converted into mechanical energy of the shaft. Finally, an exhaust diffuser often follows the rotor row to convert a part of the rotor exit velocity to static pressure. Thus radial-inflow turbines are similar to centrifugal compressors but their names and function is different while the flow and the rotation are reversed [72]. In some designs, the nozzle vanes are omitted for economical reasons and avoid eventual erosion of the blades while the scrolls are used as vaneless nozzles. Those designs are characterized by higher frictional losses mainly because of the non-uniformity of the flow at the impeller inlet and the greater distance traveled by the accelerated fluid flow. They are often used in turbochargers, in which efficiency is sometimes considered not important since in most engines the amount of energy in the exhaust gases is much more important than the energy needs of the turbocharger [72]. The main advantage of the radial-inflow technology is the work produced by a single stage is twice or more times the work achieved in an axial turbine stage because the former usually has a higher tip speed than the latter. For a given mass flow rate, because the power vary with the square of the tip speed, the work is greater than using a single-stage axial-flow turbine. The cost of radial-inflow turbines is also much lower than in axial-flow turbine but the achieved efficiency is also generally lower. Radial-inflow turbine can be cantilever type. Blades are then often two-dimensional and use non-radial inlet angles. The acceleration is entirely provided by the stator as in impulse turbines. This type of turbine is infrequently used because of low efficiency and production difficulties. The other types are the mixed-flow radial-inflow and the radial-inflow turbines that have slight differences at the blade inlet of the impeller. The radial-inflow impeller provides a full 90° change to the flow from the inlet to the exit. In the mixed-flow impeller, the blade inlet is at a 45° angle with the axis [72].

The first use of radial-flow turbine in gas application was in jet engine flight in the late 1930s. It was considered natural to combine the RIT with a centrifugal compressor, matching the thrust from the two rotors. The turbine efficiency would also be higher than for a compressor with the same rotor because of the accelerating nature of the flow. The interest in the technology is now growing in the transportation and chemical industries. The turbine can be used in turbochargers for both SI and CI engines or to power helicopters and as standby generating units. RIT are also used in the petrochemical industry as gas liquefaction expanders, and other cryogenic systems. Those are only few of the many existing applications [72].

2.7.7 Operating limits

The description of the operating limits is required for the future simulation of the expansion devices.

Displacement and rotational speed

In practice, the range of scroll machine sizes is very broad and extends from mini-scroll of a few cubic centimeters to very large machines. For instance, displacements of air-conditioning and refrigeration scroll compressors available on the market range commonly from 3 to 850 cm^3, with built-in volume ratios close to 3, which means expander displacements range approximately from 1 cm^3 to 283 cm^3. Currently, the trend in the compressor industry is to increase their size. According to the values observed in literature, the displacement of the scroll expander generally varies from 12 cm^3 up to 73 cm^3. Regarding the rotational speed, it often varies within a range of values between 1000 and 4000 RPM. However, speeds around 10,000 RPM are reached with scroll compressors in vehicle air-conditioning applications. This maximal speed is, among other things, limited by the anti-rotation mechanism.

Currently, screw expanders are often characterized by high capacities. Thus expanders whose capacity varies between 10 and 1100 l/s for produced powers of around 20kWe to 1 MWe can be found in the literature [74]. Regarding the speed of these machines, it can reach relatively high values, up to 25000 RPM [75].

In theory, the displacement and rotational speed of piston expanders can reach values similar to those obtained for internal combustion engines. In practice, displaced volume flow rates for ORC applications currently range from approximately 1.25 to 75 l/s. In Exoes [33], for example, the rotational speed of these machines usually varies between 500 and 6000 RPM. The upper limit of the speed may be due to mechanical constraints on the valve mechanisms. The limit on the rotational speed can also be resulting from the importance of friction losses. The lower bound of the speed is relatively low and results from reduced internal leakage in this type of machine.

According to Badr [76], displacements of vane expanders vary from 3 to 40 cm^3 with a maximal rotational speed of 4000 rpm.

Roots expanders show power ranging approximately from 1 to 30 kW with a maximal rotational speed of roughly 20000 rpm. They are typically equipped with timing gears [13].

For radial-inflow turbine, the speed limitation is generally expressed in terms of blade speed ($U = \omega r$) and limited to 500 m/s [77].

Built-in volume ratio and pressure ratio

In air-conditioning and refrigeration applications, the built-in volume ratio of scroll machines generally ranges from 1.5 and 3.5. Beyond 3.5, it becomes difficult to ensure adequate performance of the machine for a reasonable manufacturing cost because of the difficulty to maintain a good lateral seal between the spirals while increasing the number of pairs of contact points. Air compressors however are characterized by higher volume ratios (up to 4). Machines with built-in volume ratio greater than 4 exist (e.g., a scroll with a built-in volume ratio of 5.25

was proposed by Air Squared). The limitation on the pressure ratio of scroll machines is usually a consequence of the maximum allowable inlet temperature (compressor mode). However, an higher pressure also implies an higher load on the bearings of the machine. In air-conditioning and refrigeration systems, the pressure ratio can reach a value of 11. In expander operation, a pressure ratio of 15 was achieved with water vapor [78]. The Eneftech company is working on the development of an expander capable of operating under a pressure ratio of 25 [79].

In literature the built-in volume ratio of the screw machines is often limited to values of 4 or 5. Nevertheless, some studies show values of up to 8 [80]. Screw expanders can be subjected to high pressure ratios. For example, Nikolov considers a value of 50 with ethanol [81].

The built-in volume ratio of the piston expander can also reach high values similar to those obtained with internal combustion engines. However, for a given displacement, an increase in the built-in volume ratio yields a decrease in specific work produced by the machine and a relative increase in friction losses. This is why, in practice, the value of built-in volume of piston machines is limited to 15. The operation of an axial piston expander under a pressure ratio of 50 is reported [66].

The maximal pressure ratio of radial-inflow turbines is generally around 5 but values around 9 have been reached in the design and test of a small high pressure ratio radial turbine [82].

Inlet temperature

In scroll compressors, a limitation concerns the discharge temperature. The maximum discharge temperature is usually around 160 $°C$ for a hermetic compressor to avoid excessive thermal expansion, increasing the internal leakage of the machine, and a potential degradation of the lubricant and/or the sealing devices. In expander mode, an inlet temperature of 165 $°C$ was achieved with air [79] and a temperature of 215 $°C$ was reached with water vapor [78]. Approximately the same limit is also found on the exhaust temperature of open-drive air scroll compressors.

Screw expanders can be exposed to high inlet temperatures. For example, Hutker considered a value of 490 $°C$ with water vapor [83].

Piston expanders can tolerate high inlet temperatures beyond 500 $°C$ [84].

Vane machines are often limited in temperatures otherwise friction in the vanes increases significantly due to the thermal expansion, eventually leading to a lock up of the vane and its destruction. A maximal temperature of 140 $°C$ is reported in [76].

Radial-inflow turbines use as turbochargers can tolerate high inlet temperatures above 550 $°C$ [85].

Performance

The scroll expander is generally characterized by high performance and reliability. It is composed of a limited number of moving parts and can typically operate over a wide range of pressure ratio with a high isentropic effiency. The first record of a scroll machine used as expander appeared in 1994 [65]. Over the years, many authors ([86], [87], [88], [89]) showed maximal efficiencies generally always above 65 %.

Brasz et al [90] reached an adiabatic isentropic efficiency of 70 % with a 20 kW twin screw expander using fluid R113 to replace a throttle valve in a chiller. More recently, a 10 kW single screw has been tested with refrigerants SES36 and R245fa and presented a maximum isentropic efficiency of 65 % ([91]). A 10 kW single screw expander has also been tested with refrigerant R123 and an efficiency up to 58 % has been reached ([92]). Hsu et al tested a 50 kW twin screw that showed an isentropic efficiency of 72.4 % with r245fa ([93]). In 2015, a 5 kW single screw expander has been tested with R123 with a maximum isentropic efficiency of 49.5 % ([94]). Nonetheless, it is worth noting the differences can also partly be explained by the lack of harmonization in the definition of the isentropic efficiency.

Seher et al. [95] reported tests conducted on a single-cylinder double-acting oil-free piston expander using steam as working fluid and producing 18 kW with an isentropic effiency of 65 %. A single-cylinder piston expander fed by steam was also tested by Daccord et al. [66] and produced around 2.5 kW with an isentropic effiency of 55%.

In 2015, Colletta [96] investigated an ORC system to recover the heat from a rotary vane compressor. Fluid R236fa was used and 3 different prototypes of vane expanders were investigated, with 7, 14 and 7 vanes respectively. The temperature of the heat source was relatively limited, around 90 $°C$. The first expander presented a maximal isentropic efficiency of 64.7 % and a maximal mechanical power of 2.29 kW at the maximum. An isentropic efficiency of 64.1 % was achieved with the second expander, whose maximal mechanical power reached 2.57 kW. The third expander presented a maximal isentropic efficiency of 54.8 % while the maximal mechanical power was 3.23 kW. The reduced efficiency compared to 2 other machines was justified by over expansion. Vodicka [97] tested and modeled a vane expander integrated in an ORC system recovering the heat from an industrial process. Hexamethyldisiloxane was used as working fluid and a power output of 1 kW was reached while the recorded isentropic efficiency was ranging from 40 to 58%.

2.8 Pumping devices

The pump is a key element of the ORC system. A lot of attention should be payed to this component and its efficiency since the power it consumes has to be directly subtracted of the power produced by the expander. Volumetric pumps generally have a nominal isentropic efficiency around 70%. But for small electric pumps, the efficiency of the motor is generally low, around 50%, and reducing therefore the global efficiency of the motor-pump group below

30-35%. Experimental data from several volumetric pumps is available for this study. The investigated technologies are described in [44]. In addition a new piston and membrane pump is experimentally investigated in the frame of this work. Performance are discussed in the next chapters.

2.9 Conclusion

This Chapter justifies the introduction of WHR ORC system in HDT applications. The main drivers leading to the improvement of the engine thermal efficiency are first described. They are environmental, regulation and fuel economy. Indeed, reducing the GHG emissions is a major objective for the European Comission in order to limit the global warming to 1.5 to 2 $^{\circ C}$ in 2100 compared to 1900 and avoid the potential catastrophic consequence of the climate change. The European Union also aims to implement Euro standards in order to reduce emissions of polluting gases. The pollutants emissions from vehicles with a growth vehicle weight rating higher than 3.5 tonnes are governed by increasingly restrictive European standards, from Euro 0 in 1990 to Euro VI since 1 January 2014. This severity of the emission standards added to a continuous growth of the oil price and the need for sustainability have led manufacturers to identify innovative solutions in order to improve the engine thermal efficiency the engine. The resulting fuel consumption reduction should also represents a significant economy for the truck owner. Multiple sources of improvement are investigated but the main contribution to the engine efficiency will probably result from improving the combustion process. Waste heat recovery system can also play a significant role considering the large amount of energy content in the exhaust gases and engine coolant. Among the available technologies, the ORC system is probably the most promising solution with a potential fuel reduction around 4-5 %. The recirculated and exhaust gases are identified as the most promising sources based on a second law analysis while the ram air through an indirect condenser is probably the safest approach to reject the heat of the ORC system. Combining these heat source and sink, 5 possible typologies are proposed to be investigated. Moreover, the introduction of the ORC technology on a truck requires specific R&D activities particularly concerning the selection of the architecture, working fluid and components. Because numerous working fluids are available on the market a selection method is proposed in this study, eliminating fluids dangerous for the environment and the human health. Considerations on the thermophysical properties of the fluid are also introduced. From the initial set of 122 pseudo-pure working fluids available in the Coolprop fluid library, 15 satisfy the selection criteria. The component selection is another challenging task. A model based approach is proposed assuming only validated model can be reliable. Thus the investigated technologies of heat exchanger is limited on the high pressure side of the Rankine system to the shell and plate type since it has been experimentally investigated. On the other hand a brazed-plate type condenser is considered. Many technologies of expansion devices have been investigated on test rigs, including positive-displacement machines (scroll, screw, piston, vane and root expander) and a radial-inflow turbine. In the same manner, experimental data is available

for several volumetric pumps and an additional piston and membrane type has been tested in laboratory. The operating principle of each component technology is briefly described and the operating limits are reported based on a literature review. All this information will be exploited in the next chapters to build and validate the component models as well as for the optimization and simulation process of the investigated ORC candidates.

3 | Experimental study of a radial inflow turbine

Abstract

In this Chapter the performance of an Organic Rankine Cycle system equipped with a radial-inflow turbine is investigated with two working fluids: R245fa and R1233zd. The radial-inflow turbine is a small-scale prototype designed to convert the waste heat from the exhaust gases of a truck combustion engine and was developed using mainly components of truck turbochargers. It is directly connected to a high-speed synchronous generator. The bearings and the generator have the particularity to be respectively lubricated and cooled down by the working fluid so no additional lubricant or coolant is needed.

The experimental study is carried out over a test-rig equipped with the radial turbine. The heat wasted by the truck through the exhaust gases is simulated using an electric oil boiler coupled to the ORC loop. The electrical power supplied by the turbo generator, limited to a maximum of 3.5 kWel by the generator, is dissipated in a load bank composed of truck fans while the condenser is cooled by a water loop.

Measurements in steady-state regime are performed in order to evaluate the performance of the turbo generator when varying the pressure ratio, the rotational speed, the inlet temperature and the mass flow rate of the turbine, and the lubrication flow rate of the bearings, for various oil temperature and mass flow conditions. A total of 1260 and 325 steady-state points are collected for R245fa and R1233zd respectively. The turbo generator being a prototype, potential sources of improvements are proposed and discussed.

In order to identify the most suitable fluid, between fluids R245fa and R1233zd, for the Waste Heat Recovery application, 2 comparison methods are proposed and discussed based on the measurements.

Keyword

Waste Heat Recovery, Organic Rankine Cycle, Experimental comparison, Radial Inflow Turbine, Working fluid, R245fa and R1233zd

3.1 Introduction

The deployment of ORC systems for mobile Waste Heat Recovery (WHR) applications is still at a research stage. Specific R&D activities are required to select and develop the components and identify the most appropriate system architecture. Particularly, the selection of the working fluid and of the expansion machine technology constitutes an important part of this research.

The working fluid selection process has been widely investigated in several studies [76], [98], [99], [100], [101]. For instance, V. Macian et al. [60] selected R245fa and water for their optimization of a bottoming Rankine cycle. Nonetheless no universal optimal fluid is indicated since the choice is highly dependent on the targeted application. A detailed list of the guidelines and indicators that should be taken into account when selecting an organic fluid for power generation are reported in [102]. In general the critical temperature of the selected fluid should be slightly higher than the target evaporation temperature. Therefore for low quality waste heat recovery, refrigerants are often selected due to the low critical temperature value [98].

Regarding the expansion machines, there are two paths for the ORC designer to choose from : turboexpanders and positive displacement (or volumetric) machines. In the power range of 3 to 20 kWel (micro ORC systems) the latter are often preferred over turbo-expanders because of their low rotational speed, high single-stage expansion ratio and the low flow rate they can admit [103]. In addition, positive-displacement machines can handle two-phase expansion that can occur when operating with "wet fluids" [104]. On the other hand, for a same power level, turbomachines can theoretically achieve higher efficiency and be more compact than the equivalent volumetric machine [77]. Indeed, for a same compactness level, the turbo-expander can handle a larger mass flow rate of working fluid thanks to its continuous working principle compared to the sequential working principle of positive displacement machines [77]. Another advantage of turbomachines is the high reliability resulting from the reduced number of moving elements. Two categories of turbines are generally identified: the axial and the radial types. Fewer stages are required in the case of an organic fluid and even single-stage turbines can be employed for low or medium temperature ORC cycles. Another characteristic of organic fluids is the low speed of sound. As a result, this speed is reached much sooner with organic fluids than with water. Compared to axial turbines, the stage of radial inflow-turbines is designed for higher pressure ratios and lower working fluid mass flow rates. The geometry allows higher peripheral speeds than with axial turbines, and therefore a higher enthalpy drop in the stage. Turbines are indeed devoted to the transformation between work and other forms of energy including internal, potential, and kinetic energy (and to a much lesser extent, heat).

The provided work results from the ability of the machine to first produce and then reduce the angular momentum of the working fluid. Where a large mass flow is going through the turbine, the angular momentum change can be carried out at essentially a constant radial position from axis of rotation of the rotor (axial turbine). However, where only a small mass flow is available, a reduction in both tangential velocity component and radial position of the fluid is necessary to achieve the greatest possible angular momentum change (radial turbine). Once designed, the turbine is submitted to a series of tests in order to evaluate its performance, i.e. the pressure ratio or the enthalpy drop, the efficiency, the mass flow rate and the rotational speed, in the overall operating range. Radial-inflow turbines also have the advantage of maintaining an acceptable efficiency over a large range of part-load conditions [77].

Several couples of working fluid and expansion machine used in ORC systems to recover the waste heat from vehicles also have been considered in literature. Zheng and al. [62] investigated a rolling piston to recover the waste heat of a low temperature ($90\,°C$) heat source. Costall [105] selected toluene in a design methodology of a radial turbo expander. Song and al. [106] considered a screw expander using water for the LT loop in the analyse of the performance of a dual-loop ORC. Di Battista and al. [107] investigated a rotary vane expander using R236fa for the waste heat recovery of a light duty engine .

A significant number of studies dedicated to the waste heat recovery on trucks using ORC systems is also available ([108], [61], [109], [57], [110]) but only a few of them are considering experimental investigations ([111], [112]). The positive displacement machines that have been used up to now are often prototypes derived from existing compressors in order to be cost-effective [102], [113], [114]. Micro ORC integrating turbines are even rarer [115], [116].

In this Chapter, an experimental campaign is achieved to evaluate and compare the performance of a radial-inflow turbine, installed in an ORC system, with two working fluids: R245fa and its probable substitute R1233zd. The expansion machine is a small-scale prototype designed to convert the heat wasted in the exhaust gases and recirculated gases (EGR) of a truck. It was developed using mainly components of truck turbochargers and it is directly connected to a high-speed synchronous generator. The bearings and the generator have the particularity to be respectively lubricated and cooled down by the working fluid so no additional lubricant or coolant is needed.

Measurements in steady-state have been performed in order to evaluate the performance of the turbo generator when varying the pressure ratio, the rotational speed, the inlet temperature and the mass flow rate of the turbine and the lubrication flow rate of the bearings for various oil temperatures and mass flow rates.

The cycle operates between a maximum heat source temperature of 180°C and a minimum heat sink temperature of 10°C. The latter temperatures could be varied in order to cover a wide range of boundary conditions. Based on the measurements, the thermodynamic performance of the ORC unit is evaluated and compared with the two fluids.

A particular attention is here dedicated to the analysis of the turbo generator which is a key component in affecting the performance of the ORC unit. Potential sources of improvements of the prototype are discussed based on the experimental measurements.

3.2   Description of the ORC test cell

3.2.1   ORC system

A schematic and a picture of the layout of the ORC test rig are given in Figure 3.1a and 3.1c respectively. The system is equipped with the prototype of turbo generator.

The radial-inflow turbine itself consists in 3 main components, the volute, the stator and the rotor, as depicted in Figure 3.1b. The incoming fluid is accelerated and distributed uniformly around the periphery of the stator by the volute. Further acceleration and increase in the circumferential component of velocity is provided by the nozzle row (stator). Then the kinetic energy of the fluid is converted into mechanical energy as it expands through the rotor [73]. In order to achieve the lubrication of the bearings and the cooling of the generator with the working fluid, 2 refrigerant lines go directly from the pump outlet to the bearings and generator casings, in parallel to the main flow driven to the evaporator, as shown in Figure 3.1a.

The variable speed membrane pump, through an asynchronous motor, is connected to a Variable Frequency Drive (VFD) that aims at controlling the rotational speed of the machine. The waste heat is simulated using an electric oil boiler coupled to the ORC loop. The electrical power, produced by the turbo generator and limited to 3.5 kWe, is dissipated in a load bank composed of truck fans while the condenser is cooled by a water loop. A liquid receiver is placed between the condenser outlet and the subcooler inlet to ensure a sufficient height of liquid at the inlet of the pump.

A summary of the main ORC components characteristics is reported in Table 3.1. The working fluid in liquid state is pumped and split into 3 lines. The main part of the high pressure liquid is driven to the evaporator to recover the heat provided by the thermal oil of the boiler. The resulting high pressure vapor is then expanded in the turbine where the thermal energy is converted into mechanical energy and then electrical energy through the high speed generator. The remaining liquid coming from the pump is driven to the bearings and to the generator in order to lubricate and cool down those components as previously explained.

The 3 aforementioned flows are combined downstream the expander before entering the condenser where the fluid goes back to saturated liquid state based on the heat exchange with the cooling water.

The saturated liquid finally fills the liquid receiver, in which the accumulated mass of liquid enables to dump the transient variations occurring during the operation of the system, before being further cooled down in the subcooler. This last step ensures the fluid is in a low

temperature liquid state at the inlet of the pump and thus avoid cavitation.

Table 3.1 – Summary of the specifications of the main ORC unit components.

System component	Specifications
Heat exchangers	Brazed plate type
	$T_{max} = 180\,^{\circ}C$, $P_{max} = 30$ bar
Pump	Volumetric Membrane pump
	3 kW motor, $N_{nom} = 1500$ rpm, $P_{max} = 70$ bar
Expansion machine	Radial-Inflow turbine
	3.5 kW generator, $\dot{M} = 0 - 350$ g/s,
	$r_p = 2 - 5$ [-], $N = 50000 - 80000$ rpm
	$\dot{M}_{lub} = 0.04 - 0.1$ [kg/s]
Liquid receiver	8 l

3.2.2 Heating and cooling loops

The thermal energy source is provided by means of an electrical boiler where thermal oil, Pirobloc HTF-Basic, is pumped through to temperatures of up to 300 °C. The boiler has a maximum power of 150 kW$_{th}$. A proportional integral (PI) controller is implemented to maintain the temperature of the oil at the inlet of the evaporator constant during transient in the ORC test rig (e.g. change in the pump rotational speed of the ORC). The oil mass flow rate provided by the boiler being too large for the ORC application, it is manually controlled through a by-pass loop by means of needle valves located at the inlet of the evaporator.

Variable flow rates of water are used as heat sinks to cool down the working fluid in the condenser and the subcooler.

3.2.3 Data Aquisition Systems

On the working fluid side, absolute pressure sensors (APS) and Type-T thermocouples at the inlet and outlet of the different components allow for the determination of the energy balance for each component and the management of the plant. The working fluid mass flow rates are measured by means of three Coriolis flow meters (CFM) installed in parallel at the pump outlet.

The condenser and subcooler cooling loops are equipped with two type-T thermocouples to measure the temperature of the cooling fluid at the inlet and outlet of the components. The water mass flow rate in the condenser is deduced from the mass accumulated in a tank over a given time period.

In the heat source circuit, the temperature of the oil is measured at the inlet and outlet of the evaporator using type-K thermocouples and a high temperature volume flow meter is used to
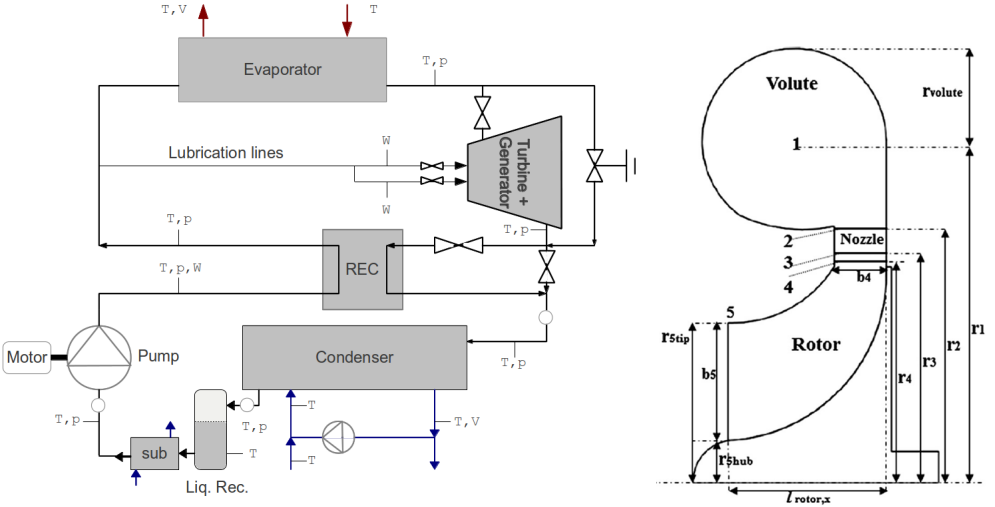
(a) Schematic layout of the ORC test rig

(b) Schematic of the radial turbine meridional view [73]

(c) Picture of the ORC test rig

Figure 3.1 – Description of the experimental setup

measure the oil flow rate.

The generator electrical power is measured by means of a 3-phase wattmeter. The characteristics of the measurement devices are reported in Table 3.2.

Table 3.2 – Range and precision of the measurement devices.

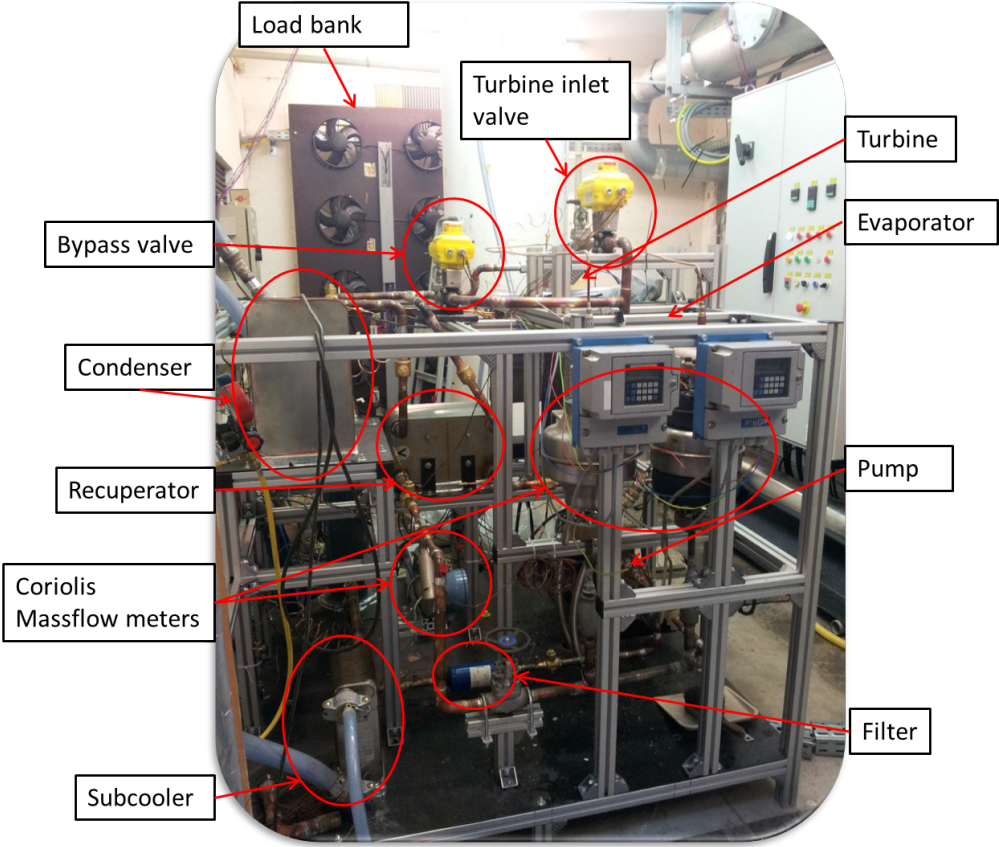| Variable	Device type	Range	Uncertainty
Mass flow	CFM	0 kg/s to 0.5 kg/s	± 0.1%
T (ORC)	type-T thermocouples	0°C to 150°C	± 0.5K
T (heat sink)	type-T thermocouples	0°C to 15°C	± 0.5K
T (heat source)	type-K thermocouples	0°C to 180°C	± 1.5K
p	APS	0 bar to 30 bar	± 0.03 bar
El. Power	Wattmeter	0 to 10 kW	± 0.1%

3.2.4 Working fluid selection

Different studies focus on the characteristics required by the fluid in order to retrieve the highest efficiency or power out of the given thermal energy source [98] [102]. For low quality waste heat recovery, the choice of the working fluid is often restricted to the refrigerant fluid family because of their low critical temperatures and pressures. However, the availability on trucks of high temperature heat sources such as the recirculated gases (EGR) could also lead to the use of ethanol or water as working fluid.

In the present study, the turbine was designed to operate with R245fa. This fluid is not toxic and not flammable. It is easily available on the market and has null Ozone Depletion potential (ODP). However it is also characterized by a medium Global Warming Potential (GWP=1030) and should therefore gradually be removed from the market. Therefore, in addition to an experimental campaign with R245fa, another campaign is then realized with a probable replacement for R245fa: R1233zd (GWP=4.5). More information on the investigated working fluids can be found in Table 3.3 and Appendix A.

Table 3.3 – Fluid properties of R245fa and R1233zd.

Fluid property	R245fa	R1233zd
Molar mass [kg/mol]	0.1340	0.1305
Critical pressure [bar]	36.51	36.24
Critical temperature [°C]	153.86	165.60
GWP	1030	4.5
Boiling point at 1 bar [°C]	14.72	17.97

3.2.5 Experimental Investigation

A total of 1260 and 325 measurement points are taken with R245fa and R1233zd and are used for the determination and the comparison of the turbine performance achieved with the two fluids. These points are obtained by keeping the system at a stable condition for a minimum of 15 minutes and by averaging the measurements over a period of 2 minutes. The turbine inlet temperature is adjusted to match 3 different levels of superheating, 25, 35 and 50K. The condensing pressure is varied between 2.5 and 4.5 bar absolute for R245fa and between 3 and 4 bar absolute for R1233zd, by step of 0.5 bar, modifying the mass flow rate of the cooling water. The turbine mass flow rate is regulated between 0.15 and 0.35 kg/s by varying the pump rotational speed. For given heat source temperature and mass flow rate, the evaporating pressure is then imposed by the turbine. The rotational speed of the turbine is varied (from 50000 to 70000 rpm), as well as the bearings lubrication flow rate (from 0.04 to 0.1 kg/s) which influences the internal losses in the bearings.

Based on these measurements, performance maps of the turbo generator can be drawn. Then, applying the mass and energy conservation laws and assuming there is, at this stage, no heat or mass transfer between the subsystems, performance maps of the turbine, bearings and generator can in turn be drawn. This is done here following a system approach and emphasis is thus placed on the characterization of the energy flows in the system and its subsystems as well as their efficiency. In the next Chapter, dedicated to the modeling of the prototype, geometric considerations are introduced and typical performance indicators for turbomachinary are presented. Also in this Chapter, interactions between the subsystems are considered and particularly the heat transfer between the turbine and the bearing flows.

Finally, 2 methods are proposed to compare the two investigated working fluids and their impact on the turbine performance.

- For given heat source and sink conditions (in terms of temperatures at the inlet of the heat exchangers and of mass flow rates), a first comparison is performed operating the two fluids at the same evaporating and condensing temperatures. 108 experimental points are used for this comparison, 54 with each fluid.

- In second method, it is proposed to compare both fluids for the same low and high pressure levels to investigate the influence of the fluid used on the turbine performance in terms of power output, isentropic efficiency, mass flow rate, rotational speed and lubrication mass flow rate. 578 experimental points are selected for this comparison, 289 with each fluid.

3.2.6 Definition of the subsystems

The turbo generator consists in three subsystems: the turbine, the bearings and the generator (Figure 3.2).

The temperature, pressure and mass flow rate of the working fluid are measured at the inlet and outlet of each of the three subsystems. Therefore, it is possible through an energy balance to evaluate the energy flows between the subsystems.

Based on the electrical power produced, the energy balance over the generator leads, assuming there is no heat transfer neither with the neighboring subsystems nor with the ambient environment, to identify the energy flow exiting the bearings and entering the generator. In the same manner, using the same assumptions for the bearings subsystem, the energy balance over the latter component enables to identify the energy flow exiting the turbine and entering the bearings. Finally, the energy balance over the turbine leads to identify the ambient losses of the turbo generator assuming there is no heat transfer between the turbine and the neighboring subsystems.

Two assumptions are thus stated in the frame of this analysis:

- The ambient losses of the turbo generator are localized in the turbine. This is reasonable according to the temperature levels of the working fluid in the latter component compared to the levels in the bearings or the generator.

- There is no heat transfer between the subsystems. This assumption can lead to an overestimation of the turbine efficiency and of the losses in the bearings. However it reduces the complexity of the analysis of the performance of the turbo generator based only the measurement performed on test rig while evaluating the heat transfer between the subsystems requires indeed a heat transfer model and a better knowledge of the sources of losses taking place in both components as well as of their geometry.
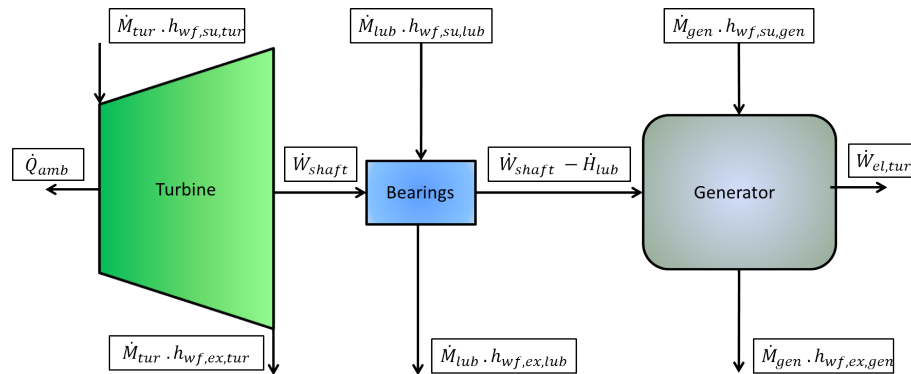

Figure 3.2 – Schematics of the three subsystems consituting the turbo generator

3.3 Processing of the experimental data

Firstly the energy balance over the ORC system components is investigated, to cross-check the precision and the quality of the measurements. This step, although often overlooked,

is of primary importance because of the numerous measurement issues that can arise in experimental campaigns.

The three mass flow rates required to investigate the performance of the turbo generator are then detailed.

Finally, the efficiency of the pump, of the expansion machine and of the ORC system are defined in order to compare, for both fluids, the performance achieved according to the different test conditions.

3.3.1 Thermal Energy Balance

Possible unbalances can indicate measurement errors or unconsidered parasitic phenomena such as ambient losses. The energy balance over the components is calculated as follow:

$$\dot{Q}_{amb} + Er + \dot{W}_{sh} = \dot{M}_{sf} \cdot c_{psf} \cdot (T_{sf,I} - T_{sf,II}) - \dot{M} \cdot (h_{wf,II} - h_{wf,I}) \tag{3.1}$$

where h_I, T_I and h_{II}, T_{II} are the inlet (I) and the outlet (II) enthalpy and temperature values of both the working fluid (wf) and the secondary fluid (sf). Specific enthalpies are calculated using the open-source CoolProp library [117]. $\dot{M}_{sf}$ and $c_{p,sf}$ are the mass flow rate and the specific heat capacity of the secondary fluid while $\dot{M}$ is the working fluid mass flow rate. $\dot{Q}_{amb}$ corresponds to the heat ambient losses of the component, Er is the measurement error and $\dot{W}_{sh}$ is the shaft power supplied or consumed by the component.

3.3.2 Mass flow rates

The flow sent by the pump is split in three parallel flows: the main flow that is expanded in the turbine ($\dot{M}_{tur}$), the flow required for the lubrication of the bearings ($\dot{M}_{lub}$) and the flow devoted to the cooling of the generator ($\dot{M}_{gen}$). These mass flow rates are measured using Coriolis flow meters and the total mass flow rate can therefore be computed as follow:

$$\dot{M} = \dot{M}_{tur} + \dot{M}_{lub} + \dot{M}_{gen} \tag{3.2}$$

3.3.3 Pump efficiency

The global isentropic efficiency of the pump is defined based on measured electric power consumption and takes the losses of the pump, motor and inverter into account (Equation

3.4). The volumetric efficiency of the pump is defined in equation3.4.

$$\varepsilon_{s,pp} = \frac{\dot{W}_{wf,s,pp}}{\dot{W}_{el,pp}} = \frac{\dot{M}\cdot(h_{wf,ex,s,pp} - h_{wf,su,pp})}{\dot{W}_{el,pp}} \tag{3.3}$$

$$\varepsilon_{v,pp} = \frac{\dot{M}}{\rho_{wf,su}\cdot N_{rot,pp}\cdot V_{s,pp}} \tag{3.4}$$

3.3.4 Efficiency of the turbo generator

A first definition of the global efficiency of the turbo generator is given in equation 3.5 to characterize the performance of the component. Then, the efficiency of each of the three main components constituting the set (i.e., the turbine, the bearings and the generator), as depicted in Figure 3.2, is defined.

$$\eta_g = \frac{\dot{W}_{el,tur}}{\dot{W}_{wf,s,tur}} = \frac{\dot{W}_{el,tur}}{\dot{M}_{tur}\cdot(h_{wf,su,tur} - h_{wf,ex,s,tur})} \tag{3.5}$$

Within a system approach, regardless of the geometry of the turbine, it is proposed to use the static-to-static definition (3.6) of the isentropic efficiency of the turbine instead of the the total-to-static definition that should be used for a single stage turbine.

$$\epsilon_{ss} = \frac{\dot{W}_{sh}}{\dot{M}_{tur}\cdot(h_{wf,su,tur} - h_{wf,ex,s,tur})} \tag{3.6}$$

The enthalpy increase of the working fluid from the inlet to the outlet of the bearings can be evaluated based on the measurements. This enthalpy increase is the result of internal losses in the bearings due to frictions and to the injection of liquid but is also the consequence of a heat transfer by convection between the fluid expanded in the turbine and the fluid lubricating the bearings. Considering these phenomena indivisible in the scope of this Chapter, the bearing efficiency is defined as follow:

$$\eta_m = \frac{\dot{W}_{sh} - \dot{M}_{lub}\cdot(h_{wf,ex,lub} - h_{wf,su,lub})}{\dot{W}_{sh}} \tag{3.7}$$

In the same way, the enthalpy increase of the working fluid from the inlet to the outlet of the generator can be evaluated and the efficiency of the generator is defined.

$$\eta_{el} = \frac{\dot{W}_{el,tur}}{\dot{W}_{sh} - \dot{M}_{lub}\cdot(h_{wf,ex,lub} - h_{wf,su,lub})} \tag{3.8}$$

These three effiencies can be linked to the global efficiency (3.5) through equation 3.9.

$$\eta_g = \epsilon_{ss} \cdot \eta_m \cdot \eta_{el} \tag{3.9}$$

The expansion, from the high pressure level at the outlet of the pump to the low pressure level at the inlet of the condenser, of the liquid going through the bearings and the generator, could be used to generate some work. This could be taken into account in the efficiency of the turbo generator as follow:

$$\eta_{g,2} = \frac{\dot{W}_{el,tur}}{\dot{W}_{wf,s,tur} + \dot{W}_{wf,s,lub} + \dot{W}_{wf,s,gen}} \tag{3.10}$$

with

$$\begin{aligned}
\dot{W}_{wf,s,lub} &= \dot{M}_{lub} \cdot (h_{wf,su,lub} - h_{wf,ex,s,lub}) \\
\dot{W}_{wf,s,gen} &= \dot{M}_{gen} \cdot (h_{wf,su,gen} - h_{wf,ex,s,gen})
\end{aligned}$$

3.3.5 Plant efficiency

The cycle efficiency is calculated based on the first law of thermodynamics.

$$\eta_{cycle} = \frac{\dot{W}_{el,tur} - \dot{W}_{el,pp}}{\dot{Q}_{ev}} \tag{3.11}$$

3.4 Results and discussion

3.4.1 Thermal energy balances

In Figure 3.3, the energy flows, computed on both sides of the evaporator for both fluids are depicted. The figures show a fairly constant unbalance between the thermal energy flows of the secondary fluid, $\dot{Q}_{hf,ev}$ and of the working fluid, $\dot{Q}_{wf,ev}$, for both fluids. This trend can be explained either by ambient losses and/or by measurement inaccuracy. The latter option is checked by means of an uncertainty propagation analysis. The vertical (resp. horizontal) error bars indicate the standard error over the secondary (resp. primary) thermal energy flow. The high level of uncertainty over the oil energy flow is mainly resulting from the low accuracy of the oil volume flow meter.

In Figure 3.4, the energy balances over the turbo generator are depicted for both fluids. The figures show a good agreement between the enthalpy flow rate over the turbine and the energy flow entering the bearings. The difference can be explained either by ambient losses and/or by

Figure 3.3 – Thermal energy balance over the evaporator with R245fa (a) and R1233zd (b) with the relative error bars. $\dot{Q}_{wf,ev}$: thermal power absorbed by the working fluid. $\dot{Q}_{oil,ev}$: thermal power transferred by the thermal oil.

measurement inaccuracy which is checked by means of an uncertainty propagation analysis.

In Figure 3.5, the energy flows, computed on both sides of the condenser for both fluids are depicted. The figures show a good balance between the water ($\dot{Q}_{cf,cd}$) and the working fluid ($\dot{Q}_{wf,cd}$) energy flows for both fluids. Based on the temperature levels, ambient losses are indeed expected to be reduced. Once again, the disagreement can be explained by measurement inaccuracy, which is checked by means of an uncertainty propagation analysis.

3.4.2 Effects of the pressure ratio on the mass flow rate

In Figure 3.6 is shown the evolution of the mass flow rate as a function of the pressure ratio for both fluids. The mass flow rate increases linearly with the pressure ratio and for a given pressure level at the inlet of the turbine, the value of the mass flow rate is the same whatever the outlet pressure. The mass flow rate of the turbine thus depends only on the turbine inlet pressure meaning the pressure information does not go up from the downstream to the upstream of the turbine and that the flow reaches sonic conditions in the turbine (at the nozzle throat according to Hugoniot).

In addition, the mass flow rate reached for a given inlet pressure level is similar for both fluids since they are characterized by similar thermophysical properties.
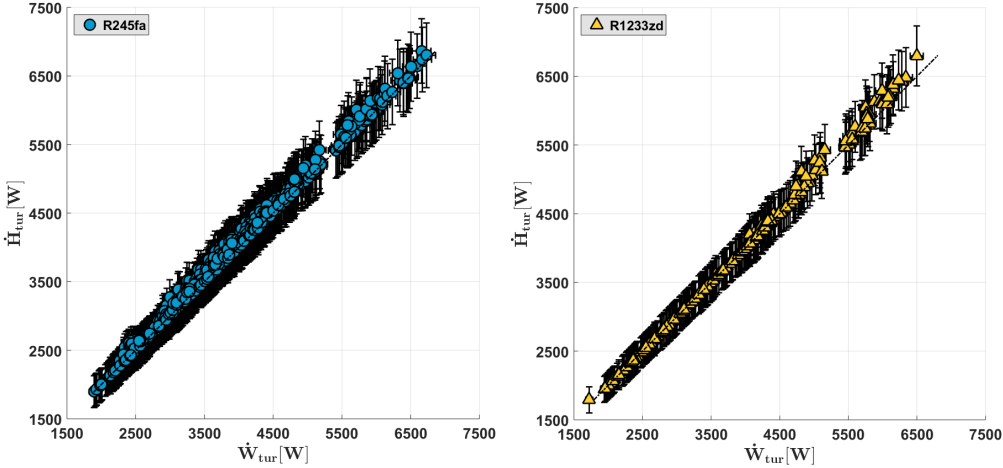
Figure 3.4 – Thermal energy balance over the turbine with R245fa (a) and R1233zd (b) with the relative error bars. $\dot{W}_{tur}$: estimated shaft power. $\dot{H}_{tur}$: enthalpy flow rate.
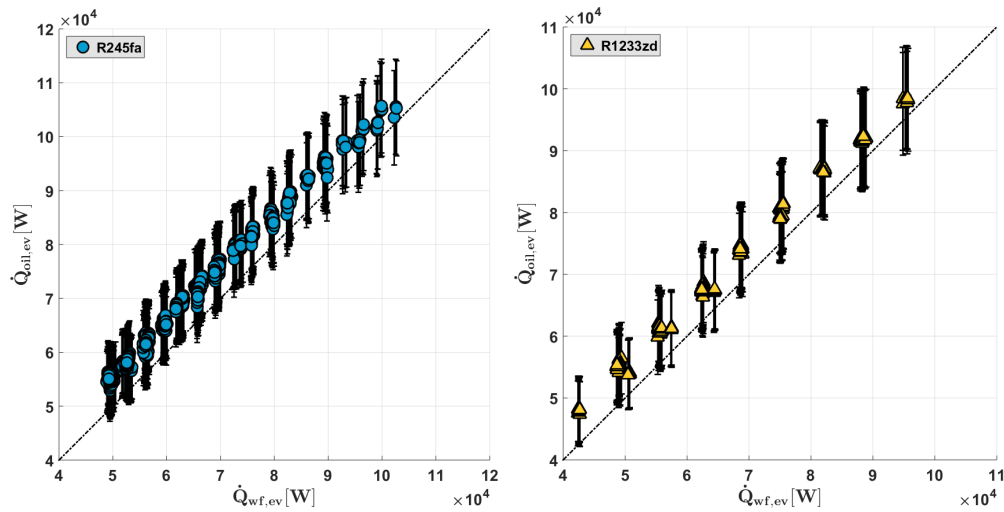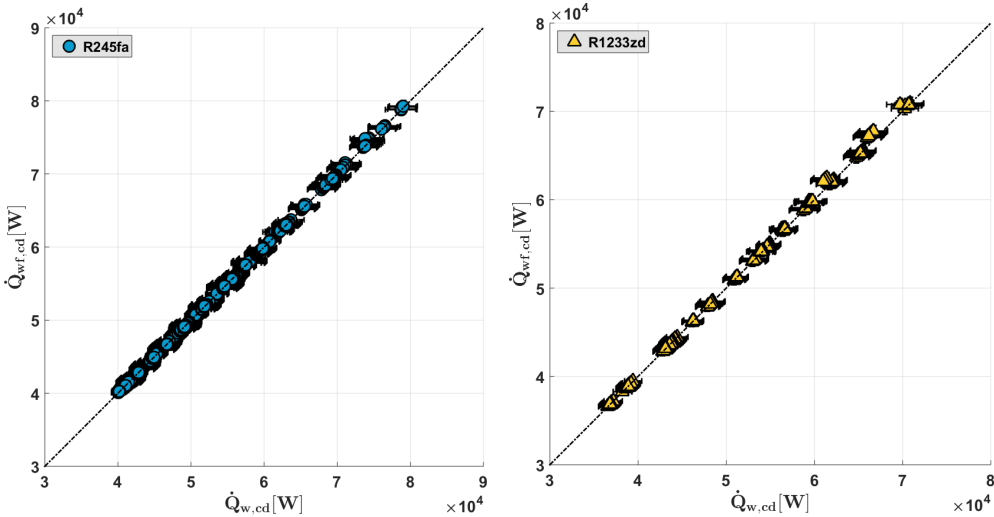

Figure 3.5 – Thermal energy balance over the condenser with R245fa (a) and R1233zd (b) with the relative error bars. $\dot{Q}_{wf,cd}$: thermal power absorbed by the water. $\dot{Q}_{w,cd}$: thermal power transferred by the working fluid.
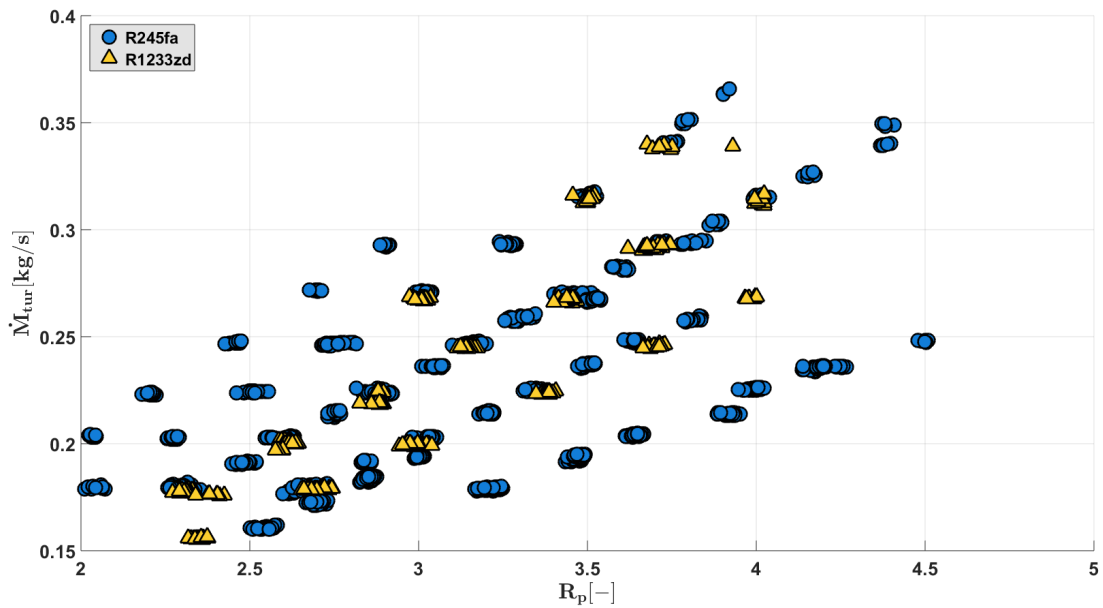
Figure 3.6 – Evolution of the turbine mass flow rate as a function of the pressure ratio with both fluids

3.4.3 Performance of the turbo generator

In average, over the 1260 and 325 measurement points taken with R245fa and R1233zd, the difference between the defined global efficiencies 3.10 and 3.5 of the turbo generator is lower than 0.6 %. Their are around 25 % and 27% with R245fa and R1233zd respectively. Consequently there is a large potential of improvement regarding the prototype.

As explained, the turbo generator can be seen as a combination of three subsystems that are the turbine, the bearings and the generator (Figure 3.2). Thus the previously defined overall efficiency of the turbo generator (3.5) can be split into:

- the turbine static-to-static efficiency (3.6)

- the efficiency of the bearings (3.7)

- the conversion efficiency of the generator (3.8)

These efficiencies can be evaluated (and linked to the overall efficiency of the turbo generator (3.9)) based on the first law of thermodynamics.

Starting from the electrical power produced by the generator, the conversion efficiency of the generator can be evaluated assuming that all the losses taking place in this subsystem are dissipated in heat, which is entirely transferred to the cooling fluid.

In the same way, the efficiency of the bearings can then be evaluated. The internal losses of the bearings are assumed to be dissipated in heat, which is transferred entirely to the lubricant. In addition, the heat transfer from the fluid expanded in the turbine to the bearings lubricant has to be taken into account. This heat transfer is assumed not to affect the intrinsic aerodynamic quality of the flow in the turbine and, in the scope of this Chapter, remains indivisible with the heat resulting from internal losses of the bearings.

Finally, the static-to-static isentropic efficiency of the turbine can be evaluated.

The evolution of the turbine isentropic efficiency, bearings efficiency, generator efficiency and of the overall system efficiency as functions of the pressure ratio for all the measurements points with R245fa and R1233zd is presented in figures 3.7 and 3.8. On those figures, a color code is used to distinguish the investigated levels of condensing pressure and overheating degree. For a given color, the dispersion observed for the 4 efficiencies mainly results from variations in the rotational speed of the turbo generator. More detailed results are given in Appendix B Several observations can be performed:

- Firstly, the value of the efficiencies does not seem affected by the choice of the working fluid. Similar values are obtained with both fluids.

- Secondly, as it could be expected, the generator efficiency (η_{el}) is increasing with the mechanical power and therefore with the turbine pressure ratio. The range of variation of this efficiency is in between 70 and 90 %.

- Thirdly, the turbine static-to-static isentropic efficiency (ϵ_{ss}) is decreasing almost linearly with the pressure ratio. However the efficiency remains acceptable over the large range of pressure conditions since it is ranging from 75 to 60 %. This behavior of the efficiency of the radial inflow technology, also pointed out in [77], added to the absence of oil are important advantages compared to other expansion machines.

- Fourthly the efficiency of the bearings (η_m) is relatively low, ranging from 29 % to 56 % . This indicates a particular attention to increase the overall efficiency of the turbo generator, should be placed on the the bearings.

To go further the turbine itself should then be investigated more into details. All the sources of losses (leakages, windage losses, incidence losses, friction losses, etc) taking place in this component could be identified and quantified in order to point out the opportunities for improvement in the design of the turbine. Such an investigation requires to develop a relatively detailed model of the turbine and is performed in Chapter 4.

In the following, it is proposed to compare the performance reached by the turbo-generator set for both working fluids. Two comparison methods are discussed.
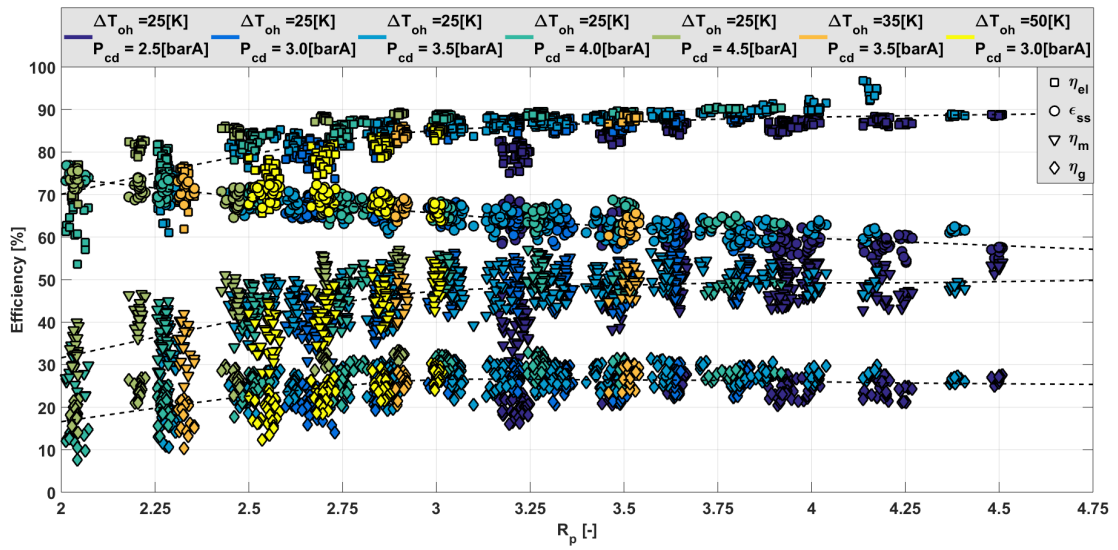
Figure 3.7 – Evolution of the generator efficiency, turbine static-to-static isentropic efficiency, bearings efficiency and overall system efficiency as functions of the pressure ratio for fluid R245fa
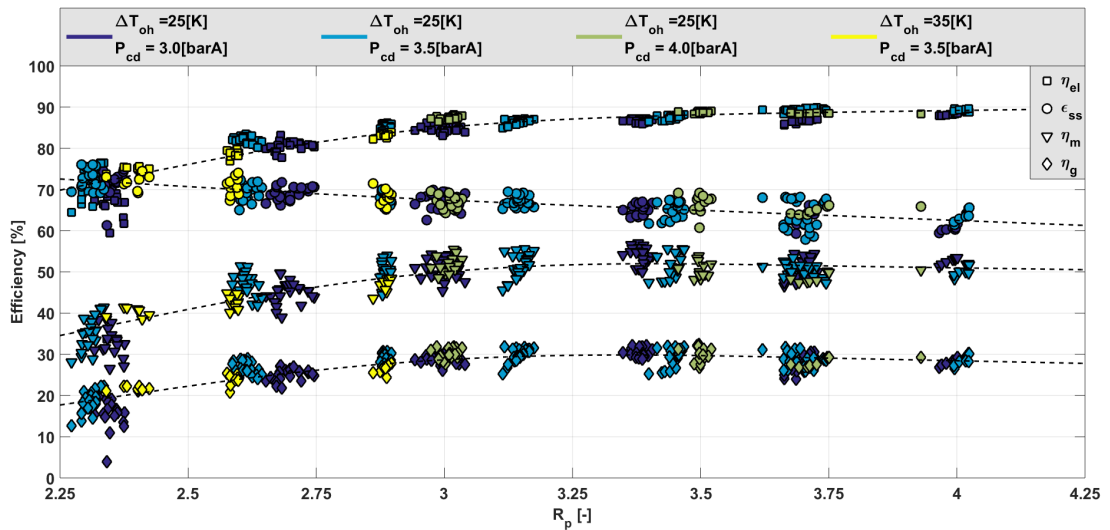
Figure 3.8 – Evolution of the generator efficiency, turbine static-to-static isentropic efficiency, bearings efficiency and overall system efficiency as functions of the pressure ratio for fluid R1233zd

Performance comparison for identical temperature levels

A thermodynamic comparison of the system performance with each working fluids for identical condensing and evaporating temperature levels is an impartial method. It enables to compare the performance of a single system, using the two fluids, in the case of similar heat

source and heat sink conditions. A T-s diagram of the cycle can be found in Figure 3.9 where the evaporating and temperatures are respectively 389 K and 323 K for both fluids.

In practice, the objective function of a WHR ORC is generally to maximize the power output of the system [102], which is achieved by optimizing the pressure ratio, the inlet temperature (TIT), the rotational speed and the mass flow rate of the expansion machine. The dependence between the mass flow rate and the pressure ratio has been shown (Figure 3.6) and the influence of the rotational speed and the inlet temperature is limited. Therefore, maximizing the output power of the turbine is mainly achieved by optimizing the pressure ratio inside the design operating range of [2-5]. However, the maximal evaporating pressure and the minimal condensing pressure are, for given heat source and heat sink conditions, limited by the efficiency of the heat exchangers. There is a minimum temperature pinch-point between the secondary and the primary fluids that can be reached in the heat exchangers. In other words, for given heat source and heat sink conditions, the pressure ratio of the cycle might be limited by the maximal evaporating temperature and minimal condensing temperature that can be achieved. This therefore justifies this first comparison based on similar levels of saturation temperature.

Looking at the fluid properties, for the 108 selected operating points (54 with each fluid), the pressure level corresponding to the same saturation temperature is lower using R1233zd than using R245fa. This phenomenon is growing with the temperature. Both the condensing pressure and evaporating pressure are therefore reduced when using R1233zd but the latter pressure level is much more affected.

From the lower evaporating pressure results, as it has been shown previously (Figure 3.6), a lower mass flow rate. The power production of the turbo generator (evaluated for same rotational speed and lubricating flow rate levels) is therefore lower using R1233zd than using R245fa. However the pump consumption is also reduced. At the end, the net output power of the system remains comparable for both fluids as it can be seen in Figure 3.10 showing the evolution of the power output of the turbo generator and of the ORC net power output as functions of the pressure ratio.

Performance comparison for same pressure levels

In order to investigate the impact of the working fluid on the turbine performance, a second comparison, involving 578 measurements (289 with each fluid) points corresponding to same evaporating and condensing pressure levels for both fluids is performed. A T-s diagram of the cycle can be found in Figure 3.11 where the evaporating pressure is 14 barA and the condensing pressure is 3.5 barA for both fluids.

The evaporating pressures being the same, the mass flow rates are the same for both fluids. The maximal powers achieved by the turbo generator with both fluids for each pressure levels are compared while the rotational speed and the lubrication flow rate are no more kept the

Figure 3.9 – T-s diagrams of both working fluids for same evaporating and condensing temperature levels (and superposed temperature profiles of the thermal oil and cooling water)

same for each fluid but both the variables are optimized.

As it can be seen in Figure 3.13, even for same pressure ratios (and mass flow rates), the power production is slightly higher using R1233zd. This can be explained by the lower lubrication flow rate required and/or the possibility to achieve a higher rotational speed closer to the turbine optimal speed with this fluid.

Indeed, the lubrication flow rate is adjusted ensuring the fluid leaving the bearings is in liquid phase. Otherwise the bearings would risk to run dry and to be quickly broken. This lubrication flow rate is responsible of additional pump consumption but also of internal losses in the bearings that consume part of the power produced by the turbine. To achieve the minimum pump consumption and the maximum overall efficiency of the turbo generator, the lubrication mass flow rate has therefore to be reduced to a minimum but must remain sufficient to guarantee a degree of sub-cooling at the outlet of the bearings. A level of sub-cooling around 5K, before reaching the saturation temperature at the corresponding condensing pressure, was kept as a safety limit.

Figure 3.10 – Comparison between the power produced by the turbo generator and the system net output power for the same condensing and evaporating temperature levels with both fluids

On the other hand, for a given lubrication flow rate, an increase in rotational speed corresponds to an increase in the temperature of the bearings and of the lubricant because of higher mechanical losses. A maximal rotational speed can thus be identified just before reaching the maximal temperature allowed in this location. Therefore the optimal speed, which is often higher and leads to the maximal turbine efficiency for a given pressure ratio and inlet temperature of the turbine, cannot always be reached.

Because the saturation temperature for a same pressure level is around 5K higher when using R1233zd compared to R245fa, the speed could be increased and/or the lubrication flow rate could be reduced in a bigger proportion as shown in Figure 3.12. This explains the better performance of the turbo generator, in terms of power produced (Figure 3.13) when using R1233zd.

Finally, it is worth noting the difference of saturation temperature between the fluids also enables to reach higher evaporating pressures and therefore pressure ratios using R1233zd before meeting the temperature limit at the outlet of the bearings. Thus, for instance, in the case where the condensing pressure is 3 barA, a maximal evaporating pressure of 12 bar could be reached during the experiments using R1233zd while it was limited to 11.5 bar absolute with R245fa.
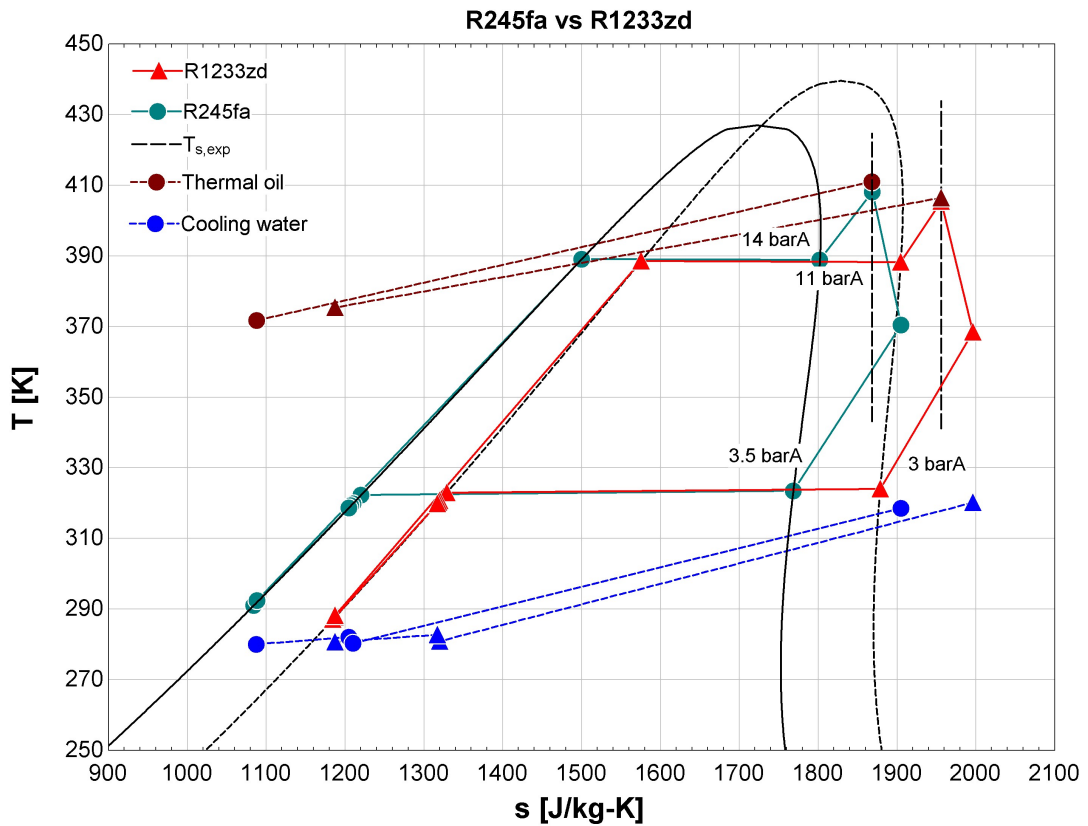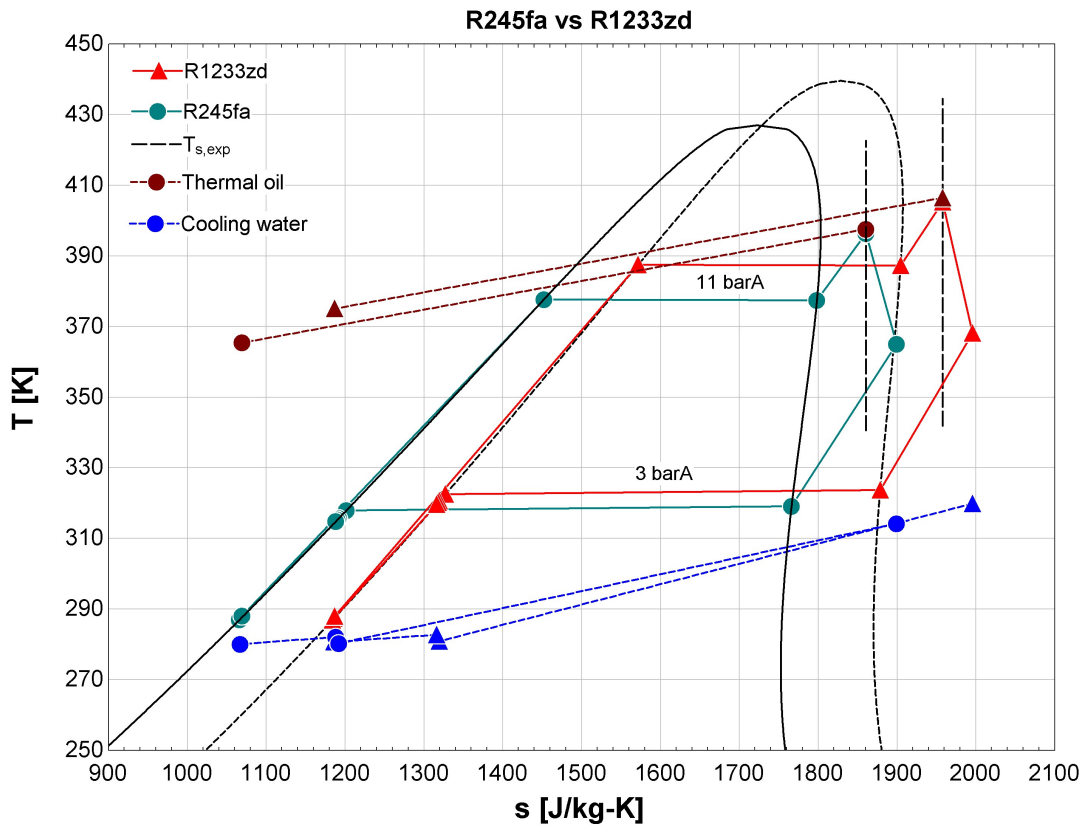
Figure 3.11 – T-s diagrams of both working fluids for the same evaporating and condensing pressure levels (and superposed temperature profiles of the thermal oil and cooling water)

3.4.4 Performance of the ORC system

The minimum and maximum performance obtained during the measurement campaign for R245fa and R1233zd are reported in Table 3.4.

Table 3.4 – Min/Max performances achieved during the measurement campaigns for R245fa and R1233zd.

Performance	$\dot{M}_{tur}$ [kg/s]	$\dot{M}_{lub}$ [kg/s]	$P_{su,tur}$ [bar]	$P_{ex,tur}$ [bar]	$T_{su,tur}$ [°C]	$N_{rot,tur}$ [RPM]	$\epsilon_{s,tgs}$ [%]	$\epsilon_{g,tgs}$ [%]	$\epsilon_{s,pp}$ [%]
				R245fa					
Min	0.1599	0.0392	7.48	2.42	106.76	45231	7.65	7.49	42.86
Max	0.3659	0.0970	16.13	4.57	135.49	68681	33.26	32.81	28.31
				R1233zd					
Min	0.1551	0.0393	7.03	2.95	108.07	45236	3.98	3.92	41.44
Max	0.3400	0.0828	15.29	4.16	142.16	71287	32.35	31.87	26.33

Combining this performance with the efficiency of the pump system varying between 29 and
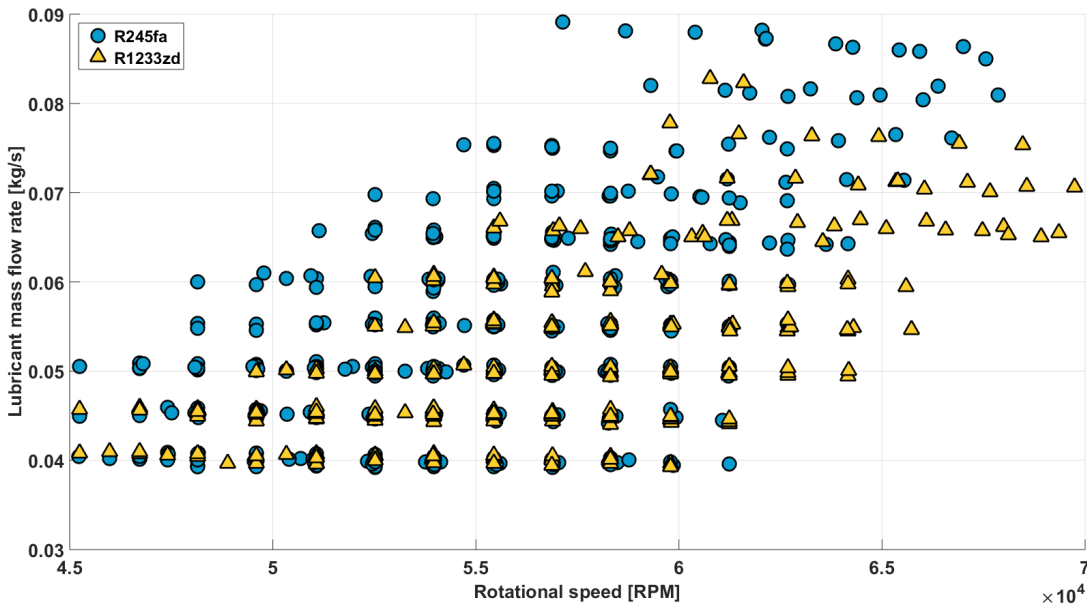
Figure 3.12 – Comparison between the turbine rotational speed and the lubrication flow rate for the same evaporating and condensing pressure levels with both fluids
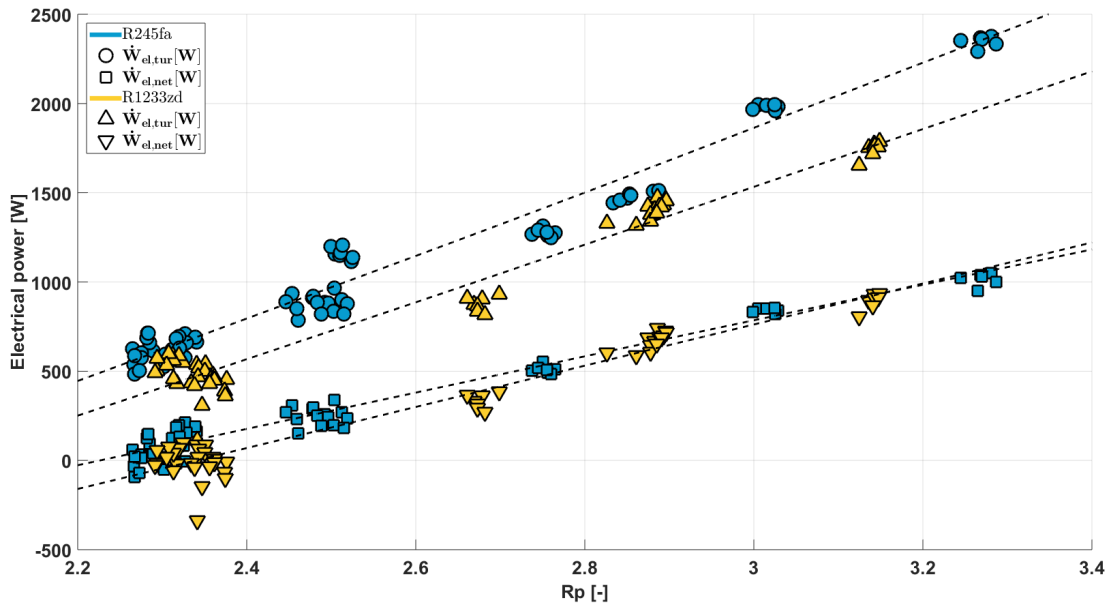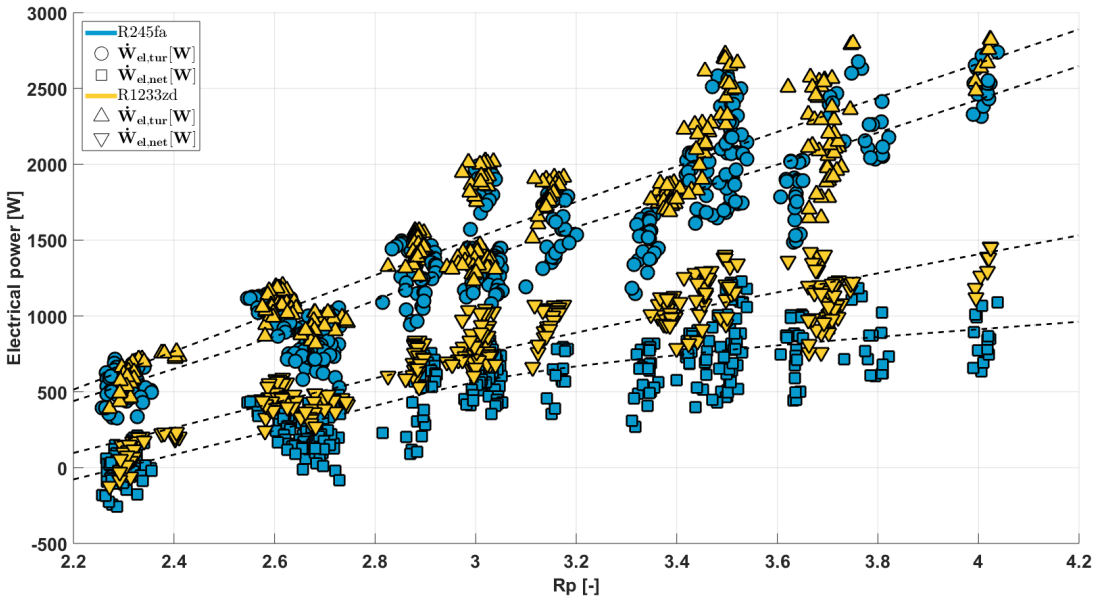

Figure 3.13 – Comparison between the power produced by the turbo generator and the system net output power for the same condensing and evaporating pressure levels with both fluids

42 % , this leads to a plant efficiency reaching 1.8 %. However, the pump system efficiency takes into account the losses of the frequency drive and of the electric motor, which is the weakness of the overall efficiency (more details on the efficiency and the losses distribution of pump systems can be found in [44]). To get rid of the electric motor for the on-board ORC application, solutions such as a mechanical coupling between the pump and engine shafts could be investigated. Nonetheless, even if an electro-mechanical efficiency of 90 % could be achieved, thus rising the pump system efficiency up to 89 %, the plant efficiency would only reach 2.5 %. Accordingly, the effort to increase the cycle efficiency should be placed on the turbo generator. Indeed, if the bearing efficiency could hypothetically reach 90 %, this would increase the average overall efficiency from 28 to 51 % and the ORC efficiency up to 4.8 %. At this stage, the generator, limiting the electrical power to 3.5 kWe, should be replaced since the produced power could rise, everything else remaining equal, up to 5.3 kWe.

3.5   Conclusion

Small scale ORC systems can play a key role for mobile low grade waste heat recovery applications but are still at research stage. In this work an experimental campaign is achieved to identify and compare the performance of a radial-inflow turbine integrated in an WHR ORC system with 2 working fluids: R245fa and its probable substitute R1233zd.

The evaporator, the condenser and the turbo generator thermal energy balances are checked and an uncertainty propagation study is performed. This step is of primary importance because of the numerous measurement issues that can arise in experimental campaigns.

Two types of experimental comparison are then proposed for the performance of the ORC components. A first comparison based on same temperature levels for both fluids enables to compare the performance of the same system for similar heat source and heat sink conditions. Because the saturation temperature is higher with R1233zd than R245fa for a same pressure level and because this phenomenon is growing with the temperature level, the pressure ratio and therefore the mass flow rate are lower using R1233zd. This leads to a lower power output of the turbo generator but also to a lower pump consumption. At the end, comparable net output power are observed using both fluids. Secondly the performance is compared for same pressure levels. This comparison is convenient to investigate the influence of the working fluid on the turbine performance, the pressure ratio being the same. The bearings being lubricated by the fluid, better results are achieved when using R1233zd compared to R245fa. Indeed, for same pressure levels (and mass flow rates), R1233zd is characterized by higher levels of saturation temperature and enables the turbo generator to be operated at higher speed and/or with a lower lubrication flow rate which is also a source of losses. This analysis experimentally demonstrates that, based on the given test-rig, R1233zd represents a better choice compared to R245fa to recover the waste heat of the exhaust gases of a long haul truck.

However there is a large potential of improvement regarding the turbo generator. The overall efficiency, indeed, averaged over the 1260 and 325 measurements points, is around 25 % and

27 % with R245fa and R1233zd respectively. Improving this efficiency requires to identify and quantify the different sources of losses so to reduce them. First, assuming there is no heat transfer between the components of the turbo generator, the global efficiency can be split in:

- the turbine static-to-static efficiency

- the efficiency of the bearings

- the efficiency of the generator

This separation is possible based on the first law of thermodynamics and using the temperature, pressure and mass flow rate measurements performed on the working fluid at the inlet and outlet of each subsystem. A static-to-static isentropic efficiency varying between 60 and 75 % is identified for the turbine and a range from 70 to 90 % is identified for the generator efficiency. The efficiency of the bearings is relatively low, ranging from 29 to 56 %. This low efficiency, taking into account the internal losses due to friction in the bearings and liquid injection but not the heat transferred from the turbine to the bearings indicates that the priority, in order to increase the overall efficiency of the turbo generator, should be placed on the improvements of the bearings and its thermal insulation.

Finally the turbine itself has to be investigated more into details. All the sources of losses (leakages, windage losses, incidence losses, friction losses, etc) taking place in this component could be identified and quantified in order to point out the opportunities for improvement in the design of the turbine.

4 Modeling of the investigated radial inflow turbine

Abstract

In this Chapter, a model of the radial-inflow turbine, investigated in Chapter 3, is proposed, described and validated against experimental data. As a reminder, the turbine is a small-scale prototype developed mainly using components of truck turbochargers and is directly connected to a high-speed synchronous generator. The bearings and the generator are respectively lubricated and cooled down by the working fluid.

First, the elements constituting the expansion machine are described and several modeling methods are reviewed. Based on this review, a mean-line model of the turbine is proposed. The ambient losses are easily evaluated based on a energy balance over the turbo generator and are lumped using a heat transfer parameter. The turbine itself is divided in several stations in which the velocity triangles of the fluid flow are computed using real gas equation of state and mass, energy and momentum conservation equations. For all the elements located between 2 consecutive stations, correlations are used to describe the loss phenomena affecting the velocity triangles of the downstream station. The model is confronted to experimental data and the results suggest that the heat exchange between the turbine and the bearing fluids should be taken into account in order to ensure a reasonable accuracy in the prediction of the shaft power and outlet temperature.

A model of the bearing system is thus proposed. Based on the energy balance over the bearings, the heat transfer from the turbine is computed and modeled. The turbine model, now including the heat loss, is finally validated against experimental data. When the possible formation of shock waves is considered between the nozzle throat and the rotor, results show a good agreement between the predictions and the measurements with relative error on the model outputs (shaft power, outlet temperature and mass flow rate) below 10 %.

Keyword

Radial Inflow Turbine, Bearings, Mean-line Model, Validation, R245fa and R1233zd

4.1   Introduction

The model conception and validation for a radial-inflow turbine devoted to operate within an ORC system is a complex task. In Chapter 2 are listed the main applications involving the radial-inflow turbine technology. It turns out the radial-inflow turbine is mainly investigated within the transport and chemical sectors. In aviation, radial-inflow turbines are used as expanders in environmental control systems. They are also used in various small gas turbines to power helicopters. In the petrochemical industry, they are used in gas liquefaction expanders, and other cryogenic systems [118]. Nonetheless, the best known use of radial inflow turbines is in automobile turbochargers [119]. Except for cryogenic systems, these applications typically involve air or combustion gases (or sometimes steam) as working fluid. Those particular fluids can be considered as perfect gases and are mainly used in gas turbines whether they are axial or radial turbines. Consequently, most of the developments in the design but also most of the characterization works and modeling tools have been achieved for turbines working with perfect gases.

Generally, a gas behaves like an perfect gas at high temperature and low pressure, as the potential energy due to inter-molecular forces becomes less significant compared with the particles kinetic energy, and the size of the molecules becomes less significant compared to the empty space between them. However, the model of perfect gas fails for most heavy gases, such as many refrigerants, and for gases with strong inter-molecular forces, notably water vapor. First, those gases are characterized by constant-volume and constant-pressure specific heat capacities that depend on temperature and pressure. Then, the perfect gas model tends to fail at lower temperatures or higher pressures, when inter-molecular forces become important. At high pressures, the volume of a real gas is often considerably greater than that of an ideal gas. At low temperatures, the pressure of a real gas is often considerably lower than that of an ideal gas. Moreover, the perfect gas model does not describe or does not allow phase transitions. Those must be modeled by more complex equations of state.

Consequently, most of the performance indicators such as the reduced mass flow rate, reduced speed, Mach number, etc, but also the relations between static and stagnation properties of the fluid, derived in turbomachinary for perfect gases, cannot be used directly. The simplifications in the conservation laws of mass, energy and momentum achieved using the ideal gas equation of state and constant values of the specific heats are no more valid for real gases. This represents the first difficulty for the development of turbine models involving real gases.

The second difficulty concerns the size required for the turbines operating in micro-ORC systems. The power levels met in those systems are generally low and lead to smaller turbines running, for a same specific speed, faster. The loss distribution might therefore differ from

what has been observed in large turbines running with air or other gases. Moreover, heavier fluid are generally characterized by a reduced speed of sound compared to air. This speed is then reached sooner in turbines operating with those fluids, which might lead to additional irreversibly.

Finally the validation of the model is another issue. Indeed, there is a lack of technical maturity when it comes to small turbines operating with heavy fluids. Most of the time, those turbines are prototypes for which the specifications and the detailed performance are kept confidential. For this reason, most of the turbine models developed in the literature for ORC applications are not confronted to experimental data and thus not validated. Their reliability might therefore be challenged.

In section 4.3, the turbo generator and its components, studied in Chapter 3, are described and a model of the turbine is proposed and validated against the experimental data. Several modeling approaches for radial-inflow turbines are identified based on a literature review. From this review, it turns out the mean-line model is the most appropriate solution for the investigated prototype. The mean-line model is based on a one-dimensional assumption that there is a mean streamline through the stage, such that conditions on the mean streamline are the average of the passage conditions [120]. The turbine is divided in a finite number of stations in which are described the flow conditions for the investigated real gas based on velocity triangles. This is achieved applying the conservation equations of mass, energy and momentum between each successive stations and taking into account the loss phenomena occurring in the turbine components in between as well as their impact on the velocity triangles. Such a model therefore takes the physical phenomena occurring during the expansion into account and could be extrapolated. Thus, once validated, the performance of the machine can be predicted for operating conditions outside the validation range (e.g., for a different rotational speed), another working fluid or even a different size of the machine. This model represents therefore a good trade-off between model accuracy, extrapolation ability and level of complexity so the model meets the requirements for the future design and optimization of the waste heat recovery system.

In section 4.3.7, an adiabatic model of the turbine is first proposed based on the mean-line approach. This model, which will be used during the ORC system design, takes into account the main loss phenomena occurring in turbine components but the heat transfer between the turbine and the bearings is not considered. However, when confronted to the experimental data, discrepancy is observed between the outputs of the model and the experimental data. In particular, the variation of the enthalpy flow rate through the turbine is underestimated leading to an outlet temperature predicted by the model higher than the measured value. Therefore it is then proposed to take the heat transfer between the turbine and the bearings into account and develop a second version of the turbine model. A model of the bearings is developed. The source of losses (friction and windage) occurring in the bearings are identified and modeled as well as the heat transfer with the turbine. Once the heat transfer has been estimated, it is included in the turbine model where it is inevitably increasing the enthalpy

flow rate variation over the component. The turbine model is finally confronted against experimental data and a good agreement between outputs of the model and measurement is now achieved.

The accuracy of the model being verified and because the latter is based on loss correlations directly available in literature and typically used in the turbomachinary field, a good representation of the loss phenomena taking place in the turbine during the fluid expansion is expected. It is thus proposed in section 4.4.2 to quantify the different sources of losses and to present the average loss distribution.

As explained in Chapter 3, the turbine was developed mainly using components of truck turbochargers. Those components can reach much higher speeds up to 350000 RPM. However the range of speeds met during the experimental campaign was limited to 80000 RPM. Results provided by the model, particularly those concerning the flow description and the velocity triangles indicate the rotational speed is often sub-optimal for the the fluid velocity. It is thus proposed in section 4.4.3 to extrapolate the model to evaluate the turbine performance once the rotational speed is optimized. The model is also confronted to the experimental data gathered with fluid R1233zd, the model parameters being kept unchanged. Finally, a method is proposed to employ the model for the preliminary design of turbine based on similarity relations of turbomachinary concerning the geometry and the operation.

4.2   The radial inflow turbine

In Figure 4.1 is presented the meridional view of a typical radial-inflow turbine. Even if multistage units are also used (e.g. [121]), most radial-inflow turbines are single stage [122]. The flow enters the stage of such a turbine through an inlet volute. The goal of the volute is to accelerate and distribute the fluid uniformly around the turbine periphery. The flow then passes through a nozzle blade row in which is provided further acceleration and increase in circumferential component of velocity [73]. The fluid then goes through a vaneless passage before it enters the rotor row, in which the kinetic energy of the fluid, as it expands, is converted into mechanical energy of the shaft. Finally, an exhaust diffuser often follows the rotor row to convert a part of the rotor exit velocity to static pressure.

A clearance must be provided between the fixed and moving parts of the machine in order to guarantee its mechanical viability. Leakage paths are resulting from these gaps and sealing systems might be considered to reduce the cross section area and thus the mass flow rates of those leakages paths.

4.2.1   Radial-inflow turbine modeling methods

Several modeling approaches are available in literature and can be categorized according to their purpose and level of complexity.
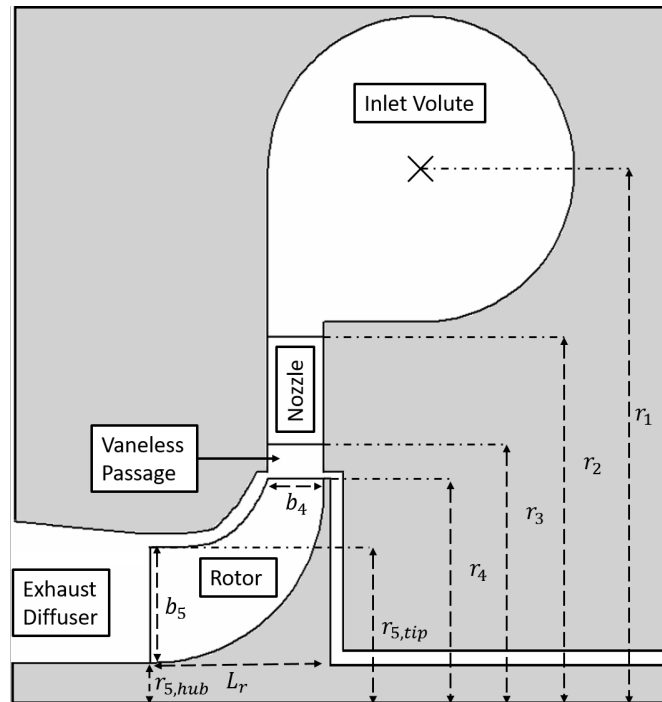
Figure 4.1 – Radial-inflow turbine stage geometry, meridional view based on [122]

Design phase

Flows in turbomachines are highly complex, often compressible and may range from subsonic, through transonic, to supersonic. Shocks may occur, leading to performance losses. The rotation of the rotor is also largely influencing the flow behavior.

Flows are mainly viscous and turbulent even if laminar and transitional regions may also be present. *"Turbulence within the flow field can occur in boundary layers and the free stream, where the level of turbulence will vary depending on upstream conditions"* [123].

Viscous flow phenomena such as three-dimensional boundary layers, interactions between blade and end-wall boundary layers, near-wall flow migration, separated flow, tip clearance vortices, trailing-edge vortices, wakes, and mixing can lead to performance losses. Time-varying conditions upstream, vortex shedding from blade trailing edges, flow separations, or the interactions between rotating and stationary blade rows can result in unsteady flows.

The flow path geometry (e.g. curvature and shape of the flow-path end walls, the spacing between blade rows, blade pitch, etc) has a direct influence on the flow fields. The configuration of the blade rows (e.g. tandem blades, splitter blades, mid-span dampers, and tip treatments) and the details related to blade shape (e.g. thickness distribution, camber, scallop, twist, aspect ratio, solidity, hub-to-tip radius ratio, radii of the leading and trailing edges, tip clearance height, etc.) are of equal importance.

Those examples illustrate the flow complexity and the influence of the flow-path geometry. *"A thorough understanding of the effects of component and flow-path geometry will allow the designer to use the resulting flow behavior to advantage. To achieve this understanding and to perform the analyses necessary to optimize the highly complex flow behavior requires the use of advanced flow modeling technology"* [123].

In design models, the level of detail of the models is generally high since the flow and geometry must be described accurately. The goal of the design process is to minimize losses and maximize aerodynamic performance of the turbine including the geometric and economic constraints placed on the component. There are typically two primary phases: preliminary design and detailed design.

On one hand, the preliminary design phase defines the overall characteristics of the component that satisfy the specifications and constraints. The basic flow-path and the initial configuration and shape of the blades are determined. The process can be highly iterative because of the large number of component and flow-path features that must be optimized. Simplifying assumptions are typically used to model the flow in less detail and thus reduce the computation time. *"Traditionally, simple flow models such as streamline curvature, radial equilibrium analyses, and blade-to-blade analyses, combined with appropriate loss models, have provided adequate information to perform an efficient preliminary design of flow-path shape and blade shape. However, although they offer speed of computation, such 2D design tools do not provide insight into 3D flow behavior"* [123].

On the other hand, the detailed design process focuses on the most promising configuration(s) resulting from the preliminary design phase and offering the best combination of features, and the highest aerodynamic performance. The objective is to predict, as realistically as possible and using the full capabilities of the available CFD analysis tools, the characteristics of the flow and the resulting aerodynamic performance of the component. To be accurate, a 3D viscous transonic flow models must be employed to evaluate the design features that are specifically three-dimensional in nature so they do not need to be evaluated on test rig, which would be costly and time-consuming. Nonetheless, the computation times required by such models (often days of calculation) are several orders of magnitude longer than those for preliminary design tools. Those duration are generally accepted because they also leads to decreases in development times reducing the redesign iterations.

In addition to the use of a detailed 3D viscous transonic flow model, in order to be sufficiently accurate to represent the flow and the aerodynamic performance, the capabilities of the flow analysis tool should include the following items [123]:

- The specification of general boundary conditions for the governing equations,

- A turbulence model that takes adequately account for the characteristics of typical turbomachinery flow fields,

- The capability to model unsteady flow and blade-row interaction.

- The selection of numerical solution techniques compatible with the flow behavior in the components (finite-difference or finite-volume approximations),

- The accurate representation of the geometric configuration of the component and the proper selection of a solution grid (accuracy of both the modeled component geometry and the flow analysis),

- Good program performance (vectorization, parallelization),

- User friendly pre- and postprocessing tools (time for preparing the input and for analyzing and interpreting the results).

Simulation phase

In simulation models, particularly when integrated in an ORC system, authors are often evaluating or assuming the total-to-static efficiency of the turbine stage on the design point and keep this efficiency constant in off-design conditions [124].

Sometimes, empirical relations are defined by the authors to consider the dependence of the efficiency in the pressure ratio and rotational speed [125]. The scaling of existing turbine characteristic maps to predict the performance of another turbine is also observed. According to Pourfarzaneh et al. [126] in their modeling of a turbocharger, constant coefficient scaling (CCS) based on the design point is only valid to predict the performance on the design point. To predict the off-design performance of the component, they proposed a variable coefficient scaling (VCS) method and confronted the prediction results against experimental data.

Less empirical models also exists in literature. Pyari et al. [127] fictively replaced for instance the turbine of a turbocharger by a succession of 2 equivalent nozzles to model the stator and rotor. Equal expansion ratios are assumed across the stator and rotor and 2 equivalent cross-sectional area are identified to predict the mass flow rate in both components. Martins et al. [128] proposed a semi-empirical model for small size radial turbines for refrigeration purposes.

The polytropic model, assuming the fluid behaves as an ideal gas, is convenient to evaluate the efficiency taking into account the irreversibilities in the components of the turbine. Those irreversibilities are taken into account assuming they are proportional to the pressure variation. Serrano et al. [129] proposed a new model based on the one developed by Payri et al. The turbine is still represented by two ideal nozzles and an intermediate volume to respectively consider pressure drops in the components and mass accumulation in the system. However, it is proposed to compute the reaction degree based only on geometrical data and corrected variables provided by the turbine manufacturer to establish the pressure drops in the nozzle and rotor taking into account the polytropic efficiency of the system.

Another approach, a priori suitable for extrapolation outside the validation range of the model, is the use of the mean-line model which is also used in the preliminary design phase of

turbines. In his report, Vilim [130] developed a mean-line model of a radial-inflow-turbine integrated in a super-critical carbon dioxide Brayton cycle system. The model prediction, after including the heat losses and a correction factor on the enthalpy drop, were compared to against data from experiments performed in laboratory. A maximal relative error of 13 % was reached on the enthalpy drop prediction. Sauret et al. [124] performed the preliminary design of several radial-inflow machines based on a number of promising ORC geothermal power systems for five different working fluids. The analysis led to the generation of turbine designs for the various cycles with similar efficiencies (77%) but with large differences in dimensions. The highest performing cycle, based on R134a, showed the maximum turbine static efficiency of 78.5 % with the turbine inlet total temperature and pressure of 413 K and 60 bar respectively. Kang [115] designed and experimentally investigated a 30 kW radial turbine for an ORC using R245fa as working fluid and obtained the turbine static efficiency of 75 % with turbine inlet total temperature and pressure of 353 K and 7.3 bar respectively. In their study, Sakellaridis et al. [131] developed a mean-line radial inflow turbine simulation model to estimate the characteristics of radial inflow turbines of turbochargers. The model was validated against experimental performance data of a variable geometry turbine and results reveal the capability of the model to successfully reproduce, interpolate and extend the efficiency and mass flow characteristics of the turbine, requiring a minimal amount of turbine geometric dimensions, experimental data and calibration parameters for its tuning. Rahbar et al. [132] developed a 5 kWe small-scale radial inflow turbine based on a mean-line model followed by a CFD analysis. The mean-line model was used to investigate the effect of key design parameters such as pressure ratio, mass flow rate and rotational speed on overall performance such as power, efficiency and rotor size and to determine the initial geometry of the expander. The CFD analysis was then used to improve the blade profile leading to a total-to-static around 80 %. The fluid was unfortunately not given by the author. Later, Rahbar et al. proposed a modeling and optimization strategy for 50 to 130 kW radial inflow turbines for ORC based on a mean-line model[73]. The model was used to identify the key variables influencing the turbine overall size and the cycle performance. These parameters were then included in the optimization process using the DIRECT algorithm to maximize the net electric power output per turbine diameter unit length for six organic fluids. Total-to-static efficiencies varied from 70 to 77 %. In another study [133], Rahbar et al. also performed a parametric analysis and optimization, through a mean line model, of 15 kW power output radial inflow turbines using the genetic algorithm with eight organic fluids. Total-to-static efficiencies typically between 83 and 84 % were achieved. Kang [121] designed and experimentally investigated a 40 kW radial turbine using R245fa and obtained a turbine static efficiency for both stages of 59 %.

4.3 Mean-line model of the radial-inflow turbine

Modeling three-dimensional, viscous, and transonic flows, including turbulence and heat transfer phenomena, considering unsteady flows and the interactions of multiple blade rows, and handling complex geometric configurations require advanced CFD tools. Moreover the

increasing level of competition and the resulting performance expectations for the new turbo-machines also justify the needs of advanced tools. In order to meet demanding performance goals, turbines must be designed to meet the requirements of increased efficiency, work and pressure ratio per stage, and operating temperatures. The improvements in performance will result from the use of advanced aerodynamic concepts. *"The components will have much greater complexity than those seen in the past, including a higher degree of 3-dimensionality in both component and flow-path configurations. The flow fields associated with these components will be equally complex and 3D"* [123].

Nonetheless, the study of the flow in a turbomachine can under certain assumptions be reduced to the study of the flow in an inter-blade channel whose unsteady effects are neglected. However, in such a channel, the flow remains basically 3D, insofar as the velocity gradients and the thermodynamic quantities exist in the 3 reference directions. Therefore, most design tools rely on a quasi-3D approach, which consists of reconstructing a 3-dimensional flow from a number of two-dimensional flows (Wu's method). Standard heat-transfer correlations are used along the predicted streamlines to compute the heat transfer to the metal surface and typically, the flow is assumed inviscid (which limits accuracy because flow separation cannot be considered)

Considering, for clarity reasons, the case of an axial turbine, a two-dimensional basic module is the flow in the blade row which develops on a surface of type S1 (blade-to-blade) and which expresses in particular the action of the deflection of the fluid by the blades. Thus, a (restricted) number of current tubes of finite thickness is considered, each represented by an average surface-current of type S1. These surfaces are typically assumed current axisymmetric. These flows in a grid of blades superposed within the machine are of course interdependent. Their compatibility is ensured by expressing, along the S2-type surfaces (hub-to-tip) containing the axis of the machine, the equilibrium of the forces acting on the fluid in the radial or normal direction at the current surfaces S1, hence the name of radial equilibrium. This equilibrium is satisfied on the basis of an average performed in the circumferential direction and constitutes a second two-dimensional module. The final Quasi-3-D solution can be achieved using an iterative technique and the continuity equation.

From the 1950s to the mid-1980s, corresponding to the availability of sufficient computing power to solve in reasonable times the fully viscous 3D Navier–Stokes equations, this method was quite popular and sufficient to design turbomachinery components. Today, more sophisticated designs (highly 3D, viscous, turbulent, and often transonic) are making these tools no longer adequate to the development of new advanced technology components but Wu's method was packaged and improved and is still used in many CFD tools, for example, to provide a starting point to the Navier–Stokes numerical solutions.

Regarding the investigated turbine, most of the geometric data is kept confidential by the manufacturer making the 3D and quasi-3D models impossible to implement. Nonetheless, all the methods can be assumed possible candidates at first. The suitable modeling approach
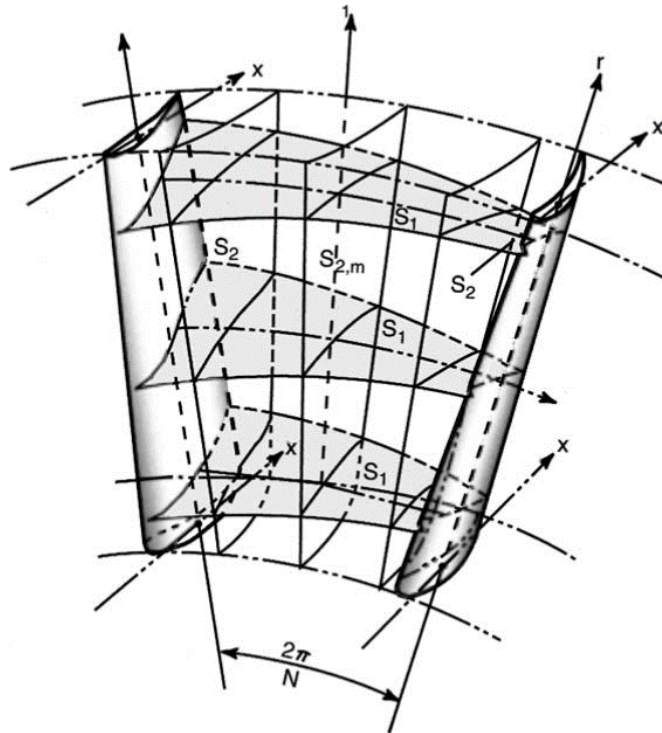
Figure 4.2 – Intersecting S1 and S2 surfaces in a blade row [123].

and corresponding level of details can be identified based on the following requirements.

The objective of the model is to predict, with a sufficient level of accuracy, the performance of the turbine detailed in Chapter 3. The model must therefore be able to predict, eventually, the characteristics of the flow, in order to understand the machine behavior and potentially its strength and weakness. It must at least predict the performance of the component over the whole range of operating conditions met during the experimental campaign. Because the final goal is to include the turbine model in a global ORC system design and optimization tool, the model needs also to be able to be used in design phase and should also require a minimal computational time. Typically, the design of turbomachines based on existing components implies the use of the laws of similarities so the description of the geometry of the component is also required. Computational time is a critical capability of the model for the following activities within this thesis. While the solution is almost instantaneous for constant efficiency, empirical efficiency and quasi-empirical models, it requires (roughly) less than 1 second for the mean-line model, several seconds to minutes for quasi-3D models and hours to days for 3D models. Adding the lack of geometrical data to build quasi-3D or 3D models, it is proposed at the end to develop a mean-line model of the turbine which, among the proposed modeling approaches, best satisfies all the prerequisites, as summarized in table 4.1. To establish quantitatively the level of accuracy of the performance prediction, the model will have to be confronted to the experimental data of Chapter 3.

Table 4.1 – Characteristics of the reviewed modeling approaches for radial-inflow turbines

Criteria	Constant Efficiency	Empirical Efficiency	Quasi-empirical model	Mean-line model	Quasi-3D model	3D model
Performance Accuracy (design and off-design)	-	-	-	+	++	+++
Flow characterization	-	-	-	+	++	+++
Use in design	-	-	-	+	+	+
Computational time	+++	+++	+++	++	-	- -
Geometric inputs	+++	+++	+++	++	+	-

Mean-line modeling is based on a 1D assumption that the flow follows an inter-blade current tube along the mean streamline through the stage and such that conditions on the mean streamline are the average of the passage conditions. The thermodynamic properties, geometry parameters and flow characteristics are determined at key stations throughout the stage, typically at the inlet and outlet of the components of the turbine.

4.3.1 Conservation laws

The Navier-Stokes equations are obtained applying the conservation laws to an open system of volume V, bounded by a Surface S. The local form of these equations is obtained by tending towards 0 the dimensions of the control volume. By nature, a flow limited by solid moving boundary cannot be in steady-state. Thus, absolute local characteristics of the fluid (e.g. pressure, velocity, etc) vary in space and time and generally global characteristics of the machine (e.g. efficiency, power, mass flow rate, rotational speed, etc.) are also varying. However it is possible to define a steady-state operation based on average values constant in time. This methodology is, for instance, also used in engine models [134] [135]. Contrary to high frequency models that calculate the complete process in the cylinders, the mean value model just gives the cycle by cycle estimation of the engine behavior.

Expressing the mass conservation for an open system can be achieved using the Reynolds transport theorem which applies to any extensive quantity R characterizing a control volume V delimited by a surface S:

$$\frac{d\mathbf{R}}{dt} = \frac{\partial}{\partial t}\int_V \rho \frac{d\mathbf{R}}{dm}dV + \oint_S \rho \frac{d\mathbf{R}}{dm}(\vec{C}\cdot\vec{n}_e)dS \tag{4.1}$$

Applying this theorem to the mass, the expression becomes:

$$\frac{\partial}{\partial t}\int_V \rho \, dV = -\oint_S \rho(\vec{C}\cdot\vec{n}_e)dS \tag{4.2}$$

Applying the divergence theorem (also know as Gauss theorem or Ostrogradsky's theorem),

the following local form of the equation can be obtained.

$$\frac{\partial \rho}{\partial t} + \vec{\nabla} \cdot (\rho \vec{C}) = 0 \tag{4.3}$$

The global form of the mass conservation for an open system in steady-state express the equality of the incoming and outgoing mass flow rates:

$$\dot{M}_{in} = \dot{M}_{out} \qquad \text{or} \qquad \boxed{(\rho AV)_{in} = (\rho AV)_{out}} \tag{4.4}$$

The Reynolds theorem applied to the linear momentum leads to the momentum conservation for an open system:

$$\frac{\partial}{\partial t} \int_V \rho \vec{C} dV = - \oint_S \rho \vec{C}(\vec{C} \cdot \vec{n}_e) dS + \sum \vec{F}_{ext} \tag{4.5}$$

The accumulation of the linear momentum component i in the control volume V is given by:

$$\frac{\partial}{\partial t} \int_V \rho c_i dV \tag{4.6}$$

The net flow of the linear momentum component i through the surface S is given by:

$$- \oint_S \rho c_i \vec{C} \cdot \vec{n}_e dS \tag{4.7}$$

The external forces acting on the fluid can be split in

the distance forces whose action on the volume is a function of the acceleration a they cause

$$\int_V \rho \vec{a} dV \tag{4.8}$$

the contact forces whose action is due to hydrostatic pressure and molecular stirring and which apply through the facets of the surface S

$$- \oint_S \vec{\theta}(\vec{n}) dS \tag{4.9}$$

There exist three types of facets and on each facet are applied 2 shear stresses and 1 normal stress (Figure 4.3).

A 3-by-3 stress tensor is therefore used so the component i of each stress vector is expressed by

$$\theta(\vec{n})_i = \sigma_{ik} n_k = \sigma_{ix} n_x + \sigma_{iy} n_y + \sigma_{iz} n_z \tag{4.10}$$

The linear momentum conservation is therefore written for the component i:

$$\frac{\partial}{\partial t} \int_V \rho c_i dV = - \oint_S \rho c_i \vec{C} \cdot \vec{n}_e dS + \int_V \rho a_i dV + \oint_S \sigma_{ik} n_k dS \tag{4.11}$$
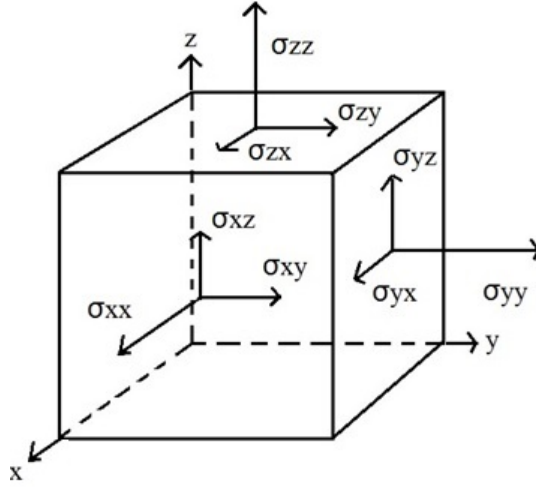
Figure 4.3 – Normal stresses and shear stresses

or in steady-state, applying the divergence theorem, the following local form is obtained

$$\frac{\partial \rho c_i c_k}{\partial x_k} = \rho a_i + \frac{\partial \sigma_{ik}}{\partial x_k} \tag{4.12}$$

The stress state of a fluid is linked to the strain rate: to deform a fluid, the higher the strain rates are the higher the stress are required. In particular Newtonian fluids are characterized by a linear relationship between strains and stresses. Considerations on isotropy lead to 6 linear relations involving 2 viscosity coefficients (μ and λ)

$$\sigma_{ij} = -p\delta_{ij} + \underbrace{\mu(\frac{\partial u_i}{\partial x_j} + \frac{\partial u_j}{\partial x_i}) + \lambda \delta_{ij} \frac{\partial u_k}{\partial x_k}}_{\tau_{ij}} \tag{4.13}$$

Vectorially, the linear momentum conservation can finally be written as follow:

$$\vec{\nabla} \cdot (\rho \vec{C} \otimes \vec{C}) + \vec{\nabla} p = \vec{\nabla} \cdot \overline{\overline{\tau}} + \rho \vec{a} \tag{4.14}$$

The angular momentum conservation, which is the basis of the description of the energy exchange between the fluid and the turbomachine blades, can in turn be expressed applying the Reynolds theorem to the angular momentum H, defined by the vector product of the position and speed vectors:

$$\vec{H} = \int \vec{r} \wedge \vec{C} dm \tag{4.15}$$

It comes

$$\vec{T}_v + \vec{T}_s = \frac{\partial}{\partial t} \int_V \rho(\vec{r} \wedge \vec{C}) dV - \oint_S \rho(\vec{r} \wedge \vec{C})(\vec{C} \cdot \vec{n}_e) dS \qquad (4.16)$$

The left member is equivalent to the Newton's second law and expresses the variation of the angular momentum is proportional to the torques of the volume and surface forces applied to the system. The first term of the right member defines the accumulation of the quantity $(\vec{r} \wedge \vec{C})$ in the control volume, which is null in steady-state. The second term is the net flow of the quantity $(\vec{r} \wedge \vec{C})$ that goes through the surface S. For single-input and single-output (SISO) system in steady-state, the angular momentum conservation thus become

$$\vec{T}_v + \vec{T}_s = \dot{M}_{out}(\vec{r} \wedge \vec{C})_{out} - \dot{M}_{in}(\vec{r} \wedge \vec{C})_{in} \qquad (4.17)$$

This law shows the modification of the angular momentum of a fluid particle between the inlet and outlet of a stator, or a rotor, of a turbomachine is resulting from the volume and surface torques that apply on the fluid. This equation is constituted of three components (r, θ, z) in the cylindrical coordinate system (respectively radial, tangential and axial). However only the axial component can contribute to the energy transfer between the fluid and the shaft of the machine. The volume forces due to gravity exert no axial torque for symmetry reasons. The pressure and shear stresses at the inlet and outlet boundaries exert a null or negligible torque. The same is for the pressure stress on the hub and housing of the machine. Only are left the shear stresses on the hub and the housing of the machine and the pressure and shear stresses applied by the moving blades on the fluid (driven machine). The latter contribution is generally called torque at the shaft of the machine but nonetheless does not include friction in the bearings, disk, mechanical end stops or sealing systems.

The first law of thermodynamic ([136], [137]) state the equivalent effect of work and heat on the internal energy of a closed system.

$$\Delta U = \int \delta W + \delta Q \qquad (4.18)$$

In the case of an open system and assuming there is no heat exchange between the working fluid and the outside, the Reynolds transport theorem can be applied to the internal, kinetic and potential energy in order to express the energy conservation. It comes for a SISO system:

$$E = \int (u + \frac{C^2}{2} + gz) dm \qquad (4.19) \qquad \boxed{\dot{M}(\Delta h + \Delta \frac{C^2}{2} + g\Delta z) = \dot{W}_{sh}} \quad (4.20)$$

4.3.2 Velocity triangles

The blades (or vanes) lead and deviate the fluid going trough the machine. In the fixed parts (volute, stator, diffuser, etc), the absolute trajectory of the fluid particles is imposed by the fixed vanes while in the rotor, the relative trajectory of those particles is provided by the

moving blades. Assuming the machine and the flow are in steady-state, an average speed of the particles at any point of the machine is supposed constant in time. Based on these assumptions, in each cross section , called station and bounded by the components of the machine, can be defined an average speed of the fluid. This speed is represented by 3 velocity vectors

- C in the absolute direction of the flow,

- W in the relative direction of the flow,

- U the blade speed.

These three velocities are linked together by the vector relation of Figure 4.4 and can be represented in a velocity triangle. In this triangle, the velocity perpendicular to the blade speed ($U = \omega r$) is the flow velocity (C_m or W_m). The angle α, between the flow and absolute velocities, measures the absolute direction of the flow. The angle β, between the flow and relative velocities, measures the relative direction of the flow. The convention is here to consider these angles are positive in the direction of the peripheral velocity. C_θ is the projection of the absolute velocity, and is positive, in the blade speed direction. W_θ is the projection of the relative velocity, and is positive, in the blade speed direction.

$\vec{C} = \vec{W} + \vec{U}$	
$C_m = C \cos(\alpha)$	$W_m = W \cos(\beta)$
$C_\theta = C \sin(\alpha)$	$W_\theta = W \sin(\beta)$
$C_\theta = W_\theta + U$	
$W^2 = C^2 + U^2 - 2UC_\theta$	
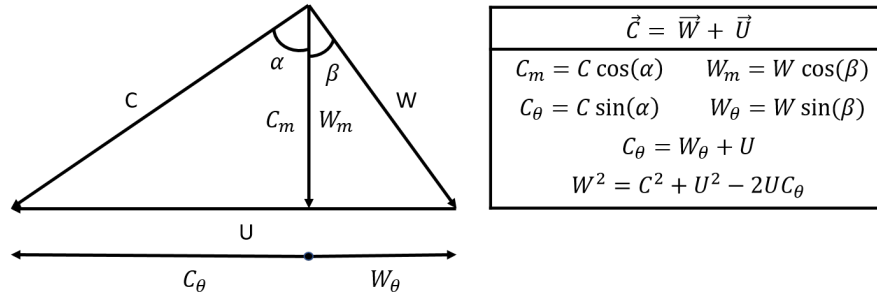
Figure 4.4 – Example of velocity triangle

In general, the housing and the hub of a turbomachine are neither cylindrical nor parallel. A straight blade grid can nevertheless be obtained by developing the intersection of a cylinder coaxial with the machine on a plane (S1 surface). Thus, the trace of the blades on this cylinder determines an infinity of identical profiles, corresponding to a purely two-dimensional problem. Figure 4.5 shows the development on a S1-type plane of 2 blades of the stator and rotor grids of a turbine. This Figure can be applicable for both axial and radial turbine. On the left is shown the geometry of the blade profiles. The superscript ′ indicates the blade angle measured between a line tangent to the camber line of the blade and the meridian line. On the right is shown the geometry of the flow at each station. The distinction between blade and flow angles at a same station is emphasized at the blade leading edge because the difference due to a misalignment results in an incidence loss. At the blade trailing edge a similar misalignment

can be defined ans is called deviation. Finally, the sum of the blade angles defines the blade camber while the sum of the flow angles on both side of a blade describe the turning of the flow and is called deflection [138].
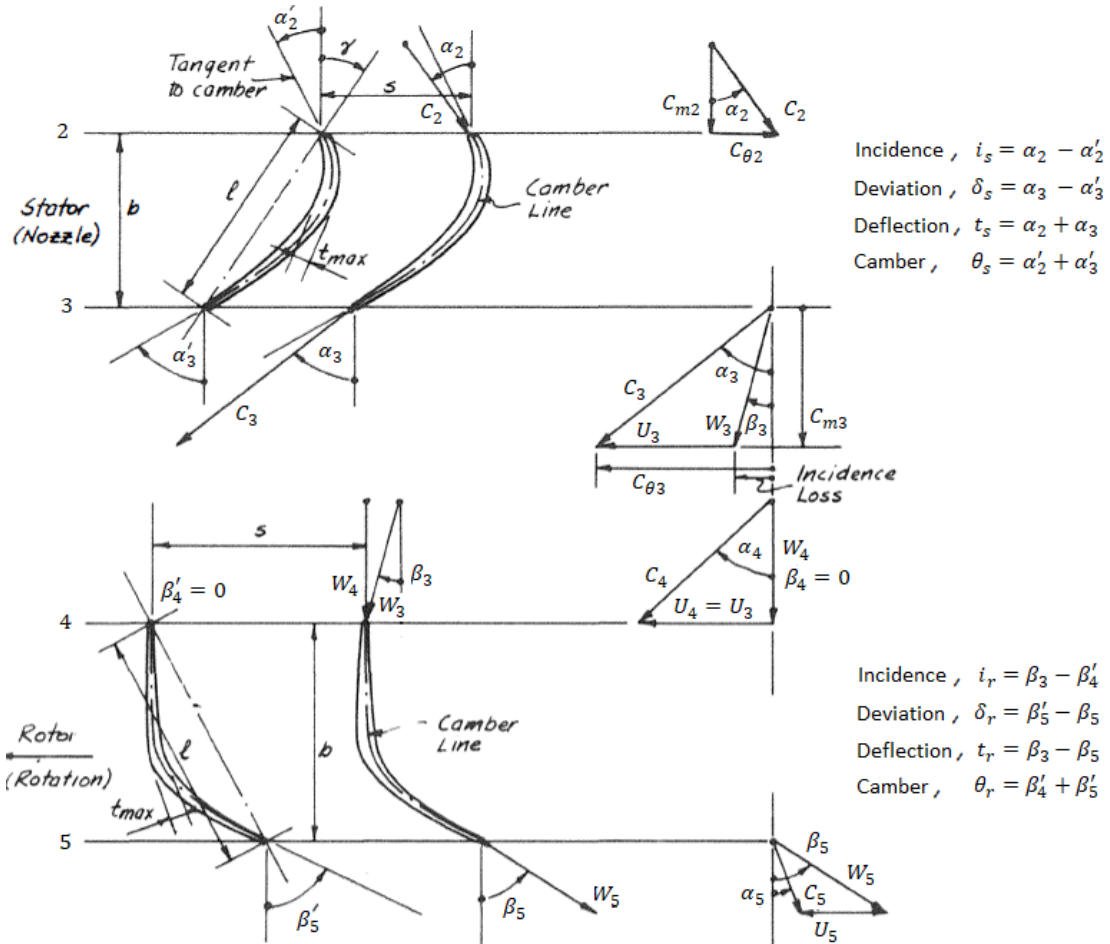
Figure 4.5 – Development of a blade grid of a turbine on a S1-type plane (2-3: stator, 4-5:rotor) [138]

4.3.3 Euler's relation

Assuming the mass flow rate is conserved between the inlet and outlet of the rotor, equation 4.17 becomes:

$$T_{sh} = \dot{M}(r_{out}C_{\theta,out} - r_{in}C_{\theta,in}) \tag{4.21}$$

The transferred power within the rotor is then obtained multiplying the torque by the rotational speed:

$$\dot{W}_{sh} = \dot{M}\omega(r_{out}C_{\theta,out} - r_{in}C_{\theta,in}) = \dot{M}(U_{out}C_{\theta,out} - U_{in}C_{\theta,in}) \tag{4.22}$$

Equation 4.22 is the well known Euler equation [139]. It is valid for any flow of compressible or incompressible fluid, viscous or non-viscous, but in steady-state. It indicates the energy exchanged is resulting on one side from the modification of the blade speed and on the other side from the modification of tangential component of the absolute velocity. Typically, in purely axial machines, the first contribution is null or negligible while it is important in radial components.

The second law of thermodynamics [140], [141], [142] complete the first and describes the direction in which work and heat exchange can occur, i.e. so that the total entropy of an isolated system undergoing a real (irreversible) process can only increase. Combining first and second law, Gibbs equation, valid for reversible and irreversible process, is obtained

$$dh = Tds + \frac{dp}{\rho}$$
(4.23)

The most common source of irreversibility in fluid flows is friction. Combining the first law 4.18, Gibbs equation 4.23 and Euler's 4.22 relation for an adiabatic fluid flow gives

$$\Delta h + \Delta \frac{C^2}{2} + g\Delta z = \frac{\Delta p}{\rho} + \Delta \frac{C^2}{2} + g\Delta z + T\Delta s = \frac{\dot{W}_{sh}}{\dot{M}} = \Delta(UC_\theta)$$
(4.24)

Because the fluid flow is adiabatic, the entropy increase can only results from irreversibilities such as friction.

Equation 4.24 applied to an adiabatic open system and neglecting the potential energy can then be written as follow:

$$\frac{\dot{W}_{sh}}{\dot{M}} = \Delta h + \Delta \frac{C^2}{2} = \Delta h_0 = \Delta(UC_\theta)$$
(4.25)

Without work production it leads to Eq. 4.26. This relation, called the St Venant relation, shows the sum of enthalpy and kinetic energy, defined as the total enthalpy, remains constant in quasi-1D adiabatic flow without moving blades. If one of the two forms changes, the other changes in opposite way. The conservation of the total enthalpy applies in particular in the fixed part of the turbine whose function is to convert the enthalpy of the fluid in kinetic energy (volute, stator, etc).

$$\Delta h_0 = \Delta h + \Delta \frac{C^2}{2} = 0$$
(4.26)

The total enthalpy being defined, Eq. 4.27, which is another form of the Euler's relation is obtained for a rotor, using the relations of the velocity triangles (Figure 4.4).

$$\Delta h_0 = \Delta(UC_\theta) = \frac{C_5^2 - C_4^2}{2} - \frac{W_5^2 - W_4^2}{2} + \frac{U_5^2 - U_4^2}{2}$$
(4.27)

Substituting the total enthalpy by its value, Eq. 4.28 is obtained, which shows the rothalpy,

defined by Eq. 4.29, is conserved in a rotor. The rothalpy is different from the relative total enthalpy, which is defined as the total enthalpy but based on the relative velocity ($h_{r0} = h + \frac{W^2}{2}$). The rothalpy is the equivalent for a rotor of the total enthalpy which is conserved for a stator while the relative total enthalpy is conserved only for rotors of axial turbines where $U_4 = U_5$.

$$\Delta h_r = h_5 - h_4 = \frac{W_4^2 - W_5^2}{2} + \frac{U_5^2 - U_4^2}{2} \quad (4.28) \qquad\qquad i_0 = h + \frac{W^2 - U^2}{2} \quad (4.29)$$

4.3.4   Non-dimensional parameters and performance indicators

Performance of a turbine stage (i.e. essentially the pressure ratio, enthalpy drop, efficiency, mass flow rate and rotational speed) are typically represented, as well as the different variables on which they depend, in a standardized form.

A classical dimensional analysis leads to a certain number of dimensionless groups. Several solutions are possible, depending on the combination of the basic variables. It is conventional to use the specific heat ratio ($\gamma = \frac{C_p}{C_v}$) and the Reynolds number (Re), which indicates the relative importance of effects due to the viscosity of the fluid. However, a single machine is supposed to operate with only one type of fluid and the experiment shows that the variation of the performance as a function of (Re) is relatively small, as long as the turbine is run in a typical operating range. The performances are therefore traditionally presented as a function of the other parameters, and the effects of γ and Re are given as corrections to be made to the results if necessary.

The isentropic efficiency of a turbine is generally defined based on the total conditions at the inlet and outlet of the component. It is called the **total-to-total efficiency** and is defined as follow:

$$\eta_{TT} = \frac{h_{01} - h_{05}}{h_{01} - h_{05,s}} \tag{4.30}$$

For single stage turbines, the kinetic energy at the outlet of the rotor is typically considered as lost and the **total-to-static efficiency** is preferably used. It is defined as follow:

$$\eta_{TS} = \frac{h_{01} - h_{05}}{h_{01} - h_{5,s}} = \frac{h_{01} - h_{05}}{h_{01} - h_{05,s} + \frac{C_5^2}{2}} \tag{4.31}$$

The Mach number, which describes the relative magnitude of the compressibility effects, is not often used. As the Mach number establishes, for a given section, the value of the mass flow rate related to the total conditions, the reduced mass flow rate is generally preferred in turbomachinary (Eq. 4.32). In the same way, the reduced rotational speed of the machine can be defined (Eq. 4.33). Expressions for the reduced mass flow rate and reduced rotational speed can be simplified if the perfect gas model can be used, considering the speed of sound
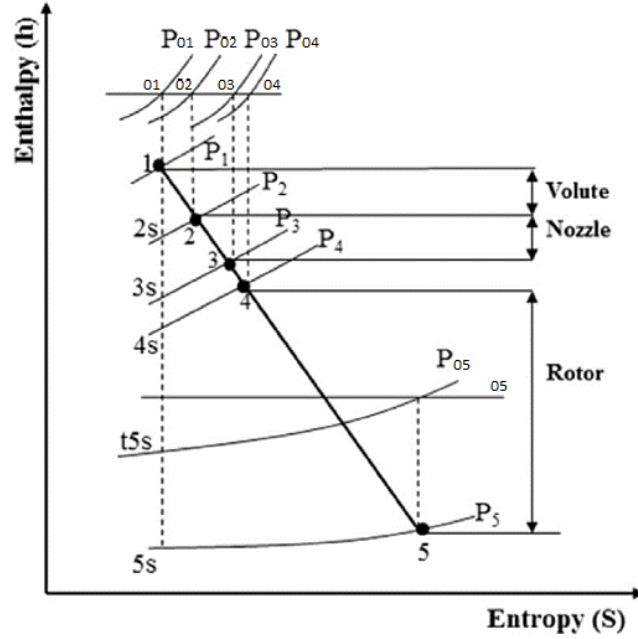
Figure 4.6 – Enthalpy-entropy (h-s) diagram of the expansion in a radial-inflow turbine [133]

can be expressed based on the temperature ($a = \sqrt{\gamma R T}$). The reduced values can also be made dimensionless based on nominal or standard conditions and they are commonly used to describe the performance of a turbine stage. Typically, the isentropic efficiency and the reduced mass flow rate are expressed as functions of the pressure ratio and reduced rotational speed.

$$\dot{M}^{co} = \frac{\dot{M} a_0}{P_0 A} \underset{P.G.}{=} \frac{\dot{M} \sqrt{T_0}}{P_0 A} \qquad (4.32)$$

$$N^{co} = \frac{N}{a_0} \underset{P.G.}{=} \frac{N}{\sqrt{T_0}} \qquad (4.33)$$

The goal of the stator is mainly to convert the fluid enthalpy drop into kinetic energy (Eq. 4.34) while the goal of the rotor is to convert this kinetic energy into mechanical energy at the shaft of the turbine (Eq. 4.35).

$$\Delta h_s = h_3 - h_2 = \frac{V_2^2 - V_3^2}{2} \qquad (4.34)$$

$$\frac{\dot{W}_{sh}}{\dot{M}} = h_05 - h_04 = U_5 V_{\theta 5} - U_4 V_{\theta 4} \quad (4.35)$$

However, an enthalpy drop can also occur through the rotor (Eq. 4.36):

$$\Delta h_r = h_5 - h_4 = \frac{W_4^2 - W_5^2}{2} - \frac{U_4^2 - U_5^2}{2} \qquad (4.36)$$

The **degree of reaction** (DR) of a turbine stage is defined as the ratio of the enthalpy drop in

the rotor over the enthalpy drop in the overall stage:

$$R_D = \frac{\Delta h_r}{\Delta h_s + \Delta h_r} = \frac{(W_4^2 - W_5^2) - (U_4^2 - U_5^2)}{(V_2^2 - V_3^2) + (W_4^2 - W_5^2) - (U_4^2 - U_5^2)} \tag{4.37}$$

According the value of the reaction degree, a turbine stage could in theory be designed to operate in one of the modes summarized in table 4.2. However, because of technical reasons, all these modes cannot be achieved and two main types of stage are mainly used in practice:

- The action stages ($R_D \leq 0$): There is no enthalpy drop in the rotor except to overcome the frictions.

- The reaction stages ($R_D > 0$): there is a significant enthalpy drop in the rotor. However, for technical reasons, the value of the reaction degree is often below 0.7. The most typical value is 0.5.

Table 4.2 – Theoritical values for the reaction degree of a turbine stage

Value	Principle	Name
$R_D < 0$	Super Action	Action
$R_D = 0$	Pure action	Action
$0 < R_D < 1$	Action-Reaction	Reaction
$R_D = 1$	Pure Reaction	Reaction
$R_D > 1$	Super Reaction	Reaction

Typically, the reaction degree of a turbine stage is chosen in the design phase to optimize the turbine with the objectives of: compactness of the machine, optimal efficiency, maximal aerodynamic load.

Flow and loading coefficients are originally defined for multi-stages axial turbines. In those turbines, the blade speed can be assumed constant along the rotor of the stage (i.e. $U_4 = U_5$) and the stages are typically designed to be repetitive (i.e. $V_2 = V_5$). Therefore, the expression of the reaction degree (Eq. 4.37) can be simplified and derived as a function of the work of the stage.

$$R_D = \frac{(W_4^2 - W_5^2)}{(V_5^2 - V_3^2) + (W_4^2 - W_5^2)} = \frac{(W_4^2 - W_5^2)}{2U\Delta V_\theta} \tag{4.38}$$

Using the relations of the velocity triangles, it comes:

$$R_D = \frac{(W_4^2 - W_5^2)}{2U\Delta W_\theta} = \frac{W_{m4}^2 - W_{m5}^2 + W_{\theta4}^2 - W_{\theta5}^2}{2U\Delta W_\theta} \tag{4.39}$$

and then, assuming the axial component of the velocity are close together

$$R_D = \frac{W_{\theta 4}^2 - W_{\theta 5}^2}{2U\Delta W_\theta} = \frac{C_m}{U} \frac{\tan\beta_4 + \tan\beta_5}{2} = -\Phi\tan\beta_m \tag{4.40}$$

where Φ is the **flow coefficient** and β_m the mean flow angle.

The **loading coefficient** represents the work performed by the turbine stage and is made dimensionless through the kinetic energy linked to the driving velocity.

$$\Psi = \frac{-\Delta h_0}{U_4^2} = \frac{h_04 - h_05}{U_4^2} = \frac{U_4 V_{\theta 4} - U_5 V_{\theta 5}}{U_4^2} \underset{axial}{=} \frac{V_{\theta 4} - V_{\theta 5}}{U} = \Phi(\tan\alpha_4 - \tan\alpha_5) \tag{4.41}$$

In the case of an axial stage, the loading factor is proportional to the flow coefficient and thus to the degree of reaction of the stage. The performance of a turbine stage is thus expressed by the work and the associated efficiency, as a function of the mass flow rate and the rotational speed. The work performed can be the pressure ratio or the loading coefficient. The flow rate is generally represented by the corrected flow rate or the flow coefficient. The corrected flow rate and rotational speed have the advantage of being independent of the conditions of use. Therefore, these quantities are used for on-board machines such as turbo-reactors. For ground-based machines, for which the ambient conditions vary considerably less, the working and flow coefficients are often preferred.

Stage loading and flow coefficients are used to the same extent in radial turbines. Unlike axial turbines, there is a wide variation in blade speed due to the radius change between inlet and outlet of radial turbines. The choice of blade speed used to define these coefficients is arbitrary. In this study, there are defined as follow:

$$\Phi = \frac{C_{m5}}{U_4} \tag{4.42} \qquad\qquad \Psi = \frac{\Delta h_0}{U_4^2} \tag{4.43}$$

A turbine stage can operate in off-design over a wide range of loading coefficient values without significant fluctuations in efficiency. This behavior is very different from compressor stage, which has an upper limit of aerodynamic load, beyond which the operation becomes unstable, and induces a pumping phenomenon. However, a turbine stage aerodynamically highly loaded can not present the same efficiency as a less loaded stage. As well, the values of the flow coefficient of a turbine stage do not show any obvious upper limit. However, from a certain values, the influence on the losses due to compressibility effects, via the Mach number of the flow, becomes important. On the other side of the operating range, very low values of flow coefficient may cause performance degradation due to a bad incidence on the blades, but the turbine operation remains stable. In order to study the performance of the turbine stage outside the nominal point, the variations in the orthogonal direction of the flow are typically considered very small, and the flow conditions on the mean line are considered representative of the global flow conditions. In many cases, the absolute and relative flow angles at the outlet

of the stator (α_3) and of the rotor (β_5), respectively, can be seen not to vary much around the nominal operating point.

4.3.5 Main loss Mechanisms

Turbine conception implies the possibility of predicting the performance as best and as early as possible from the preliminary design stage. This is particularly valid for large scale turbines such as those in large power plants where a small error on turbine efficiency can lead to significant financial losses (in millions of euros).

The isentropic efficiency of a stage can be expressed as a function of all the losses occurring in the stage during its operation. Those losses lead to a deficit of enthalpy drop that is often related to the kinetic energy downstream the blades:

For a stator: For a rotor

$$\xi_s = \frac{h_3 - h_{3,s}}{V_3^2/2} \qquad (4.44) \qquad\qquad \xi_r = \frac{h_5 - h_{5,s}}{W_5^2/2} \qquad (4.45)$$

In general, the losses are split in 3 categories: profile, secondary and additional losses.

Profile losses are mainly due to the development of boundary layers on the blade walls. They depend on the shape of the blades (curvature of the suction and pressure sides), their thickness, the inter-blade distance (a high relative pitch increases the load on a blade and can lead to a separation while a low relative pitch decreases this phenomenon but means higher number of blades and thus a bigger surface on which frictions apply), the Reynolds number, the degree of reaction of the stage, the roughness of the walls, the incidence of the upstream flow on the blades, the deviation of the flow, the compressibility effects (Mach number), the thickness of the trailing edge, etc.

Secondary losses result from the formation of secondary flows. The circumferential deviation of the flow by the blades leads to a centrifugal force exerted on the fluid particles. The reaction is a pressure gradient which is installed in the inter-blade channel, directed from the pressure side to the suction side of the adjacent blade. Boundary layers develop along the casing and hub, within which the speed is reduced. The resulting centrifugal force, which is too weak, no longer balances the pressure gradient, and in these zones a migration of the fluid particles from the pressure to the suction side occurs, which is responsible for a reduction in the performance of the stage. When the blade height is too low, the secondary flow zones coalesce, significantly increasing the losses and making impossible the distinction between profile losses and secondary losses.

Additional losses can be created by the presence of fins, placed to stiffen the blades rings, by the divergence of the fluid vein, which must compensate for the rapid increase in specific volume, by the clearances leading to vortices and leakage flow rates, by the friction of the sealing systems, and by the movement of the rotor that bathes in the fluid. In reaction axial

turbines, the leakages typically occur at the bottom of the fixed blades of the stator and at the top of the mobile blades of the rotor. In action axial turbines, leakages occur only at the passage of the shaft through the hole made in the disks. In addition to clearance losses, disk friction in axial action turbines has also to be considered. Indeed, each disk rotating in its dedicated annular space leads to a windage work inevitably reducing the work produced by the turbine. The radial turbine stage suffers from losses of the same nature as the axial stage.

Before considering loss correlations for each source in the individual components of the turbine, it is remarked here, that some authors developed general correlations of stage performance with flow conditions. According to Thompson [138], the first correlation of this kind was developed by Balje [143]. Balje found the turbine efficiency was mainly a function of specific speed and specific diameter. Later, Balje and Binsley [144], assuming that the performance of a stage could be defined by 9 independent variables, used the method of the dimensional analysis to identify the 6 dimensionless parameters.

When information on the flow process and the geometry is sufficiently complete, loss mechanisms should be preferably described in the individual elements. The main manufacturers carried out systematic tests on rotor and stator blades grids. Over the years, this information has been completed by real machine tests. One of the most well-known correlations is the Soderberg's correlation [145] for axial turbines, which was based on the work performed by Traupel [146] and on systematic tests in grids of blades, deemed to be well-designed (i.e. with a relative pitch assumed optimal). The result is a very simple correlation between the loss coefficient ξ and the deflection of the flow, the rope of the blades, their thickness, their spacing and the Reynolds number. Nonetheless this approach fails to evaluate the different types of losses separately. The Soderberg's correlation does not take into account neither the effect of the trailing edge thickness nor the effect of the degree of reaction. Despite these criticisms, the Soderberg correlation is relatively simple to use and gives precise results.

Contrary to Soderberg, Ainley and Mathieson [147] tried to split the profile, secondary and clearance losses. They expressed the losses in terms of total pressure (instead of enthalpy) drops.

Another example is Smith's work [148], which measured the efficiency of a large number of turbine stages characterized by various circumferential output components and degrees of reaction. He published a correlation in the form of an abacus in the plane of the variables (Φ, Ψ), for nominal conditions. Generally, the accuracy of Smith's correlation is slightly higher than using Soderberg's or Ainley and Mathieson's correlation.

According to Thompson [138], loss correlations in radial turbine stages were, at the time, much less complete and had been subject to far less critical evaluation than those developed for axial turbine. Nonetheless, reports of experimental programs dealing with radial turbines exist (the D.I.G.T. work in England [149], the Japanese industrial program [150] [151], the NASA space program in the USA [152]). In particular, Mizumachi [150] approaches the nozzle and rotor losses taking into account profile, end-wall and secondary effects. Based on these reports,

Benson [153] presented a loss correlation that includes nozzle passage, rotor blade incidence and rotor passage losses. In 1973, Withfield et al. [154] investigated loss due to inappropriate impeller incidence in radial compressors and turbines. They proposed to extend the incidence loss models proposed by Futral et al. [152]. More recently, Aungier [122] described all the loss mechanisms in axial and radial-inflow turbines and the corresponding total pressure losses. Suhrmann et al. [155] collected, reviewed and validated loss models used for the preliminary design of radial turbines and investigated their applicability to small-size turbines. Demierre et al [156] also collected in order to built and validate, based on experimental data, a model of turbine-compressor unit. Finally, in a preliminary design study, Rahbar et al. [73] proposed a model of radial-inflow turbine based on correlation available in literature to describe the loss mechanisms in the components.

Concerning the losses due to secondary flows, extensive work to standardize the various models proposed has been achieved. They are very complex because the blade grid model remains far from the reality: account must be taken of the centrifugation effects, Coriolis forces, and of course pressure gradients. As mentioned, Ainley and Mathieson [147] proposed a correlation for the secondary and clearance losses. Rodgers [157] also proposed correlations to describe those phenomena.

Most of the time, additional losses concern the clearance, disk friction and discharge losses. Many studies focused on the clearance and the corresponding enthalpy losses ([158],[159],[160],[161]). Correlations were established based on the axial (e_x) and radial (e_r) clearances between the rotor and the housing of the turbine. Typically, those clearances are considered identical ($e_x = e_r = e_{cl}$). Daily et al. [162] proposed a correlation, based on the rotor back plate clearance (e_b), regarding the disk friction losses. It has then been reused in references [156] and [133]. Finally, most authors agree on the discharge losses for a single stage turbine and state the kinetic energy at the exit of the component cannot be recovered.

The loss mechanisms in the turbine components being identified, a non-exhaustive list of the available loss correlations is proposed in table 4.3.

Table 4.3 – Loss Mechanisms and correlations for radial turbines

Loss mechanisms	Correlations	References
Volute passage	$\Delta h_{loss,v} = \xi_v \frac{C_2^2}{2}$ with $\xi_v = 0.1$	Moustapha et al. [161], Rahbar et al. [73]
	$\xi_v = \frac{P_{01}-P_{02}}{P_{02}-P_2} = \xi_{v,p} + \xi_{v,\theta}$	Aungier [122]
	$\xi_v = \frac{P_{01}-P_{02}}{P_{02}-P_2} = 0.1$	Rahbar et al. [133]
Nozzle passage	$\Delta h_{loss,s} = \xi_s \frac{C_3^2}{2}$ with $\xi_s = f(M_3)$ or 0.1	Benson [153]
	$\xi_s = \frac{0.05}{Re^{0.2}}\left(\frac{\tan^2(\alpha_3)}{s_s c_s} + \frac{o_s}{b_3}\right)$ with	Baines [163]
	$s_s = \frac{2\pi r_3}{N_s}$, $o_s = \frac{A_{thr}/N_s}{b_4}$, $Re = \frac{\rho_{thr,is} C_{thr,is} b_4}{\mu_{thr,is}}$	Demierre et al. [156]
	$\Delta h_{loss,s} = 4 f_s \bar{C}_s^2 \frac{I_{hyd,s}}{D_{hyd,s}}$ with	Whitfield et al. [164]
	$f_s = f(\bar{Re}, RR)$	Churchill [165]
	$\bar{Re} = \frac{\frac{C_2 b_4 \rho_2}{\mu_2} + \frac{C_3 b_4 \rho_3}{\mu_3}}{2}$	Rahbar et al. [73]
	$RR = 0.0002$ [m]	Aungier [122]
	$\bar{C}_s = \frac{C_2 + C_3}{2}$, $I_{hyd,s} = r_2 - r_3$,	Rahbar et al. [73]
	$D_{hyd,s} = 0.5\left(\frac{8\pi r_2 b_4 \cos\alpha_2}{4\pi r_2 + \frac{4\pi b_4 r_2}{\sigma}} + \frac{8\pi r_3 b_4 \cos\alpha_3}{4\pi r_3 + \frac{4\pi b_4 r_3}{\sigma}}\right)$	Rahbar et al. [73]
	$\xi_s = \frac{P_{02}-P_{03}}{P_{03}-P_3} = \xi_{s,p} + \xi_{s,inc}$	Aungier [122]
Interspace losses	$\xi_i = \frac{P_{03}-P_{04}}{P_{04}-P_4} = \xi_{i,p} + \xi_{i,in}$	Aungier [122]
Rotor Incidence	$h_4 = h_3 \frac{(\tan_{\beta_3}^2 + 1) - \xi_{inc}}{\sec^2\beta_4}$ with $\xi_{inc} = f(i_r)$	Benson [153]
	$\Delta h_{loss,inc} = \frac{W_{\theta4}^2}{2}$	Whitfield et al. [154], Suhrmann et al. [155]
	$\Delta h_{loss,inc} = 0.5 W_4^2 \sin^2(\beta_4 - \beta_{4,opt})$	Wasserbauer et al. [166], Demierre et al. [156]

Loss mechanism	Correlation	References
Rotor passage	$\Delta h_{loss,r} = \xi_r \frac{W_5^2}{2}$ with	Benson [153]
	$\xi_r = m_k(1 + (\frac{W_4}{W_5})^2)$ and $m_k = 0.468$	
	$m_k = 0.4442$	Futral et al. [152]
	$\Delta h_{loss,r} = c_f \frac{L_{hyd}}{D_{hyd}} \bar{W}^2$ with	Suhrmann et al. [155]
	$c_f = f_r \left(1 + 0.075\bar{Re}^{1/4} \sqrt{\frac{D_{hyd}}{2r_c}}\right)$	Schlichting et al. [167] Suhrmann et al. [155]
	$\frac{1}{4f_r} = -2\log\frac{RR}{3.7} + \frac{2.51}{\bar{Re}\sqrt{4f_r}}$	Colebrook [168], Suhrmann et al. [155]
	$f_r = f(\bar{Re}, RR)$	Churchill [165], Rahbar et al. [73]
	$\bar{Re} = \frac{\frac{U_4 b_4 \rho_4}{\mu_4} + \frac{U_5(r_{5,t}-r_{5,h})\rho_5}{\mu_5}}{2}$ and $RR = 0.0002$ [m]	Rahbar et al. [73]
	$I_{hyd} = \frac{\pi}{2}\sqrt{\frac{(r_4-r_{5,t}+\frac{b_4}{2})^2 + (\frac{r_{5,t}-r_{5,h}}{2})^2}{2}}$	Rahbar et al. [73]
	$D_{hyd} = 0.5\left(\frac{4\pi r_4 b_4}{2\pi r_4 + Z_r b_4} + \frac{2\pi(r_{5,t}^2 - r_{5,h}^2)}{\pi(r_{5,t}-r_{5,h})+Z_r(r_{5,t}-r_{5,h})}\right)$	Rahbar et al. [73]
	$\bar{W} = \frac{W_4 + (W_{5,h}+W_{5,t})/2}{2}$	Coppage et al., [169], Suhrmann et al. [155]
	$\bar{W} = \frac{C_{5,t}+C_4+W_{5,t}+2W_{5,h}+3W_4}{8}$	Jansen et al. [160], Suhrmann et al. [155]
	$\Delta h_{loss,r} = c_{f,new} \frac{L_{hyd}}{D_{hyd}} \bar{W}^2$ with	Musgrave et al. [158], Suhrmann et al. [155]
	$c_{f,new} = c_f \bar{Re}\frac{d_4}{2r_c}^{0.05}$	
	$\Delta h_{loss,r} = 0.5\xi_r(W_4^2 \cos^2(\beta_4 - \beta_{4,opt}) + W_5^2)$	Wasserbauer et al. [166], Demierre et al. [156]

Loss mechanism	Correlation	References
Secondary	$\Delta h_{loss,sf} = C_4^2 \frac{d_4}{Z r_c}$	Rodgers [170], Suhrmann et al. [155]
Clearance	$\Delta \eta_{ts,cl} = 0.1 \frac{e_{cl}}{b_4}$	Rodgers [171], Suhrmann et al. [155]
	$\Delta \eta_{ts,cl} = 0.35 \frac{e_{cl}}{b_4} - 0.01$	Musgrave et al. [158], Suhrmann et al. [155]
	$\Delta \eta_{ts,cl} = 2 \frac{e_{cl}}{b_4} (\frac{\bar{r}_5}{r_4} - 0.275)$	Krylov et al. [159], Suhrmann et al. [155]
	$\Delta h_{loss,cl} = 0.6 \frac{e_{cl}}{b_4} \sqrt{\frac{4}{b_4} \frac{\pi}{Z_r} \frac{r_{5,t}^2 - r_{5,h}^2}{(r_4 - r_{5,t})(1 + \frac{\rho_4}{\rho_5})}}$	Jansen et al. [160], Suhrmann et al. [155]
	$\Delta h_{loss,cl} = 0.6 \frac{e_{cl}}{b_4} C_{\theta 4}^2$	Rodgers [170], Suhrmann et al. [155]
	$\Delta h_{loss,cl} = \frac{U_4^3 Z_r}{8\pi} \Big(K_x e_x C_x + K_r e_r C_r$ $+ K_{rx} \sqrt{e_x e_r C_x C_r} \Big)$ with $C_x = \frac{1 - \frac{r_{5,t}}{r_4}}{C_{m,4} b_4}$ and $C_r = \frac{r_{5,t}}{r_4} \frac{L_x - b_4}{C_{m,5} \bar{r}_5 b_5}$ and $K_x = 0.4$, $K_r = 0.75$ and $K_x r = -0.3$	Moustapha [161] Demierre et al. [156]
Disk friction	$\Delta h_{loss,df} = \frac{0.25 \rho_4 U_4^3 r_4^2 \xi_f}{M}$ with $\xi_f = 3.7 \frac{(\frac{e_b}{r_4})^{0.1}}{Re^{0.5}}$ if $Re < 10^5$ $\xi_f = 0.102 \frac{(\frac{e_b}{r_4})^{0.1}}{Re^{0.2}}$ if $Re > 10^5$	Daily et al. [162] Demierre et al. [156] Rahbar et al. [133]
Discharge	$\Delta h_{loss,d} = 0.5 \frac{C_5^2}{2}$	Suhrmann et al. [155], Rahbar et al. [133]

Regarding the impeller, the work performed by Aungier [122] could also be considered. The rotor loss is expressed as a loss in total relative pressure and 6 contributions are identified (profile, incidence, blade loading, hub-to-shroud loading, clearance and moisture losses). The blade and hub-to-shroud loading losses accounts respectively for the blade-to-blade and hub-to-shroud pressure gradients that produces secondary flows [172]. The moisture loss

takes into account the loss in kinetic energy due to the presence of liquid droplet in the vapor flow.

$$\xi_r = \frac{P_{r05,is} - P_{r05}}{P_{r05} - P_5} = \xi_{r,p} + \xi_{r,inc} + \xi_{r,bl} + \xi_{r,hs} + \xi_{r,cl} + \xi_{r,q} \tag{4.46}$$

4.3.6 Shock waves

Organic fluids are characterized by a lower speed of sound than air or steam [102]. As a result, this speed is reached much sooner with organic fluids than with steam, which constitutes a major risk of additional irreversibilities due to the formation of shock waves in region of high Mach number. These phenomena can occur in both the stator and rotor but generally concerns the nozzles devoted to accelerate the fluid so to convert the enthalpy of the fluid in kinetic energy. The equations driving the compressible flows admit, as being part of the
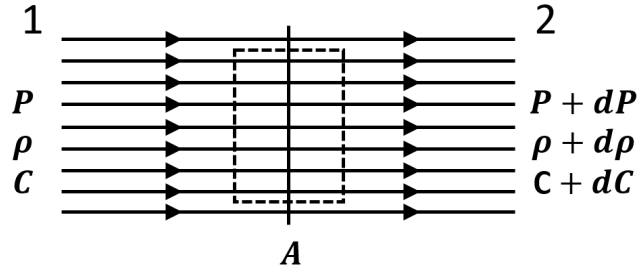
Figure 4.7 – Schematic of a normal shock wave in a duct

solution, discontinuities in pressure, density and speed. Considering the control element in Figure 4.7, the mass conservation principle results written in steady-state in equation 4.47.

$$\rho_1 C_1 = \rho_2 C_2 \tag{4.47}$$

In steady-state, the conservation of the linear momentum principle can in turn be written as follow:

$$0 = AP - A(P + dP) - \tau \zeta dx + \rho AC^2 - (\rho + d\rho)A(C + dC)^2 \tag{4.48}$$

$$0 = -AdP - \tau \zeta dx + -2A\rho C dC - AC^2 d\rho \tag{4.49}$$

$$dP + d(\rho C^2) = d(P + \rho V^2) = -\tau \frac{\zeta}{A} dx \underset{\substack{no \\ friction}}{=} 0 \tag{4.50}$$

$$\Leftrightarrow P_1 + \rho_1 C_1^2 = P_2 + \rho_2 C_2^2 \tag{4.51}$$

This last relation indicates the dynalpia of the flow $(P + \rho C^2)$ is conserved through a shock. Two categories of shock waves are distinguished. The normal shock wave switches the flow from supersonic to subsonic ($M_1 > 1$ and $M_2 < 1$) and increases the pressure of the fluid ($P_2 > P_1$).

The energy is conserved through the shock wave ($h_{01} = h_{02}$) but the entropy is increased. In addition to normal shock waves, oblique shock waves, linked to a deflection of the flow, may also arise in supersonic flows. The flow downstream an oblique shock may be subsonic or remain supersonic.

Considering a simple duct crossed by a compressible flow, important relations, such as the Hugoniot's relation, can be obtained from the conservation principles of mass, energy and linear momentum, without energy (heat or work) transfer, and introducing the definitions of the speed of sound and Mach number.

$$a \quad = \sqrt{\left.\frac{\partial P}{\partial \rho}\right|_s} \quad (Speed\ of\ sound) \quad and \quad M = \frac{C}{a} \quad (Mach\ number) \quad (4.52)$$

$$h_0 \quad = h + \frac{C^2}{2} \quad (Energy) \quad \Leftrightarrow \quad dh + CdC = 0 \quad (4.53)$$

$$dh \quad -\frac{dP}{\rho} = Tds \quad (Gibbs) \quad \underset{\substack{no \\ friction}}{\Leftrightarrow} \quad dh = \frac{dP}{\rho} \quad (4.54)$$

$$\frac{dP}{\rho} \quad = CdC \quad \Leftrightarrow \quad \frac{dP}{d\rho}\frac{d\rho}{\rho} + CdC = 0 \quad \Leftrightarrow \quad a^2\frac{d\rho}{\rho} + CdC = 0 \quad (4.55)$$

$$\rho AC \quad = c_{ste} \quad (Mass) \quad \Leftrightarrow \quad \frac{d\rho}{\rho} + \frac{dA}{A} + \frac{dC}{C} = 0 \quad (4.56)$$

$$-a^2 \quad (\frac{dA}{A} + \frac{dC}{C}) + CdC = 0 \quad \Leftrightarrow \quad \frac{dA}{A} + (1 - M^2)\frac{dC}{C} = 0 \quad (Hugoniot) \quad (4.57)$$

The Hugoniot's relation shows that the speed increases for subsonic and supersonic flows with the reduction and the increase of the duct cross section respectively. It also indicates that if the speed of sound is reached in the duct, it happens at the minimal cross section, i.e. the throat, of the duct. For a strictly convergent nozzle, the exhaust cross section is the throat cross section. Starting from an exhaust static pressure equal to the supply pressure of the convergent nozzle, the mass flow rate is null. Decreasing the exhaust pressure leads to a increase of mass flow rate which reaches a maximum when sonic conditions are achieved at the throat of the nozzle (the exhaust cross section). Doing the same experiment for a convergent-divergent nozzle leads to several possible flow configurations according to the static pressure downstream the nozzle. Two particular values of exhaust pressure, P_{ex}^* and P_{ex}^{**} can be identified. They correspond respectively to a subsonic and a supersonic flow without shock wave in the divergent part of the nozzle. Based on these two cases, the several flow configurations can be described according to the exhaust pressure.

- $P_{ex} > P_{ex}^*$: As soon as the exhaust pressure is lower than the supply pressure, the fluid begins to flow through the nozzle. In the convergent part of the nozzle, the velocity increases as the flow moves closer to the throat and the pressure decreases. In the divergent part, the velocity decreases and the pressure increases as one approaches the exhaust section. The flow is subsonic in all the nozzle (solution a Figure 4.8).

- $P_{ex} = P_{ex}^*$: The flows reach sonic conditions at the throat but remain subsonic in the divergent part of the nozzle. The mass flow rate reaches its maximal value (solution b Figure 4.8).

- $P_{ex}^* > P_{ex} > P_{ex}^{**}$: The flow reaches supersonic conditions in the divergent part of the nozzle and in function of the exhaust pressure:

  - A normal shock occurs inside the nozzle after which the flow returns to subsonic conditions (solution c Figure 4.8).

  - A normal shock occurs at the exhaust cross section of the nozzle (solution d Figure 4.8).

  - A oblique shock system combined to a normal one occurs outside the nozzle (solution e Figure 4.8).

  - A oblique shock system (only) occurs outside the nozzle (solution f Figure 4.8).

- $P_{ex} = P_{ex}^{**}$: The flows is supersonic in all the divergent part of the nozzle and no shock occurs neither inside nor outside the nozzle.

- $P_{ex} < P_{ex}^{**}$: Any additional reduction of the exhaust pressure does not affect the flow behavior in the nozzle but leads to a shock system attached to the exhaust cross section of the nozzle (solution g Figure 4.8).

The particular value P_{ex}^{**} of the exhaust pressure is sometimes said adapted to the nozzle geometry. Assuming the exhaust pressure remains below the particular value P_{ex}^* leading barely to sonic conditions at the throat; when the exhaust pressure is above (respectively below) the adapted pressure level (P_{ex}^{**}) the nozzle over-expands (respectively under-expands) the fluid. This leads, as explained, to the formation of shock waves and thus to entropy increase. Simply convergent nozzles are not spared and complex shock wave systems occur when those nozzles are used above the critical pressure ratio.
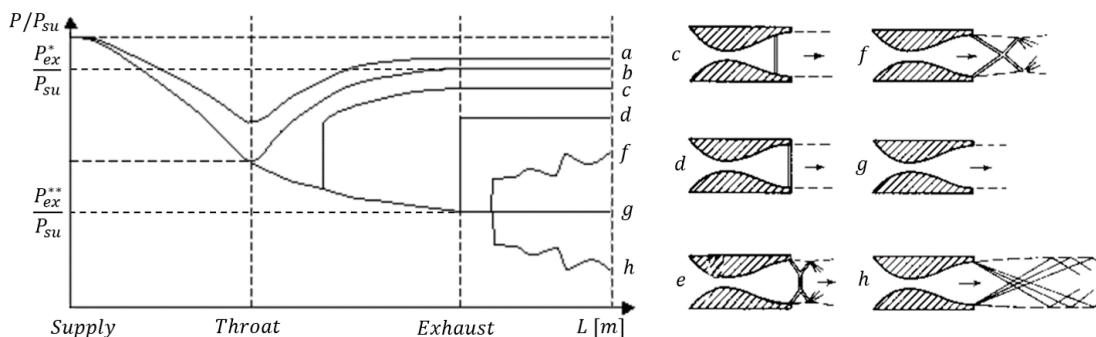
Figure 4.8 – Possible flow configurations in convergent-divergent nozzles

4.3.7 Turbine model

Models of the different components of the turbine are proposed and assembled to build the turbine model. The different dimensions presented in Figure 4.1 and required by the model are measured. The inputs of the model are the pressure levels at the inlet and outlet, the inlet temperature and the rotational speed of the turbine. The outputs are the mass flow rate, the power output and the outlet temperature. For the velocity triangles, the flow absolute angle at the nozzle inlet and outlet and the flow relative angle at the impeller inlet and outlet are imposed and optimized to minimize the error between the predicted outputs and the measurements. Mean-line modeling is an iterative process. In this study, 9 iterations variables are required. They are listed in Table 4.4.

Table 4.4 – Iteration variables required in the mean-line model

Component	Description	Variable
Volute	Outlet absolute velocity [m/s]	C_2
Nozzles	Mass flow rate [kg/s]	$\dot{M}$
	Throat critical pressure [Pa]	P_{crit}
	Outlet absolute velocity [m/s]	C_3
	Recalculated Outlet absolute velocity [m/s]	C_3^*
Vaneless space	Outlet static pressure [Pa]	P_3^*
	Outlet absolute velocity [m/s]	C_4
Rotor	Inlet static pressure [Pa]	P_4
	Outlet relative velocity [m/s]	W_5

Volute

The geometry of the inlet volute is illustrated in Figure 4.9. The cross section and the mean radius are specified in station 1 where the flow has not yet started to exit the volute. They can also be specified in station 1^* where half of the flow exited the station [122]. Finally they are defined in station 2, the annular passage at the volute exit. The inlet static temperature and static pressure at the inlet of the volute are inputs of the model. The flow conditions are calculated expressing the mass balance at station 1. The same can be achieved in station 1^* using half the mass flow and an isentropic process [122]. A the exit of the volute, the absolute tangential speed is estimated from the conservation of angular momentum between station 1 (or 1^*) and station 3 (Eq. 4.60). The mass balance using the inlet mass flow rate combined

with equation 4.60 provides the other flow conditions. The energy balance supplies the total thermodynamic conditions at the exit. However, losses in the volute must be determined and an iterative process, involving the exit absolute velocity (C_2), is required. The losses are here described as a static enthalpy loss but correlations proposed in table 4.3 give similar result whether they describe a total pressure loss or a static enthalpy loss in the volute.
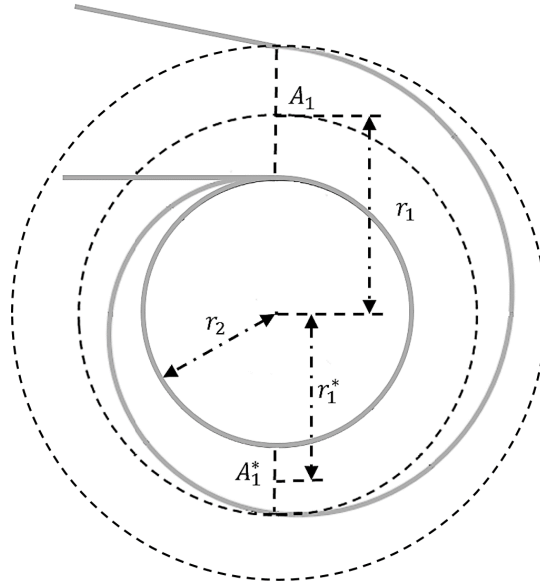
Figure 4.9 – Geometry of a typical inlet volute based on [122]

$$C_2 = \frac{a(T_1, P_1)}{3} \quad (init.val) \quad (4.58)$$

$$C_{\theta 2} = \frac{r_1 C_1}{r_2} \quad (4.59)$$

$$\rho_2 = \frac{\dot{M}}{A_2 C_2 \cos(\alpha_2)} \quad (4.60)$$

$$\Delta h_{loss,v} = k_{vol} \frac{C_2^2}{2} \quad (4.61)$$

$$h_{2,s} = \underbrace{h_{01} - \frac{C_2^2}{2}}_{h_2} - \Delta h_{loss,v} \quad (4.62)$$

$$P_2 = P(h_{2,s}, s_1) \quad (4.63)$$

$$\rho_2' = \rho(h_2, P_2) \quad (4.64)$$

$$\Delta_{C_2} = |\rho_2 - \rho_2'| \quad (4.65)$$

Nozzles

The nozzle blade row in the radial-inflow turbine constitutes a passage of fixed cross-section. The geometry is specified at the inlet, throat and exit stations designated by subscripts 2, thr and 3 respectively. The absolute inlet flow angle α_2 is assumed to be the absolute flow angle at the outlet of the volute while the absolute outlet flow angle α_3 is specified. The flow between station 2 and the throat is subsonic and supposed isentropic. Sonic conditions can be reached at the throat if the pressure ratio over the nozzles exceeds the critical pressure.

The outlet pressure P_3^* is known based on the vaneless space and rotor pressure drops. The critical pressure is computed through an iterative process so the pressure at the throat results in the maximum between P_{thr} and P_3^*. The pressure at the throat being known, all the flow conditions and the thermodynamic state can be deduced. The mass balance at the throat section then end an iterative process on the mass flow rate that was only estimated until now.
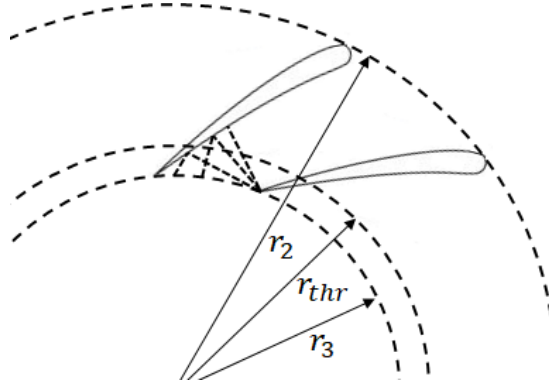
Figure 4.10 – Geometry of typical converging nozzle blade profiles

$$P_{crit} = \frac{P_1}{2} \quad (init.val.) \tag{4.66}$$

$$C_{crit} = \sqrt{h_{01} - h(P_{crit}, s_2)} \tag{4.67}$$

$$M_{crit} = \frac{C_{crit}}{a(P_{crit}, s_2)} \tag{4.68}$$

$$M'_{crit} = 1 \tag{4.69}$$

$$\Delta_{P_{crit}} = |M_{crit} - M'_{crit}| \tag{4.70}$$

$$P_3^* = 1.2P_5 \quad (init.val.) \tag{4.71}$$

$$\dot{M} = \rho_1 A_1 C_{1,ini} \quad (init.val.) \tag{4.72}$$

$$P_{thr} = max(P_3^*, P_{crit}) \tag{4.73}$$

$$C_{m,thr} = \sqrt{h_{01} - h(P_{thr}, s_2)} \tag{4.74}$$

$$\dot{M}' = \rho(P_{thr}, s_2) A_{thr} C_{m,thr} \tag{4.75}$$

$$\Delta_{\dot{M}} = |\dot{M} - \dot{M}'| \tag{4.76}$$

On the other hand, the flow between the throat and station 3 can be subsonic or supersonic depending if the pressure ratio is under or over the critical pressure ratio respectively. In the latter case, the fluid undergoes a supersonic expansion because of the increase in cross section. Otherwise, the subsonic flow slows down from the throat. In supersonic conditions, the flow expands from the critical pressure at the throat until the outlet pressure of the stator. Classically, this expansion is considered to result both in an increase of the velocity magnitude and a deviation of the flow in the meridional direction [156] and only affecting the incidence of the flow on the rotor blades. In this study, a method is proposed to estimate and distinguish the expansion loss between the nozzle throat and rotor rows and the rotor incidence losses. This is motivated by the inaccurate estimation, as it will be shown in the results, of the flow angles at the rotor outlet but also of the flow conditions at the nozzle throat consequently leading, among other, to inaccurate mass flow rate prediction with the classical approach. In the proposed approach, when sonic conditions are reached at the nozzle throat, the pressure information downstream the nozzles is assumed unable to go up to the throat. Thus, because

of the increase in cross section area the supersonic flow expands until the adapted pressure P_3, defined at the stator outlet as for a convergent-divergent nozzle. The geometry at station 3 being known, this pressure can be calculated specifying the absolute flow angle α_3. The losses in the stator are taken into account and must be determined. An iterative process, converging the exit absolute velocity (C_3), is therefore achieved.

$$C_3 = 1.5a(T_1, P_1) \quad (init.val.) \quad (4.77)$$

$$h_3 = h_{01} - \frac{C_3^2}{2} \quad (4.78)$$

$$\rho_3 = \frac{\dot{M}}{A_3 C_3 \cos(\alpha_3)} \quad (4.79)$$

$$P_3 = P(h_3, \rho_3) \quad (4.80)$$

$$\Delta h_{loss,s} = 4f_s \frac{C_2 + C_3}{2} \frac{I_{hyd,s}}{D_{hyd,s}} \quad (4.81)$$

$$h_{3,s} = h(P_3, s_2) \quad (4.82)$$

$$h_3' = h_{3,s} + \Delta h_{loss,s} \quad (4.83)$$

$$\Delta_{C_3} = |h_3 - h_3'| \quad (4.84)$$

When the pressure downstream the stator differs from the adapted pressure, a shock wave occurs to satisfy energy, mass and momentum balances. This discontinuity is assumed to be located at the outlet station of the nozzle A_3, passing the fluid from the adapted pressure P_3 to the nozzle outlet pressure P_3^*. The density of the fluid after shock is computed using the momentum conservation principle (Eq. 4.51). Implementing the energy conservation, the absolute speed C_3^* can be identified through an iteration process. The mass balance results in the absolute flow angle (after shock) at the stator outlet α_3^*. Finally the static enthalpy loss resulting from the shock can be estimated.

In subsonic conditions, the adapted pressure at the nozzle outlet has no longer any meaning and the outlet pressure remains P_3^*. The specification of the absolute outlet angle α_3 is released and its values is calculated (α_3^*) through the mass conservation principle.

$$C_3^* = a(T_1, P_1) \quad (init.val.) \quad (4.85)$$

$$\rho_3^* = (P_3 - P_3^*) + \frac{\rho_3 C_3^2}{C_3^{*2}} \quad (4.86)$$

$$h_3^* = h(\rho_3^*, P_3^*) \quad (4.87)$$

$$h_3^{*'} = h_{01} - \frac{C_3^{*2}}{2} \quad (4.88)$$

$$\Delta_{C_3^*} = |h_3^* - h_3^{*'}| \quad (4.89)$$

$$\alpha_3^* = \arccos(\frac{\dot{M}}{\rho_3^* A_3^* C_3^*}) \quad (4.90)$$

$$h_{3,s}^* = h(P_3^*, s_3) \quad (4.91)$$

$$\Delta h_{loss,sh} = h_3^* - h_{3,s}^* \quad (4.92)$$

Vaneless space

There are one or more vaneless passages between the main components of the stage. Only the space between the nozzle and rotor is investigated and it is considered as a component of the turbine. The geometry is specified at inlet and exit stations. In subsonic regime, the flow and thermodynamic conditions in station 3^* were previously obtained through energy and mass conservation principles applied in the nozzle row. The flow conditions and the absolute flow

angle at the outlet of the vaneless space are calculated from the energy and mass balances in station 4. The swirl velocity at the same station is given by the conservation of angular momentum. An iterative process is implemented to converge on the absolute outlet velocity C_4. The inlet total pressure P_{03}^* is evaluated based on a pressure loss correlation, the outlet static pressure P_4 being calculated in the rotor model. This relation is then used to converge on the inlet static pressure P_3^*, which was estimated until now. Finally, the static enthalpy loss in the passage is calculated.

$$C_4 = a(T_1, P_1) \quad (init.val.) \quad (4.93)$$

$$h_4 = h_{01} - \frac{C_4^2}{2} \quad (4.94)$$

$$\alpha_4 = \arccos\left(\frac{\dot{M}}{\rho(h_4, P_4) A_4 C_4}\right) (4.95)$$

$$C_{\theta 4} = C_4 \sin(\alpha_4) \quad (4.96)$$

$$C_{\theta 4}' = \frac{r_3 C_{theta3}^*}{r_4} \quad (4.97)$$

$$\Delta_{C_{\theta 4}} = |C_{\theta 4} - C_{\theta 4}'| \quad (4.98)$$

$$s_4 = s(h_4, P_4) \quad (4.99)$$

$$P_{04} = P(h_{04}, s_4) \quad (4.100)$$

$$P_{03}^* = P(h_{03}^*, s_3^*) \quad (4.101)$$

$$P_{03}^{*'} = P_{04}(1 - \xi_i) - P_4 \xi_i \quad (4.102)$$

$$\Delta_{P_3^*} = |P_{03}^* - P_{03}^{*'}| \quad (4.103)$$

$$h_{4,s} = h(P_4, s_3^*) \quad (4.104)$$

$$\Delta h_{loss,i} = h_4 - h_{4,s} \quad (4.105)$$

In supersonic, the expansion can be assumed to start from the throat of the nozzle to the inlet of the rotor. The outlet station of the stator is then defined as the inlet station of the rotor.

$$A_4 = A_3 \quad (4.106)$$

$$C_4 = C_3^* \quad (4.107)$$

$$P_3^* = P_4 \quad (4.108)$$

Rotor

The rotor geometry and the resulting flow passage are more complex than the other components of the radial-inflow turbine. In the impeller, the flow is usually turned by $90°C$ from radial to axial direction. Several internal losses have to be taken into account. The geometry is defined at the inlet (station 4), outlet (station 5) and can also be defined at the mid-passage to investigate eventual sonic conditions in the rotor. The rotor performance is calculated in the same manner as for the stator except for the loss models. Since it is a rotating component, the analysis is based on the relative velocities (W_4 and W_5) and flow angles (β_4 and β_5). The flow conditions are defined at station 4 through the mass balance. Through the mass balance in station 5, the relative outlet flow angle β_5 being specified, the inlet static pressure P_4 can be determined by iteration. Rotor losses generally include incidence (Δh_{inc}), clearance (Δh_{cl}), friction (Δh_f), secondary (Δh_{sf}), disk friction losses (Δh_{df}). Aungier [122] also includes moisture losses in his analysis to describe the impact of condensing working fluids on the rotor performance. The losses can be expressed using the correlations proposed

in Table 4.3. Usual velocity triangles for the impeller of a radial-inflow turbine with zero inlet blade angle are depicted in Figure 4.11. It can seen that the optimal relative inlet flow angle $\beta_{4,opt}$ is negative. This ideal value can be computed and is compared to the actual flow angle β_4 in order to evaluate the incidence losses of the rotor. The energy balance over the rotor and including all the losses results in the iterative determination of the outlet relative velocity W_5. According to Rahbar et al. [73], the absolute flow angle at the outlet of the rotor α_5 can typically vary between -15° and 15° on the design point in order to limit the load on the blades. If thermal losses are considered, the total heat transfer Q has to be identified and considered in the turbine energy balance. In this study, the heat transfer, if occurring, is assumed to take place within the rotor. This formulation makes sense assuming that the main heat transfer, in addition to the ambient losses, occurs between the fluid expanded by the turbine and the lubrication fluid going through the bearings through the metal rotor and shaft of the machine.
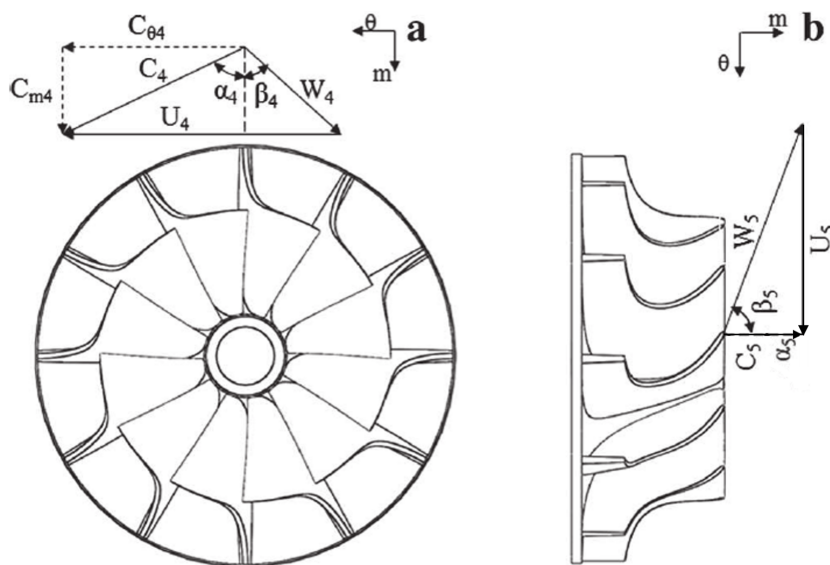
Figure 4.11 – Geometry of the rotor blade profiles with zero inlet blade angle and optimal velocity triangles [73]

$$P_4 = 1.1 P_5 \quad (init.val.) \text{ (4.109)}$$

$$W_5 = \frac{a(T_1, P_1)}{3} \quad (init.val.) \text{ (4.110)}$$

$$W_{\theta 4} = C_{\theta 4} - U_4 \text{ (4.111)}$$

$$W_4 = \sqrt{W_{m4}^2 + W_{\theta 4}^2} \text{ (4.112)}$$

$$\beta_4 = \arctan(\frac{W_{\theta 4}}{W_{m4}}) \text{ (4.113)}$$

$$W_{\theta 5} = W_5 \sin(\beta_5) \text{ (4.114)}$$

$$W_{m5} = W_5 \cos(\beta_5) \text{ (4.115)}$$

$$C_{\theta 5} = W_{\theta 5} + U_5 \text{ (4.116)}$$

$$C_5 = \sqrt{(C_{m5})^2 + (C_{\theta 5})^2} \text{ (4.117)}$$

$$\Delta h_r = U_4 C_{\theta 4} - U_5 C_{\theta 5} + Q \text{ (4.118)}$$

$$h_{5is} = h(P_5, s_1) \text{ (4.119)}$$

$$\Delta h_{is} = h_{01} - h_{5is} \text{ (4.120)}$$

$$\Delta h_{exit} = \frac{C_5^2}{2} \text{ (4.121)}$$

$$h_{05} = h_{04} - \Delta h_r \text{ (4.122)}$$

$$h_5 = h_{05} - \Delta h_{exit} \text{ (4.123)}$$

$$\rho_5 = \rho(h_5, P_5) \text{ (4.124)}$$

$$\rho_5^{'} = \frac{\dot{M}}{A_5 C_{m5}} \text{ (4.125)}$$

$$\Delta P_4 = |\rho_5 - \rho_5^{'}| \text{ (4.126)}$$

$$Z = \frac{\pi}{30}(110 - \alpha_4 \frac{180}{\pi}) \tan(\alpha_4) \text{ (4.127)}$$

$$C_{\theta 4opt} = (1 - \frac{1.98}{Z}) U_4 \text{ (4.128)}$$

$$W_{\theta 4opt} = C_{\theta 4opt} - U_4 \text{ (4.129)}$$

$$\beta_{4opt} = \arctan(\frac{W_{\theta 4opt}}{W_{m4}}) \text{ (4.130)}$$

$$inc = \beta_4 - \beta_{4opt} \text{ (4.131)}$$

$$n = 2(inc < 0) + 3(inc \geq 0) \text{ (4.132)}$$

$$\Delta h_{inc} = W_4^2 \frac{\sin(inc)^n}{2}) \text{ (4.133)}$$

$$\Delta h_{loss,cl} = 0.6 \frac{e_{cl}}{b_4} \sqrt{f(geom, \rho_4, \rho_5)} \text{ (4.134)}$$

$$\Delta h_{loss,sf} = C_4^2 \frac{d_4}{Z r_c} \text{ (4.135)}$$

$$\Delta h_{loss,f} = c_f \frac{L_{hyd}}{D_{hyd}} \bar{W}^2 \text{ (4.136)}$$

$$\Delta h_{loss,df} = \frac{0.25 \rho_4 U_4^3 r_4^2 \xi_f}{\dot{M}} \text{ (4.137)}$$

$$\Delta h_{loss,r} = \Delta h_{inc} + \Delta h_{loss,cl} + \Delta h_{loss,sf}$$
$$+ \Delta h_{loss,f} + \Delta h_{loss,df} \text{ (4.138)}$$

$$\Delta h_{loss,tot} = \Delta h_{loss,v} + \Delta h_{loss,s} + \Delta h_{loss,i}$$
$$+ \Delta h_{loss,r} + \Delta h_{loss,exit} \text{ (4.139)}$$

$$h_5^{'} = h_{5is} + \Delta h_{loss,tot} - \Delta h_{loss,exit} - Q \text{ (4.140)}$$

$$\Delta W_5 = |h_5 - h_5^{'}| \text{ (4.141)}$$

4.3.8 Summary and calibration of the parameters

Considering all the stations, the procedure involves 9 iteration variables in supersonic conditions when the possible formation of shock waves is considered. It can be reduced to 7 variables considering the supersonic flow expands from the nozzle throat to the inlet station of the rotor ($P_3^* = P_4$ and $C_4 = C_3^*$). The flow chart in Figure 4.12 summarizes the global procedure. The trust region dogleg algorithm is used to numerically solve the non-linear equation system formed by the residuals on the iteration variables.

$$F(x) = 0 \quad with \quad x = [\dot{M}, C_2, P_{crit}, C_3, P_3^*, C_3^*, P_4, C_4, W_5] \tag{4.142}$$

The inputs and outputs of the model were described in section 4.3.7 and the required geometry parameters are shown in Figure 4.1. In addition, the model requires the specification of the absolute and relative flow angles at the outlet of the stator and rotor respectively. As

explained, the flow angles does not necessarily match the metal angles of the blades. In addition, they can be considered not to vary much with the operating conditions. These angles are the 2 calibration parameters of the model. An optimization method is developed to identify the parameter values that minimize the Root Mean Squared Error (RMSE) between the measurements and the model output of enthalpy flow rate variation. The interior-point algorithm [173] is used to perform the constrained optimization and minimize the error defined as follow:

$$e(\alpha, \beta) = \sqrt{\frac{1}{N} \sum_{i=1}^{N} (\dot{H}_{mes,i} - \dot{H}_{pred,i})^2} \tag{4.143}$$

$$\min_{\alpha, \beta} e(\alpha, \beta) \begin{cases} 65° < \alpha < 75° \\ 55° < \beta < 65° \end{cases} \tag{4.144}$$

If the expansion can be considered adiabatic or if the heat loss can be evaluated otherwise, the prediction of the enthalpy flow rate variation is sufficient to evaluate the mechanical power at the turbine shaft and the turbine outlet temperature based on the model inputs. Regarding the third model output, the mass flow rate, it can be calculated based on the cross section area of the nozzle throat and the pressure conditions on both side of the nozzles.

The formation of shock waves put aside, 8 iteration variables are required by the model. The static pressure P_3^* and the absolute velocity C_3^* does not have any meaning. The absolute angle α_3 is no more specified and the static pressure P_3 is calculated by iteration from the static pressure P_4 at the inlet of the rotor and based on the pressure drop in the vaneless space. Only one calibration parameter thus remains, the relative flow angle at the outlet of the rotor.

Considering the measurements obtained with fluid R245fa, a strategy is proposed to reduce the number of measurements to consider for the calibration process, from the total amount of 1260 points. As a reminder, the experimental investigation of the prototype involved 5 degrees of freedom that could be varied. The turbine inlet temperature was adjusted so to impose 3 different overheating levels. For each overheating level, the condensing pressure was varied by step of 0.5 bar between 2.5 and 4.5 bar. In turn, the evaporating pressure was increased in order to adjust the pressure ratio from 2 to 4.5. For each combination of temperature and pressure levels, 3 levels of lubrication mass flow rate were investigated. Finally, several rotational speed levels were imposed for all the combinations of the 4 previous degrees of freedom. It is proposed to consider the point in the extreme conditions of rotational speed for each combination of the degree of freedom and to remove the intermediate points (Figure 4.13). This enables to cover all the measurement map area while reducing the number of points involved in the calibration process from 1260 to 280.
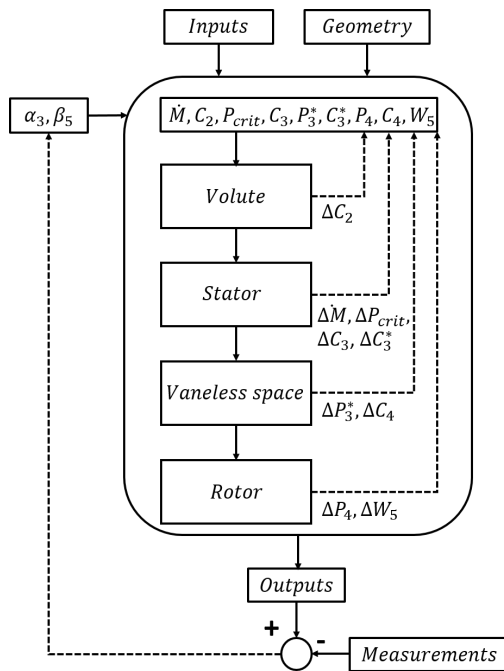
Figure 4.12 – Flow chart of the radial-inflow turbine model

Figure 4.13 – Combination of the 5 degrees of freedom available during the experimental campaign and data selection of the calibration process of the model parameters

4.3.9 Heat transfer

In turbomachinary the expansion can in a first approach be assumed adiabatic so the ambient losses and other eventual heat lost by the expanded fluid are not considered. Only few studies involving the mean-line modeling are available on the subject. For instance, Pei et al. [116] experimentally studied an ORC using R123 and a radial turbine. They investigated the ambient heat transfer and achieved a turbine isentropic efficiency of 71 % with turbine inlet total temperature and pressure of 373 K and 7.8 bar. However, the experimental study in Chapter 3 and the low value of the bearing efficiency based on energy balance, when the expanded fluid is considered not to exchange heat with the lubrication fluid, suggests these phenomena should be taken into account. The ambient losses can easily be identified by energy balance over the turbo generator and then modeled based on a heat exchange area and a convective heat transfer coefficient. The heat transfer between the expanded and lubrication fluids through the metallic rotor and shaft is more difficult to describe and requires first to understand the loss mechanisms in the bearing system.

Bearings model

Pouly et al. [174] investigated the temperature in Rolling Element Bearings (REB) and showed this value depends mainly on the applied load, the rotational speed and the lubricant type and viscosity. They proposed a model taking into account different power loss distributions

95
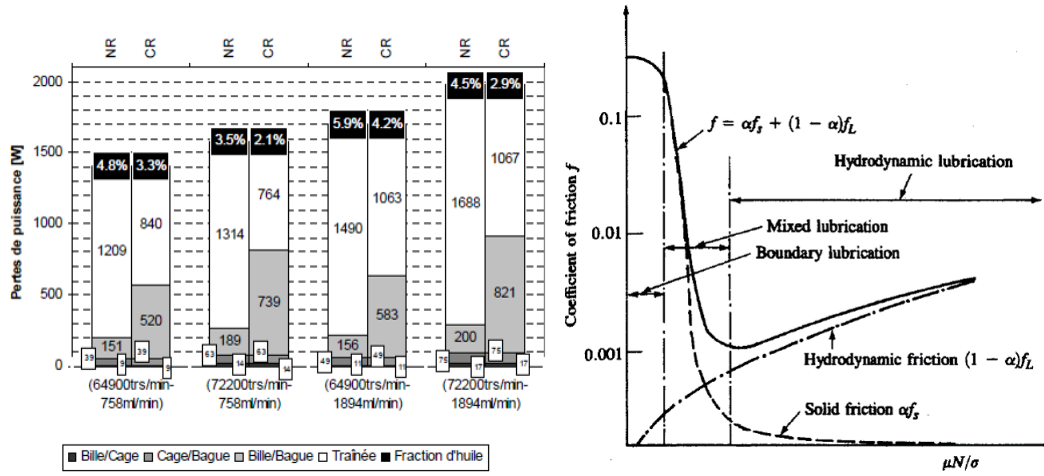
Figure 4.14 – Power loss in the bearings as a function of the lubricant mass flow rate and shaft rotational speed [174]

Figure 4.15 – Stribeck diagram for journal bearing: coefficient of friction f as a function of dimensionless duty parameter $\mu N/\sigma$ [175]

inside the bearings. Those loss distribution mostly results from the interaction between the moving parts of the bearings (Relative movement of the cage with respect to the inner and outer rings, the contact between the balls and the rings), which involves friction, and from the orbital movement of the balls through the fluid, which can cause a drag force or windage loss, the principal source of power loss (Figure 4.14). The geometry of the bearing system being poorly known, it is proposed to reduce the friction losses to a total friction torque depending on the equivalent load applied to the bearings, a friction coefficient for the bearings and the bearing bore diameter, which can be estimated. The friction coefficient can be calculated based on the Stribeck diagram (Figure 4.15) or a constant value can be imposed assuming the power loss due to friction in the bearings will be reduced compared to the windage loss. The latter loss is expressed in the same manner as for the turbine disk friction but considering the effect of the mass flow rate and using here the coefficient k_w as an adjustment parameter.

$$f \approx 0.005 \qquad (4.145)$$

$$T_f = fP\frac{d}{2} \quad [Nm] \qquad (4.146)$$

$$\dot{W}_{fr} = 2\pi T_f \frac{N}{60} \qquad (4.147)$$

$$\dot{W}_{wi} = k_w \frac{\rho U^3 r^2}{4} Re_{lub}^{0.7} \qquad (4.148)$$

The friction and windage losses in the bearings being described, the remaining contribution increasing the temperature of the lubrication fluid flow rate from the inlet to the outlet of the bearings is deduced to result from a transfer from the fluid expanded in the turbine. To check if the residual thermal energy can be explained by a heat exchange between the two fluids, a heat transfer model of co-current tube and tube heat exchanger is proposed. Simple Dittus-Boelter

type correlations are proposed to calculate the Nusselt numbers and the resulting convective heat transfer coefficients ($h_{conv,tur}$ and $h_{conv,lub}$) on both side. Those correlations are of the type $N_u = CRe^mPr^n$ and thus are based on the Reynolds and Prandtl number and involve 3 parameters. In general, the exponent of the Reynolds number is between 0.5 and 0.8, and the exponent of the Prandtl number between 1/3 and 0.4. In this study, values of 0.8 and 1/3 are imposed for the exponents of the Reynolds and Prandtl numbers respectively. The proportional coefficients on both side C_{tur} and C_{lub} are adjusted through an optimization process explained below. The conductive heat transfer coefficient depends on the metal conductivity and wall thickness($h_{wall} = \frac{k_{wall}}{e_{wall}}$). The heat transfer area is estimated based on the turbine geometry. The heat flow rate is then evaluated using the Logarithmic Mean Temperature Difference (LMTD) method for parallel flows. However it has to be noted that the present case does not verify the assumptions of the method since the enthalpy variation in the turbine is resulting from both a heat exchange and a work production. In addition, the LMTD method is valid for fluids with a constant specific heat while the specific heat of the turbine fluid varies during expansion. This will result in an effective heat exchange area that is probably different from the actual heat transfer area. However, the goal here is only to verify that the residual thermal energy necessary to achieve the measured outlet temperature of the lubrication fluid can be explained by a transfer with the expanded fluid.

$$U = \frac{1}{\frac{1}{h_{conv,tur}} + \frac{1}{h_{wall}} + \frac{1}{h_{conv,lub}}} \tag{4.149}$$

$$\dot{Q}_{HT} = A_c U \Delta T_{LM}(T_1, T_5, T_{su,lub}, T_{ex,lub}) \tag{4.150}$$

Model validation An optimization process is achieved to minimize the Root Mean Squared Error (RMSE) between predicted and measured enthalpy flow rate variations of the lubrication fluid between the inlet and the outlet of the bearings, adjusting the values of the 3 proportional coefficients k_w, C_{tur} and C_{lub}. Thermal power distribution is illustrated in Figure 4.16 where it can be seen that losses due to friction are limited compared to the windage losses in the bearings. From the optimization process, the contribution of the heat transfer in the heating of the lubrication flow rate is of the same order of magnitude as the contribution due to the windage losses. Figure 4.17 indicates the good representation of the behavior of the lubrication fluid in the bearings on the thermal point view suggesting the main phenomena have been taken into account. On the left, predicted and measured values of the variations of the enthalpy flow rates of the lubrication flows between the inlet and outlet of the bearings are superposed for all the investigated points. On the right the same values are compared against each other using the two axes of the chart. The 15% error lines are also represented. The Root Mean Squared Error (RMSE) is around 100 W and the maximal relative difference is around 15% when parameters k_w, C_{tur} and C_{lub} are respectively equals to $9e - 6$, 0.15 and 0.07. The obtained average heat transfer coefficients are around 5800 and 3500 $W/m^2/K$ for the turbine and bearing side respectively. In addition, it could be shown that the windage and friction losses alone are not sufficient to represent the enthalpy increase of the lubrication fluid in the

bearings. This is achieved in appendix C where it is shown that the maximal relative error on the lubrication enthalpy flow rate is above 40%.
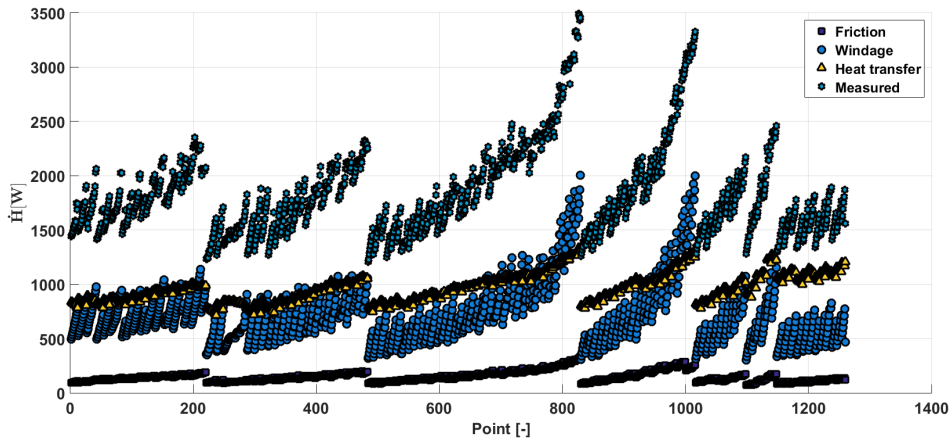
Figure 4.16 – Distribution of the sources of losses according to the bearings models for the 1260 measurement points achieved with fluid R245fa
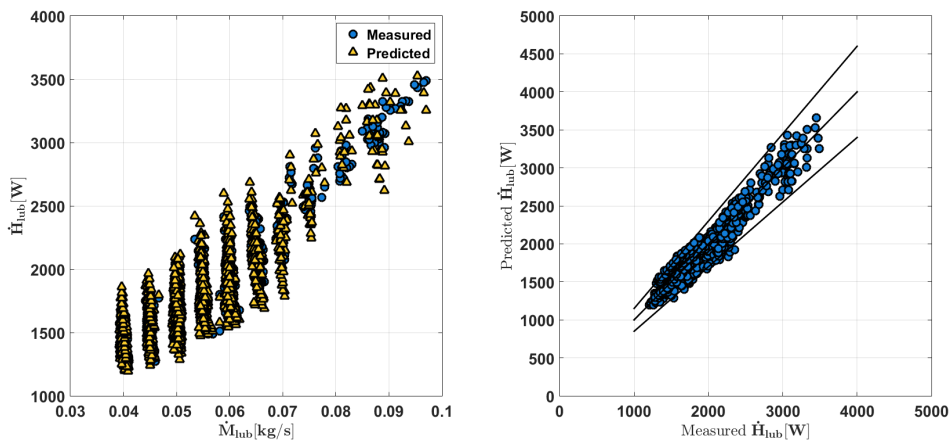
Figure 4.17 – Comparison between predicted and measured enthalpy flow rate of the lubrication fluid between the inlet and outlet of the bearings for the 1260 measurement points achieved with fluid R245fa

Heat transfer model

To take into account the heat transfer in the turbine model, the concept of co-current tube and tube heat exchanger can be included. Using the Newton's cooling law for the ambient losses and approximating the temperature of the turbine envelope, the evaluation of the total

heat exchange combined to the power production requires an additional iteration variable to treat the 2 problems separately but at the same time. The amount of heat transfer Q resulting from the ambient losses and the heat exchanged with the lubrication fluid is directly used as iteration variable. The flow chart of Figure 4.12 is updated and the new version is presented in Figure 4.18. Two additional parameters needing to be calibrated are added: the convective conductance AU_{amb} for the evaluation of the ambient losses and proportional coefficient C in the Nusselt number calculation for the heat transfer to the lubrication fluid through the metal wall.

$$Q = 0.1\Delta h_{is} \quad (init.val.) \tag{4.151}$$

$$T_{wall} = \frac{T_4 + T_5}{2} \tag{4.152}$$

$$\dot{Q}_{amb} = AU_{amb}(T_{wall} - T_{amb}) \tag{4.153}$$

$$U_c = \frac{1}{\frac{1}{h_{conv,tur}} + \frac{1}{h_{wall}} + \frac{1}{h_{conv,lub}}} \tag{4.154}$$

$$\dot{Q}_{HT} = A_c U_c \Delta T_{LM}(T_4, T_5, T_{su,lub}, T_{ex,lub}) \tag{4.155}$$

$$Q' = \frac{\dot{Q}_{amb} + \dot{Q}_{HT}}{\dot{M}} \tag{4.156}$$

$$\Delta Q = |Q - Q'| \tag{4.157}$$

In the present study, the energy part Q lost in heat during the expansion of the fluid is known in advance and therefore does not require to be calculated through the heat transfer model proposed here.

4.4 Results

Firstly, the results are reported considering the fluid expansion in the turbine is adiabatic. Figure 4.19 compares the prediction and the corresponding measurement of the variation of the enthalpy flow rate between the inlet and outlet of the turbine. As it can be seen the model underestimates this magnitude, meaning the heat exchange with the bearing fluid can not be neglected. It can be shown that this is true whatever the final values of the flow angles α_3 and β_5 and the inclusion or not of the shock wave losses.

Secondly, the results are shown considering the heat loss but not the shock wave losses. As it can be seen in Figure 4.20 an optimal combination of the flow angles α_3 and β_5 leads to an acceptable prediction of the enthalpy flow rate variation in the turbine. Since the heat losses are known, the predicted shaft power can be compared to the calculated shaft power and again, acceptable results are obtained. However, the optimal absolute value of the flow
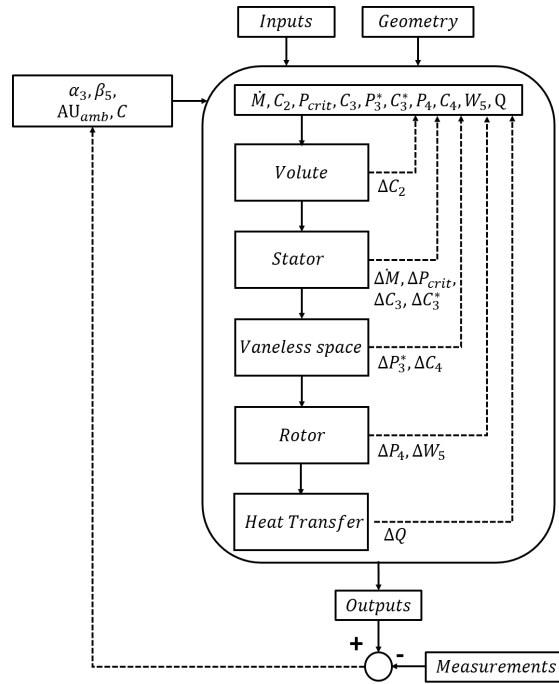
Figure 4.18 – Flow chart of the radial-inflow turbine model including heat transfer
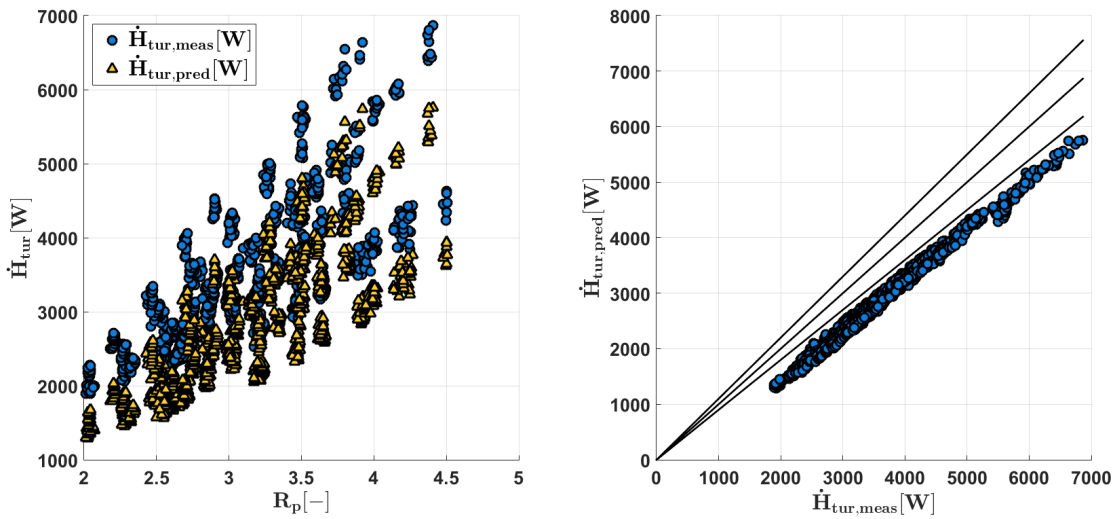
Figure 4.19 – Comparison between predicted and measured variation of enthalpy flow rate in the turbine without taking the heat losses into account (with precision lines of $\pm$ 10%)

angle β_5 is low. Typically, according to the work performed by Aungier [122], this relative angle varies between from around 40° at the shroud to around -70°. So the angle should be around -50° and -60° on the mean line. Nonetheless, in another study, Rahbar et al. [133] obtained higher absolute values, around -70°, for β_5 meaning this angle also depends on the design.
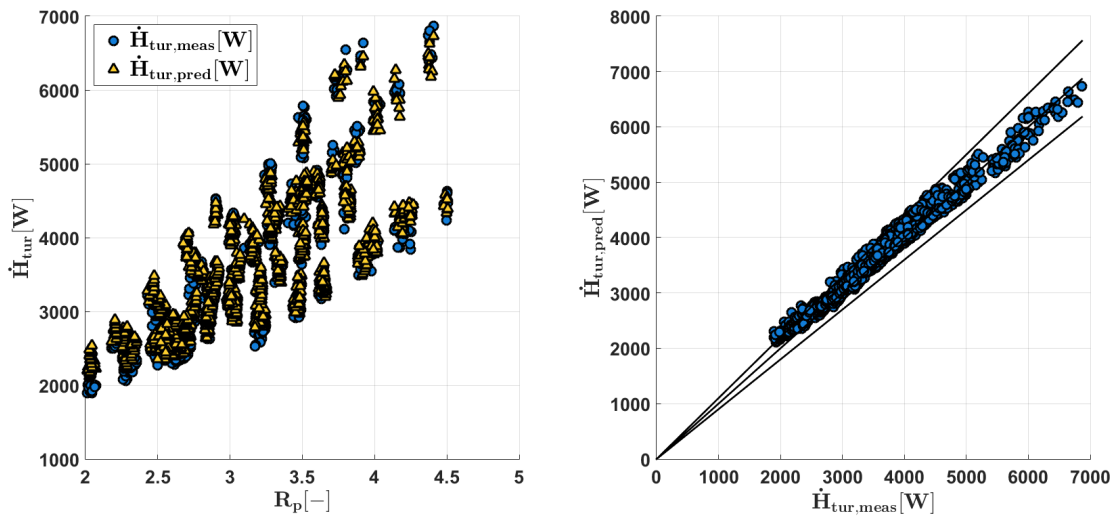
Figure 4.20 – Comparison between predicted and measured variation of enthalpy flow rate in the turbine without taking the shock wave losses into account (with precision lines of ± 10%)

When looking at the velocity triangle at the inlet station of the rotor, obtained for a particular operating point (Figure 4.21, it can be observed the rotor incidence is not optimal ($\beta_4 \neq \beta_{4,opt}$). This can be explained by a rotational speed lower than the optimal speed for the velocity conditions of the flow at the stator outlet. The turbine being built from turbocharger components, the optimal speed is easily imagined higher than the speed measured on test rig since turbochargers are designed for speeds that can go up to several hundreds of thousands RPM. This is also confirmed by the turbine manufacturer, the optimal rotational speed can reach values above 100 kRPM according to the flow conditions. If the rotational speed of the model is increased until a level avoiding incidence losses at the rotor inlet ($\beta_4 = \beta_{4,opt}$), the velocity triangle at the rotor inlet is optimal but the triangle at the outlet leads to implausible values of α_5 for the supposed optimal conditions of speed and based on the rotor geometry. To avoid this issue, the relative angle of the model, β_5, must be increased but it then leads to less accurate representation of the turbine performance as it can be shown in Figure 4.23.

Finally, both the heat and shock wave losses are taken into account in the model. Again a good representation of the measured enthalpy flow rate variation and calculated mechanical power can be achieved by the model. Nonetheless, considering the same operating point as for the previous model version, this time, the velocity triangles at both the inlet and the outlet stations of the rotor are sub-optimal for the non optimal rotational speed (Figure 4.24). The increase in the latter speed until canceling the incidence losses at the rotor inlet now leads to velocity triangles that are optimal at both the inlet and outlet stations of the rotor (Figure 4.25). The RMSE achieved in this case is around 100 W while the maximal relative error is around 10%.

The total enthalpy flow rate variation is predicted by the model with the same accuracy as
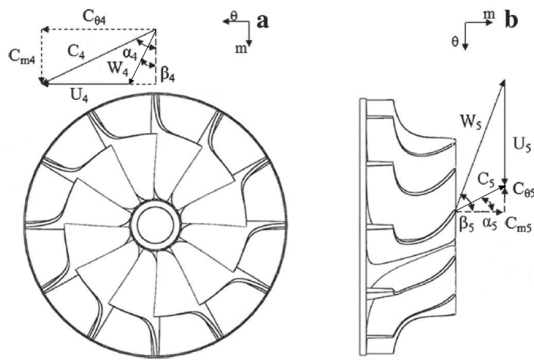
Figure 4.21 – $(P_{su} = 8e5[bar]$, $P_{ex} = 3e5[bar]$, $T_{su} = 380[K]$, $N_{rot} = 48[kRPM])$ $\alpha_5 = -25°$ and $\beta_5 = -60°$
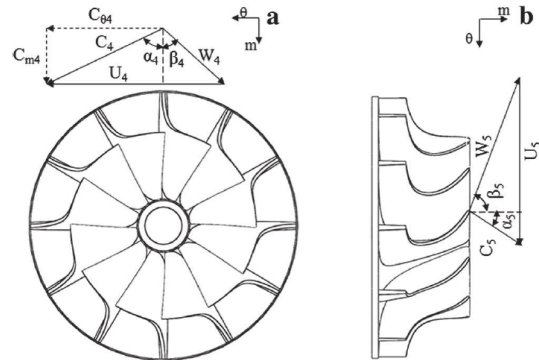
Figure 4.22 – $(P_{su} = 8e5[bar]$, $P_{ex} = 3e5[bar]$, $T_{su} = 380[K]$, $N_{rot} = 88[kRPM])$ $\alpha_5 = 30°$ and $\beta_5 = -60°$

Figure 4.23 – New comparison between predicted and measured variation of enthalpy flow rate in the turbine without taking the shock wave losses into account (with precision lines of $\pm$ 10%)

the static enthalpy flow rate variation. The prediction of the power at the turbine shaft is compared in Figure 4.27 to the power calculated based on the total enthalpy flow rate variation and the heat loss calculated in the bearing model.

4.4.1 New estimation of the turbine and bearings efficiency

Considering the heat exchange between the turbine and the bearings, a new estimation of the efficiency of the components of the turbo generator can be achieved and compared to the results of Chapter 3.
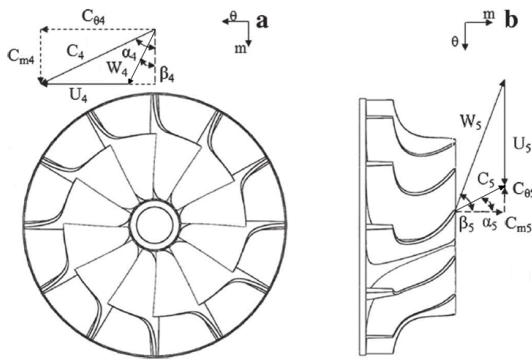
Figure 4.24 – $(P_{su} = 8e5[bar]$, $P_{ex} = 3e5[bar]$, $T_{su} = 380[K]$, $N_{rot} = 48[kRPM])$ $\alpha_5 = -38°$ and $\beta_5 = -64°$
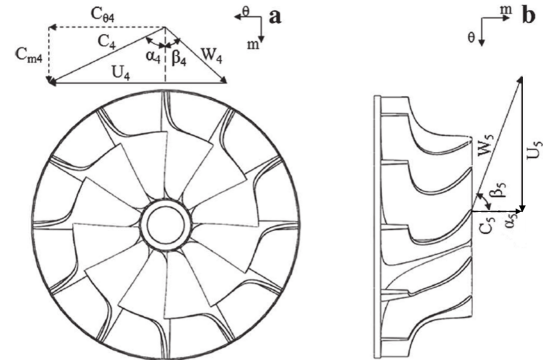
Figure 4.25 – $(P_{su} = 8e5[bar]$, $P_{ex} = 3e5[bar]$, $T_{su} = 390[K]$, $N_{rot} = 78[kRPM])$ $\alpha_5 = 0°$ and $\beta_5 = -64°$
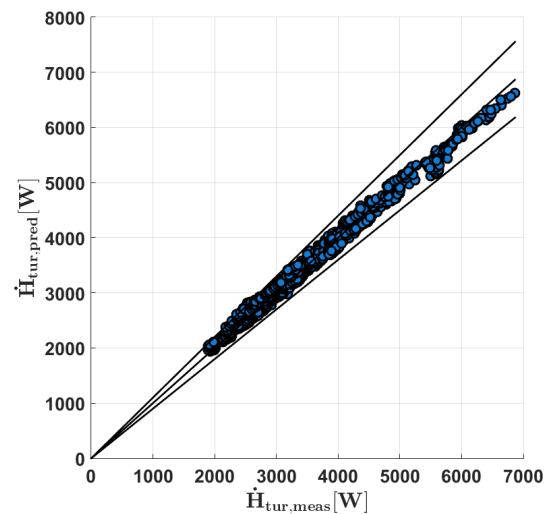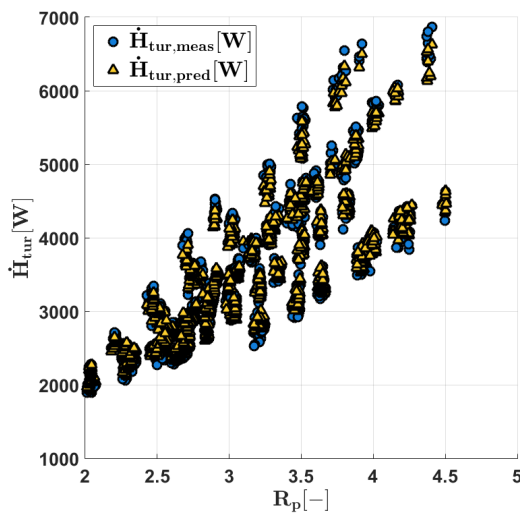
Figure 4.26 – Comparison between predicted and measured variation of enthalpy flow rate in the turbine taking both the heat and the shock wave losses into account (with precision lines of $\pm$ 10%)

First the evolution of the turbine total-to-static efficiency as a function of the pressure ratio is presented.

Then, in Figure 4.28, the evolution of the static-to-static efficiency of the turbine as well as the conversion efficiency of the bearings and generator and the global efficiency of the turbo generator are illustrated. In comparison to the results obtained in Chapter 3, it can be seen the bearings efficiency is now higher than previously and was underestimated because of the heat transfer, which is not visible.
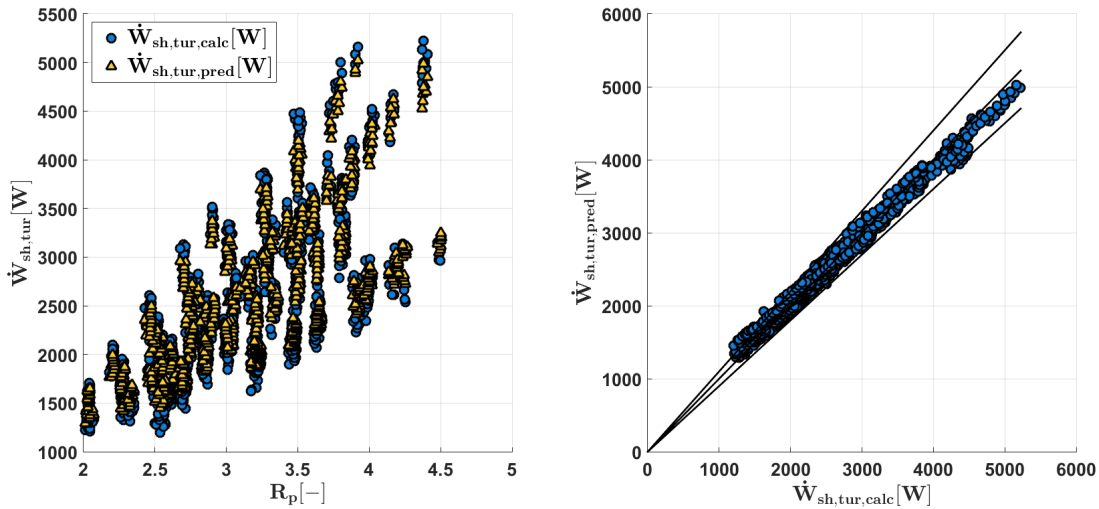
Figure 4.27 – Comparison between predicted and measured turbine shaft power taking both the heat and the shock wave losses into account (with precision lines of ± 10%)
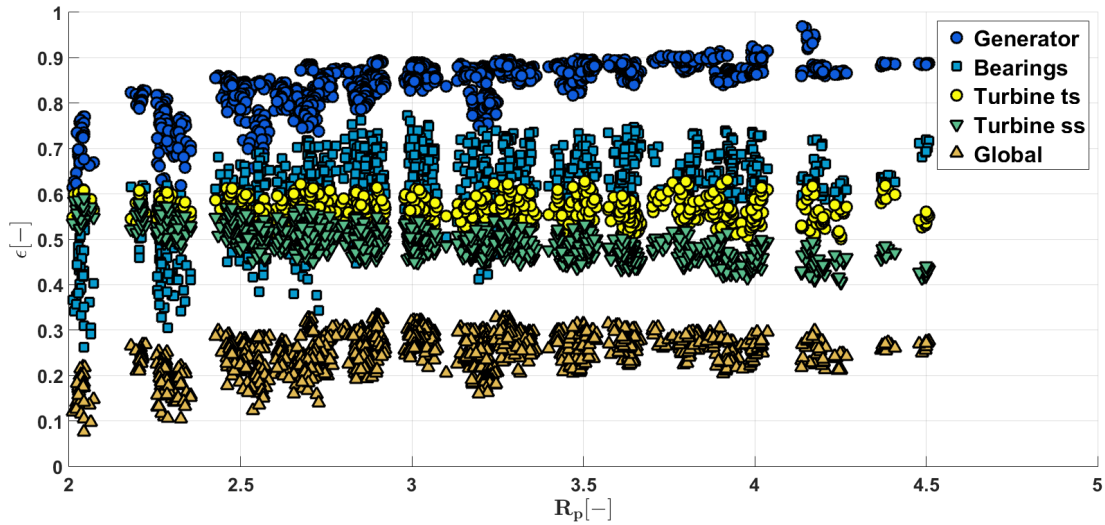
Figure 4.28 – New estimation of the turbine and bearings efficiency based on the models and taking into account the heat exchange between the fluids in the turbine and bearings

4.4.2 Losses distribution

The proposed models accurately describe the performance of the turbine in terms of mass flow rate, mechanical power and outlet temperature. As explained those models involve only conservation laws of mass, energy and momentum and loss correlations found in literature and which have been developed for turbomachinary. As a consequence the number of calibration parameters is limited and only involves the absolute blade angle and the relative flow angle at the outlet of the stator and rotor respectively. The physical phenomena occurring during

the expansion of the fluid can be expected to be correctly represented, at least the trends and the orders of magnitude since a 3D CFD model is required to achieve a high level of details in describing the flow and the thermodynamic conditions in the turbine. So the distribution of the source of losses and the results can be treated with confidence.

The values of the investigated losses are presented for model with shock losses in figures 4.29 and 4.30 while the distributions are presented for both models, in average on the 1260 measurement points obtained with fluid R245fa, in Figure 4.31. As it can be seen, the main total enthalpy loss is due to the heat exchange between the expanded and lubrication fluids. This loss is significant since it does not only reduce the available power at the turbine shaft and the turbine efficiency but it is also responsible for a large amount of the temperature increase of the lubrication fluid in the bearings. Consequently, it also limits the inlet temperature and pressure as well as the rotational speed of the turbine.

In the turbine, the main sources of losses are the stator, the clearance, the secondary and incidence or shock losses according to the model. Clearance losses are typical for small expansion devices because of the relative importance of the clearance compared to the expander size. Secondary flow are also typical of small machines. The friction loss in the nozzles can not easily be reduced. On the another hand, incidence losses are mainly resulting from the suboptimal rotational speed conditions compared to velocity of the flow at the inlet of the rotor. High incidence losses meaning here the speed of the rotor is too low compared to the absolute velocity, a simple way to increase the performance of the turbine is too increase the rotational speed until avoiding incidence losses. A parametric analysis on the rotational speed is achieved in the following in order to estimate the performance of the turbine for optimal speed as well as the resulting speeds.
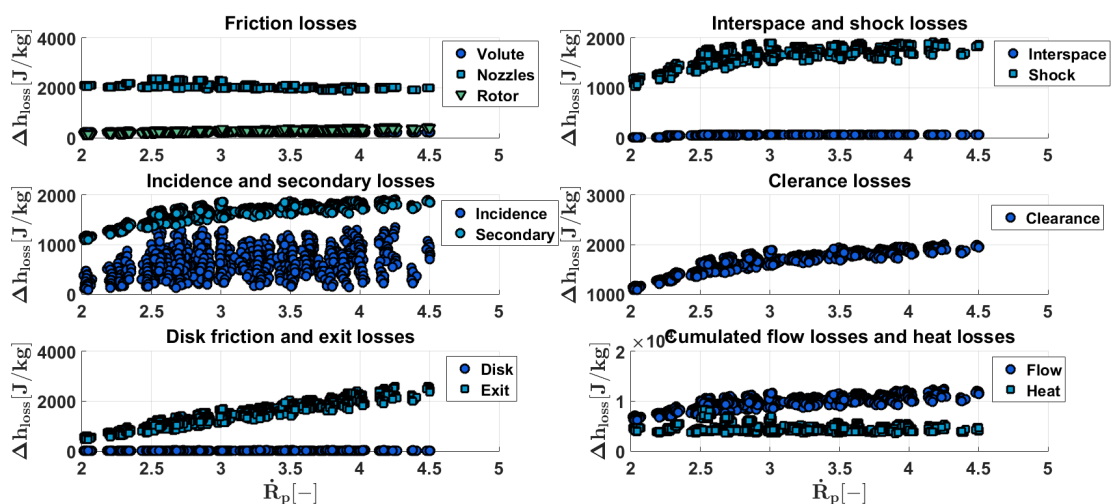
Figure 4.29 – Quantitative comparison of the sources of losses for the model including heat and shock wave losses
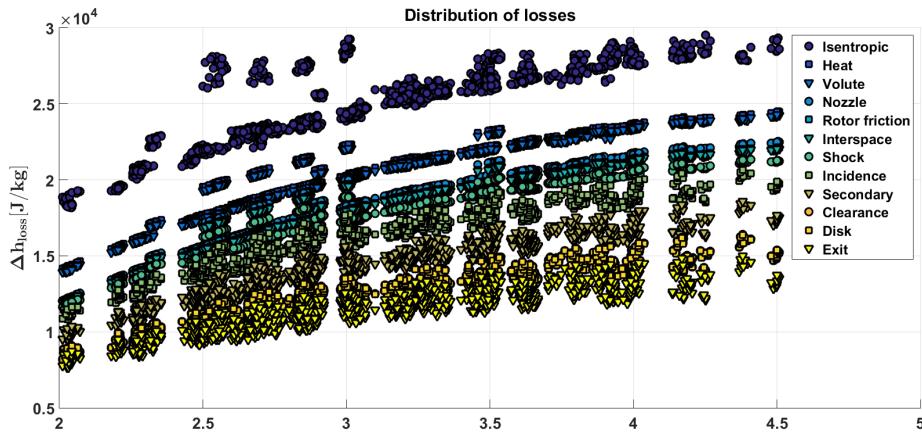
Figure 4.30 – Quantitative analysis of the sources of losses for the model including heat and shock wave losses
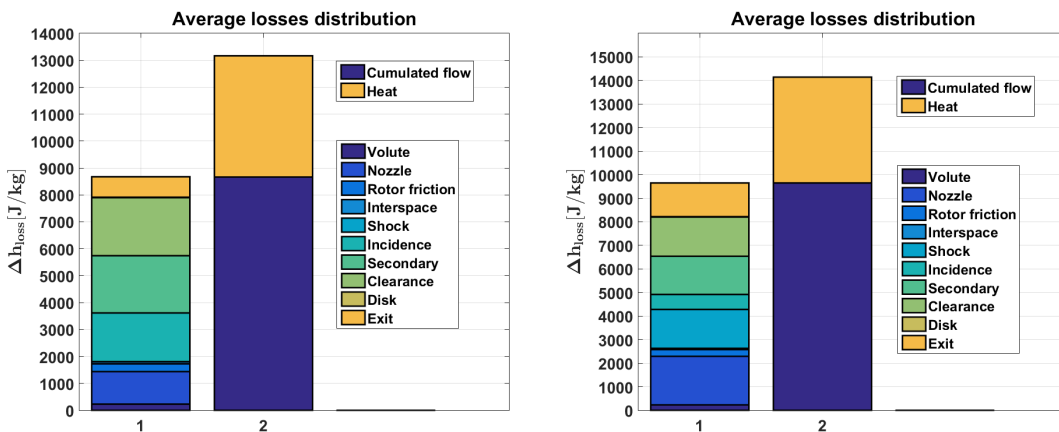
Figure 4.31 – Distribution of the sources of losses averaged on the 1260 measurement points achieved with fluid R245fa and considering the shock loss (right) or not (left)

4.4.3 Performance extrapolation

It has been shown the rotor incidence loss could be reduced by optimizing the rotational speed of the component. The model can thus be used to reach rotational speeds that could not be achieved during the tests.

Then, because the turbine has also been investigated experimentally on test rig using fluid R1233zd, it is proposed to quantify the accuracy of the proposed models when predicting the turbine performance with the new fluid.

In a third step, because the model is at the end devoted to be integrated into an ORC design

and simulation tool, the modifications required for the model to be operated in design mode are discussed.

Extended speed range

The pressure ratio, mass flow rate and inlet temperature are kept constant while the rotational speed is increased, using the model, from a minimal value around 50 kRPM to a maximum close to 140 kRPM. The results are shown in Figure 4.32 where it can be seen, for various pressure ratios, the power output of the turbine passes through a maximum corresponding to an optimal value of rotational speed. The optimal speed increases with the pressure ratio so to adjust the velocity triangles at the inlet of the rotor to the increased speed of the working fluid.
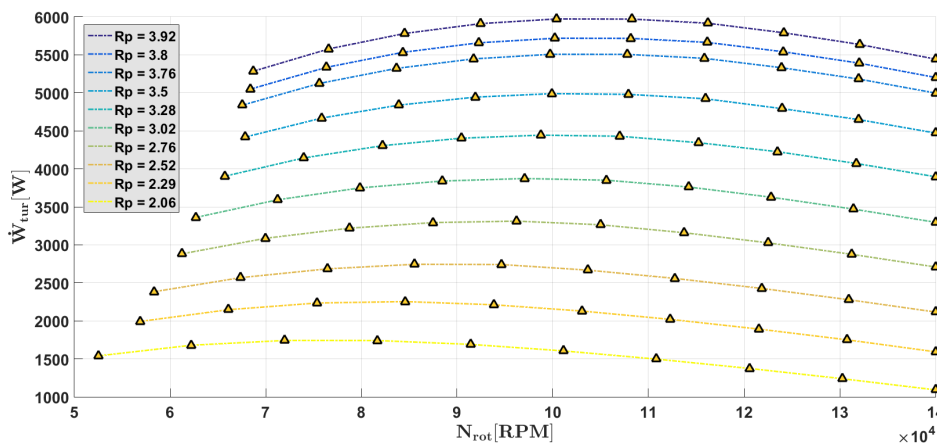
Figure 4.32 – Extrapolation of the turbine performance with increased speed based on the developed model

Use of another fluid: R1233zd

The model can be used to predict the performance of the same turbine using R12333zd as working fluid. Results are then compared with experimental data in terms of power output, mass flow rate and exhaust temperature. As it can be observed, a good agreement is achieved.

Design model

The complexity of turbine design process will no more be discussed and the complete task is beyond the scope of this study. However, an estimation of the performance and the preliminary design of a turbine using a fluid other than R245fa (or R1233zd) is already feasible based on the proposed model. Nonetheless, the latter requires some modifications to be used in (preliminary) design mode. The geometry is currently unknown, as well as the absolute and relative angle at the outlet of stator and rotor respectively, while the mass flow rate is
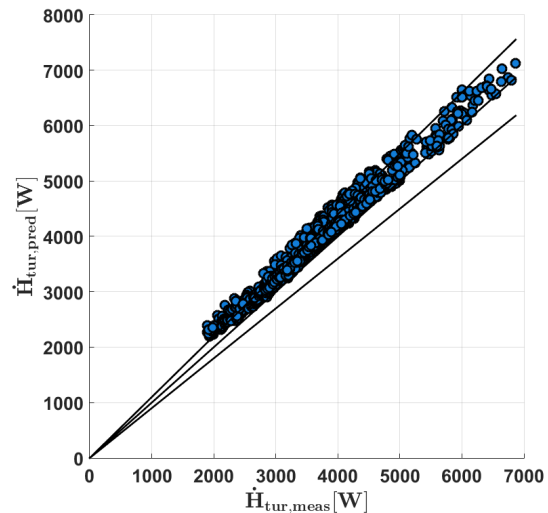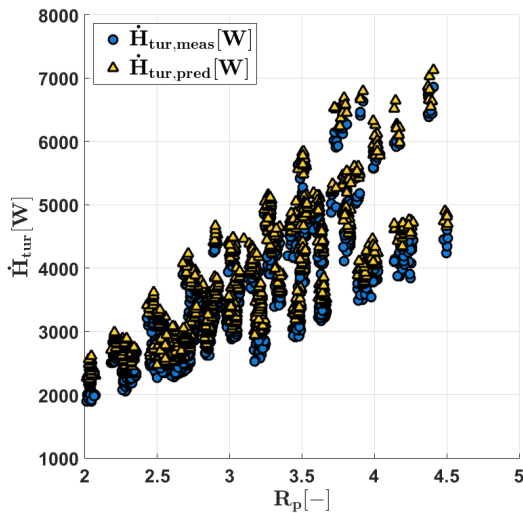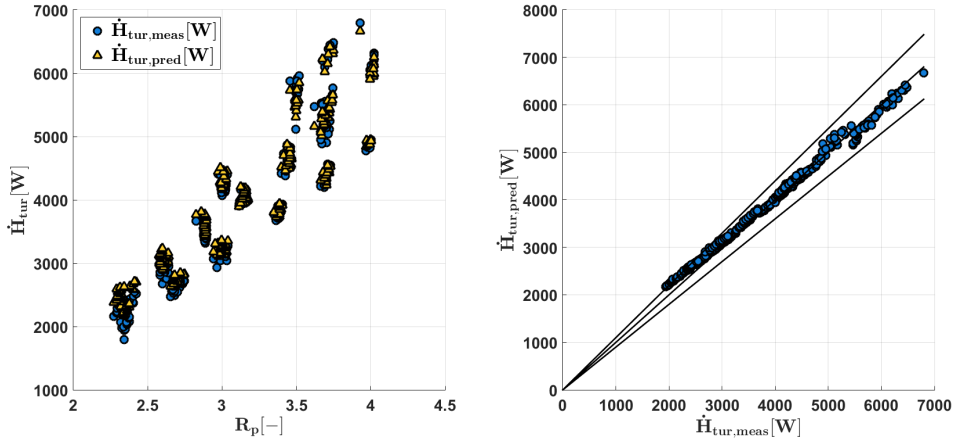
Figure 4.33 – Comparison between predicted and measured variation of enthalpy flow rate in the turbine with fluid R1233zd taking both the heat and the shock wave losses into account
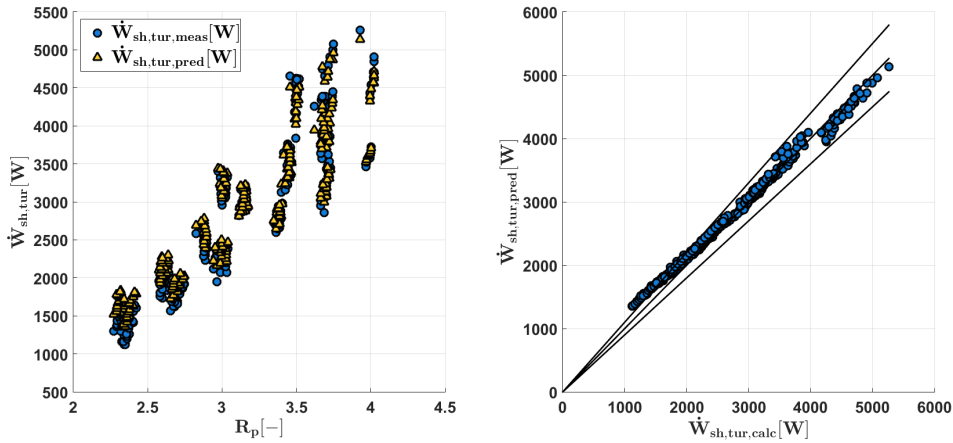
Figure 4.34 – Comparison between predicted and measured variation of enthalpy flow rate in the turbine with fluid R1233zd taking both the heat and the shock wave losses into account

set as input. The proposed process is inspired by the similitude theory of turbomachines regarding the geometric properties. Ratios between the dimensions presented in Figure 4.1 and a reference D are defined for the turbine experimentally investigated.

$$\frac{l_1}{D}, \frac{l_2}{D}, ..., \frac{l_3}{D}, \frac{d_1}{D}, \frac{d_2}{D}, ..., \frac{d_n}{D} \tag{4.158}$$

Assuming a similar level of compactness, those ratios are kept constant for the design of a new machine, meaning that the only geometric output to be identified by the model is the reference D. The latter is chosen to be the wheel diameter so, that it can be easily identified based on the speed input and the definition of the flow coefficient (Eq. 4.40). Because the velocity

triangles are supposed to be optimal and shock waves can be considered not to occur on the design point, the first version of the model, without shock, is used. The absolute flow angle at the rotor outlet α_5 is set to 0 assuming an axial flow at the outlet of the machine. The design process is then achieved in Chapter 5 optimizing the flow coefficient and the rotational speed in order to maximize the power performance of the turbine. The design model procedure is summarized in Figure 4.35.
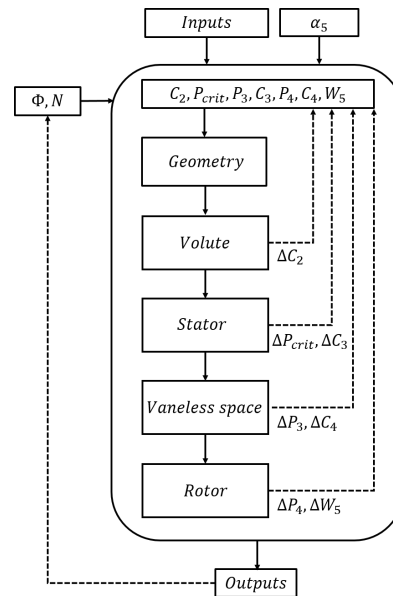
Figure 4.35 – Flow chart of the radial-inflow turbine model in design mode

4.5 Conclusion

In this Chapter, a model of the radial-inflow turbine, studied in Chapter 3, is proposed, described and validated against experimental data. First, the elements constituting the expansion machine are described and several modeling methods are reviewed. Based on this review, a mean-line model of the turbine is proposed. The ambient losses are evaluated based on a energy balance over the whole turbo generator and are lumped using a heat transfer parameter. The turbine itself is divided in several stations in which the velocity triangles of the fluid flow are computed using real gas equation of state and mass, energy and momentum conservation equations. For all the elements on both sides of the stations, correlations are used to describe the loss phenomena affecting the velocity triangles of the downstream station. The inclusion of the heat transfer from the fluid expanded in the turbine and the lubrication fluid going through the bearings is discussed. It is shown that the latter cannot be neglected.

A model of the bearing system including friction and windage losses is proposed. Based on the energy balance over the bearings, the heat transfer from the turbine is evaluated and is modeled. Taking this heat loss into account, two versions of the turbine model are compared

and confronted to experimental data. Because the pressure ratio was always above the critical pressure ratio, sonic conditions are reached for all the measurement points at the throat of the nozzle. The first model version consider the supersonic expansion in the vaneless space without formation of shock waves, thus only increasing the incidence losses at the rotor inlet. In the second version the stator is treated in the same manner as a convergent-divergent nozzle row. This is justified by the fact that the nozzles formed by the stator blades cannot be purely convergent. The cross section increases downstream the throat of the nozzles and even more in the vaneless space. It is therefore assumed the pressure information at the inlet of the rotor is unable to go up to the nozzle throat. The fluid therefore expands because of the increase in cross section area. This expansion would ideally occur until a pressure, called adapted pressure in reference of convergent-divergent nozzle theory, which can be calculated based on the definition of the absolute blade angle at the stator outlet α_3. Based on this assumption, it is shown that, if the adapted pressure does not match the rotor inlet pressure, the fluid is submitted to a compression shock wave so to verify energy, mass and linear momentum conservation. The actual absolute flow angle α_3^* is then calculated for those conditions.

Results show a good agreement of the prediction compared to the measurements with relative error on the model outputs globally below 10 %. Those results are achieved optimizing

- the absolute and relative outlet flow angles of both the stator and rotor when considering the formation of shock wave losses

- the relative outlet flow angle of the rotor only when formation of shock waves are not considered.

The optimization of the parameters is performed in order to minimize the RMSE on the measured and predicted turbine enthalpy flow rate variation. The mass flow rate, the third output of the model, is easily predicted based on the throat cross section area, in which sonic condition are always reached.

The obtained value of the relative flow angle at the outlet of the rotor is observed to be too low for the turbine geometry in the first version of the model. Indeed, measurements on test rig were most of the time performed for rotational speeds lower than the optimal rotational speed. Using the model to predict the turbine performance and the velocity triangles for the optimal speed condition that avoids incidence losses at the inlet of the rotor results in adapted velocity triangle at the inlet of the rotor but suboptimal triangle at the outlet. The flow angle is therefore increased so to reach optimal velocity triangle on both sides of the rotor for the estimated optimal speed condition, which results in a decrease in the accuracy of the model.

This behavior is not met in the second version of the model which is able to more accurately predict the mechanical power and the outlet temperature while leading to optimal velocity triangles on both sides of the rotor for the optimal rotational speed.

The models are then used to estimate the distribution of the source of losses in the turbine and the results are given in average for the 1260 measurement points achieved with R245fa. The models are also used to predict the performance obtained with fluid R1233zd on test rig while keeping the optimization parameters constant. Again the model with shock loss gives more accurate results.

Another way to verify the validity of the models could be to consider the input conditions of pressure ratio and rotational speed provided by the manufacturer for the same turbine running with air.

In the last part of the Chapter, a method to use the turbine model in the design in order to be integrated into the ORC optimization process of the next Chapter is proposed. A geometric similarity is assumed so the ratio between the different length and diameter of the tested turbine as well as the obtained flow angles are kept constant. A similarity of operation is also assumed so the turbine is designed for same flow and work coefficient. This enables to deduce the geometry and speed of the turbine for given input conditions of mass flow rate, inlet pressure and temperature and outlet pressure.

To properly conclude, perspectives are investigated. The first perspective concerns the evaluation of the heat transfer between the expanded and the lubrication fluids. Because this heat transfer has a large impact on the performance, it would be worth investigating the bearing more into details based on a reliable geometry description. On test rig, tasks could also be achieved to evaluate the heat loss in the turbine without production of work, feeding the turbine and bearings with fluid while the rotor is kept at rest for instance. Once clearly identified solutions should be proposed to reduce the heat transfer. Indeed, the phenomenon is not only reducing the power available at the turbine shaft but also increasing the temperature of the bearing lubrication fluid. Therefore it limits the inlet temperature and pressure and the rotational speed that can be reached by the turbine.

Another perspective concerns the investigation of the flow behavior in the vaneless space. The consideration of shock wave formation in the model leads to more accurate results in terms of performance and flow description. However, more detailed 3D-CFD models should be employed to verify these phenomena actually take place or not during the supersonic expansion between the nozzle throat and the rotor inlet.

Finally, as explained in the description of the turbine components, clearance must be provided between the fixed and moving parts of the machine in order to guarantee its mechanical viability. Leakage paths are resulting from these gaps. Sealing systems are considered to reduce the mass flow rates of the leakages paths. Nonetheless it would be worth investigating and quantifying those leakage mass flow rates, particularly going from the turbine to the bearings. This could be achieved through CFD but also experimentally with proper measurement of the mass flow rate and based on a mass balance.

5 Design and optimization of the waste heat recovery systems

Abstract

This Chapter focuses on the design phase of ORC systems recovering the heat wasted from two of the sources available on a HDT: the exhaust and recirculated gases. From these heat sources and their combinations, 5 possible architectures are considered. The main components (i.e. the heat exchangers, the pump and the expander) of the WHR systems are investigated and modeled. Plate type heat exchangers are considered for both the hot and cold sides of the system. Regarding the expansion devices, 5 positive displacement machine technologies, the scroll, screw, piston, vane and roots expanders, are considered and modeled while, among the turbo-expanders, the radial-inflow turbine is taken into consideration. A semi-empirical model is also proposed to simulate a volumetric pump. The models of components are first confronted against experimental data. The validated models are then used as reference for the design of the new components, which is achieved following similitude rules. This leads at the end to 30 typologies which will be used with 6 of the various investigated working fluids. In order to identify the most promising system(s), a three-step optimization tool is developed. First, the most suitable conditions are identified for the design of the ORC systems using a simplified model of expansion machine. In a second step, the design phase, using more detailed models for the expanders and a proposed economic model for the overall system, a thermo-economic optimization is performed. In a third step, the output power of the obtained system models is maximized, optimizing the evaporating pressure and the overheating degree for various off-design conditions. The average power, weighted using the frequency distribution of the gas operating conditions is computed and used to compare the 180 systems. Finally, because power is not the only standard to select the most suitable system topology, additional criteria are taken into consideration and a decision matrix is proposed.

Keyword

Organic Rankine Cycle, Waste Heat Recovery, Heavy Duty Trucks, Thermo-Economic optimization.

5.1 Introduction

This Chapter attempts to address the problematic of selecting the architecture, the expander technology, and the working fluid for a waste heat recovery organic (or non-organic) Rankine cycle system devoted to be coupled to a truck engine. Many studies have already been conducted on the subject ([22], [53], [46] [108], [61], [109], [57], [110]). However, in most of the existing works, because it is generally a design process, the proposed ORC models are not validated while important differences appear between theoretical predictions and measured performance in real cases [176]. In addition, the level of detail of the models is most of the time reduced advocating a decrease in computational time [177]. It is not uncommon for instance to find constant efficiency values for most of the component models of the ORC system when it comes to working fluid and component selection, particularly in thermo-economic optimization studies, which can be greedy in computational resources [57]. If this assumption can be acceptable for the design point, it is of course not true for most of the components in off-design and particularly for volumetric expansion machines. Sometimes, authors also consider the design point as the single point for the performance comparison of the various systems they investigate. Nonetheless, on-board ORC systems are operating only a fraction of the time on their design point because of the highly transient temperature and mass flow rate conditions of the heat sources and heat sinks. These are several factors which could raise some questions as to the reliability of the results.

In this study, it is proposed to first build and validate the component models against experimental data before trying to predict their performance within the design phase of the on-board system. A lot of experimental set-ups could be used to this end. In particular, a Rankine test-bench, using water as working fluid, and devoted to recover the heat from the exhaust gases of a gasoline engine, enabled to calibrate the parameters of a Nusselt correlation on the gas side and to validate the plate heat exchanger model to be placed on the high pressure side. Regarding the plate heat exchangers on the cold side, because the pinch-point is generally low, it is proposed to directly use correlations available in literature to evaluate the heat transfer coefficients on both sides of the heat exchanger.

Numerous test rigs have also been built over the past few years to characterize the performance of ORC systems including various expansion machine technologies. Thus several scroll expanders, a screw, a piston and a roots expander were tested in laboratory, using R245fa as working fluid. The rigs were also equipped with different volumetric pump technologies (single or multi diaphragm, piston, gear pumps). All this data has been used to calibrate the parameters of the proposed pump and expander models and validate those models. Finally a

collaboration with the Czech Technical University in Prague enabled to validate a model of vane expander, which was installed on test-rig using hexamethyldisiloxane (MM) as working fluid.

The resulting validated models are used as reference for the design process whose strategy consists in scaling the components for the new application following specific rules. Thus, for instance, the similitude of Reynolds numbers is used for the exchangers recovering the thermal energy from the hot gases. The efficiency drops due to the source of losses in the volumetric pump and expander models are conserved on the design point. For the radial-inflow turbine, as explained in Chapter 4, a geometric similitude is applied.

Numerous design steady-state models of ORCs are built. From the 5 architectures proposed in Chapter 2 and the 6 expander technologies result 30 different typologies. Considering the 6 working fluids identified in Chapter 2, it leads at the end the optimization of 180 ORC system models. A 3-step optimization tool is developed in the Matlab environment [178]. The method starts with the selection of the design conditions. In this first step, the model of expansion machine is simplified to only take the impact of the pressure ratio on the expander isentropic efficiency into account. The evaporating pressure and the pinch-point of the heat exchangers are optimized under several constraints, for various gas conditions coming from a combination of various truck driving cycles, so to maximize the power produced and identify the most suitable design point. Then, for the obtained design conditions, a thermo-economic optimization is performed to design the systems. In this second step, more detailed models of expansion machines are used, an economic model is proposed and additional optimization variables (e.g. expander rotational speed) and constraints (e.g. limited expander rotational speed) are taken into consideration. Finally, the performance of the resulting systems is optimized and evaluated for various off-design conditions, optimizing the evaporating pressure and the overheating degree. A weighted average of the power produced by the systems is then found based on the frequency distribution of the considered operating conditions in the driving cycle. In order to locate the sources of entropy increase in the proposed systems, and thus identify the possible weakness of the designed external combustion engine, an exergetic analysis is performed. A basic sensitivity analysis is also done to evaluate the impact of a variation of the system cost on the optimal specific investment cost of the system. The power produced by the system is an objective comparison standard but it is obviously not the only selection criterion. Many other factors have to be considered to identify the most suitable system architecture, working fluid and component for a given application. A non-exhaustive list of these factors is thus established and a comparison methodology based on the obtained criteria is proposed.

5.2   Model of the waste heat recovery systems

In this section, the models of the heat exchangers, pump and expansion machines are described. All the models are implemented in the Matlab environment. Then the WHR system

architectures are achieved by interconnecting the component models together, according to the investigated typologies. The model of radial-inflow turbine proposed in Chapter 4 is also considered.

5.2.1 Modeling the heat exchangers

Heat exchangers transfer thermal energy from one fluid to another. The process can be either direct or indirect depending on whether the thermal energy is directly transferred from one fluid to another, typically through a separating solid wall, or not. Many different configurations exist in order to accommodate different fluid properties and operating conditions. The simplest configuration is probably the concentric tube heat exchanger whose arrangements can be classified in parallel and counter flows. Among others, compact heat exchangers is an important class used to achieve very large heat transfer area per unit volume. *These devices have dense arrays of finned tubes or plates and are typically used when at least one of the fluid is a gas, and is hence characterized by a small convection coefficient [179].* In ORC power systems, Brazed Plate Heat Exchangers (BPHE) are often considered, in particular for the evaporator whose heat transfer performance is a key element in defining the system overall efficiency. The device is typically a once-through heat exchanger covering the phase transition from liquid to vapor. Thus when modeling the evaporator, the liquid, two-phase and vapor regions have to be taken into account.

The proposed heat exchanger model consists in a combination of a thermodynamic and a geometric model. The inputs of the exchanger model are the inlet temperatures and pressures and the mass flow rates on both sides (primary and secondary fluid sides), while the outputs are the outlet pressures and temperatures on both sides. The heat flow rates on both sides can then be computed. The components are modeled by means of the Logarithmic Mean Temperature Difference (LMTD) method for counter flow heat exchangers. The exchangers are subdivided into three moving-boundaries zones corresponding to the three phases in which the working fluid can be found. In addition, the two-phase region is divided in N finite volumes. Each of the single-phase zones and each cell of the two-phase region is characterized by a heat transfer area A_i and a heat transfer coefficient U_i whose product is known based on the LMTD and the heat flow rate on both sides (Eq. 5.1). The heat flow rate on the working fluid side can be calculated once the outlet temperature is known, so it is computed through an iterative process. The ambient losses added to this heat flow rate leads to a first evaluation of the outlet temperature of the exhaust gases.

$$AU_i = \frac{\dot{Q}_i}{\Delta T_{LM,i}} \quad with \quad i = 1, ..., N+2 \tag{5.1}$$

The heat transfer coefficient U_i is calculated for each zone i considering 2 convective and 1 conductive heat transfer resistances in series (secondary fluid side, metal wall and primary

fluid side)

$$\frac{1}{U_i} = \frac{1}{h_{sf,conv,i}} + \frac{1}{k_{wall}/e_{wall}} + \frac{1}{h_{wf,conv,i}} \quad with \quad i = 1,...,N+2 \tag{5.2}$$

The area of each zone can therefore be computed from the sum of which the resulting total heat transfer area of the heat exchanger can be deduced.

$$A_{tot} = A_{liq} + \sum_{i=1}^{N} A_{tp,i} + A_{vap} \tag{5.3}$$

A summary of the model procedure is given in Figure 5.1. In this Figure is also shown the optimization process implemented for the calibration of the model parameters. The latter process is described below.
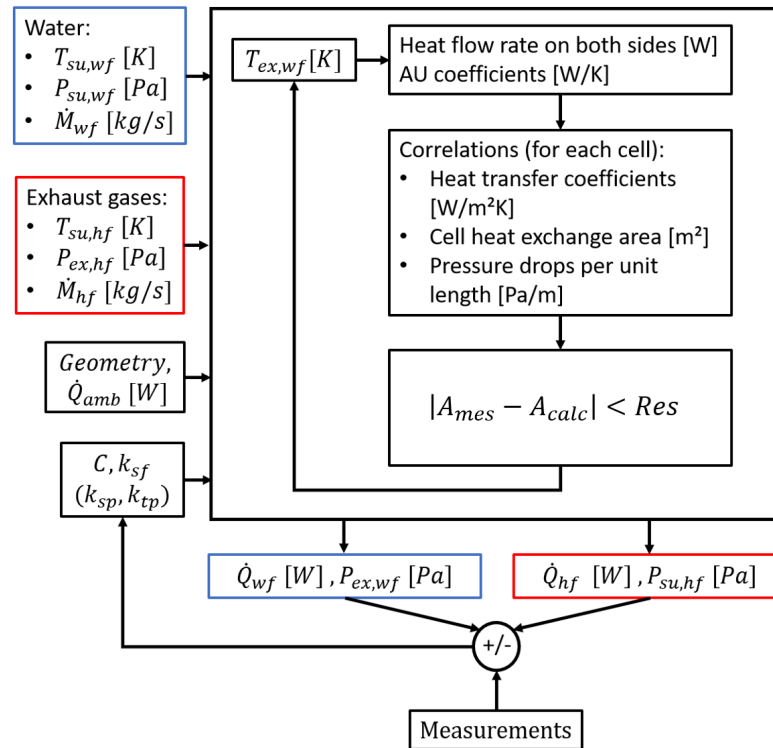
Figure 5.1 – Flow chart describing the inputs, outputs, modeling process and parameter calibration phase of the heat exchanger model

Descritpion of the heat exchanger geometry

As the name suggests, the BPHE is composed of plates. The number of those plates can vary depending on the BPHX size. The fluid streams enter and leave the channels through collectors at the corners of the plates. Open and blind holes define the path of the fluids through the

different channels. An exploded view of a counter-flow BPHE is shown in Figure 5.2 to describe the flow arrangement. To enhance the heat transfer mechanism, the plates are corrugated. Many patterns have been developed for those corrugations but chevron pattern is currently the most common choice [180]. The geometric characteristics of a plate are described in
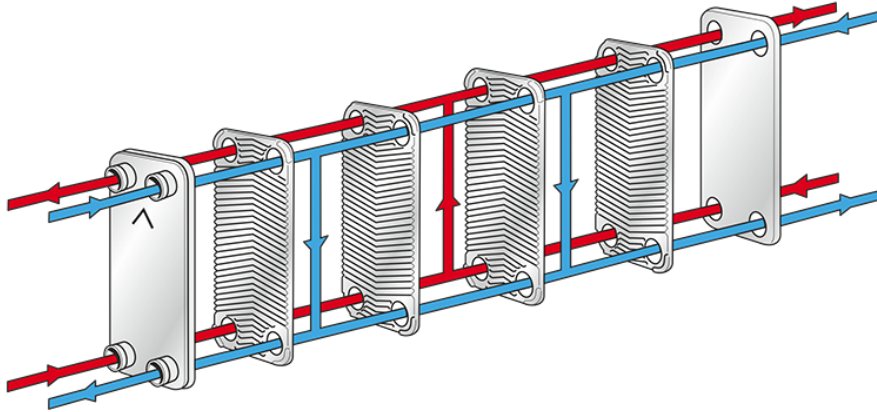
Figure 5.2 – Schematic of a brazed plate heat exchanger operating principle - exploded view. [181]

Figure 5.3 based on the work performed by Martin [182]. The chevron angle is denoted β whose extreme values range from 0° for corrugation parallel, to 90° for corrugation normal to the flow direction respectively. In practice, the chevron angle varies between $22-65°$ [180]. The Chevron corrugation pattern is defined by two geometric characteristics, the amplitude of the sinusoidal corrugation denoted with b, and the phase or wavelength denoted with λ. Other important geometric characteristics of BPHE which are used in the computation of heat transfer correlations are the dimensionless corrugation parameter or wave number X, the enlargement factor Φ (ratio of the actual and protracted plate surfaces), the plate thickness t, the vertical length of the plate measured between the center of the upper and lower port hole L_v, the total vertical length of the plate L_{tot} and the width of the plate L_w.

$$X = \pi \frac{P_s}{\lambda} \tag{5.4}$$

$$\Phi = \frac{(1 + \sqrt{1 + X^2} + 4 * \sqrt{1 + \frac{X^2}{2}})}{6} \approx 1.22 \tag{5.5}$$

$$D_e = 4b \tag{5.6}$$

$$D_h = \frac{D_e}{\Phi} \tag{5.7}$$
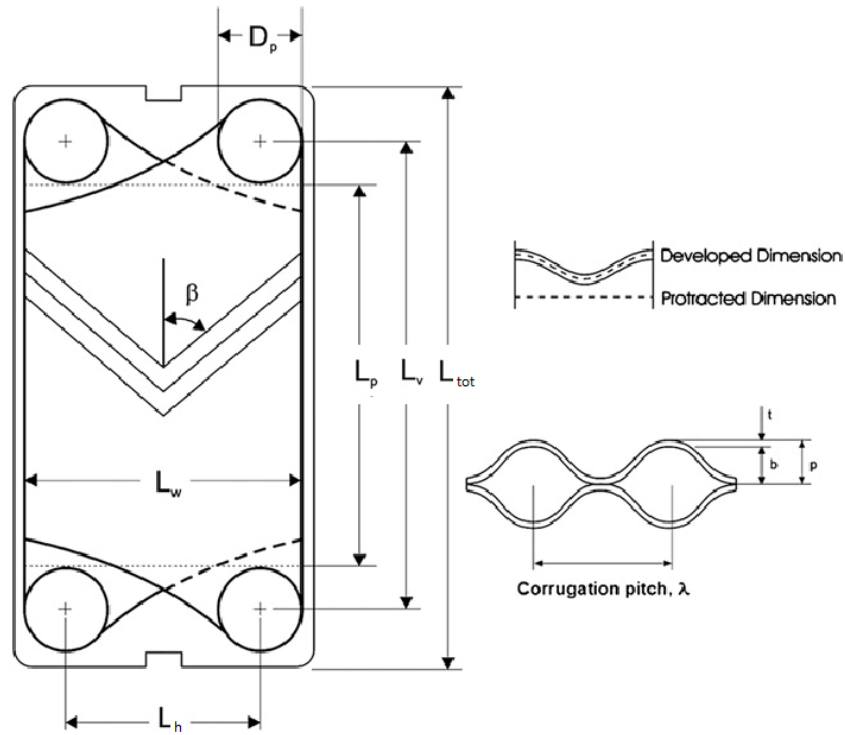
Figure 5.3 – Geometric characteristics of chevron plates[183]

Single phase heat transfer coefficients and pressure drops

In single phase, the convective heat transfer coefficients (h_{conv}) and Fanning friction coefficients (f) are evaluated using Martin's correlation [182] on the working fluid side. Many correlations for the calculation of single phase heat transfer coefficients are available in literature and are generally obtained for a particular working fluid, a particular flow regime (range of Reynolds number) and plate geometry (e.g. chevron angle). Among other, Ayub [180] achieved a literature review and established a large list with available correlations. Martin's correlation is a standard because of its simplicity, accuracy and ability to predict both the heat transfer coefficient and friction factor for common geometries whether the flow is laminar or turbulent. It is also used as reference in [13] and, in a recent study, Dickes et al. [184] also compared several correlations and showed that Martin's correlation is the most suited for a plate heat exchangers with fluid R245fa as working fluid.

$$f = \left(\frac{\left(0.045 \tan(\beta) + 0.09 \sin(\beta) + \frac{F_0}{\cos(\beta)} \right)^{0.5} + \left(1 - \frac{\cos(\beta)}{\sqrt{3.8 F_1}} \right)}{\cos(\beta)} \right)^2 \tag{5.8}$$

$$Nu = 0.205 Pr^{1/3} \left(f Re^2 \sin(2\beta) \right)^{0.374} \tag{5.9}$$

$$h = \frac{Nu \cdot k}{D_h} \tag{5.10}$$

with

for laminar flow ($Re < 2000$):   for turbulent flow ($Re \geq 2000$):

$$F_0 = \frac{16}{Re} \ , \ F_1 = \frac{149.5}{Re} + 0.9625 \qquad (5.11) \quad F_0 = (1.56\log(Re) - 3)^{-2} \ , \ F_1 = \frac{9.75}{Re^{0.289}} \quad (5.12)$$

In those equations β is the chevron angle in rad according to Martin's definition, G is the mass velocity in $kg/s.m^2$, D_h is the hydraulic diameter in m. The friction pressure drops are computed with the following relation:

$$\Delta P = \frac{2fG^2}{\rho D_h} L \qquad (5.13)$$

where ρ is the mean density of the fluid in kg/m^3 and L is the plate length in m.

On the secondary fluid side, the Martin's correlation can directly be used for the water cooled heat exchanger. A good agreement can be achieved when comparing the model outputs to experimental data. One reason is the low pinch-point that is typically reached. On the other hand, for the gas heat exchangers, correlations from literature for plate heat exchangers typically lead to large errors on the heat flow rate prediction (up to 50 %). If the heat exchanger conductance must be predicted accurately, then it is necessary to focus on the gas-side heat exchanger coefficient. Measurements were performed on an existing plate type heat exchanger built for an automotive ORC application and a Dittus-Boelter type correlation is derived to evaluate the Nusselt number and the heat transfer coefficient on the gas side.

$$Nu = C \ Re^m Pr^n \qquad (5.14)$$

The C parameter is calibrated minimizing the error between the measured heat flow rate and the prediction of the model while the m and n parameters are set to 0.7 and 1/3 respectively. In addition, a proportional calibration parameter k_{sf} is added to the pressure drop evaluation on the gas side so to fit the experimental data.

Two phase heat transfer coefficients and pressure drops

Convective heat transfer coefficients (h_{conv}) and Fanning friction coefficients (f) are evaluated using correlations for boiling and condensation proposed by Han et al. [185], [186]. As in single-phase, many correlations for the calculation of two phase heat transfer coefficients are available in literature. Eldeeb et al. [187] achieved a literature survey and compared several correlations in boiling and condensation in terms of heat transfer coefficients values and friction pressure drops for various refrigerants. According to this study, the correlation proposed by Han leads to similar results in boiling when compared to other correlations such as the one proposed by Ayub [180] and more recently by Almalfi [188]. However, in condensation, Han's correlation leads to higher values of heat transfer coefficient compared to what is obtained with Shah's correlation [189] or more recently with Longo's correlation

[190]. Nonetheless, Han's correlation presents the advantage to be simple to implement, to be applicable for both boiling and condensation and, for several chevron angles, but in addition to predict both the heat transfer coefficient and friction factor for common plate heat exchangers geometries. It is also used as reference in [13]. As remarked in the latter study, two-phase heat transfer correlations in plate heat exchangers should be used with caution and *"regarded as a rough guide, because they are not supported by sufficiently broad experimentation"*.

Evaporation: Condensation:

$$G_{e1} = 2.81(\frac{p_{co}}{D_h})^{-0.041}\beta^{-2.93} \quad (5.15) \qquad G_{e1} = 11.2(\frac{p_{co}}{D_h})^{-2.83}\beta^{-4.5} \quad (5.21)$$

$$G_{e2} = 0.746(\frac{p_{co}}{D_h})^{-0.092}\beta^{0.61} \quad (5.16) \qquad G_{e2} = 0.35(\frac{p_{co}}{D_h})^{-0.23}\beta^{1.48} \quad (5.22)$$

$$G_{e3} = 64710(\frac{p_{co}}{D_h})^{-5.27}\beta^{-3.03} \quad (5.17) \qquad G_{e3} = 3524.1(\frac{p_{co}}{D_h})^{-4.17}\beta^{-7.75} \quad (5.23)$$

$$G_{e4} = -1.314(\frac{p_{co}}{D_h})^{-0.62}\beta^{-0.47} \quad (5.18) \qquad G_{e4} = -1.024(\frac{p_{co}}{D_h})^{-0.0925}\beta^{-1.3} \quad (5.24)$$

$$Bo_{eq} = \frac{q}{G_{eq} \cdot i_{fg}} \quad (5.19) \qquad Nu = G_{e1}Re_{eq}^{G_{e2}}Pr_l^{1/3} \quad (5.25)$$

$$Nu = G_{e1}Re_{eq}^{G_{e2}}Bo_{eq}^{0.3}Pr_l^{0.4} \quad (5.20)$$

Where β is the chevron angle in rad according to Martin's definition, p_{co} is the corrugation pitch in m, Bo_{eq} is the equivalent boiling number, q is the heat flux in W/m^2 and G_{eq} and Re_{eq} are the equivalent mass velocity in $kg/s.m^2$ and Reynolds number defined as a function of the fluid vapor mass fraction x and densities of the saturated liquid ρ_l and vapor ρ_v in kg/m^3. In both evaporation and condensation, the friction coefficient and resulting pressure drops are calculated as follow

$$Re_{eq} = \frac{G_{eq}D_h}{\mu_l} \quad (5.26) \qquad G_{eq} = G\left(1-x+x\frac{\rho_l}{\rho_v}\right) \quad (5.28)$$

$$f = G_{e3}Re_{eq}^{G_{e4}} \quad (5.27) \qquad \Delta P = \frac{fG_{eq}^2}{\rho_l D_h}L \quad (5.29)$$

Experimental investigation of a plate heat exchanger

BPHEs are particularly suitable as evaporators of ORC systems in which liquids are considered as heat sources. When exhaust gases are involved, technologies such as shell and tubes or tube and fins are more suitable since they provide an increased cross sectional area on the gas side, limiting pressure drops and thus the back pressure at the exhaust of the engine. Fins and/or multi-passes are generally used to increase the heat transfer area on the gas side and try to counterbalance the effect of the low heat transfer coefficients. Indeed, *the heat transfer coefficient for the gas-side of a gas-to-liquid heat exchanger is often orders of magnitude smaller*

than the heat transfer coefficient on the liquid side [191]. Therefore the heat transfer resistance between the gas and the metal is usually the major heat transfer resistance.

On the other hand, brazed exchangers cannot be mechanically cleaned and thus are limited to non-fouling applications only. [180]. However other plate technologies are available for gas applications. Shell and plate is probably the most recent design and has unique features [180]. It combines the advantages of shell and tube and plate technologies (high mechanical integrity inherent to shell and tube and superior thermal characteristics of plate heat exchangers). A plate pack is welded together ensuring the shell side is isolated from the plate side, and there is no gasket for sealing purposes [180]. Such an evaporator has been experimentally investigated in laboratory. It consists in two plates welded together and bent into a spiral shape. More information about the component can be found in [192]. The device has been integrated into a Rankine system and connected to the exhaust pipe of a gasoline engine. Temperature and pressure measurements have been achieved at the inlet and outlet of the exchangers on both side. The mass flow rates have also been recorded. A picture and schematic of the test unit are proposed in Figure 5.4. At the end, around 40 steady-state measurement points have been achieved and are used to calibrate and validate the model of heat exchanger proposed above. The evaporator is thus modeled as a counter-flow BPHE whose plate spacing depends
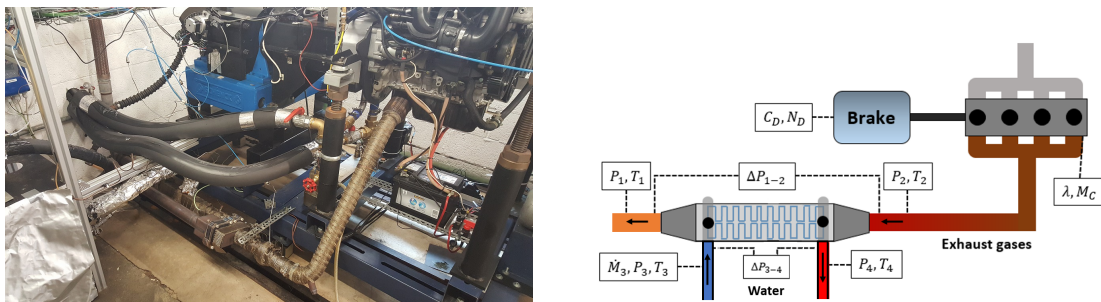
Figure 5.4 – Picture and schematic of the evaporator of the Rankine cycle connected to the exhaust pipe of the gasoline engine [192]

on whether the gas side or the working fluid side is considered. An optimization process, illustrated in Figure 5.1, is implemented so to calibrate the 2 model's parameters C and k_{sf} minimizing the weighted MAPE (5.30) between measured and predicted heat flow rates and pressure drops on the gas side. The ambient heat losses of the heat exchanger are not directly modeled and are considered as an input of the model here. This is justified by the fact the heat exchangers will be assumed thermally insulated in the ORC design process and the ambient losses will be neglected.

$$e(C, k_{sf}) = \frac{100}{N} \left(w_1 \sum_{i=1}^{N} |\frac{\dot{Q}_{hf,pred} - \dot{Q}_{hf,mes}}{\dot{Q}_{hf,mes}}| + w_2 \sum_{i=1}^{N} |\frac{P_{hf,su,pred} - P_{hf,su,mes}}{P_{hf,su,mes}}| \right) \qquad (5.30)$$

$$\min_{C,k_{sf}} e(C, k_{sf}) \begin{cases} 0 < C < 0.2 \\ 0.1 < k_{sf} < 2 \end{cases} \qquad (5.31)$$

The values of the resulting parameters C and k_{sf} are respectively 0.1 and 0.7. The validation process consists in comparing the outputs of the model with the measured heat flow rate, exhaust temperature and pressure drop on both sides of the heat exchanger. The results are presented in Figure 5.5 to 5.8. First a T-s diagram (Figure 5.5) including the saturation curves of the working fluid and the temperature profiles of the primary and secondary fluids and of the wall during the vaporization process. As it can be seen the temperature profile of the wall is close to the temperature profile of the working fluid. This is explained by the heat transfer coefficient which are 1 to 2 order of magnitude higher on the water side compared to the gas side, depending on whether water is in single or two phase state respectively.

The comparison of the pressure levels on both fluid sides between measured and predicted values is achieved in Figure 5.6 where the inlet and outlet pressures of the gas and the working fluid respectively are reported according to the corresponding measured values. The maximal absolute error on the outlet pressure of the working fluid and inlet pressure of the secondary fluid are around 0.4 and 0.008 bar respectively.

The maximal relative error between measured and predicted heat flow rates is around 3% (Figure 5.7). A maximal absolute of 10 K is also achieved on the prediction of the gas outlet temperature. The prediction of the water outlet temperature is more complex (Figure 5.8). Mean and maximal absolute errors are around 17 and 37 K respectively. Indeed, water is characterized by significantly different specific and latent heat values, compared for instance to organic fluids. Considering as an example the T-s diagram in Figure 5.5, the average pressure level in the evaporator is around 6.75 $bar A$ and the water mass flow rate is 5.6 g/s. For this pressure condition, the specific heat of the liquid and vapor phases, averaged on the temperature conditions at the inlet and outlet of the corresponding zones, are around 4.2 and 2.3 kJ/kgK. Thus, the specific energy required to increased the temperature until the saturation temperature and to reach an overheating degree around 63 K are around 56.3 and 15 kJ/kg respectively. On the other hand, the latent heat of vaporization in those conditions is around 2071 kJ/kg. Therefore the heat flow rates in the liquid, two-phase and vapor zones of the heat exchangers are respectively around 3.15, 11.5 and 0.8 kW. If the model underestimate the heat flow rate in the vapor region of 100 W for instance, it already leads to a reduction of the overheating degree of 10 K. As a consequence, the heat flow rates in the 3 zones corresponding to the 3 fluid states must be described accurately. Otherwise, small variations in the heat flow rates of each zone can lead to significant variations of the predicted water outlet temperature.

Several factors can affect those results and are mainly related to the correlations used for the calculation of the heat transfer coefficients and pressure drops on the gas and water side.
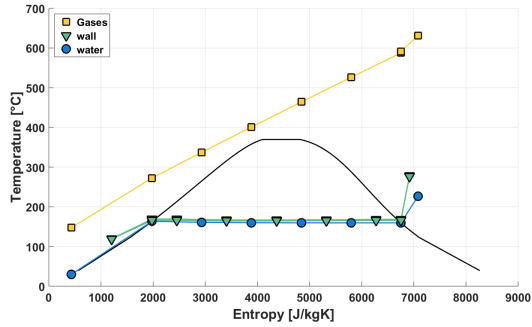
Figure 5.5 – T-s diagram of water and predictions of the temperature profiles of water, exhaust gases and metal wall along the counter-flow heat exchanger
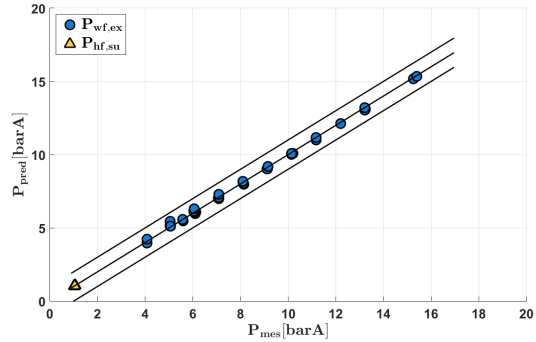
Figure 5.6 – Comparison between measured and predicted pressure values at the inlet and outlet of the heat exchanger for the gases and water respectively (with precision lines of ± 1 bar).
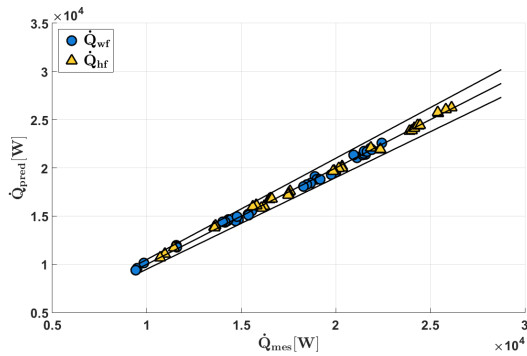
Figure 5.7 – Comparison between measured and predicted heat flow rates on both sides of the heat exchanger (with precision lines of ± 10 %)
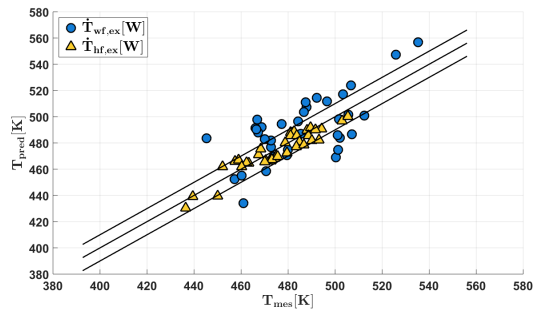
Figure 5.8 – Comparison between measured and predicted outlet temperature on both sides of the heat exchanger (with precision lines of ± 10 K)

This behavior is not expected to occur with organic fluids, the latent heat level being much more reduced, even with ethanol. This could be shown for instance using the experimental data obtained for the evaporator operated with fluid R245fa in Chapter 4 where maximal absolute error of 2K is then achieved on the outlet temperature of R245fa.

The model is thus considered valid and is integrated into the ORC system model. Caution will be taken in results regarding the outlet temperature of the evaporator when water is used as working fluid. However this behavior is also expected to be reduced when the evaporating pressure of the steam is increased.

To be used in design some modifications must be applied to the model. The heat transfer area becomes an output of the model and the corresponding input becomes the pinch-point of the heat exchanger. The length of the evaporator is computed through an iterative process on the width of the plates so to keep the pressure drop on the working fluid side under a limit fixed a priori (0.5 bar). The initial plate width is obtained based on a first estimation of the cross sectional area on the gas. The latter value is computed assuming the average Reynolds number obtained for the heat exchanger experimentally investigated is conserved for the new conditions of exhaust gas temperature and mass flow rate.

5.2.2 Modeling the expansion machines

The expansion machine is probably the most critical and the most widely investigated component of ORC systems, either through experimental studies or simulation works. Indeed, the device is responsible for the conversion of the working fluid energy content into mechanical energy at the shaft and several investigations have demonstrated the influence of the expander efficiency over the global performance of ORC system (e.g. [193], [194]). Among the existing expander technologies, none has been identified to be the optimal one ([194]), partly because the selection of the expander depends on various parameters such as compactness, cost, availability, etc. In literature, the device is often a compressor adapted to operate in expander mode. Otherwise experimental studies are done on prototypes. Most studies focus on volumetric expanders because of their ability to handle large pressure ratio while keeping the rotational speed limited. In his thesis, Declaye [44] proposed an overview of the experimental studies achieved on volumetric expanders between 1985 and 2012. Nonetheless, more recent studies have been achieved since then as it will be shown in the following. Turbo-expanders are also more and more investigated because they can handle larger mass flow rate and lead to a more important specific power.

As explained in Chapter 2, each technology has different characteristics. In order to select the most suitable expander for the WHR application, 5 of the main technologies of volumetric expanders are investigated and compared here: the scroll, screw, piston, vane and roots expanders. Few authors have compared the performance of expander experimentally (e.g. [195], [196]). Here, the 5 machines have been investigated experimentally, whether directly in the Thermodynamic laboratory of the University of Liege (scroll, screw, piston and roots expanders) or in foreign laboratory through collaborative works (vane expander). The expansion devices investigated on test rig are first described and compared. Then the measurements are used to calibrate and validate simulation models of the devices. In order to be integrated into a design optimization tool of WHR ORC system, modifications required to get design models for the expansion machines are proposed.

Scroll devices, as explained, can be classified into 2 categories: open-drive and hermetic machines. Several hermetic devices have been tested in the Liege laboratory during the past few years. They are generally refrigeration expanders modified to operate in expander (e.g.,
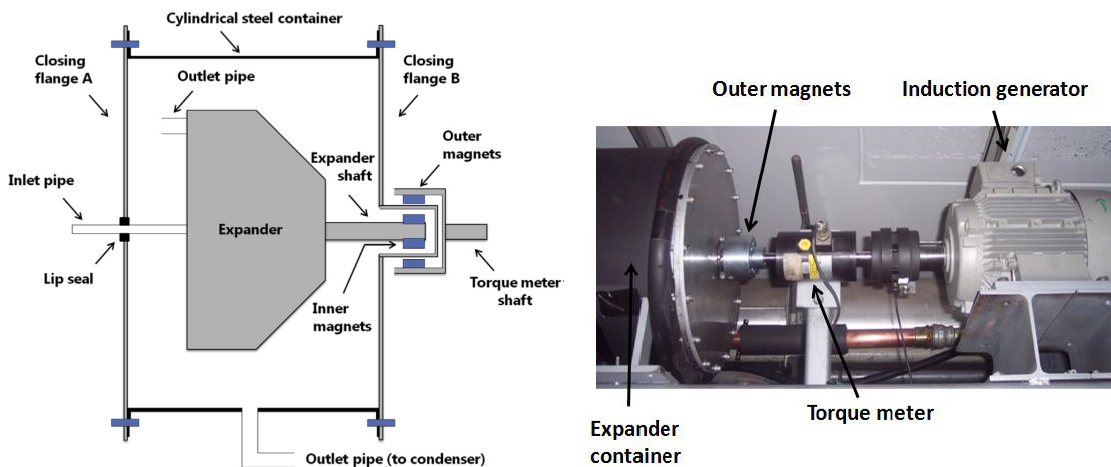
Figure 5.9 – Schematic of the open-drive scroll expander experimentally investigated [114]

[196], [197]). However the need for lubrication added to the direct coupling of the generator to the expander within the hermetic container limits largely the maximal achievable inlet temperature (130-150°C). An open-drive scroll expander has also been investigated [114] and led to much higher achievable inlet temperature (around 200°C). A schematic and a picture of the device, which is originally a 120 cm^3 air scroll compressor, are given in Figure 5.9. The volume ratio of the machine is around 4.2 and the nominal output power is 2 kW. As it can be seen, a containment strategy had to be imagined in order to avoid leakage of refrigerant to the ambient. A magnetic coupling has been installed to link the expander and the asynchronous generator shafts outside the container. More information about the components and the experimental campaign can be found in [114].

Screw expanders can also be split into 2 categories: single and twin-screw expanders. A 20 cm^3 unsynchronized twin-screw expander has recently been tested using R245fa as working fluid [198]. As for the open drive scroll-expander, the link between the expander and generator shaft is achieved through a magnetic coupling. The built-in volume ratio is around 2.5 and the nominal output power is around 2 kW. A picture of the expander-generator set is given in Figure 5.10. Detailed information about the device and the performed experiments are reported in [198].

The piston expander is a swash-plate piston expander characterized by a total cylinder capacity of 195 cm^3. The built-in volume ratio is around 5 and the nominal output power around 4 kW. The lubrication is performed by an external circuit with oil injection at mains friction points. The admission and exhaust processes of R245fa are achieved by means of a valve-less system that induces symmetric opening and closing of the cylinder volumes. The expander is connected to an asynchronous electrical motor and a four-quadrant variable-frequency drive is used to control the shaft speed. Oudkerk [199] reported all details about the prototype and the experimental work achieved.
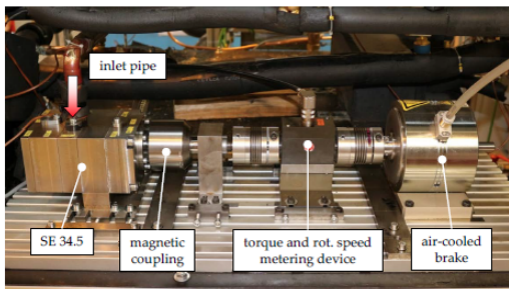
Figure 5.10 – Picture of the twin-screw expander experimentally investigated [198]
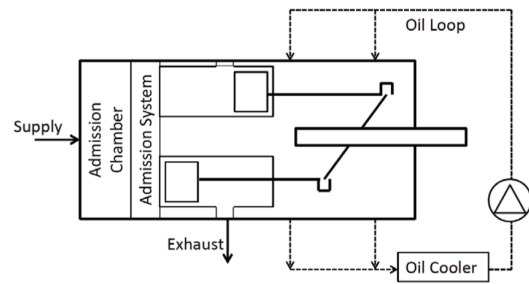
Figure 5.11 – Schematic of the swash-plate piston expander experimentally investigated [199]
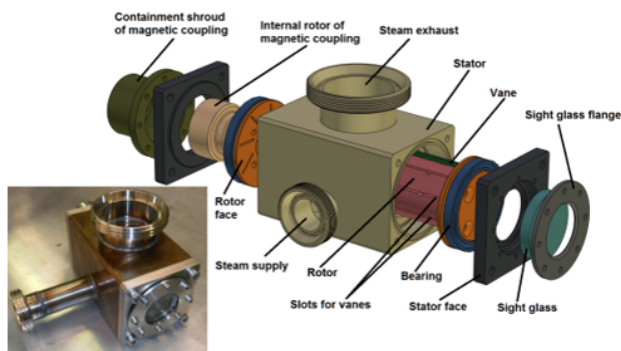
Figure 5.12 – Schematic of the swash-plate piston expander experimentally investigated [97]
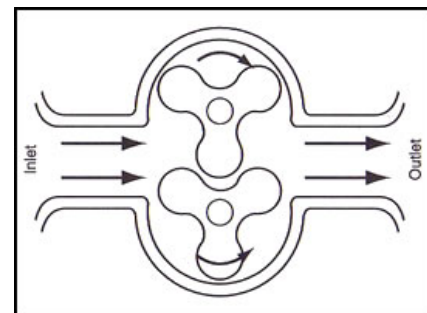
Figure 5.13 – Schematic of a roots expander

The vane expander consists of 8 chambers and an overall displacement of around 60 cm^3. The maximal inlet temperature reached with the machine was around $150°C$ using Hexamethyldisiloxane (MM) as working fluid. The nominal output power is around 1kW. Technical information about the components and experimental investigation can be found in [97].

The roots expander has a displacement of 100 cm^3. The maximal inlet temperature reached with the machine was around $150°C$ using R245fa as working fluid. The nominal output power is around 3.5 kW. Detailed information about the component and the experimental campaign can be found in [71].

All machines are thus open-drive devices. Their main characteristics are summarized in Table 5.1. Adding the turbine studied in Chapters 3 and 4, it leads at the end to 6 expansion machines to consider for the comparison.

Semi-empirical models are proposed to predict the mass flow rate, the outlet temperature and the mechanical power produced by the investigated expanders. These models retain the most important physical phenomena inherent to the expansion machine and involve a

Table 5.1 – Main characteristics of the 5 investigated volumetric expanders

Technology	Scroll	Screw	Piston	Vane	Root
Type	open-dr.	open-dr.	open-dr.	open-dr.	open-dr.
Displacement (cm^3)	29	19.96	33	61.3	100
Built-in Volume ratio	4.2	2.5	5.6	3	1.1
Nominal speed (RPM)	3000	12000	2000	3000	5000
Nominal flow rate (kg/s)	0.06	0.144	0.095	0.06	0.202
Nominal mech. power (W)	2000	3000	4000	1000	3500
Working fluid	R245fa	R245fa	R245fa	MM	R245fa

limited number of parameters (around 10) that are identified on the basis of the performance points. Studies in laboratory showed that these models can predict the performance of the expansion machines with good accuracy. Moreover, their semi-empirical nature enables to extrapolate the performance [200] of the machine for different operating conditions and design characteristics (displacement, sections of the inlet and exhaust ports, etc). The model used as starting point is the one proposed by Lemort et al. [201].

In this approach, the pressure drops at the inlet and outlet ports of the expander, as well as the internal leakage, are each modeled assuming an isentropic expansion of the flow in a simply converging nozzle followed by an isobaric diffuser converting the kinetic energy is static enthalpy. Globally the process is isenthalpic if the velocity variation between the inlet and outlet of the system is negligible. The conservation of the total enthalpy and of the mass enables to identify

- the outlet pressure of the nozzle (pressure drop) if the mass flow rate is used as input,

- the mass flow rate (internal leakage) if the outlet pressure is used as input.

The required parameters are the cross sectional areas at the nozzle throats.

$$P_{crit} = \frac{P_{su}}{2} \ (init.val.) \quad (5.32)$$

$$h_{crit} = h(P_{crit}, s_{su}) \quad (5.33)$$

$$a_{crit} = a(P_{crit}, s_{su}) \quad (5.34)$$

$$C_{crit} = sqrt(2(h_{0,su} - h_{crit}) \quad (5.35)$$

$$M_{crit} = \frac{C_{crit}}{a_{crit}} \quad (5.36)$$

$$\Delta P_{crit} = |M_{crit} - 1| \quad (5.37)$$

$$P_{thr} = max(P_{ex}, P_{crit}) \quad (5.38)$$

$$h_{thr} = h(P_{thr}, s_{su}) \quad (5.39)$$

$$C_{thr} = \sqrt{2(h_{0,su} - h_{thr})} \quad (5.40)$$

$$\rho_{thr} = \rho(P_{thr}, s_{su}) \quad (5.41)$$

$$\dot{M}_{thr} = C_{thr}\rho_{thr}A_{thr,i} \quad (5.42)$$

$$i = su, ex, leak \quad (5.43)$$

The model also considers heat transfers between the fluid and the metal wall assuming an isothermal equivalent wall. The Newton law is used to evaluate the corresponding heat flow

rates. The parameters to identify are the global heat transfer coefficients AU.

$$\dot{Q}_i = AU_i(T_{wf,i} - T_{wall}) \quad i = su, ex \tag{5.44}$$

The indicated power, resulting from the expansion of the internal flow rate, can then be evaluated. The expansion is, in the model, achieved in 2 steps, assuming an isentropic expansion until the adapted pressure, which corresponds to the built-in volume ratio of the machine, followed by a constant machine volume expansion or compression according to pressure conditions on both side of the machine (under or over expansion).

$$\dot{M}_{in} = \dot{M} - \dot{M}_{leak} \tag{5.45}$$
$$\dot{W}_{in} = \dot{M}_{in}(w_s + w_V) \tag{5.46}$$

The output power at the shaft is computed from the internal power and the mechanical losses, which can be calculated based on 1 to 3 parameters.

$$\dot{W}_{loss} = \dot{W}_{loss,0} + K_{loss,0}N_{exp} + \alpha \dot{W}_{in} \tag{5.47}$$
$$\dot{W}_{sh} = \dot{W}_{in} - \dot{W}_{loss} \tag{5.48}$$

Finally, the ambient losses are computed based on an additional heat transfer coefficient between the wall and the ambient while the energy balance over the equivalent isothermal wall leads to the temperature of the latter.

$$\dot{Q}_{amb} = AU_{amb}(T_{wall} - T_{amb}) \tag{5.49}$$
$$\dot{Q}_{amb} = \dot{Q}_{su} + \dot{Q}_{ex} + \dot{W}_{loss} \tag{5.50}$$

For the piston expander, the compression of the remaining fluid in the cylinder (clearance volume) after the closing of the outlet valve has to be considered. As the expansion, the process is split in 2 steps, assuming an isentropic compression followed by a constant machine volume compression.

The isentropic effiency, based on the mechanical power at the shaft, and the filling factor of the machine are evaluated as follow.

$$\epsilon_{g,exp} = \frac{\dot{W}_{sh,exp}}{\dot{M}_{wf,exp}(h_{wf,su,exp} - h_{wf,ex,s,exp})} \qquad \Phi_{f,exp} = \frac{\dot{M}_{wf,exp}}{\rho_{wf,su,exp}N_{rot,exp}V_{s,exp}} \tag{5.52}$$
$$\tag{5.51}$$

A optimization tool is developed in order to, for each expansion machine, calibrate the model

parameters minimizing the MAPE (5.53) between the model outputs and the measurements.

$$e(p) = \frac{100}{N}\left(w_1 \sum_{i=1}^{N} |\frac{\dot{W}_{sh,pred} - \dot{W}_{sh,mes}}{\dot{W}_{sh,mes}}| + w_2 \sum_{i=1}^{N} |\frac{\dot{M}_{wf,pred} - \dot{M}_{wf,mes}}{\dot{M}_{wf,mes}}|\right) \quad (5.53)$$

$$+ w_3 \sum_{i=1}^{N} |\frac{T_{wf,ex,pred} - T_{wf,ex,mes}}{T_{wf,ex,mes}}|\Big) \quad (5.54)$$

$$\min_{p} e(p) \left\{ \; p_{min} < p < p_{max} \right. \quad (5.55)$$

The resulting parameters are given in table 5.2.

Table 5.2 – Model parameters of the 5 investigated volumetric expanders

Technology	Scroll	Screw	Piston	Vane	Roots
$D_{su}(mm)$	4	6.2	3.5	13	14.3
$D_{ex}(mm)$	17.5	50	9.5	12.5	25
$A_{leak}(mm^2)$	1	8.02	1.22	14.3	35
$R_{v,in}(-)$	4.2	2.5	5.6	3	1.1
$\dot{W}_{l,0}(W)$	0	0	0	0	0
$K_{l,0}(-)$	0.09	0.05	0.13	0	0.16
$T_{l,0}(Nm)$	0	0	0.000065	0.87	0
$AU_{su}(W/K)$	7.5	32.7	6.7	8	9.7
$AU_{ex}(W/K)$	5.8	35.67	15	7.75	4.9
$AU_{amb}(W/K)$	5.8	5.5	5.5	3.5	5

The quality of the models is assessed comparing the outputs of the model with the measurements. This is performed for the five machines together in 5.14, 5.15, 5.16 for the shaft power, rotational speed and outlet temperature. The rotational speed, normally an input of the model, has been set as output instead of the mass flow rate (Figure 5.17), which is now an input, to reduce the computational time during the optimization process. The mean relative error on the speed and power prediction is around 6 %. The maximal error on both outputs reaches 15 % for the vane expander model. The outlet temperature is generally predicted within a 10 K absolute error.

The models are used to extrapolate the performance of each expander for its nominal speed (Figure 5.18). A constant 5 K overheating and an ambient temperature of $25°C$ are considered while the pressure ratio is varied increasing the inlet pressure of the expander for a given outlet pressure (e.g. 3 barA with R245fa). It can be seen the scroll expander presents the highest isentropic efficiency with a maximal value above 75 % around the adapted pressure ratio. The efficiency decreases slowly with the pressure ratio (under-expansion region) and remains above 60 % for a pressure ratio of 15. The main source of losses of the expander typically results
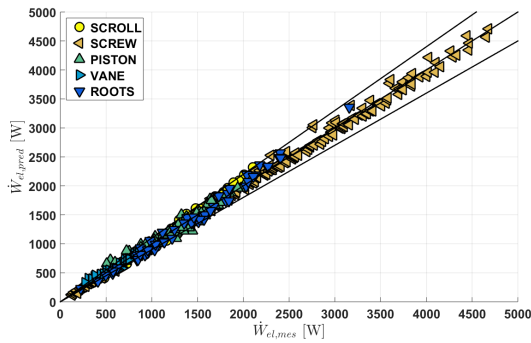
Figure 5.14 – Comparison between measured and predicted shaft power production of the 5 expander technologies (with precision lines of ± 10 %)
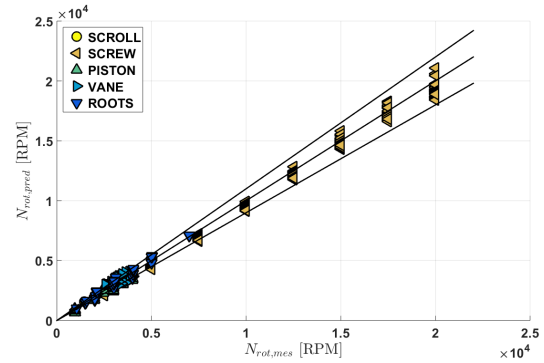
Figure 5.15 – Comparison between measured and predicted rotational speed of the 5 expander technologies (with precision lines of ± 10 %)
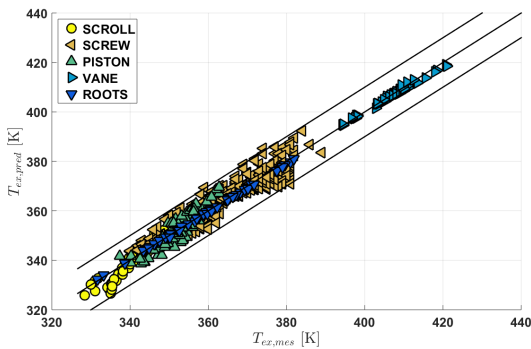
Figure 5.16 – Comparison between measured and predicted outlet temperature of the 5 expander technologies (with precision lines of ± 10 K)
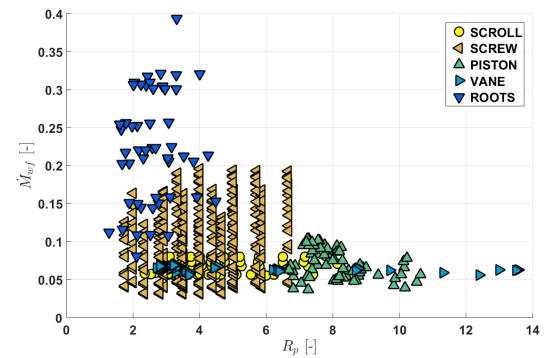
Figure 5.17 – Evolution of the measured mass flow rate with the pressure ratio for the 5 expander technologies

from the internal leakage. However, even without lubricant and with a limited rotational speed, the impact of the loss is reduced. The screw expander efficiency follows the same trends as the scroll efficiency but the maximal value is now around 65%. For a pressure ratio of 15 the efficiency drops until 50 %. As the scroll expander, the main source of losses of the screw device is the internal leakage. The use of a lubricant and the possibility to reach high rotational speed (compared to scroll expander) enable to reduce the loss. The piston expander shows a maximal efficiency slightly above 50 %. This low value compared to scroll and screw machines is due to high mechanical losses, because of the high number of moving parts, but also due to a high clearance volume (around 10 % of the displacement) which leads to a important work of compression. The clearance volume also limits the mass of fluid entering in the machine during the admission process. The filling factor reaches values between 0.2 and 0.5. The actual adapted pressure of the piston expander seems larger than pressure corresponding to

built-in volume ratio of the machine because of the important pressure drops in the valve system, which also reduces the indicated power. Reducing the clearance volume from 10 to 2 % and bringing the friction torque parameter to 0 would lead to a machine with an isentropic efficiency profile comparable to the one achieved with the screw expander. The vane expander was tested with MM contrary to the other machines which were tested with R245fa. The maximal isentropic efficiency achieved by the machine is around 45 %. The main losses, according to the model are the leakage losses. An important leakage path is apparently present in the machine, whether between the vanes and the stator housing, whether between the vanes and the rotor in the vanes slots. The filling factor reached is therefore high, around 1.4. The roots expander is characterized by no built-in volume ratio and shows a maximal efficiency of 43 % for a pressure ratio between 1 and 2. The main reason for this low value is the large internal leakage flow rate between the roots and between the roots and the housing. The filling factor reached is also high, around 1.2. All the expanders are also characterized by reduced performance in the over-expansion region. The isentropic efficiency rapidly decreases when the pressure ratio decreases under the adapted pressure ratio corresponding to the built-in volume ratio of the machine During design, the displacement becomes an output of the model
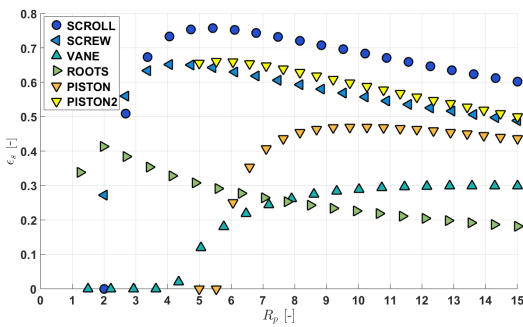
Figure 5.18 – Evolution of the isentropic efficiency at nominal speed of the the 5 expander technologies with the pressure ratio
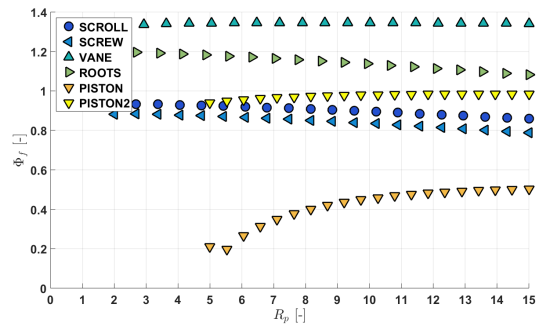
Figure 5.19 – Evolution of the volumetric efficiency at nominal speed of the the 5 expander technologies with the pressure ratio

so the rotational speed of the machine has to be imposed. The model parameters of the new machine have also to be identified. To this end, performance indicators are defined for each source of losses presented above. For each loss parameter corresponds 1 indicator. The latter are then evaluated on the operating point corresponding to the maximal efficiency at nominal speed for each expander. Assuming the new expander must be at least as efficient as the device investigated on test rig, the indicators are conserved during the design of the new machine and then enable to evaluate the new loss parameters. The preponderant sources of losses in the volumetric expander experimentally investigated are the internal leakage and mechanical losses. The leakage area can be easily identified by conservation of the filling factor on the design point. Concerning the coefficients of the mechanical losses correlation, the friction mean effective pressure (fmep) is defined by analogy with Internal Combustion Engines (ICE) [175]. In order to compare the work delivered by engines together and independently from their capacity, mean effective pressures (e.g. brake mean effective pressure, indicated effective

pressure, friction mean effective pressure), ratio of a power (e.g. shaft power, indicated power, mechanical power loss) and the engine capacity, product of the engine displacement and speed, are used. The fmep is often modeled through correlations taking into the account the main influential parameters. In ICE, these parameters are typically the rotational speed and the peak pressure (load). Nonetheless, Taylor [202] also considered a term proportional to the total indicated work, defined as the sum of the work produced during the expansion and the work consumed during the compression [45]. Regarding the inlet and outlet pressure drops, relative pressure drop defined as the ratio of the pressure loss over the corresponding absolute pressure are conserved to size the nozzle throats. Finally the heat losses are expressed through a heat exchange effectiveness for instance based on the $\epsilon - NTU$ method. Those effectiveness are conserved to evaluate the new global heat transfer coefficients.

$$\Phi_f = \frac{\dot{M}_{in} + \dot{M}_{leak}}{\dot{M}_{th}} \tag{5.56}$$

$$K_{fmep,0} = \frac{\dot{W}_{l,0}}{\frac{N_{rot}}{60} V_s} \tag{5.57}$$

$$K_{fmep,1} = \alpha \tag{5.58}$$

$$K_{fmep,2} = \frac{2\pi T_{l,0}}{V_s} \tag{5.59}$$

$$fmep = K_{fmep,0} + K_{fmep,1} \frac{\dot{W}_{in}}{\frac{N_{rot}}{60} V_s} + K_{fmep,2} \tag{5.60}$$

$$\dot{W}_{loss} = fmep \frac{N_{rot}}{60} V_s \tag{5.61}$$

$$\frac{\Delta P_i}{P_i} = c_{ste} \quad i = su, ex \tag{5.62}$$

$$\epsilon_i = 1 - \exp \frac{-AU_i}{\dot{M}cp_i} \quad i = su, ex \tag{5.63}$$

The design procedure adopted for the 5 volumetric expanders is summarized in Figure 5.20.

Finally it should be noted that the comparison between the different types of expander can not be entirely objective since they are characterized by different levels of maturity. Scroll compressors have been produced in large series for many years and have reached a commercial maturity. On the other hand, the tested piston, screw, vane and roots expanders are prototypes whose performance could evolve in the future. Nonetheless, scroll compressors are not designed to be operated in expander mode meaning potential sources of improvement can also be found.
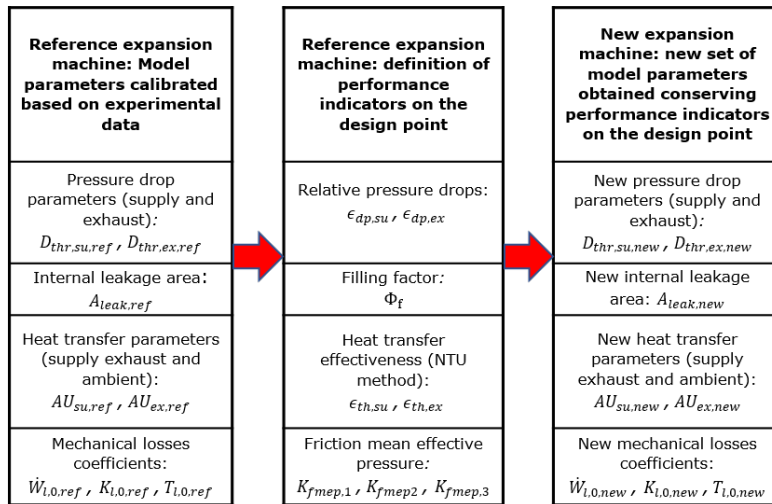
Figure 5.20 – Design procedure based on the models developed for the 5 volumetric expander technologies

5.2.3 Modeling the pump

While it is not often considered in literature, the pump is a key component of the ORC system. In his thesis, Declaye [44] reviewed several publications dedicated to pump systems. He showed only a limited number of authors have experimentally investigated pump system performance into details. Otherwise authors generally focused on the other ORC components and a constant efficiency is often considered in numerical studies. Nonetheless, the pump efficiency can deeply affect the performance of the overall unit and it seems today unlikely to operate without it. Indeed, Declaye also presented studies in which the pump has been removed and the mass flow rate along the ORC system results from a density gradient going from the evaporator to the condenser. However only limited performance have been achieved until now. From this state of the art, a maximal isentropic efficiency of 81 %, based on the pump mechanical power consumption, has been reached by Lin [203] with a piston pump operating with water as working fluid.

In addition, Declaye also experimentally investigated 5 different pump technologies: a single-membrane, a multi-membrane, a gear, a plunger and an open piston pump. More information about the test-rigs and sensor properties can be found in the document. All machines together, the maximal achieved isentropic efficiency was around 50%. This includes however, the loss of the driving and speed regulation systems. In laboratory, the pump is typically coupled to an electrical motor whose rotational speed can be regulated through a variable frequency drive. Those devices are leading to additional irreversibilities particularly in part load operation. One of the keys for an increased output power from a waste heat recovery ORC system might well be, among others, to propose an alternative to the electric motor for the pump system. A mechanical coupling with the engine shaft could be envisaged. Declaye also proposed a direct coupling of the pump and turbine shafts. However those solutions also imply an increase in

the complexity of the regulation of the working fluid mass flow rate. Other alternatives could be imagined and one in particular is introduced in the final Chapter of this thesis.

The open piston pump put aside because of sealing issues, the multi-membrane pump, Hydracell G10, experimentally investigated in Chapter 3 can be added to the pump comparison performed by Declaye. In this regard, the main characteristics of the 5 pumps are gathered (Table 5.3) and models are built and validated against experimental data.

Table 5.3 – Main characteristics of the 5 investigated volumetric pumps

Technology	Diaphragm	Multi-diaphragm		Gear	Plunger
Manufacturer	Doseuro	Wanner Hydracell		Viking	Hypro
Model	B250N40B	G13XKB	G10XKC	SG80550	5315C-CX
Nominal speed [RPM]	120	725	1450	1450	1450
Nominal flow rate (l/s)	0.058	0.48	0.081	0.105	0.2517
Max. Outlet pressure ($barA$)	11	70	70	34	207
Max. Temperature (°C)	60	120	120	230	70
Weight (kg)	26	12.7	22	3.2	9
Working fluid	R245fa	R245fa	R245fa	R245fa	R134a
Flow regulation	Displacement	VFD	VFD	VFD	VFD
Motor nominal power (kW)	0.55	0.37	3	0.75	1.5

Because the considered pumps are volumetric devices, a similar modeling approach as the one proposed for the expansion machines is used. Considering the leakage, mechanical and electric conversion losses while putting aside the limited pressure drop losses at the inlet and outlet ports of the system and neglecting the compressiblility effects, an explicit model can be achieved. In theory, the P-V diagram of volumetric pumps is rectangular and the total power required to pump the fluid is calculated based on the volumetric flow rate and the pressure difference between the inlet and outlet of the device. It is the power required to reach the desired hydraulic height considering the pressure drops in the installations.

$$\dot{W}_t = \dot{V}_{wf}\Delta P_t = \dot{V}_{wf}\Delta P_{hyd} + \xi_{pipe} \tag{5.64}$$

However in practice, the power required at the pump shaft is larger in order to overcome the different losses of the pump. The efficiency that consider all the pump losses into account is called the hydraulic efficiency and can defined as the product of the piping efficiency and the pump efficiency. The latter can in turn be desegregated as the product of the

- volumetric efficiency: taking into account the internal leakage in the pump,

- indicated efficiency: taking into account the pressure losses through the pump inlet and outlet ports,

- mechanical efficiency: taking into account the friction losses in the moving parts of the pump

When connected to an electric motor driven by a VFD, additional conversion efficiencies for both devices have to be considered in order to evaluate the global efficiency of the pump-motor-VFD system. In this study, the volumetric efficiency is defined as the ratio of mass flow rate entering the machine and the sum of this mass flow rate and the leakage flow rate. The isentropic efficiency is defined as a global efficiency of the pump-motor-VFD system. The piping efficiency of the ORC is not considered and the pressure drops in the pump inlet and outlet ports are neglected. At the end 3 calibration parameters need to be identified, the leakage area, A_{leak}, and 2 parameters for the electro-mechanical losses, $\dot{W}_{l,0}$ and $K_{l,0}$.

$$N_{pp} = \frac{\dot{M} + A_{leak}\sqrt{2\rho_{su}(P_{ex} - P_{su})}}{60V_s\rho_{su}} \tag{5.65}$$

$$\epsilon_v = \frac{\dot{M}}{\rho_{su}\frac{N_{rot}}{60}V_s} \tag{5.66}$$

$$\dot{W}_t = \frac{\dot{M}}{\rho_{su}(P_{ex} - P_{su})} \tag{5.67}$$

$$\dot{W}_{pp} = \dot{W}_{l,0} + (1 + K_{l,0})\dot{W}_t \tag{5.68}$$

$$\epsilon_s = \frac{\dot{M}(h_{ex,s} - h_{su})}{\dot{W}_{pp}} \tag{5.69}$$

As for the expander models, the calibration of the pump models is achieved minimizing the weighted MAPE between the predicted outputs of the model and the corresponding measured values of electric power consumption, mass flow rate (or rotational speed) and exhaust temperature. The validation is achieved comparing the predicted outputs with the measured values. It is done in figures 5.21 to 5.23 for the 5 investigated pumps. The model parameters are given in table 5.4.

Table 5.4 – Model parameters of the 5 investigated volumetric pumps

Technology	Diaphragm	Multi-diaphragm		Gear	Plunger
Manufacturer	Doseuro	Wanner Hydracell		Viking	Hypro
Model	B250N40B	G13XKB	G10XKC	SG80550	5315C-CX
$A_{leak}(mm^2)$	0.01	0.01	0.48	0.52	0.62
$\dot{W}_{l,0}(W)$	180	300	87.5	109	217
$K_{l,0}(-)$	0.35	0.15	0.69	1.9	0.6

The prediction of the electric power consumption (Figure 5.21), all pumps together, leads to average and maximal relative error around 2.4 % and 7.8% respectively. As for the expander models, the rotational speed is chosen as output instead of the mass flow rate and the obtained maximal and average relative errors on the speed prediction (Figure 5.22) are around 5.3 and

1.4 % respectively. Finally the maximal and average errors on the prediction of the working fluid temperature (Figure 5.23) are both below 0.3 K.

Based on the model, the efficiency of each pump can be evaluated according to pressure difference between the outlet and inlet of the pump. This is achieved in Figure 5.25 considering the nominal speed of each pump. For the single diaphragm pump, the swept volume is set at the maximum. The inlet pressure is kept constant and the outlet pressure is progressively increased taking the limitations on the outlet pressure of table 5.3 into account. As it can be observed, the achieved isentropic efficencies are relatively low. The maximal values are reached with the multi-diaphragm pump G10, which has been studied in Chapter 3. A maximal value around 54 % is achieved for a pressure difference of 28 bar with working fluid R245fa.
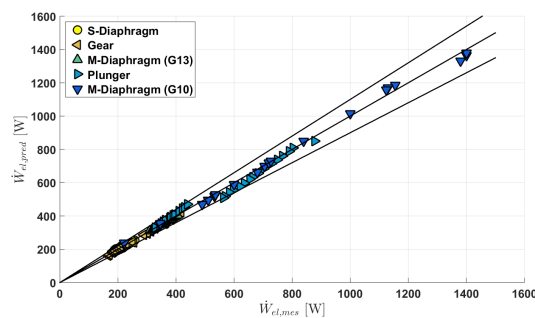
Figure 5.21 – Comparison between measured and predicted electric power consumption of the 5 investigated pumps (with precision lines of ± 10%)
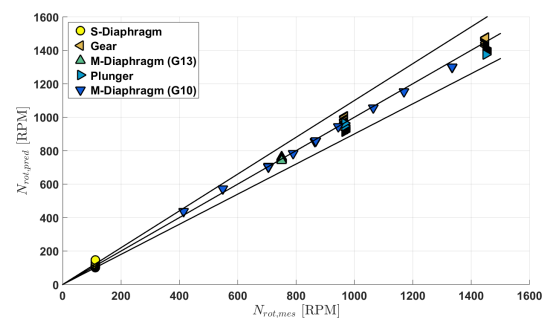
Figure 5.22 – Comparison between measured and predicted rotational speeds of the 5 investigated pumps (with precision lines of ± 10%)
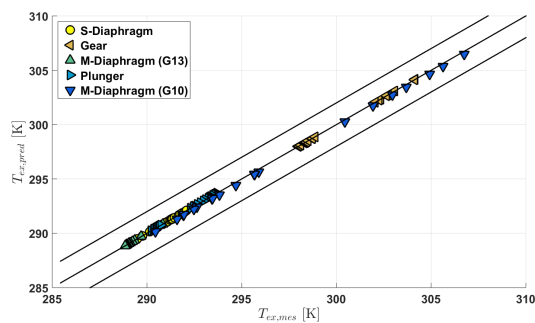
Figure 5.23 – Comparison between measured and predicted outlet temperatures of the 5 investigated pumps (with precision lines of ± 2 K)
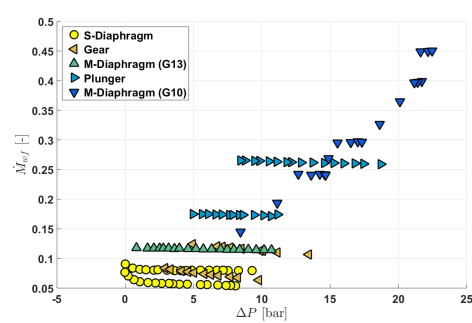
Figure 5.24 – Evolution of the mass flow rates reached with the 5 pumps with the pressure difference

The pump metallic head of the G10 pump also leads to an higher limit of outlet pressure compared to other technologies. The polymer in used also enable an higher temperature level compared to the other pump single-diaphragm and plunger technologies. For all these
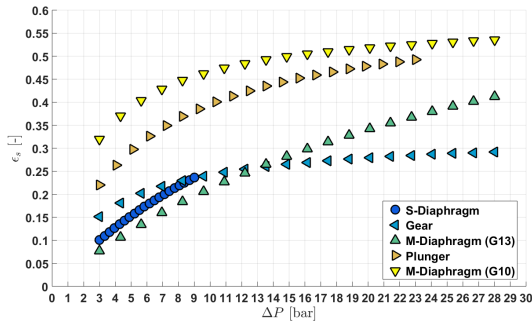
Figure 5.25 – Evolution of the isentropic efficiency at nominal speed of the 5 pumps with the pressure difference
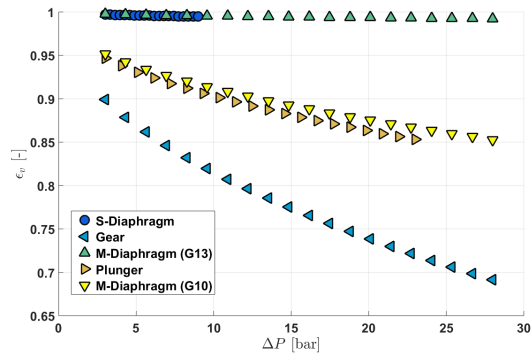
Figure 5.26 – Evolution of the volumetric efficiency at nominal speed of the 5 pumps with the pressure difference

reasons it is proposed to size the pump of the ORC system based on the model of the pump G10. By analogy with the expander models, the volumetric efficiency and 2 terms of friction mean effective pressure are identified based on the measurement point leading to the maximal isentropic efficiency. Those values are conserved on the design point of the new pump so to identify the parameter set (A_{leak}, $\dot{W}_{l,0}$ and $K_{l,0}$) of the corresponding model.

5.2.4 Modeling the complete ORC systems

The global model of the system is obtained by interconnecting the component models together. The inputs of the model are the inlet conditions of mass flow rate and temperature of the heating and cooling fluids. The evaporating pressure and the overheating degree are also selected as inputs. The outputs are the thermodynamic state at each point of the cycle as well as the heat flow rates on both sides of the exchangers and the mechanical power of the rotating machines. The resolution of the model is an iterative process that involves 2 to 5 iteration variables according to the architecture complexity. The model procedure is given in Figure 5.27 for the most simple of the investigated configurations, which involves a single heat source. In that case, it is proposed to iterate on the mass flow rate and the condensing pressure until converging on 2 criteria related to the heat exchangers. Those criteria vary according to the model configuration. In design mode, the pinch point of the heat exchangers are defined as optimization variables, as it will be seen. They are thus used to converge on both variables. In simulation mode, the heat transfer areas of the evaporator and condenser are known and are then used to solve the system. The system model also requires the parameters of each component model. Those are the heat transfer parameters of the heat exchanger and the loss parameters of the rotating machines discussed above. Finally, additional outputs are available for the various components and they vary according to system model configuration (design or simulation mode). In design, the model provides the heat transfer areas of the heat exchangers as well as the displacements of the pump and expander (or the turbine dimensions). The rotational speeds of the pump and expander are then imposed. In simulation, the model

provides the pinch-points of the heat exchangers and the rotational speeds of the pump and expander, the geometry of the component (heat transfer areas and displacement or cross section area of the nozzle throat) being known. In practice, pump and expander speeds are the 2 main degrees of freedom for the operator of an ORC system. The regulation of the pump speed enables to control the overheating degree at the expander inlet while the regulation of the expander speed (in the case of volumetric machines) enables to control the evaporating pressure for given working fluid mass flow rate and heat input. However, the model is numerically more robust when using directly the evaporating pressure and working mass flow rate as inputs.
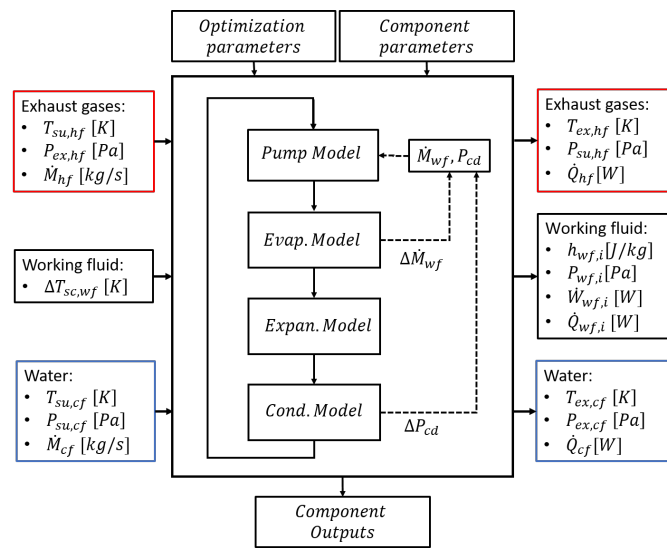
Figure 5.27 – Schematics of the ORC system model using 1 heat source

The main assumption for the evaluation of the performance in design and off-design is the sub-cooling degree at the outlet of the condenser which is imposed to 5K. This assumption is relevant during the design phase. In simulation, however, it should be relaxed and the sub-cooling degree should become an output of the model and calculated, for instance applying the mass conservation of the working fluid used in the system. Nonetheless, this calculation would largely increase the computational time during the optimization phase without providing a significant increase in the prediction accuracy of the performance of the system at this stage. During the dynamic investigation, the assumption will be released.

Economic model

The objective of the design optimization process is the minimization of the specific investment cost (SIC), defined as the ratio between the Total Investment Cost (TIC) and the net power output of the system. The TIC is calculated following the procedure proposed in [204] and [205] in the case of ORC plants and adapting the assumption to a small scale WHR ORC. The TIC is the sum of the Direct Costs (DC) and Indirect Costs (IC). In the DC can be found

the cost of the system components (C_{syst}), of the fluid (C_{wf}), of the piping (C_{piping}) and of the instrumentation and control of the system ($C_{instr,ctrl}$). The IC are mainly composed of the engineering (C_{eng}) and contingency costs (C_{cont}). Except for the cost of the system, assumptions are achieved for the DC and the IC based on discussion with manufacturers. They are described in equation 5.72 to 5.77. The cost of the ORC systems is calculated based on the cost estimation of the components, which was achieved from available data. These costs are listed in Table 5.5.

$$C_{syst} = C_{PP} + C_{HX,EGR} + C_{HX,EG} + C_{HX,EGR2} + C_{EXP} + C_{HX,CD} + C_{LTC} \qquad (5.70)$$

$$C_{instl} = 0.3 C_{syst} \qquad (5.71)$$

$$C_{piping} = 0.15 C_{syst} \qquad (5.72)$$

$$C_{instr,ctrl} = 0.2 C_{syst} \qquad (5.73)$$

$$DC = C_{syst} + C_{wf} + C_{instl} + C_{piping} + C_{instr,ctrl} \qquad (5.74)$$

$$C_{eng} = 0.08 DC \qquad (5.75)$$

$$C_{cont} = 0.15 C_{eng} \qquad (5.76)$$

$$IC = C_{eng} + C_{cont} \qquad (5.77)$$

$$TIC = DC + IC \qquad (5.78)$$

The costs of the expansion machine technologies are estimated using Solidworks software [206]. 3D sketches have been performed or directly used when available, to establish the list of the main parts of the machines and to evaluate their cost as a function of the displacement of the expander. The process has been achieved assuming the type of material, the fabrication process and a serial production of 20.000 machines per year. Stainless steel material has been selected for parts directly in contact with the working fluid while carbon steel has be chosen for the other so to decrease the price. Molding process has generally been preferred to machining in order to reduce the fabrication costs. The detailed description of the component costs is given for the piston expander in Appendix D. Curves are shown in Figure 5.28 for the cost each of the 6 expander technologies as a function of the characteristic length defined as the cubic root of the displacement for the volumetric machines and the rotor diameter for the radial-inflow turbine (RIT).

Optimization variables an constraints

As explained, the selection process is split in 3 steps. First the most suitable design conditions are identified. Then the design is made through a thermo-economic optimization. Finally the performance are optimized in off design to evaluate the power output and fuel economy obtained with the systems. In each of those 3 steps different optimization variables and
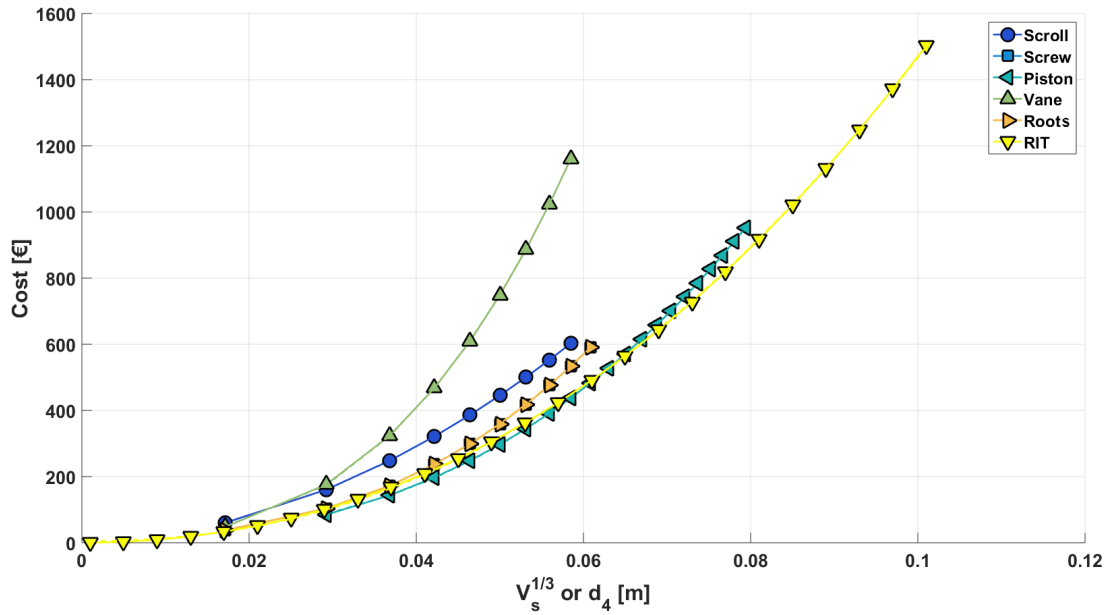
Figure 5.28 – Evolution of the cost of the 6 investigated expansion machines as a function of the characteristic length

Table 5.5 – Cost models of the ORC system components

Component	Dependent variable	Cost (€)
Heat exchanger	M_{HX}: Metal mass (kg)	
Plate HX		$C_{HX} = 250 + 5.M_{HX}$
Volumetric Expander	Discharge volume (cm^3)	
Scroll		$C_{EXP} = 21.556 V_{s,cp}^{0.6271}$
Screw		$C_{EXP} = 10.445 V_{s,cp}^{0.7342}$
Piston		$C_{EXP} = 6.0999 V_{s,cp}^{0.8095}$
Vane		$C_{EXP} = 11.111 V_{s,cp}^{0.8716}$
Roots		$C_{EXP} = 10.445 V_{s,cp}^{0.7342}$
Turbo expanders	Rotor diameter (m)	
Radial inflow turbine		$C_{EXP} = 164337.68 d_4^{2.08}$
Pump	Consumed Power (W)	
		$C_{PP} = 150 * (\frac{\dot{W}}{300})^{0.25}$
Low temperature circuit	none	200
Working fluid	M_{wf}: Mass (kg)	
R245fa		$C_{wf} = 25 M_{wf}$
Ethanol		$C_{wf} = 1.096 M_{wf}$
Water		$C_{wf} = 0.124 M_{wf}$

constraints are involved. When *selecting the design conditions,* a simplified model of the expansion machine is used. The number of optimization variables is thus reduced. The

overheating degree is fixed while the evaporating pressure as well as the pinch-point of the heat exchangers are optimized to minimize the specific investment cost. The constraints mainly concern the temperature of the gases at the outlet of the heat exchangers. This temperature must be kept above a limit, considered here at $100°C$, to avoid the condensation of acids. The return temperature of the EGR gases has also to be maintained below a certain level to limit the impact of the waste heat recovery system on the NOx reduction strategy. In this work, $120°C$ is selected as the upper limit. The maximal pressure of the system is limited to 32 bar while a minimal pressure of 1 bar is imposed. The gas mass fraction of the working fluid at the end of the expansion is also characterized by a lower limit. A minimal vapor quality of 0.85 is selected. The optimization of the pinch-point of the heat exchangers affects the size of the corresponding heat transfer surface. typically, the lower the pinch-point, the larger the heat transfer area. This also implies an additional weight that should be limited for a mobile application. Because the geometry of the heat exchanger is considered in the model, it is possible to evaluate the weight of the devices based on the heat transfer area and the geometric characteristics. In this work, the weight of the heat exchangers is limited to 60 kg. Finally, even if typically oversized, the radiator at the front end of the truck, or more generally, the heat rejection capacity of the truck is limited. Above a defined temperature level of the engine coolant (around $90°C$), the fan is activated to increase the mass flow rate of the cooling air. The fan is an important power consumer whose activation should be limited as much as possible to avoid consuming a part of the output power of the waste heat recovery system. For this reason the heat rejection at the condenser of the ORC system should be limited. A limit of 50 kW is considered in this work. It can be noted that the typologies involving the recirculated gases as heat source present an advantage regarding this constraint since the gases are already cooled down using water in the basic version of the truck (without WHR system).

When considering the detailed models in the *design phase*, additional optimization variables and constraints can be considered. The overheating degree is now optimized. The impact of the overheating on the expander performance is often limited, particularly for volumetric machines. The turbine efficiency increases with the TIT but this effect remains marginal compared to effect of the pressure ratio and rotational speed. Nonetheless, for given operating conditions,the overheating is a direct image of the working fluid mass flow rate and, in the design phase, therefore influence the size of the heat exchangers and the other ORC components. For volumetric expanders, the built-in volume ratio and the rotational speed can be optimized. For turbine, the built-in volume ratio is replaced by the flow coefficient. The inlet temperature, the built-in volume ratio (resp. the flow coefficient), the rotational speed and the pressure ratio are generally limited for each volumetric (resp. turbine) machine technology. Constraints are also considered for the blade angles and dimension of the turbine. The considered validity ranges for all these parameters are summarized in 5.6.

Finally during the *off-design optimization*, the geometry of the components is fixed and the pinch-point of the heat exchanger become outputs of the model. In practice, the rotational speeds of the expander and pump should be regulated to optimize the evaporating pressure and working fluid mass flow rate (or overheating degree) respectively. However, it is proposed

to optimize directly the latter values and set the rotational speeds of the two components as outputs to improve the robustness of the numerical model.

Table 5.6 – State of the art performed for the expansion machine technologies

Expander technology	Scroll	Screw	Piston	Vane	Roots	RIT
Rotational speed range ($kRPM$)	0.5-10	0.5-25	0.5-6	0.5-4	0.5-20	5-350
Maximal inlet temperature ($^\circ C$)	250	490	500	165	165	550
Range of built-in volume ratio (-) (or wheel diameter)	1.5-4.9	2.5-6	3-14	2-4.5	1-1.1	0.1-0.5
Maximal pressure ratio (-)	25	50	50	20	20	9

5.3 Selection of the design conditions

The first step of the design process is the selection of the design conditions. To this end, the frequency distribution of the pairs engine torque, engine speed over the driving cycle is mapped. In this study, 5 torque and 6 speed levels are considered, which leads to 17 operating points. For each of these points, the systems are designed based on a model including a simplified version of the expansion machine (only considering over- and under-expansion losses). The overheating degree and the built-in volume ratio of the expander are fixed and the evaporating pressure and the pinch-point of the heat exchangers of the various typologies are optimized for the investigated working fluids so to minimize the specific investment cost of the system. The mass of the heat exchangers is constrained to a limit of 60 kg while the pressure is limited to a maximum of 32 bar based on the information coming from a truck manufacturer. Then the power produced by each topology is maximized in off-design for the other 16 operating points, still optimizing the evaporating pressure. Finally, for each of the 17 systems designed, an average is performed on the power produced and weighted over the 17 points using the frequency distribution so to identify the most promising design conditions for each topology and each fluid. Results are shown in Figure 5.30 where the specific investment cost is drawn against the heat flow rate available in the gases for 3 typologies using ethanol as working fluid and 2 values of built in volume ratios. As it can be seen, the curves passe through a minimum which should be selected as design point. However, values of SIC on the right of this minimum remain close to minimal value for each curve. So the most important trend is to avoid the 6 operating points corresponding to a lower heat level available in the gases.

5.4 Design phase: thermo-economic optimization

This study is a prediction work, which is obviously limited by the assumptions made. On the other hand, a higher accuracy would require more complex and deterministic models of the ORC components (CFD). However, it would also lead to unacceptable calculation times at this stage because of the number of typologies to investigate and the number of optimization to perform. Here a good trade-off between accuracy and calculation time is expected because of
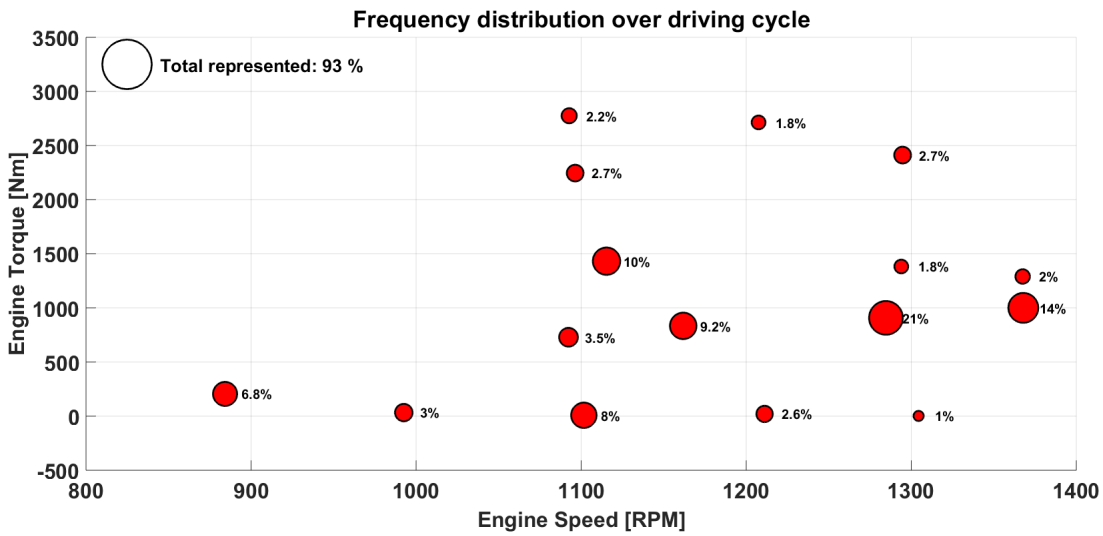
Figure 5.29 – Frequency distribution of the engine operating point in terms of torque according to the rotational speed based on the definition of 5 torque and 6 speed levels
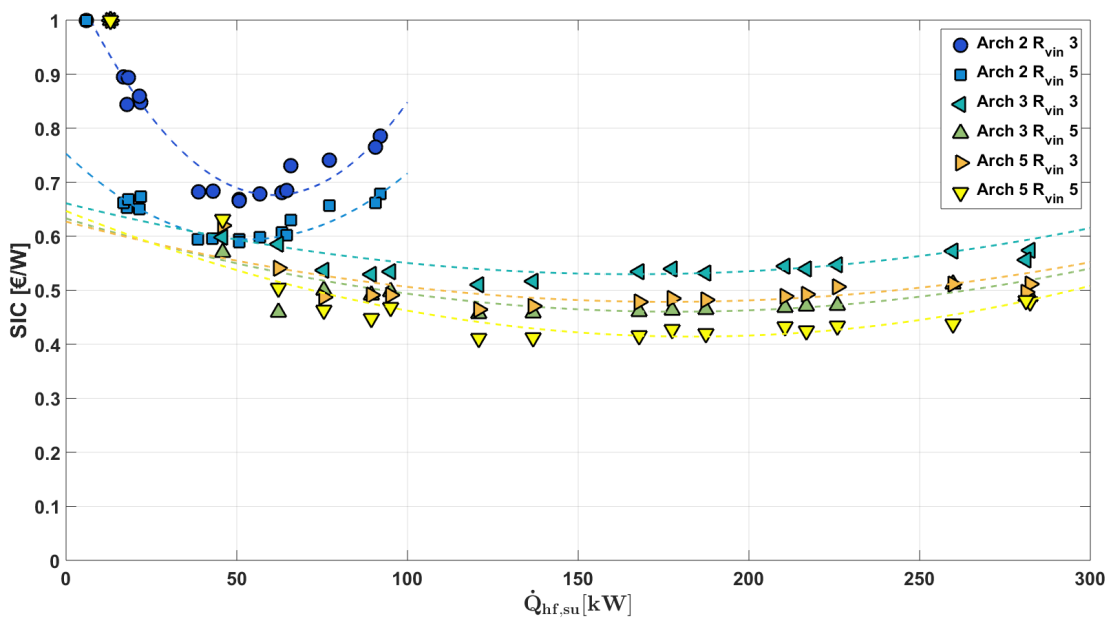
Figure 5.30 – Evolution of the specific investment cost, obtained with the simplified model, as a function of the available supply heat flow rate for 3 typologies and ethanol as working fluid

the use of validated but still relatively simple semi-empirical models (0D). The interior-point algorithm through the Matlab optimization toolbox is used to perform the minimization of the SIC of each system. The typologies are first compared in terms of net power output and specific investment cost. The influence of the working fluid and of the expansion machine is also discussed. Based on the results, the distribution of the costs and the fuel economy

expected on the design point are presented for the most promising architectures. For the latter, a basic sensitivity analysis is then performed on the expander cost to evaluate the impact on the SIC. Finally, an exergetic analysis is achieved so to evaluate the strength and weakness of the system components.

5.4.1 Performance comparison

Results are shown in Figure 5.31 and 5.32 in terms of SIC and net power output respectively. It can be observed that typologies 2 to 5, including the EGR as heat source are the most promising whatever the working fluid. Topology EGR Last is generally unfeasible because of the upper limit on the outlet temperature of the EGR gases ($120°C$). The use of the recirculated gases as single heat source presents the advantage not to increase the heat rejection of the truck. In general, ethanol seems to be the most appropriate working fluid. Also, because of the low temperature of the heat source, water should be avoided using topology 1. Moreover, water is not well suited with the vane and roots expanders. This is explained by the constraint on the maximal inlet temperature within this technology. Fluid R245fa generally leads to higher SIC and should be avoided, except when the exhaust gases are used as single heat source. This is due to the relatively low temperature level of those gases. The most promising expansion devices seem to be the scroll and screw expander while the piston and turbine expanders lead to slightly higher SIC. The vane and roots expanders generally lead to higher SIC because of their corresponding limitations (Table 5.6). Finally, the most appropriate solution, based on the assumptions made here is the use of the screw expander integrated in the parallel topology and using ethanol as working fluid. In this configuration, the SIC is below 0.23 while the net output power of the system almost reaches 10 kW. More details about this configuration are given in Figure 5.33. However the results obtained with the scroll expander in the same conditions remain very similar. Cyclopentane, water and acetone also show good performance when used in architecture 2, 3 and 5 with the scroll and screw expander. At this stage no conclusion can thus really be drawn.

5.4.2 Sensitivity analysis

The results of the design phase rely on the estimation of the system costs and performance (net power output). The economic model is based on several assumptions regarding the costs of the individual components that are directly influencing the total and specific investment costs of the systems. For this reason the sensitivity of the SIC to a modification of the TIC should be investigated. It is proposed to keep the task simple and to evaluate the impact on the SIC of a modification of the TIC of $+/- 10$ %. The thermoeconomic optimization is thus performed reducing and then increasing the TIC predicted by the economic model by 10 %. Results are shown in Figure 5.34 for the 6 working fluids in the case of the system recovering the heat from the recirculated gases only and using the screw expander. In this case, the optimization leads to similar results in terms of thermodynamic conditions of the ORC system, meaning that the over/under estimation of the TIC of 10 % also leads to an over/under estimation of the SIC of
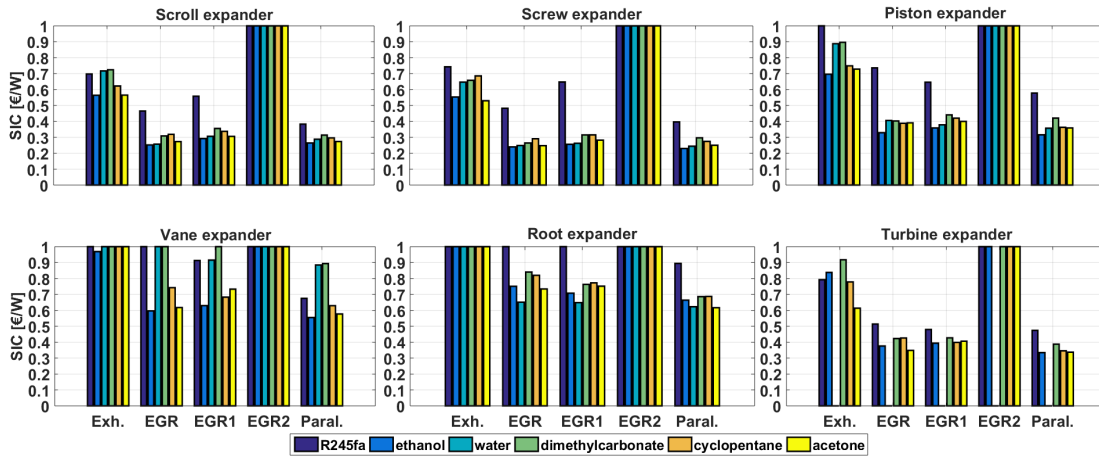
Figure 5.31 – Specific Investment Cost of the ORC systems achieved on the design point with the different architectures, working fluids and expansion machines
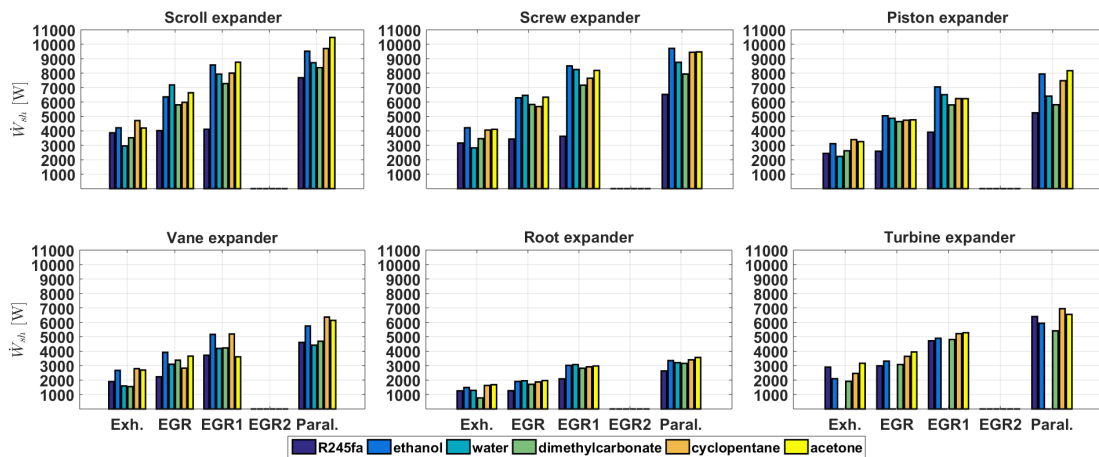
Figure 5.32 – Net power outputs of the ORC systems achieved on the design point with the different architectures, working fluids and expansion machines

about 10 %. In these conditions, the observations achieved in the previous section remain unchanged. The scroll and screw expanders remain the most suitable expansion machines. Architectures 2,3 and 5 (EGR only, EGR First and EGR Parallel) remain the most promising choices. Regarding the working fluids, trends are still very similar and the only fluid that could be rejected is R245fa.

5.4.3 Exergetic analysis

In order to identify the identify the main sources of exergy losses and evaluate the weaknesses of the ORC systems as well as the potential improvement, an exergetic analysis is performed.

Net power output: 9.72 kW

TIC: 2.23 k€

SIC: 0.2294 [-]

Evaporating pressure: 20.6 bar

Condensing pressure: 1 bar

Rotational speed: 25 kRPM

Displacement: 6.93 cm³

Overheating degree: 24 K

Built-in volume ratio: 6 [-]

Pinch-point

- EG: 14.9 K   EGR: 38.2K

- CD: 5.9 K
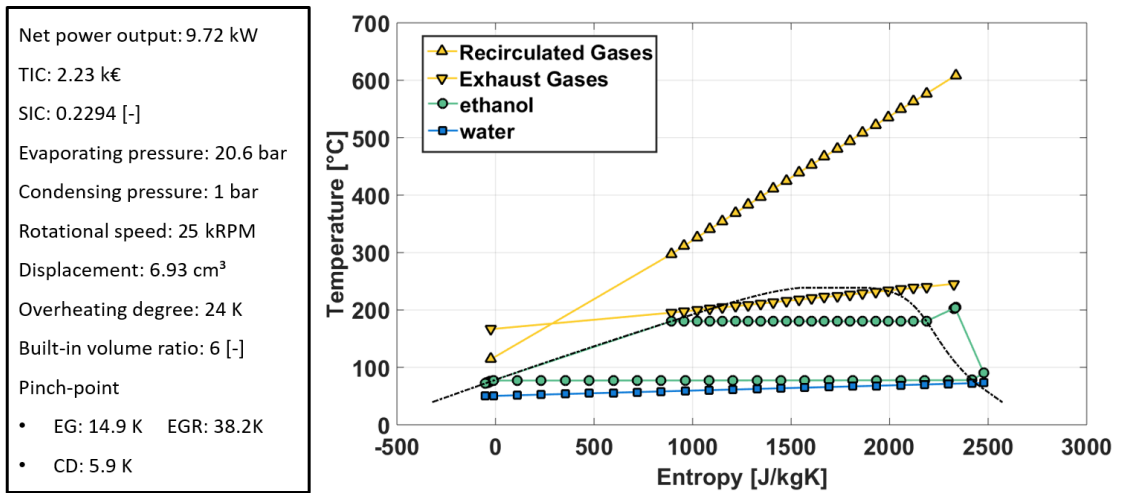
Figure 5.33 – Detailed outputs of the thermoeconomic optimization for the topology including the screw expander, using ethanol as working fluid and when the heat is recovered from both the exhaust and recirculated gases placed in a parallel configuration
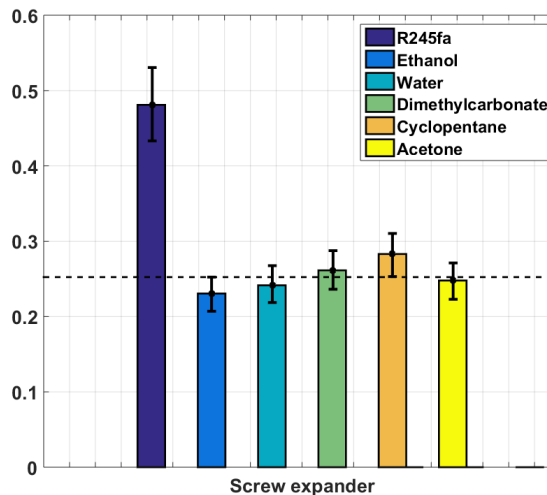
Figure 5.34 – Influence on the SIC of a 10% modification of the TIC for the 6 working fluids, and the system recovering only the heat from the recirculated gases and using the screw expander.

The exergy flow rate is defined in Equation 5.79 where

$$and$$

are the specific enthalpy and entropy of the considered fluid at the reference temperature and pressure. In this analysis, the atmospheric pressure ($1\ bar A$) is defined as the reference pressure while the inlet temperature of the condenser cooling fluid ($333.15K$) is set as the

147

reference temperature.

$$\dot{E} = \dot{M}_i\Big((h - h_0) - (T_0 + 273.15)(s - s_0)\Big) \tag{5.79}$$

The exergy balance over system is expressed identifying the passive and active parts of the exergy flow rates, i.e. the exergy flow rates leaving and entering an investigated system respectively. The active part of an ORC system consists in the exergy flow rate of the heat sources at the inlet of the exchangers and the pump electrical power. The passive part consists in the mechanical power at the expander shaft and the exergy flow rates of the fluids leaving the system and the rate of irreversibilities of the system components (heat exchangers, pump and expander). Based on the measurements, the exergy flow rates of the fluids entering and leaving the components can be identified. The mechanical and electrical powers produced and consumed by the expander and the pump respectively can also be evaluated. The rate of irreversibilities of each component can thus be evaluated based on the exergy balance over this component.

$$\Delta \dot{E}_{HX} = ||\dot{E}_{su,1} - \dot{E}_{ex,1}| - |\dot{E}_{su,2} - \dot{E}_{ex,2}|| \tag{5.80}$$

$$\Delta \dot{E}_m = ||\dot{E}_{su,1} - \dot{E}_{ex,1}| - \dot{W}_m| \tag{5.81}$$

The rate of irreversibilities and the exergy flow rate exiting the heat exchanger on the secondary fluid sides are stacked in Figure 5.35 for each of the system architectures using the screw device as expander and ethanol as working fluid. It is shown the main sources of irreversibilities result from the heat transfer with the recirculated gases. Indeed, it represents 40 to 60% of the total exergy loss. Reducing the irreversibilities could be achieved increasing the heat transfer area of the heat exchanger so to reduce the pinch point of the exchanger. However this would also mean an increase in cost and weight of the component. Others possibilities could be imagined such as the use of zeotropic mixtures. Partial evaporation, triangular or trans-critical cycle could also be set up but it would also imply an increase in evaporating pressure, limited until now to an upper limit of 32 bar. The second main source of exergy loss, around 10 to 20%, is the exergy content leaving the heat exchanger with the exhaust gases. The optimization procedure generally tends to increase the evaporating pressure of the system, reducing the heat recovery from the exhaust gases whose inlet temperature is limited compared to the recirculated gases (Figure 5.33). Indeed the heat exchanger is placed after the exhaust-after treatment system of the truck. The reaction in the catalytic system being highly endothermic, the temperature of the exhaust gases is significantly reduced compared to the temperature level at the outlet of the engine. Finally, the expansion is the third main source of exergy loss (10 to 20 %), the isentropic efficiency of the machine being limited (Figure 5.18).

Figure 5.35 – Exergetic losses calculated for the 5 architectures using the screw expander and ethanol as working fluid

5.5 Off design performance: thermodynamic optimization

Finally, the performance of the 3 most promising architectures (2, 3 and 5) are maximized optimizing the evaporating pressure and the overheating degree for each of the 16 off-design operating points of the frequency distribution map (Figure 5.29). It is worth to note that the optimization of the evaporating pressure (or expander rotational speed) implies the use of an electrical generator and a speed regulation mechanism. Whether turbines or volumetric machines are considered, the control of the expander rotational speed enables to optimize the power production and adapt it to the vehicle electrical consumption. However, the latter can hardly be predicted and is today too low (around 1.5 kW [53]) to absorb the production of an ORC system which could be up to 10 kW depending on the engine operating point. An alternative enabling to estimate the fuel economy is to couple the ORC generator to an electric motor through batteries. A mechanical coupling of the engine and expander shafts is probably the simplest solution but it also implies the loss of a degree of freedom for the optimization and control the WHRS: the regulation of the evaporating pressure through the rotational speed of the (volumetric) expander is no more possible. A weighted average based on the frequency distribution is performed for the net power outputs of the systems. This is achieved here for the 2 most promising expansion machines, the scroll and the screw expander. However the same exercise could be done for the other technologies. Fluid R245fa has also been removed of the comparison. The piston expander is pushed aside. Nonetheless, as shown in Appendix D, lower SIC and higher power output could be achieved on the design point if the clearance volume and mechanical losses of the machine were reduced.

New estimation of the SIC and Average power output

Results are reported in Figure 5.36 in terms of weighted average net power output. A new estimation of the SIC is provided based on the latter weighted average power. In general, using the recirculated gases as the single heat source is less suited compared to the 2 other typologies. The average power is reduced, leading to a higher SIC. The parallel topology gives slightly better results compared to the serial topology. It enables to extract more heat from the heat source thanks to an additional degree of freedom (2 working fluid mass flow rates). Results are similar when comparing the performance of the systems using the scroll and the screw expanders. The lowest SIC values are achieved with ethanol as working fluid. However, the average output power obtained with cyclopentane and acetone is of the same order of magnitude and even higher sometimes.
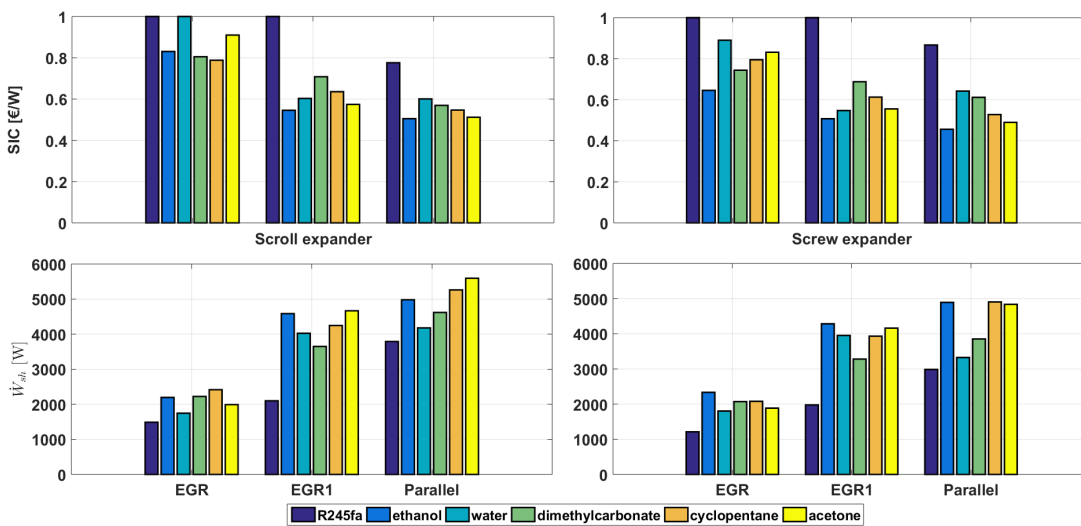
Figure 5.36 – Weighted average of the net power outputs of the ORC system and resulting specific investment costs achieved over all the investigated operating conditions for the 3 most promising architectures, the 6 working fluids and the scroll and screw expanders

Additional heat rejection and fuel economy

Additional heat needed to be rejected at the front end of the truck is reported for the investigated typologies in Figure 5.37. The share resulting from the recovery of the recirculated gases is considered not affecting the heat rejection. In the original truck, those gases are cooled down by mean of a coolant in an EGR cooler so approximately the same amount of energy has to be rejected. Therefore topology EGR Only leads to an additional heat rejection equal to 0. On the other hand, topology EGR First leads to a reduced heat rejection compared to the parallel topology. At the end the impact on the activation of the truck fan has to be identified to establish the most suitable architecture. Based on the power output weighted

150
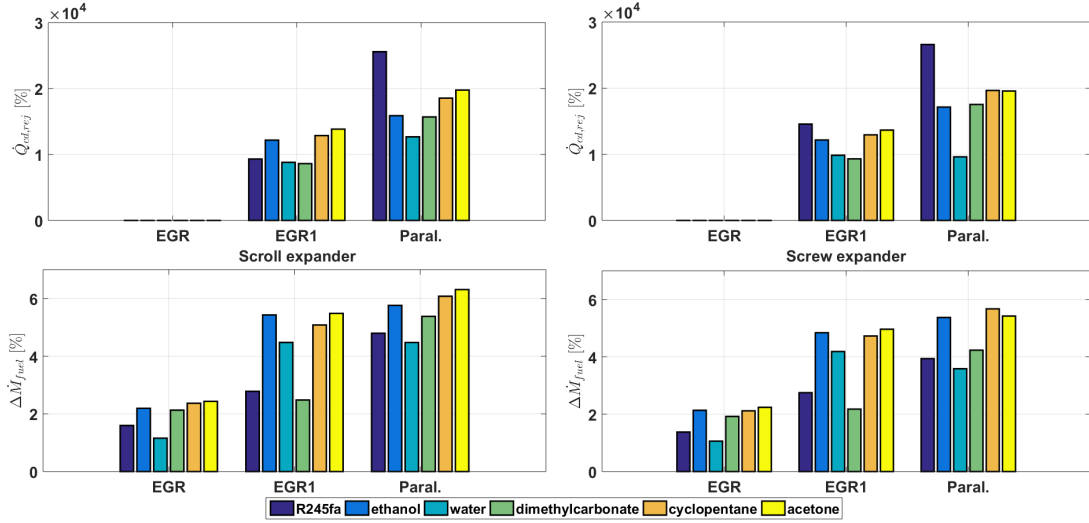
Figure 5.37 – Weighted average of the fuel economy and additional heat rejection achieved over all the investigated operating conditions for the 3 most promising architectures, the 6 working fluids and the scroll and screw expanders

over the 17 investigated operating conditions, the increase in engine efficiency can computed, all other thing being equal. The current engine efficiency is calculated for each operating conditions based on the engine speed, torque and fuel consumption measurements. The Lower Heating Value (LHV) of $43.4 MJ/kg$ is assumed for the fuel. The engine efficiency of the truck equipped with the WHR system is computed taking into account the net output power of the ORC system. Finally the fuel consumption reduction could be estimated equal to the gain in efficiency. Here an approximation is provided computing the fuel quantity required to achieve the same torque and speed values as the original engine based on the new efficiency. Being more accurate would probably require a complete model of the vehicle.

$$\eta_{eng,1} = \frac{2\pi \frac{N}{60} T}{\dot{M}_{fuel} LHV} \tag{5.82}$$

$$\eta_{eng,2} = \frac{2\pi \frac{N}{60} T + \dot{W}_{ORC,net} (\eta_{gen} \eta_{l,bat} \eta_{mot})}{\dot{M}_{fuel} LHV} \tag{5.83}$$

$$\dot{M}_{fuel,new} = \frac{2\pi \frac{N}{60} T}{\eta_{eng,2} LHV} \tag{5.84}$$

Results are depicted in Figure 5.37 where fuel consumption reduction can exceed 6 %. Those results should be treated with caution. Indeed, part of the 17 operating conditions are characterized by low engine torque values (below 50 Nm) and by a reduced engine efficiency (below 20 %). Even, if the net power output of the ORC system is of a few hundred Watts, the increase in overall efficiency is significant and if the frequency of apparition in the driving cycle of

the considered operating conditions is not negligible, it affects the average fuel consumption reduction in the same manner. However, the driving cycle can hardly be reduced to 17 operating conditions while hoping accurate results in the engine performance improvements. In addition, the steady-state nature of the present simulation also does not consider the thermal inertia of the components so the performance of the ORC system are probably lower in reality. Dynamic simulation of the most promising typologies is the subject of the next Chapter to the en of which, the performance indicators of this section will be updated. Finally, the fan eventual additional fan consumption resulting from the increase in heat to reject at the front end of the truck is not taken into account. Nonetheless, based on this first estimation, economic indicators can already be introduced and evaluated. The first introduced indicator is the payback period, which is commonly defined for project investments. This period (P) is the length of time needed to recover the cost of an investment (C_0), i.e. the recover the capital investment thanks to the fuel savings in the present study. It is assumes, the investment to be made by the future truck owner, or the price of the WHR system, is 1.5 the manufacturer TIC. Considering HDT travel 150000 km per year, are characterized by a life length of 10 years (or 1500000 km) and consumes in average $35l/100km$ with a diesel price of 1.1 €/l, the time required to recover the investment of the WHR ORC systems is:

$$C_0 = 1.5TIC \tag{5.85}$$
$$P = \frac{C_0}{AFS} \tag{5.86}$$

where the annual fuel savings (AFS) are the product of the amount of fuel saved per year thanks to the WHR system and the fuel price in €/l. The payback period unlike other methods, does not consider the time value of money. "*Because of the time value of money (TVM), money in the present is worth more than the same amount in the future. This is both because of earnings that could potentially be made using the money during the intervening time and because of inflation. In other words, a dollar earned in the future won't be worth as much as one earned in the present*" [207]. The Net Present Value (NPV), through the discount rate, is a way to account for this characteristics of money. The NPV, defined as follow, is the net values of the cash inflow and is used to investigate the profitability of a project.

$$NPV = \sum_{t=1}^{N} \frac{C_t}{(1+r)^t} - C_0 \tag{5.87}$$

where C_t is the net cash inflow of the period t, r is the discount rate and N the number of investigated periods. When positive, the NPV indicates the earnings of a project are above the expenses and the project is profitable. The challenging part in using the NPV is the identification of the discount rate and future cash inflows and outflows of the project. A discount rate of 10% is considered while the only cash inflows and outflows are the annual fuel savings tanks to the WHR system and the annual maintenance costs (100 €/year [33]. Starting from a fuel price of 1.1 €/l a yearly increase of 5 % of this price is also assumed. A
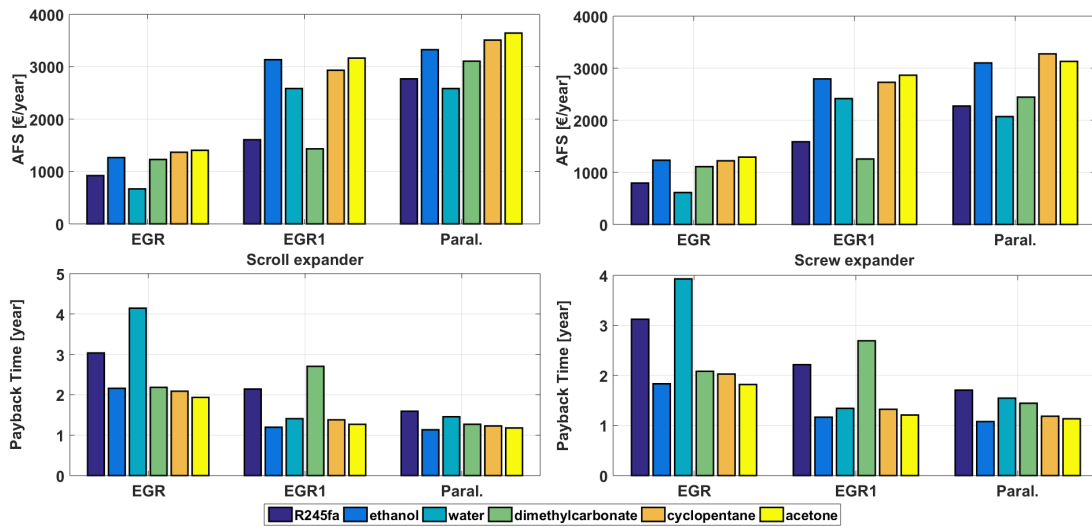
Figure 5.38 – Weighted average of annual fuel savings and payback time achieved over all the investigated operating conditions for the 3 most promising architectures, the 6 working fluids and the scroll and screw expanders

third economic indicator is the Internal Rate of Return (IRR) of investment. The formula used is the same as the NPV. However the method consists in identifying the discount rate that makes the NPV of all cash flows equal to 0 at the end of the project. In general, the higher the IRR, the higher the chance of a project to be profitable. The IRR is also representative of the rate of growth of a project. Indeed, even if the IRR differs from the actual rate of return, the project with the higher IRR provides more chance to be substantially profitable. Based on the IRR definition, and because the TIC for the manufacturer results from a series of assumption, although the sensitivity of the SIC to the TIC variations has been studied, it is proposed to evaluate the TIC that would make the NPV equal to 0. In other words, this fourth indicator, called here Maximal Acceptable Investment (MAI) gives the investment above which the project is not profitable for the future truck owner based on the fuel economy and the maintenance costs of each year of the project. The same exercise is also performed to estimate the minimal Acceptable Fuel consumption reduction (mAF) that makes the project profitable based on its price $C_0 = 1.5TIC$. The indicators are computed assuming the truck owner sells the truck after 3 years of usage. The time of the project is thus reduced from 10 years (truck lifetime) to 3 years. Results are shown in figures 5.39 and 5.40 and are refined in the next chapter for the 4 most promising architectures (EGR First and Parallel typologies, using ethanol as working fluid and the scroll and screw expanders).

5.6 Conclusion and perspectives

Attempting to select the architecture, the expander technology, and the working fluid for a waste heat recovery organic (or non-organic) Rankine cycle system devoted to be coupled
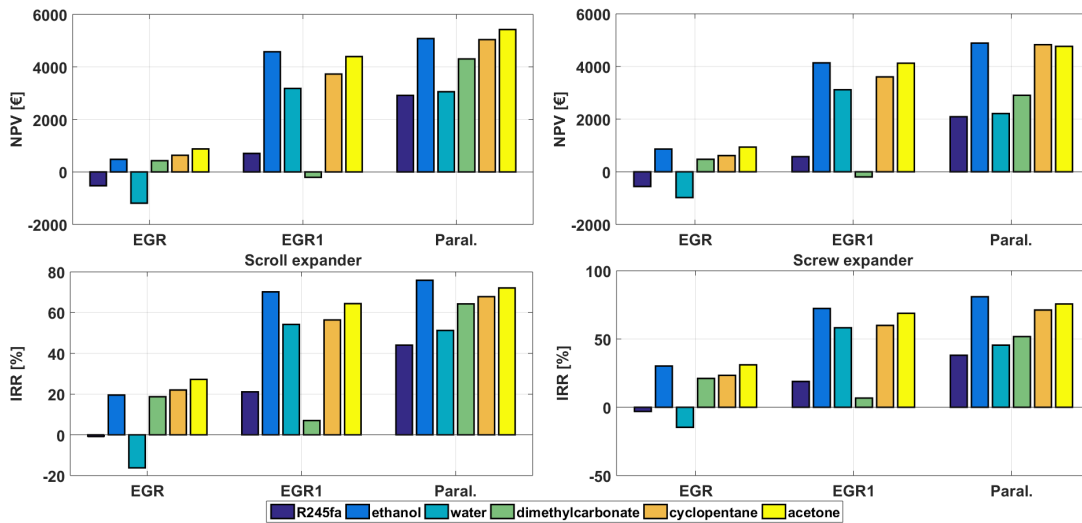
Figure 5.39 – NPV and IRR achieved over all the investigated operating conditions for the 3 most promising architectures, the 6 working fluids and the scroll and screw expanders
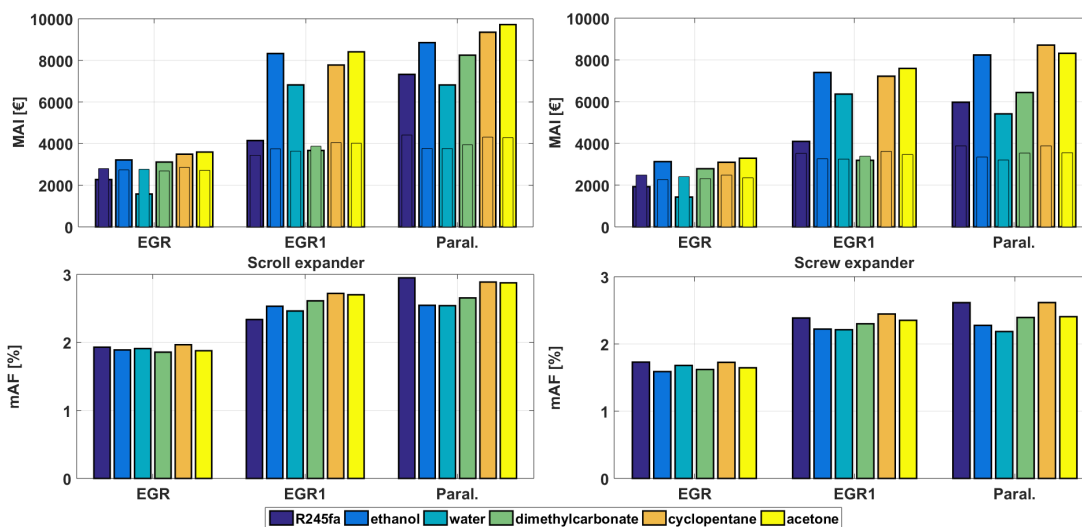
Figure 5.40 – MAI (and superposed C_0) and mAF achieved over all the investigated operating conditions for the 3 most promising architectures, the 6 working fluids and the scroll and screw expanders

to a truck engine, it is proposed to first build and validate the component models against experimental data before trying to predict their performance within the design phase of the on-board system. A Rankine test-bench, using water as working fluid, and devoted to recover the heat from the exhaust gases of a gasoline engine, enabled to validate the plate heat exchanger model to be placed on the high pressure side of the ORC system. Regarding the plate heat condensers, because the pinch-point is generally low, it is proposed to directly use

correlations available in literature to evaluate the heat transfer coefficients on both sides of the heat exchanger. In the same manner, models of scroll, screw, piston, vane, root expanders and of a piston and membrane pump could be validated in addition to the model of radial-inflow turbine proposed in Chapter 4. The resulting validated models are used as reference for the design process whose strategy consists in scaling the components for the new application following specific rules. Numerous design steady-state models of ORCs are built. From the 5 architectures proposed in Chapter 2 and the 6 expander technologies result 30 different typologies. Considering the 6 working fluids identified in Chapter 2, it leads at the end the optimization of 180 ORC system models. A 3-step optimization is proposed. The method starts with the selection of the design conditions. Then, for the obtained design conditions, a thermo-economic optimization is performed to design the systems. Finally, the performance of the resulting systems is optimized and evaluated for various off-design conditions, optimizing the evaporating pressure and the overheating degree. It is therefore assumed the expander speed can be controlled. On the other hand, a mechanical coupling of the engine and expander shafts could be investigated but it would also imply the expander speed is imposed by the engine through a gear ratio. A weighted average of the power produced by the systems is then done based on the frequency distribution of the considered operating conditions in the driving cycle. In order to locate the sources of entropy increase in the proposed systems, and thus identify the possible weakness of the designed external combustion engine, an exergetic analysis is achieved. A basic sensitivity analysis is also achieved to evaluate the impact of a variation of the system cost on the optimal specific investment cost of the system. Based on the results, it is shown that ethanol is the most appropriate working fluid while the EGR First and parallel typologies are the most promising. The use of the screw expander leads to the best average performance. However, results are similar between the scroll, the screw expanders. At the end, 4 architectures are then retained. Quasi-static simulations could be performed along driving cycles of the truck to evaluate the energy recovered by the systems and thus the fuel consumption reduction. To be more accurate, dynamic simulations are performed over the entire driving cycle in the next Chapter based on new component models.

6 Dynamic modeling and simulations of the ORC systems

Abstract

Because of the transient nature of the heat sources encountered on a truck, dynamic simulations are an essential part of the design process of ORC systems for truck applications. Dynamic models are particularly useful for component design, control design and transient evaluation of ORC systems. To ease the burden of building numerous dynamic models of different candidate ORCs while the design process is ongoing, a library of generic dynamic models of ORCs is built in this work. These models work in synergy with the steady-state ORC design tool in which is added a function to automatically populate the parameters of the dynamic models. In this Chapter, the dynamic model library and their parameterization process in LMS AMESim are described. The platform is largely used in automotive industry and offers a variety of libraries: Engine, Control, Two-Phase Flow, etc. The models of the different components are described. Because the dynamic behavior of the ORC system is dominated by the heat source temperature and mass profiles as well as the time constant of the heat exchangers, a particular attention is dedicated to the evaporator model. A finite-volume model of the device is developed and confronted to dynamic experimental data. The condenser is modeled using the same approach and enables to quantify the heat rejected by the ORC systems. The dynamic behavior of the rotating machines is not taken into account and efficiency maps are drawn for both the expander and the pump based on the steady-state models for several operating conditions. In order to quantify the performance of the ORC systems, resulting from the combinations of the different components, a control strategy is developed. In this work, this strategy is kept simple and consists in the regulation of the pump and expander speeds in order to achieve an overheating and evaporating pressure set-point respectively. Simulations are performed over several driving cycles which are representative of the truck real operation. The performance of the systems is evaluated and presented in terms of ORC net power output, condenser heat rejection and truck fuel economy.

6.1 Introduction

Dynamic simulations consist in evaluating the time varying behavior of a system based on a model, which is commonly described by ordinary or partial differential equations. Because the model also incorporates real-world constraints, those equations, typically nonlinear, require numerical methods to be solved. Industrial applications are various and range from nuclear power plants ([208], [209] to drug dose migration in the human body ([210]). Because of the transient nature of the heat sources encountered on a truck, dynamic simulations are an essential part of the design process of ORC systems for truck applications. Dynamic models are particularly useful for component design transient evaluation of ORC systems and in process control systems for tuning the automatic controllers before they are implemented or to train the personnel before controlling the real system [211]. Over the past decades, the interest in dynamic simulation and the need for simulating multi-domain dynamic systems have significantly grown exploiting the increasing power of computing machines. Indeed, simulation are generally cheaper and safer than conducting real experiments. Dynamic simulations also enable to achieve experiments that would not be feasible in practice because of the time constant involved. The latter could be too small and therefore hardly be experienced by the user or too big leading to a long-time experiment. Simulations, typically faster than real time, through, among other, variable time step integration enables to avoid this issue during simulation. Simulations also allow accessing to all state variables and parameters of the process model and to investigate the model out of the feasible range of the system with no additional cost [104].

Depending on the level of details, dynamic models can typically be split into 2 categories: low order models and detailed physics-based models. The first category generally rely on simple modeling paradigms and high computational efficiency. " *They are usually linear models suited for long time frame simulation, e.g., yearly-based analysis* " [104]. The second category corresponds to more detailed models based on conservation laws (mass, energy and momentum) devoted to accurately predict the dynamic behavior of a component or an entire system. Those models are useful to investigate the system response to a transient modification of the boundary conditions and are often most suited for limited time frame ranging from some minutes to several hours. They are also suited for the development and testing of controllers. In general these models are mathematically expressed by a system of differential algebraic equations (DAE) subject to various numerical problems and challenges [212].

The need for multi-domain dynamic simulation has led to the development of numerous software (AMESim [213], Dymola [214] -Modelica [215], SimulationX [216], etc). Recently, the Thermocycle library [217] has been built for the simulation of small scale thermal systems through Modelica [215], which is an object-oriented equation based language. The tool is a fully open source solution that aims at addressing three typical challenges inherent to the modeling of thermo-flow systems [104]

- Computing the thermo-physical properties of working fluids (using the CoolProp [64] fluid library)

- Computational efficiency: The tool provides component models as generic as possible trying to minimize the overall complexity and computation time. Lumped models and distributed parameter models limited to one-dimensional discretization are included in the library.

- Robustness during initialization and integration: Several numerical methods have been developed and implemented in order to enhance the robustness and the simulation speed of the models during initialization and integration.

On the other hand, LMS AMESim is a commercial solution, including, through the Imagine suite, numerous libraries, which are written in C language but also support Modelica language. The tool also aims at addressing the three aforementioned challenges. Computing the thermo-physical properties of working fluids is achieved through a Refprop [63] based fluid library

Modelica is a non-causal programming language that makes easier the problem formulation but also leads to large implicit equation systems, which from the author experience, makes the numerical resolution, typically achieved in Dymola, more difficult and thus reduces the robustness of the tool. For this reason, the complexity or size of a system model is often limited and the level of details of the components is also reduced. Commonly, in the heat exchanger models of Thermocycle, pressure drops are lumped at the end of the component while the heat transfer coefficients are computed based on scaling relations from a nominal heat exchange coefficient based on the mass flow rate or the vapor quality. The mass flow rate is an input and the use of heat transfer and presssure drops correlations is generally avoided. Although, Desideri [104] recently added the possibility of computing the heat transfer coefficient based on detailed correlations. The absence of detailed correlations makes the tool very efficient, reducing the computational time but makes it specific and valid for boundary conditions close to the conditions on which the nominal heat transfer coefficient has been identified.

In AMESim, the causality is insured through the bond-graph theory which leads most of the time to entirely explicit models. The formulation of the problem by the user is more complex but the robustness is largely improved. In a heat exchanger model, the mass flow rate and heat transfer coefficients are computed directly through pressure drops and heat transfer correlations so to satisfy the conservation laws of mass, energy and momentum. In addition, the AMESim solver is constituted of numerous algorithms which are selected automatically by the software according to the problem to solve. However, the use of detailed correlations typically leads to an increased computational time. In this work, because it is a design process, which often results in simulating numerous ORC system designs, the robustness of the AMESim solver and the generality of the physics-based models has been retained as the most important criteria, even if it can imply an higher computational time.

As explained in Chapter 2, two heat sources are investigated: the exhaust gases and the recir-

culated gases. Combining these sources, 5 possible configurations are proposed, considering a single heat sink. In small-scale ORC systems the governing dynamics are generally located in the heat exchanger. For this reason particular attention has been paid to the modeling of those components and specially on the high pressure side of the cycle. In order to accurately predict the heat exchange but also the temperature profiles of the two fluids going through one heat exchanger, 2 modeling approaches are commonly adopted in literature: the finite volume and the moving boundary approach [218]. Both methods are based on the conservation laws of mass, energy and momentum over a defined control volume. In a moving boundary model the fluid flow in the heat exchanger is divided in various region corresponding to the states the working fluid can be in (e.g. liquid, two-phase, vapor). The position of the boundaries varies in time during transients, following the saturated liquid and the saturated vapor states. In the finite volume approach the heat exchanger is discretized in finite number of control volume often equal and constant in size. Bendapudi et al. [219] compared the moving boundary and finite volume techniques for transients in a 300 kW centrifugal chiller equipped with shell and tube heat exchangers. It was concluded that the moving boundary formulation led to 3 times faster simulation with the same level of accuracy but is less robust through start-up and all load-change transients. An under-prediction of the fluid charge was also observed as a consequence of the homogeneous flow assumption in the two-phase region resulting in an over-prediction of the void fraction. A literature review on transient heat exchanger modeling techniques can be found in [220] and provides similar conclusions: the moving boundary results in faster but sometimes less robust models [218]. On the other hand, the AMESim platform has been designed for the the finite volume approach so the latter method is used to develop the heat exchanger models. The transient response in outlet temperature of the evaporator model to series of steps on the working mass flow rate is then confronted to experimental data (section).

For both volumetric rotating components, the displacements are fixed and the evolution of the isentropic and volumetric efficiencies with operating parameters are set through performance maps obtained with the steady-state models.

To facilitate the parameterization process and to compare the steady-state response of the dynamic models against the steady-state model results, an interface has been developed in Matlab. For the heat exchangers, the steady-state model consists of a detailed analysis incorporating detailed geometry-based correlations for the heat transfer and friction coefficients. The dynamic model on the other hand consists of a counter-flow heat exchanger with a simple Dittus-Boelter type Nusselt correlation for the secondary fluid side and correlations for flow in a circular tube on refrigerant side. A transformation from the steady-state model parameters to the dynamic model parameters is required. This transformation ensures that the steady-state and the dynamic model predict the same steady-state behavior for a variety of different working conditions.

The ORC system models are achieved interconnecting the components. The performance of the systems can be evaluated along driving cycles of the truck so to predict, among other, the

power output of the WHR system and the resulting fuel economy for the engine. The heat rejection at the condenser of the system is also an important output. In this work, this task is achieved for several driving cycle provided by a truck manufacturer and representative of a truck real-life operation. However the prediction requires an appropriate control strategy. The development of an efficient control strategy is a complex task and can not be investigated into details within this work. Many authors have investigated the subject that can be the center of entire PhD thesis. Nonetheless, an objective comparison of several ORC system performance require to use similar control strategy. Grelet [53] compared and implemented several control methods from constant gain Proprtional-Integral-Derivative (PID) controllers to complex Model Predictive Controller (MPC) with observer. It was showed that the gain scheduling method, which consists in interpolating the respective gains of various PID controllers identified for different boundary conditions of the system already provides good results. In this work it is thus proposed to regulate, through PID controllers, the speed of the pump and expander so to keep respectively the overheating degree and evaporating pressure close to defined set-points. Two PID controllers are thus required. They are assumed independent and their gain values are identified for the 17 operating points of the frequency map proposed in Chapter 5.

6.2 Model of the waste heat recovery systems

The modeling approach of the AMESim software relies on the bond graph theory. In general bond graphs are a graphical representation of the energy flows in a physical dynamic system and are based on power conservation. They are often compared to block diagrams. However they differ from the latter since the bonds are bidirectional and the graphs are multi-energy domain, i.e. a bond graph can incorporate multiple domains seamlessly. The bonds represent the instantaneous energy flows between components. Those flows are denoted by a pair of variables, called power variables and that can be categorized into flow and effort variables. The product of the power variables (flow and effort) of a bond is the instantaneous power of the bond. Components can be single, double or multiple ports elements. In this work, only 2 single-ports elements, in addition to the sources and sinks, are considered: resistance (R) and capacitance (C). The notion of causality is introduced in the graph indicating which side of the bond determines the effort and which side determines the flow. This causality results in compatibility constraints, thus implying the R and C components can only be connected in an alternative manner through bonds, as illustrated in Figure 6.1, and defines which are the dependent and independent variables of each modeling element. The components in the AMESim libraries can be purely resistive, purely capacitive or can already combine the constitutive elements in particular patterns (R-C, C-R, R-C-R, C-R-C).
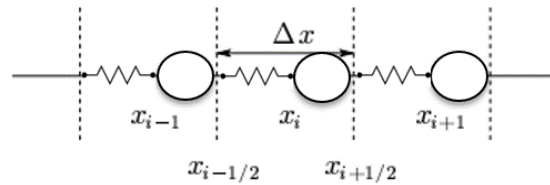
Figure 6.1 – Illustration of the alternation of the R and C components in the AMESim software based on the bond graph theory.

6.2.1 Modeling the heat exchangers

The structure of the finite volume heat exchangers is shown in Figure 6.2. It results from the interconnection of elementary elements of the required libraries following the bond graph rules. In each volume, energy, mass and momentum conservation laws are expressed considering the dynamic contribution. Typically, pipes on both fluid sides are R-C components so to compute the mass flow rate going through the resistive part according to the pressure difference and the temperature of the volume based on the incoming and outcoming energy flows. The two-phase flow library is used on the working fluid side while the pneumatic library and the thermal hydraulic library are used on the exhaust gases and the cooling water sides respectively. The thermal library is used to model the capacity of the metal wall of the heat exchanger. The finite volume model can be also seen as the interconnection of heat exchanger cells constituted by one element of each library as represented in Figure 6.2. The number of cell plays a significant role in the accuracy of the results and the apparition of potential numerical issues as explained in the following.

The modeling approach relies on various assumptions. Each side of the heat exchanger is considered as a 1-dimensional tube in the flow direction. The time constant characterizing the pressure propagation being much more lower than those related to mass and thermal energy transfer, a static momentum balance is considered. The correlation used for pressure drop and heat transfer correlation assume the two-phase flow is homogeneous. Axial heat conduction is neglected in the fluid element as well as the kinetic energy, gravitational forces and viscous stresses. Radiative heat transfer is not considered. The wall of the heat exchanger is modeled through a single thermal capacity in the transversal direction so its temperature is assumed uniform. The conduction in the longitudinal direction of the wall is not considered.

The mathematical formulations adopted in Thermocycle and AMESim can be compared. In Thermocycle, the conservation laws for each control volume are expressed as follow where the specific enthalpy and pressure have been selected as state variables. However, since pressure drops in the elements are not considered, the input mass flow rate is also required. The partial derivatives of the density according to the specific enthalpy and the pressure are considered as thermodynamic properties while the time derivative of the pressure is neglected. At the end, a system of 2 equations and 2 unknows (the time derivative of the specific enthalpy and the exhaust mass flow rate) is solved by iteration.
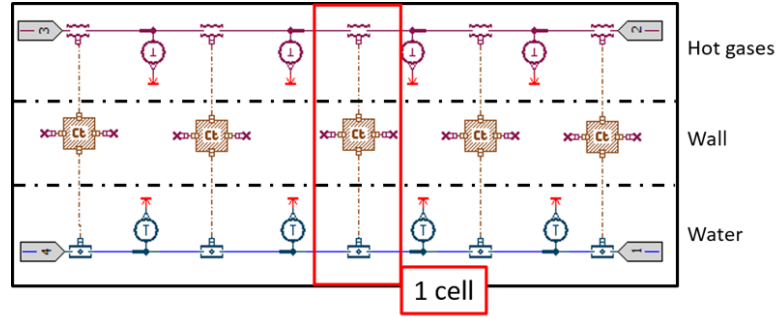
Figure 6.2 – Finite volume model of heat exchanger developed in the AMESim software. A cell is composed of pipes with heat exchange for the gases and working fluid and the thermal capacity for the meaal wall. Pipes are RC components.

$$\frac{dM}{dt} = \dot{M}_{su} - \dot{M}_{ex} \tag{6.1}$$

$$= V\left(\frac{\partial \rho}{\partial h}\bigg|_P \frac{dh}{dt} + \frac{\partial \rho}{\partial P}\bigg|_h \frac{dP}{dt}\right) \tag{6.2}$$

$$V\rho\frac{dh}{dt} = \dot{M}_{su}(h_{su} - h) - \dot{M}_{ex}(h_{ex} - h) + V\frac{dP}{dt} + \dot{Q} \tag{6.3}$$

$$P_{su} = P_{ex} \tag{6.4}$$

In AMESim, the 3 conservation laws are also expressed for each control volume where the fluid density and pressure (through the intermediate of the temperature) have been selected as state variables. A single element placed between pressure source and sink has to be of R-C-R type. The mass flow rate is computed in the R elements based on its pressure difference through a pressure drop correlation. The inlet and outlet mass flow rate being computed, the time derivative of the density can be evaluated through mass balance. The energy conservation then enables to compute the time derivative of the temperature. Finally, the Maxwell equation based on the density and temperature derivatives leads to the time derivative of the pressure making the equation system fully explicit.

$$\frac{d\rho}{dt} = \frac{1}{V}(\dot{M}_{su} - \dot{M}_{ex}) \tag{6.5}$$

$$\frac{dv}{dt} = -\frac{1}{\rho^2}\frac{d\rho}{dt} \tag{6.6}$$

$$\frac{dT}{dt} = \frac{1}{mc_v}\left(\dot{M}_{su}(h_{su} - h) - \dot{M}_{ex}(h_{ex} - h) - m(P + \frac{\partial u}{\partial v}\bigg|_T)\frac{dv}{dt} + \dot{Q}\right) \tag{6.7}$$

$$\frac{dP}{dt} = \frac{\partial P}{\partial v}\bigg|_T \frac{dv}{dt} + \frac{\partial P}{\partial T}\bigg|_v \frac{dT}{dt} \tag{6.8}$$

Heat transfer and pressure drops correlations

In the AMESim v14 default version, correlations for the heat transfer and friction coefficients, whether in single or two-phase regions, are imposed and limited in number for the tube components of the two-phase flow library. By default, the Gnielinski [221] and Churchill [165] correlations are used to evaluate the heat transfer and friction coefficients in single phase while correlation from VDI [222] and the Mac Adams correlations are respectively used to compute the heat transfer and friction coefficients in two-phase regions. On the secondary fluid side, Dittus-Boelter type Nusselt correlations can be implemented. Therefore transformations are required to parameterize the dynamic models from the steady-state models. For the heat exchangers on the high pressure side, a Dittus-Boelter type correlation is already used in the steady-state models. However for the condenser, the Martin correlation for BPHE has to be transformed. The C and m parameters of a the Dittus-Boelter type Nusselt correlation are thus adjusted through an optimization process so to minimize the error between the Nusselt number predicted by both correlations. Results are shown as a function of the Reynolds number for a given case in Figure 6.3.
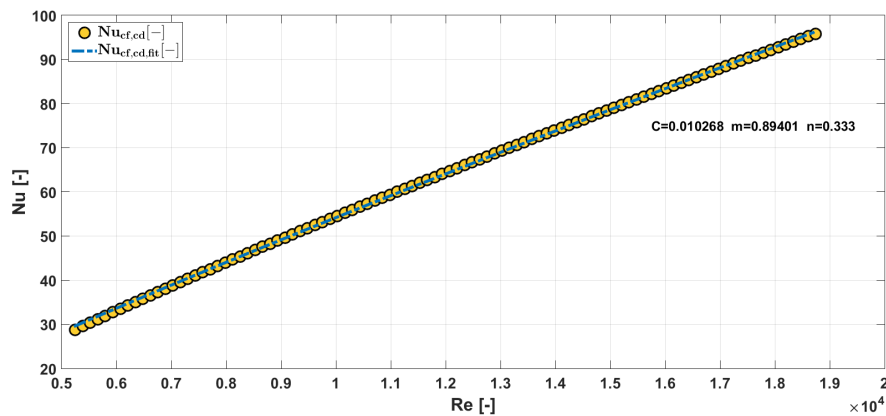
Figure 6.3 – Comparison between the Nusselt number obtained with Martin and the proposed Dittus-Boelter type correlations as a function of the Reynolds number

Regarding the heat transfer coefficients on the working fluid side, a similar procedure can be used directly on the heat transfer coefficients through an additional parameter. Indeed, even if the heat transfer correlations cannot be directly modified in AMESim v14 basic version for the components of the two-phase flow library, a gain on the heat transfer k_{HT}, defined in Equation6.9, can be adjusted. It is thus possible to vary this gain in each region of the heat exchanger (liquid, two-phase, vapor) in order to minimize the error between the heat transfer coefficients predicted by the reference correlations (e.g., Martin and Han) and the product of the gain and the heat transfer coefficient obtained from the correlation available in AMESim (e.g., Gnielinski and VDI). Nonetheless, this implies to implement the correlations available in

AMESim in the Matlab tool.

$$\dot{Q}_i = k_{HT,i} h_{conv,i} A_i (T_{wall,i} - T_{cell,i}) \qquad (6.9)$$

Experimental investigation of a plate heat exchanger

Dynamic simulations enable to evaluate the response of a system to transient boundary conditions and to develop and test control strategies. Nonetheless, the capability of the model to predict the driving physical phenomena of the real system must be ensured beforehand. Moreover, properly predicting the heat exchanger dynamic behavior is an essential task towards the modeling of a whole ORC system. In other words, the validation of the system dynamic models, and more particularly the heat exchanger models, is a essential step. Nonetheless, only few works are covering the validation of dynamic models for small scale ORC power systems. To the author's knowledge the 2 main works addressing the validation of dynamic model of ORC units were performed by Casella et al. [223] and Desideri [104].

In this section, the shell and plate type heat exchanger investigated in Chapter 5 is submitted to a set of dynamic experiments and the simulation results are confronted to the experimental data. The measurements have been performed in open-loop in order to avoid the interference of controllers in the measured dynamic response. Successions of downwards and upwards steps downwards have been imposed to the volumetric pump rotational speed, causing respectively sudden decreases and increases in water mass flow rate. During the experiments, the temperature and mass flow conditions on the exhaust gas side were kept unchanged. The effect of the pump speed step changes on the water temperature at the outlet of the heat exchanger were recorded with a sampling time of 1 seconds and compared against the finite volume model.
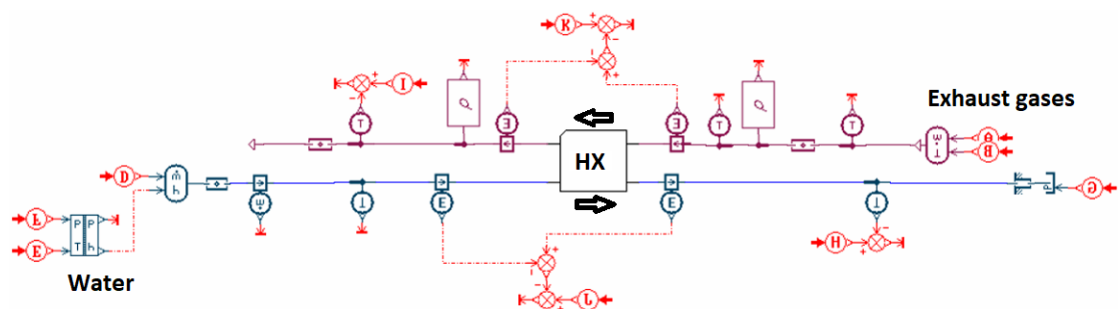
Figure 6.4 – Layout of the evaporator model with sources and sinks and developed in the AMESim sketch interface.

The layout of the model from the AMESim sketch interface is shown in Figure 6.4. The heat exchanger model is connected on both fluid sides to a mass flow and temperature source and a pressure sink. The water mass flow rate sent by the pump and the corresponding temperature

are set as inputs and imposed by the source while the pressure sink fixes the outlet pressure of the evaporator. The architecture is similar on the gas side where the mass flow rate and the inlet temperature of the gases are set as inputs and imposed by the source while the pressure sink imposes the atmospheric pressure at the outlet of the exchanger. In this case, the ambient losses are considered as inputs of the model. In order to increase the robustness of the model and reduce the computational time, the exogenous inputs of the model, obtained experimentally, are smoothed using spline functions. The parameters of the model (i.e. on both sides, the hydraulic diameters, cross sectional areas, heat exchange areas and lengths) are set based on the geometric characteristics of the heat exchanger. The outputs of the model are the heat flow rate, the outlet temperature and the inlet pressure on both sides of the heat exchanger and are compared to the corresponding measurements.
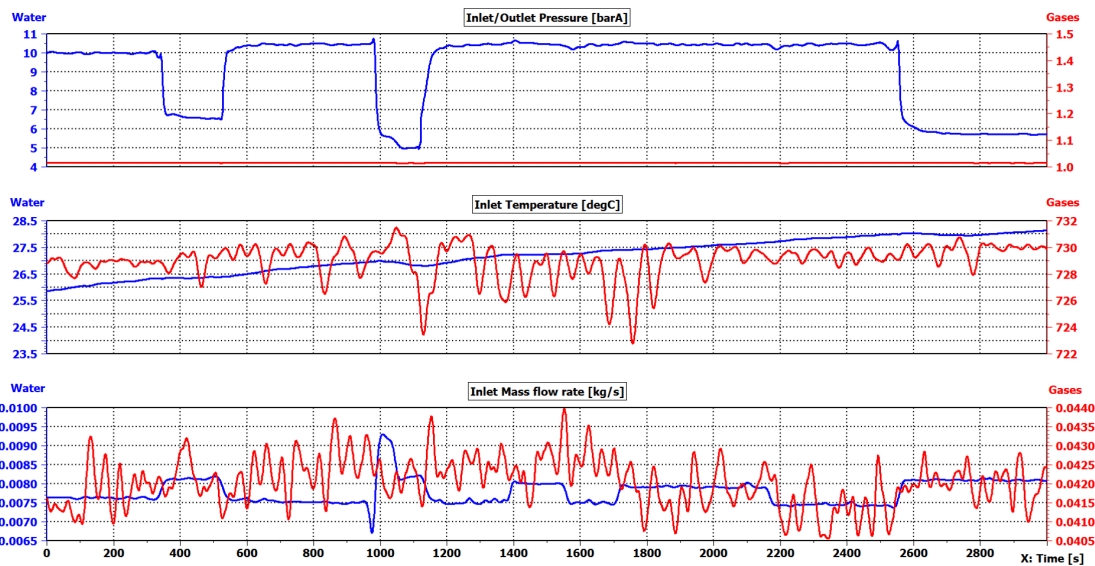
Figure 6.5 – Time evolution of the exogenous inputs considered for the AMESim dynamic model of evaporator. Top: inlet and outlet pressure on the water and gas side respectively. Mid: Inlet temperatures of the working fluid and exhaust gases. Bottom: Inlet mass flow rates of the working fluid and exhaust gases

The level of discretization, i.e. the number of cells in the heat exchanger model, is an important parameter and still has to be identified. Indeed, increasing the number of cells theoretically leads to better representation of the actual system and thus improves the accuracy of the model. It also enable to apply of the conservation laws to volume sizes closer to the assumptions in which the have been defined (infinitesimal volumes) and reduces the risk of numeric mass flow rate generation. However, the number of cells of the heat exchanger is directly linked to the number of state variables so the refining of the disctretization level also implies a more important computational effort resulting in an increased simulation time. Therefore, a trade-off between the level of details and the simulation should be identified. To this end, a parametric study is achieved on the number of cells of the heat exchanger. Five level of

discretization are considered (1, 5, 10, 15 and 20 cells), for which the mean integrated absolute error (Eq. 6.10) between the measured and predicted water heat flow rates as well as the process time (CPU time) are evaluated and compared. Results are reported in Figure 6.6 and show the improvement of the precision of the model is decreasing as the number of cells increases. From 10 to 15 cells, no significant improvement is observed since the mean integrated error is decreased from 7 to 4 %. From 15 to 20 cells, the improvement is marginal, the mean integrated error is reduced from 4 to 3.5 %. On the other hand, the computational time continues to increase with the number of cells. It should be noted that CPU time just remains an indication of the simulation time. From those observation the use of 15 cells appears to be the best trade-off for the finite volume heat exchanger model.

$$e(t) = \frac{1}{T_f - T_i} \int_{T_i}^{T_f} \frac{|\dot{Q}_{mes} - \dot{Q}_{pred}|}{\dot{Q}_{mes}} dt \qquad (6.10)$$
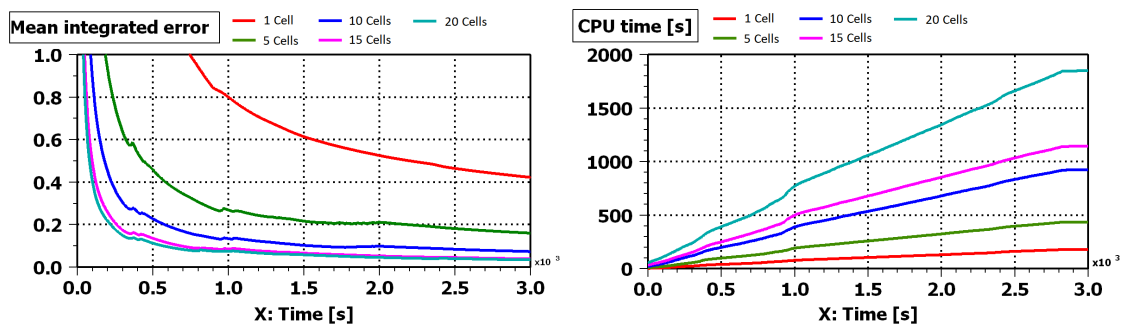
Figure 6.6 – Influence of the level of discretization on the results accuracy (left) and computation time (right).

In Figure 6.7 are compared the predicted and measured water heat flow rates for the 15 cells finite volume heat exchanger. As it can be seen, the major differences arise during the most severe step inputs that lead to discontinuities in the water mass flow rate and peaks of heat flow rates. Outside those regions, the latter is in fact close to 1 % as in can bee seen in the graph enlargement of Figure 6.7.

In Figure 6.8 are compared the predicted and measured water outlet temperature for the 15 cells finite volume heat exchanger. Numerical issues are visible at the same location as those observed for the heat flow rate. Outside those regions, the difference between predicted and measured values is really limited. In those regions, the time constant of the model step response is also close to the time constant of the real system. The maximal relative error is below 4%.
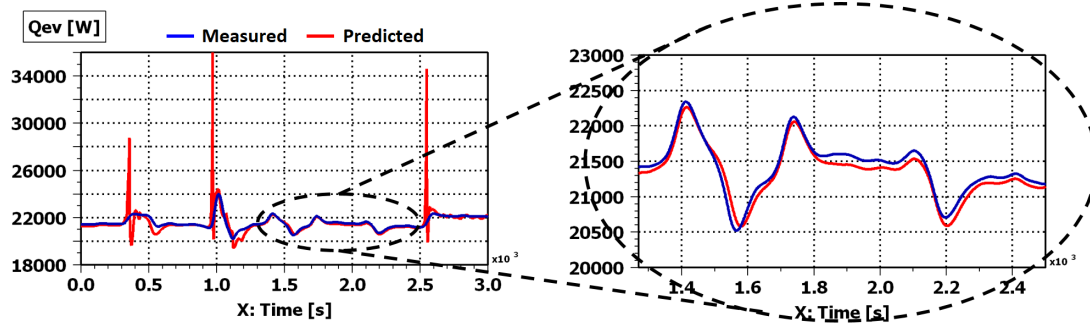
Figure 6.7 – Left: Comparison between the time evolution of the evaporator heat flow rate on the water side experimentally measured and predicted by the model. Right: Enlargement.
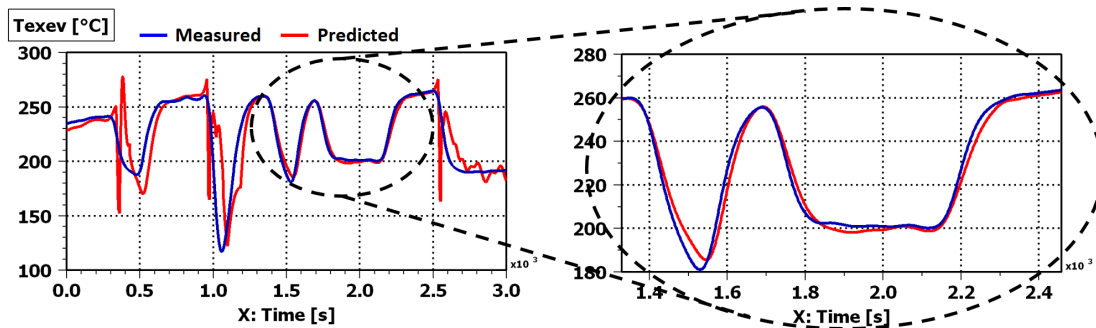
Figure 6.8 – Left: Comparison between the time evolution of the evaporator outlet temperature experimentally measured and predicted by the model. Right: Enlargement.

Numerical artifacts

The rise of numerical artifacts is a well-known issue in discretized two-phase flow models, which has been described by several authors, e.g., [224], [225]. It arises out of discontinuities in the model state variables or their derivatives. In particular, in two-phase flow models, numerical artifacts typically results from discontinuities in the fluid thermodynamic properties across the saturation lines or in the calculation of the heat transfer coefficients [225]. This phenomenon can lead to extremely high computational time or even simulation failures. Different methods have been proposed to avoid those simulation issues. Some are implemented at the system model level while others require a modification of the thermodynamic properties of the working fluid. A non-exhaustive list of the existing methods is proposed here under.

- Filtering the fast variations of the density with respect to time in order to avoid abrupt variations of the flow rate.

- The truncation of the peak in the density derivative occurring after the transition from liquid to two-phase is truncated. It reduces the numerical flow rate generated by the density derivative discontinuity.
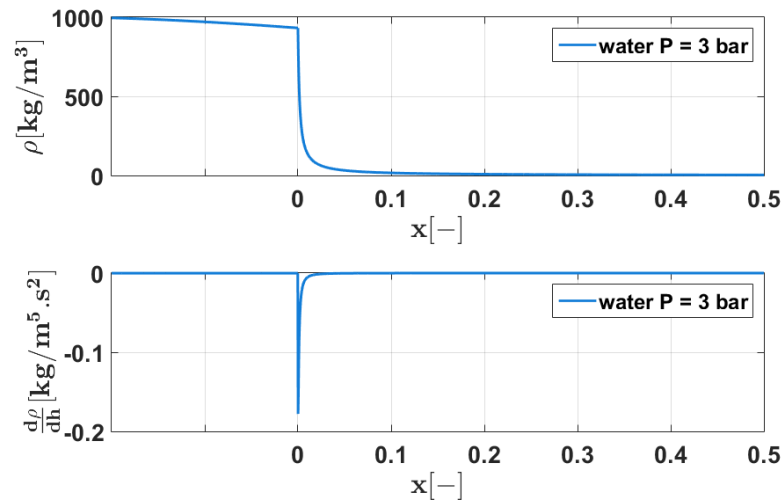
Figure 6.9 – Evolution of the density and density derivative with respect to the specific enthalpy according the vapor quality.

- Smoothing of the density derivative using a spline function in order to avoid the discontinuity. It implies modifications of the fluid thermophysical properties at the level of the equation of state, i.e. in the fluid library. Nonetheless the density function is remains calculated with the original equation of state so an inconsistency between the smoothed density derivative and the density provided by the EOS arises. This might cause a mass defect during the simulation.

- Smoothing of the density function directly in order to avoid the inconsistency of the smoothing of the density derivative. It implies recalculating its partial derivatives in the smoothed area. In this situation, the density derivatives are continuous but not smooth, which should still be manageable for the solver.

- The mean densities method, originally proposed by Casella [226] and tested by Bonilla et al. [227]. A mean density and its partial derivatives are computed in volumes where phase transitions occur as a function of the node densities, which eliminates the discontinuity in the partial derivatives.

The use of these methods nevertheless generally leads to errors in the simulation results and possible unbalance of mass and energy. More information on the issues and the possible solutions can be found in [225] and [104] in which comparisons of the different methods are done in terms of simulation speed, simulation accuracy. Mass and energy imbalance show that adopting the proposed methods can dramatically improve the simulation performance.

In the present case, the issue is illustrated in Figure 6.10. The variation of mass flow rate due to the step input leads to a sudden phase transition in one of the cells of the finite volume models, from liquid to two-phase state. The fluid density in the cell is therefore rapidly reduced which

leads to the rise of a peak and oscillations of numerical flow rate at the outlet of the cell and explains the behavior of the water heat flow rate and outlet temperature.
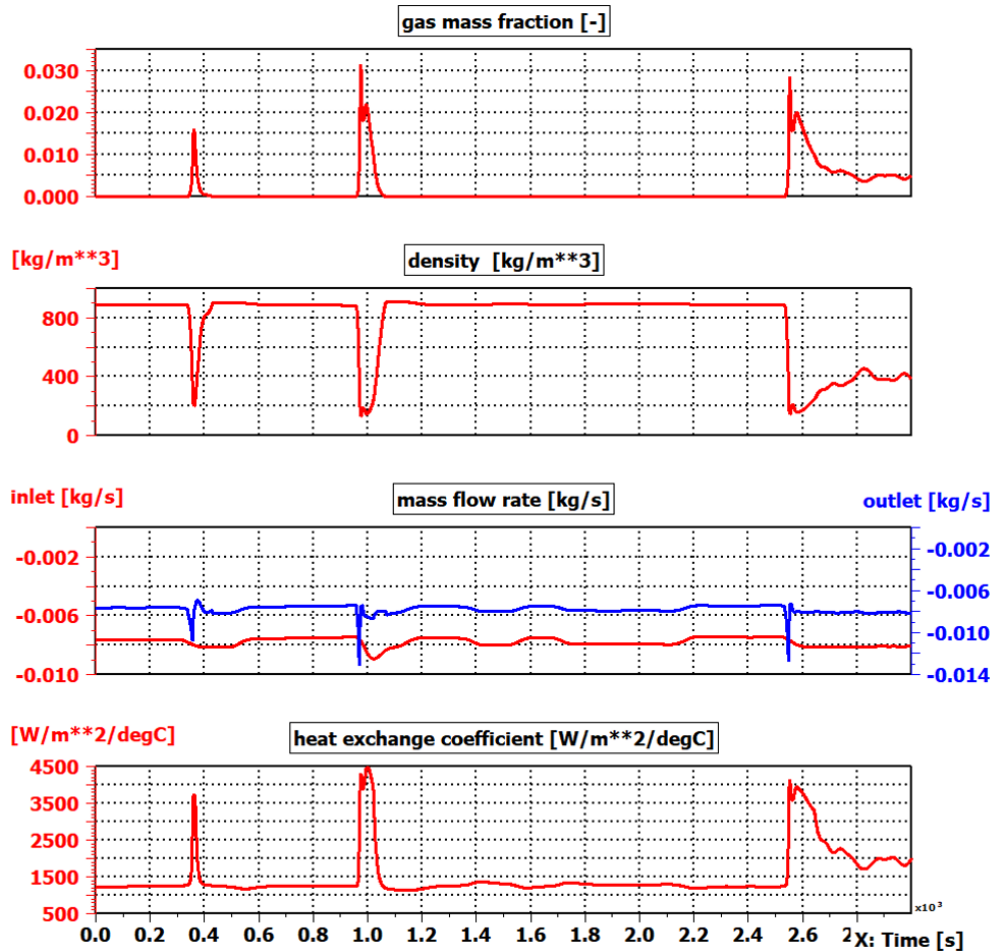
Figure 6.10 – Generation of numerical artifact due to the use of the finite volume approach for the modeling of the heat exchangers. results are presented in terms of gas mass fraction, density, mass flow rate and heat exchange coefficient in the cell the numerical issue arises (transition from liquid to twp-phase state).

6.2.2   Modeling the pump and expansion machines

Because the time constant of the rotating machines is smaller compared to those of the heat exchangers, the dynamics of those components is not taken into consideration. Considering positive-displacement machines and neglecting the ambient losses of the device models, the latter can be reduced to the expressions of the global isentropic effiency and the filling factor.

The two variables are defined, in equation 6.12 and 6.12 in the case of an expander.

$$\epsilon_s = \frac{\dot{W}_{sh}}{\dot{M}_{wf}(h_{wf,su} - h_{wf,ex,s}}$$ (6.11)

$$\Phi_f = \frac{\dot{M}_{wf}}{\rho_{wf,su} N_{rot} V_s}$$ (6.12)

The semi-empirical models developed in Chapter 5 are used to generate maps of isentropic effiency and filling factor required for the dynamic models. This enables to reduced the time of the dynamic simulations. To this end, the inputs of the steady-state models, i.e. the inlet and outlet pressures, the inlet temperature and the rotational speed, are varied in large ranges for which the model outputs, i.e. here the isentropic efficiency and the filling factor are evaluated. Results are stored into a text file and are presented through an example in Figure 6.11 for the isentropic efficiency of a screw expander.
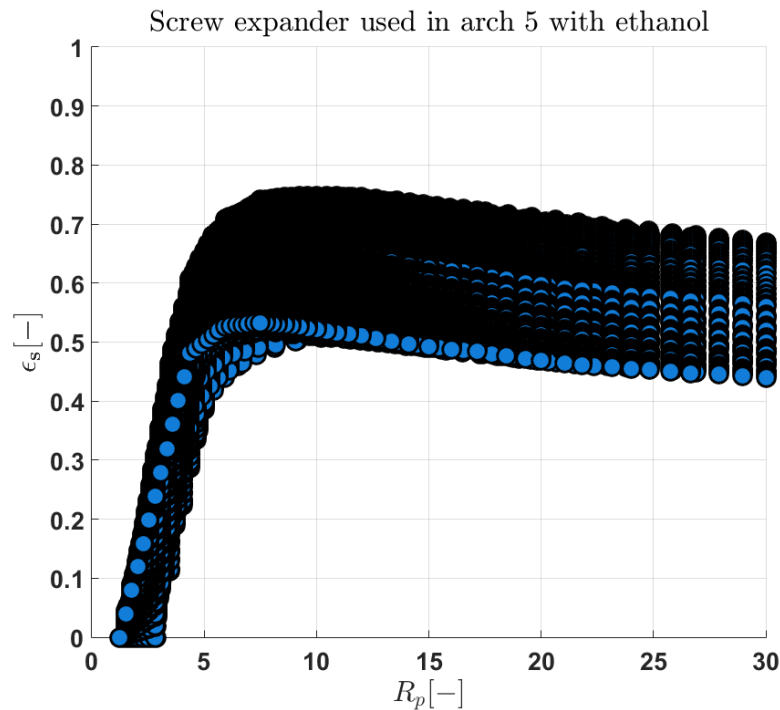
Figure 6.11 – Example of isentropic efficiency map of the screw expander built based on wild ranges of inlet and outlet pressure, inlet temperatures and rotational speeds. Results are showed as a function of the pressure ratio

6.2.3 Modeling the complete ORC systems

As for the steady-state models, modeling the complete ORC is achieved interconnecting the various components of the corresponding topology together. This achieved following the

bond graph rules through connectors transmitting the flow and effort variables from the exit of a component to the entrance of the next component.

In order to verify the reliability of the complete ORC models, the steady-state response of the different components is compared to the results obtained in Chapter 5 for the 17 investigated operating points. This is achieved for instance in the case of the third topology (EGR First) using the scroll expander and ethanol as working fluid. Results are presented for the second heat exchanger in Figure 6.12 in terms of water heat flow rate and outlet temperature. In Figure 6.13 are reported the mass flow rate and power outputs for the expander from the steady-state and dynamic simulations. As it can be observed for both components, the difference between steady-state responses of the AMESim model and the simulation results of the Matlab model are reduced. The maximal relative error on the heat exchanger ethanol heat flow rate is around 1% while the the absolute error on the water outlet temperature is around 4 K at the maximum. It is worth to note that the error on the later temperature also results from the model of the previous exchanger in the considered topology. Regarding the expander, the maximal relative error on the mass flow rate prediction is around 5 % but is lower than 1% in average. On the other hand, maximal relative error on the shaft power output prediction below 3 % while the mean relative error is below 1 %.
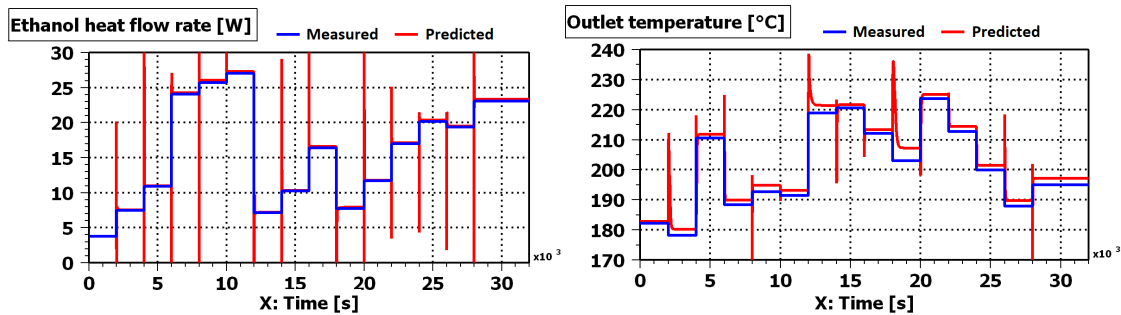
Figure 6.12 – Comparison in steady-state between the evaporator heat flow rate (left) and outlet temperature (right) obtained with the dynamic and steady models.
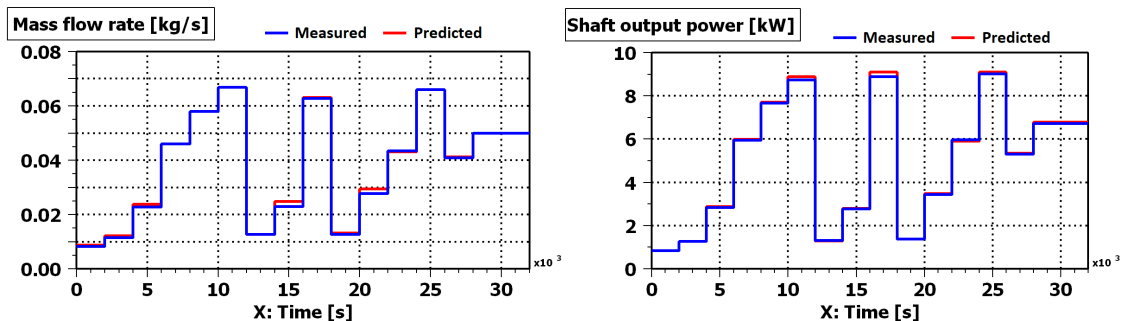
Figure 6.13 – Comparison in steady-state between the expander mass flow rate (left) and shaft power (right) obtained with the dynamic and steady models.

6.3 Control strategy

In order to operate waste heat recovery systems for the transient conditions of truck driving cycles, a control strategy has to be defined and implemented. Interest in power system control has grown significantly since the past few years, the goal being generally to maximize the performance of the system while the latter is run under safe conditions.

Many studies have been done in the field of stationary applications. For instance Quoilin [228] developed a dynamic model of a small-scale ORC unit equipped with a volumetric expander, to analyse and compare different control strategies based on the regulation of the pump and expander rotational speed. Hou et al. [229] proposed a decentralized predictive controller to track the working fluid temperature after the evaporator. Zhang et al. [230] designed and validated a multi-variable control strategy for one operating point. Zhang et al. [231] [232] also proposed advanced controllers, such as model predictive controllers in order to handle multi-variable constrained problems.

The task is more complex in the field of mobile applications because of the transient nature of the heat sources and sinks, as well as because of the interaction of the ORC system with the vehicle and its limitations. Stobart et al. [233] highlighted the influence of the system architecture on the control ability. Control variables were shown more suited to enhance the system performance. Willems et al. [234] developed an optimal control strategy for the entire powertrain in order to maximize the NOx-CO2 trade-off. Luong et al. [235] presented a linear quadratic integral controller for a system recovering heat from exhaust and recirculated gases in parallel. Peralez [51] presented the experimental validation of different controller structures. Feru et al. [52] reported the development of linear and non linear MPC and their performance but no experimental validation is proposed. Grelet [53] compared various control strategies from PID controllers with gain scheduling to complex model predictive controllers to regulate the overheating degree of the working at the outlet of the evaporator. It was also pointed out the automotive electronic control units are not as powerful as current computers, which should be taken into account when designing control strategies for automotive waste heat recovery devices. Indeed, despite the increasing number of electronic systems in nowadays vehicles, the control complexity level has not increased so much because of cost and complexity reasons. Most of the controllers are open loop and based on maps, which result from experimental measurements achieved during the engine development [53]. When closed loop control strategies are used, they are generally based on the proportional-integral-derivative (PID) controller because, among other, of their low computational complexity.

PID controllers have three main tuning parameters, often called gains (proportional, integral and derivative). In 1942, Zielgler and Nichols [236] proposed probably the first systematic and robust tuning procedure. The method is based on a quarter decay ratio response and known to provide good disturbance rejection but often results in too aggressive controllers. Over the years, various authors investigated the subject. Skogestad [237] introduced the rules of the SIMC methods, for first and second order models, which may be derived from the direct

synthesis proposed by Smith et al. [238] or the IMC-PID tuning rules proposed by Rivera et al [239]. Madhuranthakam et al [240] proposed generalized correlations for optimal tuning of PID controllers for different processes: first order and second order plus time delay systems. The tuning is achieved in order to minimize of the integrated absolute error either on a load or a set point change [53].

Because of the non-linearity of the ORC system and of the highly transient nature of the heat sources and sinks, linear type invariant (LTI) controllers are not suited to manage the process variables during dynamic driving cycles. To overcome this issue, various approaches have been proposed. Grelet [53] reviewed those methods and compared their performance. The first approach is the schedule of the controller parameters according to the operating conditions in order to take into account those non-linearities of the system to control. A nonlinear command is thus built by interpolation of several linear command defined locally (Figure 6.14). The method relies on a multi-linear model approach where each linear model represents the system on one of the multiple considered operating points. The global model results from the combination of the linear models and is used to approximate the true behavior of the nonlinear system. Therefore, linear models have first to be developed. In this design
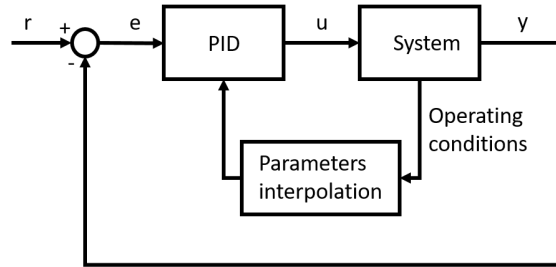
Figure 6.14 – Schematic of the feedback loop and interpolation process involved in the method proposed to schedule the gain of the controllers.

procedure it is achieved by linearization of the existing validated detailed nonlinear models considering those model as single input single output (SISO) system of the form:

$$\dot{x} = f(u, x) \tag{6.13}$$

$$y = g(u, x) \tag{6.14}$$

where u and y are respectively the manipulated and controlled variables. In the present case, the dynamic relation between the variation of u and y around an operating point can be described by a First Order Plus Time Delay (FOPTD) Transfer Function (TF):

$$H = \frac{y}{u} = \frac{G}{1 + \tau s} e^{-\theta s} \tag{6.15}$$

which is a commonly adopted linear model in the industry [53].

The nonlinear behavior of the system can thus be split into several local operating regimes identifying for each one an equivalent linear system H_i, FOPTD type transfer function, in which the model parameters are the static gain G_i, the time constant τ_i and the delay θ_i. In this work the 17 operating conditions of the frequency map considered in Chapter 5 and used for the steady state simulations of the ORC systems are used to this end. The strategy is also kept simple and consists in controlling the speed of the pump and expander to achieve set points, defined a priori, of overheating degree and evaporating pressure respectively. According to the topology, 2 to 3 systems are involved in this control strategy and have to be approximated for each operating conditions:

- the system(s) composed of the pump and the evaporator

- the expander system

For the pump-evaporator systems, the manipulated variable (u) is the pump speed while the controlled variable (y) is the overheating degree. On the other hand, for the expander system, the manipulated variable is the expander speed and the controlled variable is the expander inlet pressure. For each system and each operating conditions, a pseudo random binary sequence (PRBS) is carried out over the input and used for the simulation of the detailed nonlinear system, during which the system response (or output) is recorded. Based on the input/output of each plant, a FOPTD transfer function is identified for each operating conditions adjusting the transfer function parameters so to minimize the NRMSE (Eq. 6.16 between the linear and non linear model outputs obtained for the corresponding input. To illustrate the method, Figure 6.15 reports the results in the case of the topology EGR first, using the scroll expander and ethanol as working fluid.

$$NRMSE = 100\left(1 - \frac{|y_{mes} - y_{pred}|}{|y_{mes} - \bar{y}_{mes}|}\right) \tag{6.16}$$

The linear model being identified, the PID controller parameters can be tuned based on the FOPTD transfer function parameters for the various operating conditions of each system, i.e. for each transfer function and corresponding pair of input/output. Nonetheless, the issue with this approach is the variation of the parameters between two operating points. A simple scheduling approach is to interpolate the controller parameters accordingly to the heat flow rate for for the ORC system, introducing the saturation of the working fluid so the input of the command parameters includes the four main input disturbances [53]:

$$\dot{Q}_{hf,su} = \dot{M}_{EGR}C_{p,EGR,su}(T_{EGR,su} - T_{wf,sat}) + \dot{M}_{EG}C_{p,EG,su}(T_{EG,su} - T_{wf,sat}) \tag{6.17}$$

In this study, it is proposed to subtract the mean values of the input and output signals before the identification of the first order transfer function and evaluate. This leads to more accurate first order models but also to a more effective control. The mean values of the manipulated
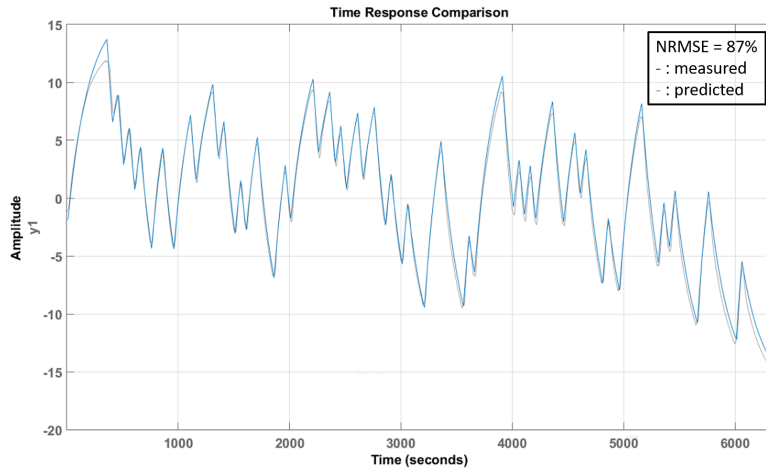
Figure 6.15 – Comparison between the measured and predicted responses of the detailed non linear model and by the equivalent linear system respectively to the PRBS inputs for a given set of gas and coolant conditions (or one of the 17 investigated operating points)

variables are interpolated according to the available heat flow rate as the gains of the pid controllers and are added to the PID outputs (Figure 6.16). In other words, based on the steady-state model and the identification process, the manipulated variables are estimated based on the available gas heat flow rate while the pid only aim at adjusting the manipulated variable in a limited range based on the input error.

$$H = \frac{y - \bar{y}}{u - \bar{u}} = \frac{G}{1 + \tau s} e^{-\theta s} \tag{6.18}$$

This decentralized strategy assumes independent controllers. However, because the process are coupled, the control strategy is generally more complex even if this one is facilitated by the slow nature of the input disturbances and the predictable operation [232]. This is particularly true in mobile applications because of the highly transient nature of the heat sources and the system limitations (e.g. cooling margin). However the pid controllers of the expander and of the pump are also characterized by very different time constant which should avoid conflicts.

6.3.1 Scripting

The parameterization process and the validation of the AMESim models in steady-state is facilitated through a script written in the Matlab environment. The steady-state models are used to identify the main geometric parameters of the ORC components. Thus, the heat transfer areas, the cross sectional areas, the hydraulic diameters, the lengths, etc can be identified for the heat exchangers while the displacements of the expander and of the pump can be evaluated. The parameters needed for the AMESim simulations are thus stored and
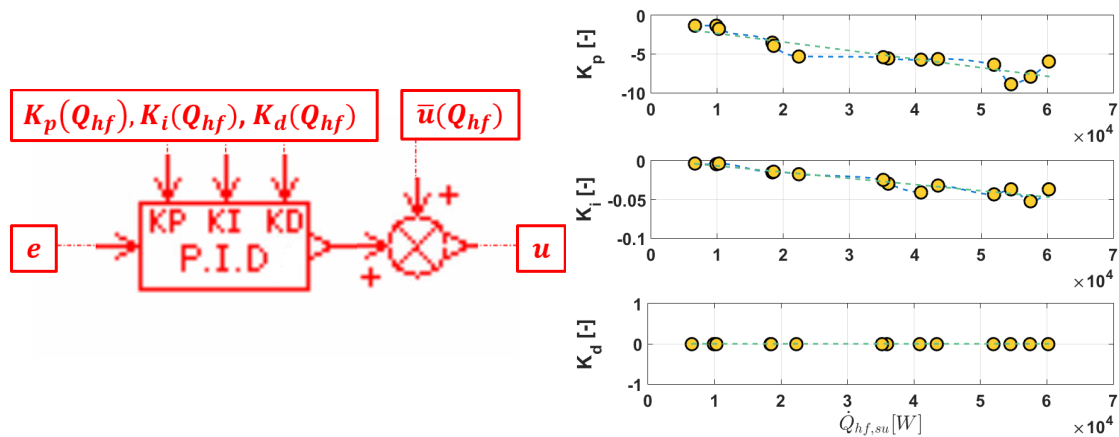
Figure 6.16 – Left: Schematic of the controllers developed in AMESim to regulate the speed of the expander and pump. Right: Example of gain controller set obtained for the pump controller and the investigated operating conditions

loaded in the AMESim model. In a second step, the exogenous inputs of the AMESim models as well as the model outputs are identified in the Matlab environment, using the steady-state simulation results, stored and loaded in the AMESim platform in order to compare the steady state responses of the dynamic models to the steady-state results. Finally, the script generates the *prbs* inputs required for the system identification process previously described. Dynamic simulations are performed for those excitation signals and the script then collects the interest variables (working fluid temperature at the outlet of the evaporator and inlet pressure of the expander). Based on the inputs/outputs, the identification process of equivalent linear systems, first order transfer function with time delay type, is achieved for the various operating conditions. Those linear systems are then used to tune the pid controller gains for each operating conditions. The corresponding gains are interpolated according to the heat available in the recirculated and/or exhaust gases and loaded in the AMESim model. The exogenous inputs are now the gas and water conditions from the driving cycle data.

6.4 Simulation results

6.4.1 Duty cycles

In order to accurately assess the potential of the ORC system, dynamic driving cycles are used to complete the study and check whether the performance found with the steady-state simulation is correct. The driving cycle used is split into 7 phases supposed to represent all conditions met in a long haul truck usage. Each phase is considered as a unique driving cycle and assigned to a weight according to its contribution in the real life road profile (for a long haul truck highway is predominant). The driving cycle characteristics are summarized in table 6.1 while the mass flow rate (left) and temperature (right) profiles of the exhaust and

recirculated gases are reported in Figure 6.17.

Table 6.1 – Characteristics of the 7 investigated driving cycles

Driving cycle	1	2	3	4	5	6	7
Road type	Extra urban	Highway	Highway	Extra urban	Extra urban	Extra urban	Hilly
Vehicle speed	Mid	High	Mid	Low	Mid	High	High
Weight	0.1	0.1	0.5	0.075	0.1	0.075	0.05
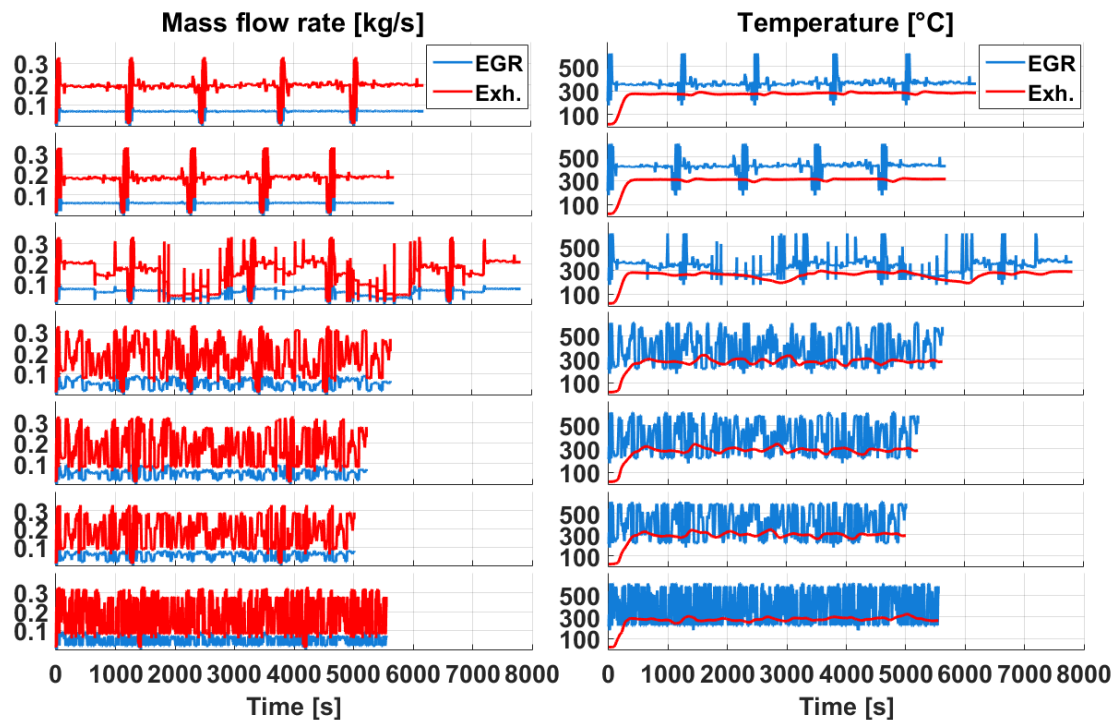
Figure 6.17 – Mass flow rates and temperature profiles of the exhaust and recirculated gases recorded for the 7 investigated driving cycles

6.4.2 Pressure and temperature control

An overheating of 20 K is set as reference for the pump controllers for simplicity reasons while the reference for the expander controller is derived based on the steady results. Indeed for each of the 17 operating conditions of the steady-state simulations, the evaporating pressure has been optimized. An interpolation is achieved between those values, as for the controllers gain, as a function of the available heat flow rate. This interpolated signal is then used as input of optimal pressure for the expander controllers. The control accuracy is showed through an example in Figure 6.18 for both controllers of the same architecture. As it can be seen, the error on the expander inlet pressure is very limited while the error on the overheating set

point is of a few K. For all the driving cycle, the overheating degree is kept above zero ensuring safe operation of the expansion machine except during phases in which the engine torque is close to 0. The introduction of a valve bypassing the expander might therefore be envisaged. However it might also be unnecessary since the failures in keeping a positive overheating level of the controller are unusual while scroll and screw expanders can be designed to withstand those failures. In addition, a more advanced control strategy might also manage to avoid those failures.
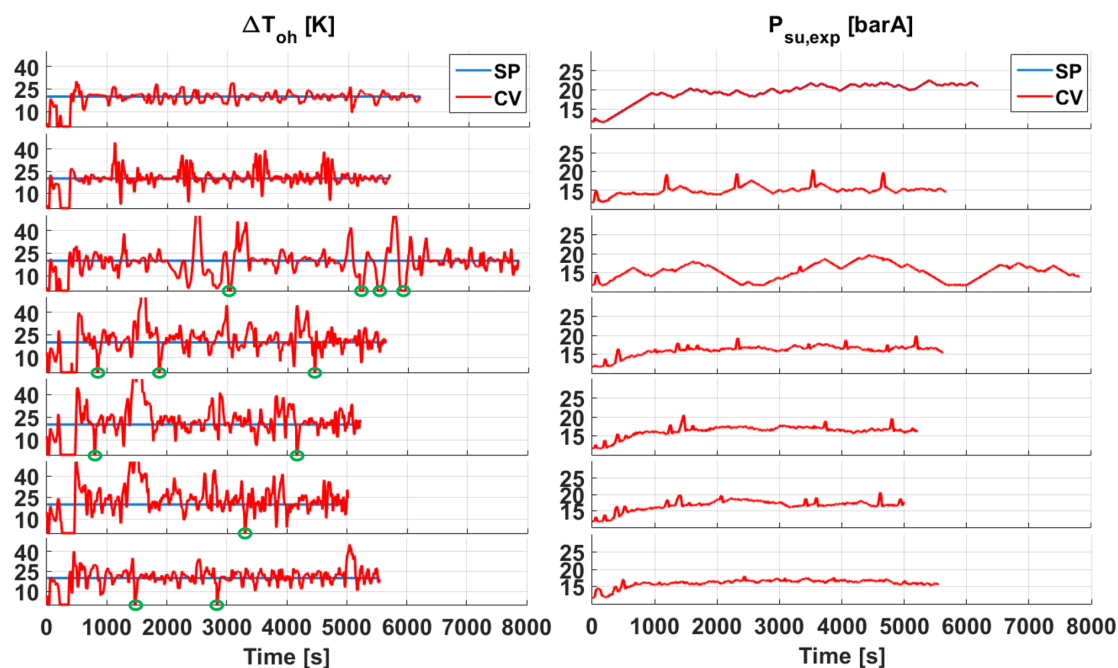
Figure 6.18 – Time evolution of the controlled variables and corresponding set point of the different controllers obtained for the 7 investigated driving cycles

6.4.3 Constraints and performance

The constraints established for the evaluation of the off-design performance in Chapter 5 must also be observed within the dynamic simulations. They concern the maximal inlet temperature of the expander, the minimal vapor quality at the end of the expansion, the limited heat capacity margin of the front end radiator and the temperature of the exhaust and recirculated gases at the outlet of the ORC heat exchangers. The inlet temperature and outlet vapor quality limits are always observed. If they were not, a solution would be to adjust the temperature and pressure set points at the inlet of the expander. On the other hand, the limit on the heat rejection at the ORC condenser as well as the impact on the fan activation require a model of the engine cooling loop to be estimated. The limit is therefore unknown here. Here, the heat flow rates on the secondary fluid side of each heat exchanger of the parallel topology including the screw expander and using ethanol as working fluid are

reported in Figure 6.19. A first estimation of the additional heat rejection might be provided subtracting the EGR heat flow rate from the condenser heat flow rate. The resulting additional heat rejection is comparable to the EGR heat flow rate level (red) and is therefore not presented for clarity reasons. In average, the level is around 20 kw with peak values up to 40 kW. Another challenging part consists in keeping the recirculated gases temperature in range between 100 and 120 $°C$ and the exhaust gases temperature above 100 $°C$ at the outlet of the ORC heat exchangers. As it can be seen in Figure 6.19, the adopted control strategy is able of observing those constraints the major part of the time for the investigated systems and driving cycles based on the expander inlet pressure and temperature set-points. However, to make sure those constraints are always observed a more advanced control strategy might be established. In
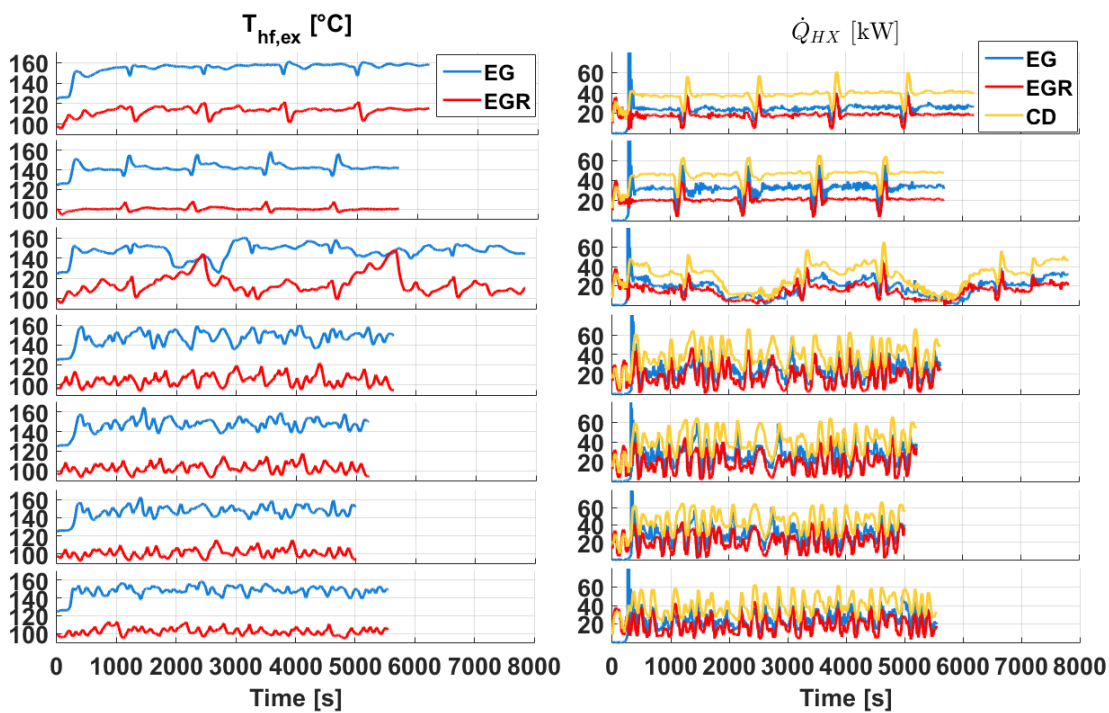
Figure 6.19 – Left: Time evolution of the gas temperature at the outlet of both exchangers for the 7 investigated driving cycles. Right: Time evolution of the heat flow rates obtained on the working fluid side of the different heat exchangers of the ORC system for the 7 investigated driving cycles.

Figure 6.20 are reported, for the 7 investigated driving cycles, the time evolution of the power at the shaft of the expander and pump as well as the time evolution of the global isentropic efficiency of those components.

6.4.4 Fuel savings and economic indicators: weighted averaged values

As explained an average is calculated on the relevant quantities based on the seven driving cycle and their respective weight to identify the mean performance of the ORC systems and its
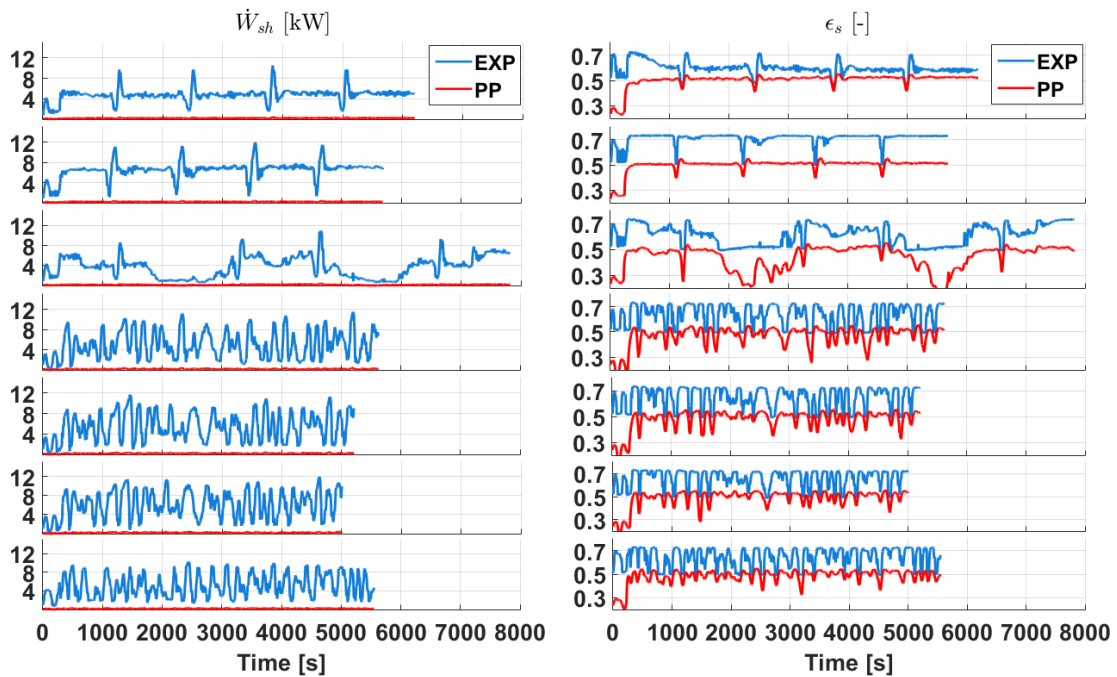
Figure 6.20 – Left: Time evolution of the input (resp. output) power at the shaft of the pump (resp. expander) for the 7 investigated driving cycles. Right: Time evolution of the isentropic efficiency reached by the pump and the expander for the 7 investigated driving cycles

consequence on the engine efficiency and economic indicators. Additional heat needed to be rejected at the front end of the truck is reported for the investigated topologies in Figure 6.21. Again here, the share resulting from the recovery of the recirculated gases is considered not affecting the heat rejection. Topology EGR First leads to a reduced heat rejection compared to the parallel topology. At the end the impact on the activation of the truck fan has to be identified to establish the most suitable architecture. Based on the power output weighted over the 7 investigated driving cycles, the increase in engine efficiency can computed, all other thing being equal. As in Chapter 5 the current engine efficiency is calculated based on the engine speed, torque and fuel consumption measurements. The Lower Heating Value (LHV) of $43.4MJ/kg$ is assumed for the fuel. The engine efficiency of the truck equipped with the WHR system is computed taking into account the net output power of the ORC system. Finally the fuel consumption reduction is estimated computing the fuel quantity required to achieve the same torque and speed values as the original engine based on the new efficiency. Results are depicted in Figure 6.21 where fuel consumption reduction ranges from 2.3 to 3.2%. The parallel topology, whether the scroll or the screw expander is considered lead to a more important fuel economy but also to an higher additional heat rejection. The obtained fuel economy can be compared to the steady-state results of Chapter 5 where fuel economy higher than 6% was reached. The difference is justified by the consideration of operating conditions corresponding to to reduced engine torque in the steady-state simulations. It turns out those points are mainly located in the beginning of the driving cycles where the engine

starts. It is observed through the dynamic simulations that the net output power of the ORC system, which is also starting, is null in those region while steady-state simulations led to a non negligible fuel economy. A new estimation can thus be provided based on the steady simulations taking off the operating conditions corresponding to reduced engine torques (for instance below 50 Nm). Results are shown in Figure 6.22 and are now similar, using ethanol as working fluid, to the results obtained through the dynamic simulations. Acetone and cyclopentane also lead to fuel economy comparable or even higher than ethanol, but as in Chapter 5, the NPV (updated) after the 3 tears project is lower with those fluids compared to ethanol 6.23.

The economic indicators introduced in the previous Chapter can be updated. Again it is assumed, the investment to be made by the future truck owner, or the price of the WHR system, is 1.5 the manufacturer TIC. The HDT is considered to travel 150000 km per year and is characterized by a life length of 10 years (or 1500000 km) and consumes in average $35 l/100 km$ with a diesel price of 1.1 €/l. The indicators are computed assuming the truck owner sells the truck after 3 years of usage. The time of the project is thus reduced from 10 years (truck lifetime) to 3 years. Results are shown in figures 6.21 and 6.24. The annual money savings based on the fuel consumption reduction range from 1310 to 1830 €/year. Based on this values, the payback period ranges from 2 years for the parallel topologies to 2.5 to 2.6 years for the topology EGR first. The Net Present Value is computed assuming a discount rate of 10% while
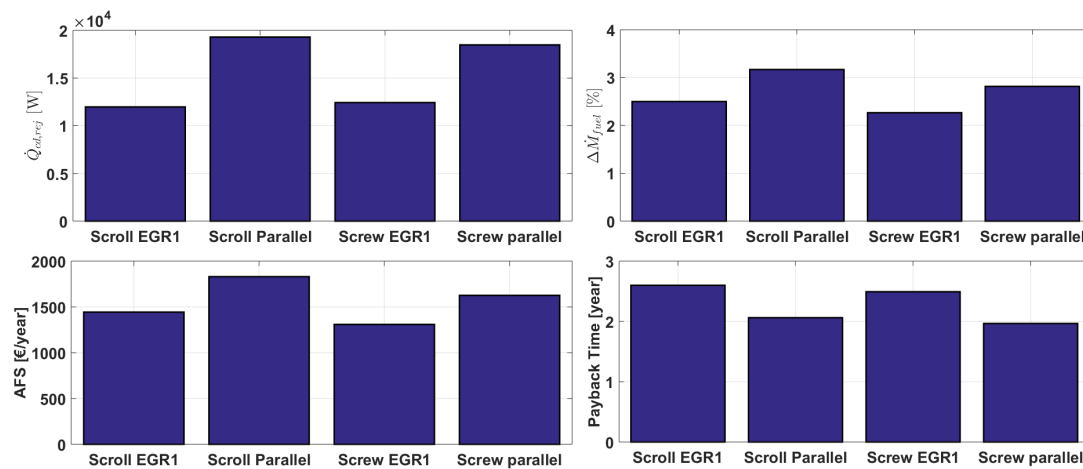
Figure 6.21 – Top-left corner: Mean value of the additional heat rejection due to the integration of the ORC system obtained with the 4 investigated topologies. Top-right corner: Mean value of the fuel consumption reduction obtained with the 4 investigated topologies. Bottom-left corner: Annual money savings resulting from the fuel consumption reduction obtained for the 4 investigated topologies. Bottom-right corner: Payback period, based on the TIC and mean fuel consumption reduction of the 4 investigated topologies.

the only cash inflows and outflows are the annual fuel savings tanks to the WHR system and the annual maintenance costs (100 €/year [33]. A yearly increase of 5 % of this price is also assumed. Only the parallel topologies appear to be profitable with a NPV of 1000 € at the end of
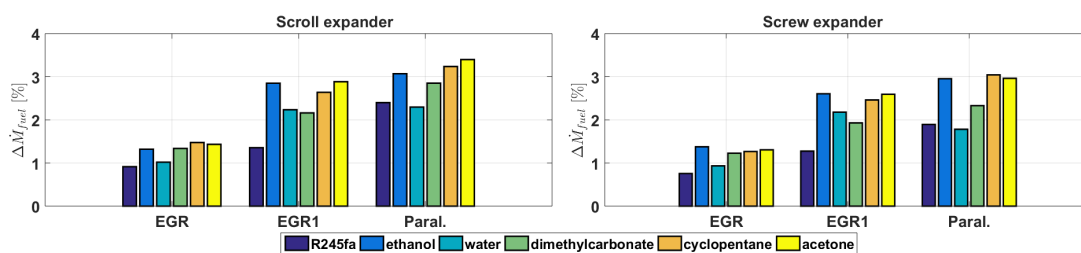
Figure 6.22 – New estimation of the fuel consumption reduction using the steady-state model and taking of the operating conditions corresponding to a reduced engine torque ($\leq 50 Nm$)
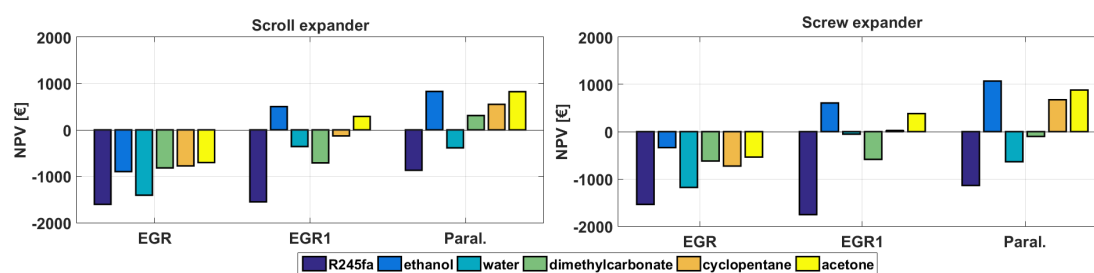
Figure 6.23 – New estimation of the NPV using the steady-state model and taking of the operating conditions corresponding to a reduced engine torque ($\leq 50 Nm$)

the 3 years project while the topology EGR First using the screw expander leads to a NPV of 70 € and the last topology to a negative NPV (-51 €). This partly results from the selected discount rate. The Internal Rate of Return (IRR) of investment, value of the discount rate that makes the NPV equal to 0, indeed ranges from 9.2 % for the topology EGR First using the scroll expander to 26.75 % for the parallel topology with the screw expander. By analogy to the IRR definition, the TIC that would make the NPV equal to 0 is evaluated. This Maximal Acceptable Investment (MAI) gives the investment above which the project is not profitable for the future truck owner based on the fuel economy and the maintenance costs of each year of the project. Only the parallel topologies are characterized by a MAI significantly higher than the TIC. The same exercise is also performed to estimate the minimal Acceptable Fuel consumption reduction (mAF) that makes the project profitable based on its price $C_0 = 1.5 TIC$. To be cost effective, the topologies using the crol expander should lead to a minimal fuel economy of 2.5 % while the topologies using the screw expander are profitable as soon as the fuel economy is above 2.2 %.

It is worth to note the results highly depend on the fuel price, investigated engine and driving cycle. Based on an average annual increase of the fuel price of 5 %, a system leading to 1.5% of average fuel consumption reduction would be profitable in 2025. On the other hand, the TIC does not take the cost of the additional electric motor, generator and batteries into account. However a 50 % profit for the manufacturer is probably overestimated. The weight of the ORC system also implies a penalty in fuel consumption or a reduction of the trailer load. The
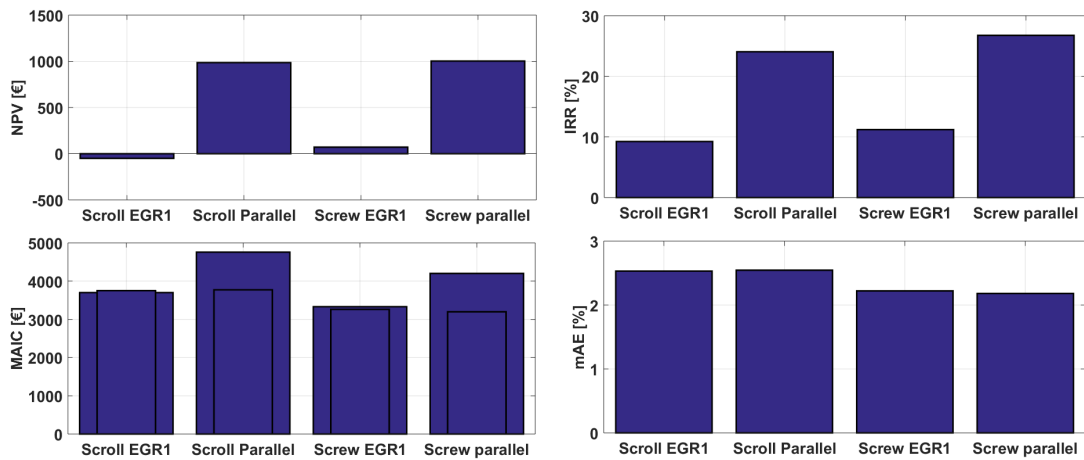
Figure 6.24 – Top-left corner: Net present value of the 4 investigated topologies. Top-right corner: IRR value of the 4 investigated topologies. Bottom-left corner: Maximal acceptable investment cost (and superposed TIC) estimated for the 4 investigated topologies. Bottom-right corner: Minimal acceptable engine efficiency improvement estimated for the 4 investigated topologies.

eventual wider use of the cooling fan should also be considered. Another interesting fact concerns the engine start up. During this phase a major part of the energy is devoted to heat up the engine, coolant and lubricating oil. Even if the net power output of the ORC system is null in this phase, transferring part of the thermal energy content of the gases to the coolant contribute to accelerate the heat up of the engine during the start up phase and reduce the fuel consumption. Finally, in order to be complete, the mechanical coupling of the expander and engine shafts through a gear ratio should also be investigated.

6.5 Conclusion and perspective

The importance of dynamic simulation in the design phase of ORC systems for waste heat recovery from engines of heavy duty trucks is demonstrated in this Chapter. The transient nature of the heat sources coupled to the interaction of the ORC system with the truck engine and cooling loop are the main reasons. Dynamic models are also useful in process control systems for tuning the automatic controllers before they are implemented or to train the personnel before controlling the real system. The need for multi-domain dynamic simulation has led to the development of numerous software. The Thermocycle library developed in Modelica language for Dymola in University of Liege and the AMESim software have been briefly compared and the robustness of the AMESim solver as well as the generality of the physics-based models has been retained as the most important criteria, even if it can imply an higher computational time.

Models of the 5 system topologies presented in Chapter 2 and varying according to the number

of heat sources used for the heat recovery are developed. These dynamic models are built using a finite volume approach for the heat exchangers. Care must be taken regarding the dynamic models. Indeed, because of the finite volume approach used to model the heat exchangers, numerical issues can sometimes be observed, mainly if the mass flow rate of the working fluid is low. Properly predicting the heat exchanger dynamic behavior is an essential task towards the modeling of a whole ORC system. A validation of the heat exchanger model has been done. The shell and plate type heat exchanger investigated in Chapter 5 has been submitted to a set of dynamic experiments and the simulation results are confronted to the experimental data. During the experiments, the temperature and mass flow conditions on the exhaust gas side were kept unchanged. The effect of the pump speed step changes on the water temperature at the outlet of the heat exchanger are compared against the finite volume model. The level of discretization on the prediction accuracy and computational time has also been investigated. The rise of numerical artifacts inherent to the finite volume approach has been discussed and some of the existing solutions to those numerical issues have been reviewed.

For both volumetric rotating components, the displacements are fixed and the evolution of the isentropic and volumetric efficiencies with operating parameters are set through performance maps obtained with the steady-state models of Chapter 5.

The ORC system models are assembled interconnecting the required components. In order to verify the reliability of the complete ORC models, the steady-state response of the different components is compared to the results obtained in Chapter 5 for the 17 investigated operating points. The performance of the systems can then be evaluated along driving cycles of the truck so to predict, among other, the power output of the WHR system and the resulting fuel economy of the engine. The heat rejection at the condenser of the system is another important output.

However evaluation the ORC systems performance in transient regime require an appropriate control strategy. The gain scheduling method, which consists in interpolating the respective gains of various PID controllers identified for different boundary conditions of the system already provides good results. In this work it is thus proposed to control, through PID controllers, the speed of the pump and expander so to keep respectively the overheating degree and evaporating pressure close to defined set-points. Two PID controllers are thus required. They are assumed independent and their gain values are identified for the 17 operating points of the frequency map proposed in Chapter 5. Linear models have first to be derived. In this design procedure it is achieved by linearization of the existing validated detailed nonlinear models considering those models as single input single output (SISO) systems and using a First Order Plus Time Delay (FOPTD) Transfer Function (TF).

To facilitate the parameterization process and also compare the steady-state response of the dynamic models against the steady-state model results, an interface has been developed in Matlab. The script also generates the input signal required for the system identification

process previously described. Dynamic simulations are performed using those excitation signals and the script then collects the interest variables (working fluid temperature at the outlet of the evaporator and inlet pressure of the expander). Based on the inputs/outputs, the identification process of equivalent linear systems, FOPTD TF type, is achieved for the various operating conditions. Those linear systems are then used to tune the pid controller gains for each operating conditions. The corresponding gains are interpolated according to the heat available in the recirculated and/or exhaust gases and loaded in the AMESim model.

The required controllers being developed, simulations along driving cycles can be achieved. The driving cycle used consists in 7 phases supposed to represent all conditions met in a long haul truck usage. Each phase is considered as a unique driving cycle and assigned to a weight according to its contribution in the real life road profile. The exogenous inputs of the AMESim model are the gas and water conditions from the driving cycle data. Simulations results are reported for the 4 most promising architectures identified in Chapter 5. An average is achieved on the relevant quantities based on the seven driving cycle and their respective weight to identify the mean performance of the ORC systems and its consequence on the engine efficiency and economic indicators. Based on the power output weighted over the 7 investigated driving cycles, the increase in engine efficiency can computed, all other thing being equal. The fuel consumption reduction ranges from 2.3 for the topologies EGR First to 3.2% for the parallel topologies. However the parallel topologies also leads to an higher heat rejection at the conser compared to the serial architectures. The annual money savings based on the fuel consumption reduction range from 1310 to 1830 €/year. Based on this values, the payback period ranges from 2 years for the parallel topologies to 2.5 to 2.6 years for the topology EGR first. Only the parallel topologies appear to be profitable with a NPV of 1000 € at the en of the 3 years project while the topology EGR first using the screx expander leads to a NPV of 70 € and the last topology to a negative NPV (-51 €). The Internal Rate of Return (IRR) of investment, value of the discount rate that makes the NPV equal to 0, indeed ranges from 9.2 % for the topology EGR First using the scroll expander to 26.75 % for the parallel topology with the screw expander. The Maximal Acceptable Investment (MAI) gives the investment above which the project is not profitable for the future truck owner based on the fuel economy and the maintenance costs of each year of the project. Only the parallel topologies are characterized by a MAI significantly higher than the TIC. To be cost effective, the topologies using the scroll expander should lead to a minimal fuel economy of 2.5 % while the topologies using the screw expander are profitable as soon as the fuel economy is above 2.2 %. Those results depend on the fuel price, investigated engine and driving cycle. Based on an average annual increase of the fuel price of 5 %, a system leading to 1.5% of average fuel consumption reduction would be profitable in 2025. On the other hand, the TIC does not take the cost of the additional electric motor, generator and batteries into account but a 50 % profit for the manufacturer is probably overestimated. The weight of the ORC system also implies a penalty in fuel consumption or a reduction of the trailer load and the eventual wider use of the cooling fan should also be considered. Finally it might also be interesting to investigate the influence of the ORC system on the heat up of the engine during the start up phase.

7 Conclusion

The integration of the Rankine technology in the automotive domain requires specific R&D activities. In particular the identification and optimization of the architecture, the selection of the working fluid and components maximizing the system performance are of primary importance during the design phase of the system. The control of the system is another key element in order to maximize the system performance and guarantee its safe operation. Nonetheless, it should be kept in mind the automotive sector is an economical market. Performance is thus not the only factor to take into consideration during the design but the minimization of the costs and maximization of the profit have also to be guarantied for the actors so that a new technology can be introduced in the field. In this regard, the present work contributes to the design activities of the ORC system devoted to recover the heat wasted from engines of long haul trucks taking into consideration both performance and economical aspects. A model-based methodology is proposed to identify the design conditions of the WHR system, to minimize the specific investment cost of the system and to optimize the performance of the ORC unit in off-design conditions. Because the reliability of the model is essential, a major part of this work has also been devoted to the experimental study of various components of ORC systems. Thus many prototypes of expanders, heat exchangers and volumetric pumps have been investigated on test rig. The resulting data has been used to validate the models of ORC components in both steady-state and transient regimes if needed.

In this Chapter, the work achieved is first summarized Chapter by Chapter. Then scientific contributions are listed and perspectives for future work are discussed.

7.1 Summary

Chapter 2 justifies the introduction of Waste Heat Recovery Organic Rankine Cycle systems in Heavy Duty Truck applications and sets the boundary of the study. The main drivers leading the engine designers to constantly improve the engine efficiency are introduced. It is worth noting the potential sources of improvement are multiple on a truck and there is no unique solution. The future improvements in the engine thermal efficiency will certainly result from

combination of various innovative solutions concerning most parts of the truck. The use of a waste heat recovery system is one of those solutions, which can contribute in a relevant way considering the large amount of energy content in the exhaust gases and engine coolant. Among the existing technologies the ORC system is shown as the most promising solution with a potential fuel reduction around 4-5 %. Regarding the architecture of the system, the recirculated and exhaust gases are identified as the most promising sources while the ram air through an indirect condenser is probably the safest approach to reject the heat of the ORC system. Combining these heat sources and sink, 5 possible architectures are investigated. The choice of the working fluid can be fastidious according to the number of substances available on the market. A method is proposed, eliminating fluids dangerous for the environment and the human health, and based on considerations on the thermophysical properties. For the component selection, based on the necessity to get reliable models, only experimentally investigated technologies are taken into consideration. Thus the investigated technologies of heat exchangers are limited to the shell and plate type on the high pressure side and brazed plate type on the low pressure side of the system. On the other hand various expansion devices have been investigated on test rigs, including positive-displacement machines (scroll, screw, piston, vane and roots expander) and a radial-inflow turbine. In the same manner, experimental data is gathered for several volumetric pumps.

Chapter 3 presents the experimental campaign carried out on a radial-inflow turbine integrated in a small scale organic Rankine cycle power unit for low grade waste heat recovery application built at the Thermodynamic Laboratory of the University of Liege. The performance of the different components are analyzed over a wide range of working conditions for two low critical temperature organic fluids: R245fa and its probable substitute R1233zd. Because of the numerous measurement issues that can arise in experimental campaigns the energy balance over the components are checked and an uncertainty propagation study is performed. Two types of comparison are then proposed for the performance of the ORC components according to the used working fluid. A first comparison based on same evaporating and condensing temperature levels for both fluids is performed. Secondly, the performance is compared for same pressure levels. This analysis experimentally demonstrates that, based on the given test-rig, R1233zd represents a better choice compared to R245fa to recover the waste heat of the exhaust gases of a long haul truck. It is also shown there is a large potential of improvement regarding the turbine-generator set and a first attempt to identify the performance of each subsystem, assuming there is no heat transfer between the latter subsystems, is proposed.

In Chapter 4 a model of the radial-inflow turbine, studied in Chapter 3, is developed, described and validated against experimental data. Modeling techniques for turbomachines are first reviewed as well as the main physical phenomena to take into account. The model is then confronted to the available experimental data and the ways to extrapolate the model are discussed. The turbine model is split in several stations in which the velocity triangles of the fluid flow are computed using real gas equations of state and mass, energy and momentum conservation equations. Correlations are used to describe the loss phenomena of each turbine

component located between 2 consecutive stations. The consideration of the heat transfer from the fluid expanded in the turbine and the lubrication fluid going through the bearings is discussed and estimated based on a model of the bearings. Two versions of the turbine model are compared and confronted to experimental data. Because the pressure ratio was always above the critical pressure ratio during the experiments, sonic conditions are reached for all the measurement points at the throat of the nozzle. The first model version considers the supersonic expansion in the vaneless space without formation of shock waves, thus only increasing the incidence losses at the rotor inlet. In the second version, the stator is treated in the same manner as a convergent-divergent nozzle row. The models are then exploited to estimate the distribution of the source of losses in the turbine. The models are also used to predict the performance obtained with fluid R1233zd on test rig. Again the model with shock loss gives more accurate results. The model being validated, it is also employed to extrapolate the performance of the turbine and evaluate the optimal speed of the component and the resulting efficiency of the machine. Finally a method to operate the turbine model in design in order to be integrated in an ORC optimization process is proposed.

Chapter 5 is dedicated to the design of the ORC system architectures and the validation of the other components of the ORC systems. Experimental works achieved on the heat exchangers, volumetric expanders and pumps are first presented. The models of those components are then described and confronted to experimental data. Numerous design steady-state models of ORCs are built interconnecting the required components. From the 5 proposed architectures and the 6 investigated expander technologies result 30 different topologies. A three-steps optimization is proposed for the design, performance evaluation and optimization of the ORC systems. First a methodology to identify the most suitable design conditions is exhibited. A thermo-economic optimization is then achieved for the obtained design conditions in order to minimize the specific investment cost of the ORC systems varying according to considered heat sources, ORC components and working fluid used. Constraint inherent to the integration of the ORC technology in the truck are taken into account. Finally, the performance of the resulting systems is evaluated for various off-design conditions representative of the truck driving cycle, optimizing the evaporating pressure and the overheating degree. In order to locate the sources of entropy increase in the proposed systems, and thus identify the possible weakness of the designed external combustion engine, an exergetic analysis is achieved. A sensitivity analysis is also performed to evaluate the impact of a variation of the system cost on the optimal specific investment cost. A first estimation of economical indicators (payback period, Net Present Value, etc) is provided based on the resulting fuel economy. Based on the results, it is shown that ethanol is the most appropriate working fluid and the use of the screw expander leads to the best average performance. Nonetheless, results are similar between the scroll, the screw expanders.

Chapter 6 demonstrates the importance of dynamic simulation in the design phase of ORC systems for waste heat recovery from engines of heavy duty trucks. The transient nature of the heat sources coupled to the interaction of the ORC system with the truck engine and cooling loop are the main reasons. On the other hand, dynamic models are useful in process

control systems for tuning the automatic controllers before they are implemented or to train the personnel before controlling the real system. Models of the 5 system architectures are developed in the AMESim software. These dynamic models are built using a finite volume approach for the heat exchangers. Properly predicting the heat exchanger dynamic behavior is an essential task towards the dynamic modeling of a whole ORC system. Therefore a validation of the heat exchanger model is achieved. The component has been submitted to a set of dynamic experiments and the simulation results are then confronted to the experimental data. The influence of the level of discretization on the prediction accuracy and computational time is also investigated. The rise of numerical artifacts inherent to the finite volume approach is discussed and some of the existing solutions to those numerical issues have been reviewed. For both volumetric rotating components, the displacements are fixed from the design step and the evolution of the isentropic and volumetric efficiencies with the operating parameters are set through performance maps obtained with the steady-state models. The ORC system models are again assembled interconnecting the required components. In order to verify the reliability of the complete ORC models, the steady-state response of the different components is compared to the results obtained in Chapter 5 for the 17 investigated operating points. Moreover, the evaluation of the ORC system performance in transient regime requires an appropriate control strategy. The gain scheduling method, which consists in interpolating the respective gains of various PID controllers identified for different boundary conditions of the system, is implemented to regulate, through PID controllers, the speeds of the pump and expander so to keep respectively the overheating degree and evaporating pressure close to defined set-points. The required controllers being developed, simulations along driving cycles can be achieved. The driving cycle used consists in 7 phases supposed to represent all conditions met in a long haul truck usage. Each phase is considered as a unique driving cycle and assigned to a weight according to its contribution in the real life road profile. The exogenous inputs of the AMESim model are the gas and water conditions from the driving cycle data. Simulations results are reported for the 4 most promising architectures identified in Chapter 5. The fuel consumption reduction ranges from 2.3 for the topologies EGR First to 3.2% for the parallel topologies. However the parallel topologies also lead to an higher heat rejection at the condenser compared to the serial architectures. The annual money savings based on the fuel consumption reduction range from 1310 to 1830 €/year. Based on this values, the payback period ranges from 2 years for the parallel topologies to 2.5 to 2.6 years for the topologies EGR first. Only the parallel topologies appear to be profitable with a NPV of 1000 € at the end of the established 3 years project while the topology EGR first using the screw expander leads to a NPV of 70 € and the last topology to a negative NPV (-51 €). The Internal Rate of Return (IRR) of investment, value of the discount rate that makes the NPV equal to 0, indeed ranges from 9.2 % for the topology EGR First using the scroll expander to 26.75 % for the parallel topology with the screw expander. The Maximal Acceptable Investment (MAI) gives the investment above which the project is not profitable for the future truck owner based on the fuel economy and the maintenance costs of each year of the project. Only the parallel topologies are characterized by a MAI significantly higher than the TIC. To be cost effective, the topologies using the scroll expander should lead to a minimal fuel economy of 2.5 % while

the topologies using the screw expander are profitable as soon as the fuel economy is above 2.2 %.

7.2 Contributions

- A methodology for the selection of the ORC working fluid candidates for the application has been proposed. To this end a data base gathering relevant thermophysical and safety properties has been built for a large range of pure and pseudo pure fluids. The typical prices of the substances as well as the applications in which in they are commonly involved have also been established. This database can be employed in the frame of any applications involving the selection of the working fluid (ORC systems, heat pumps, air-conditioning circuit, etc).

- A small scale ORC test-rig has been built and tools for the analysis of the experimental data have been developed (energy balance analysis, uncertainty propagation analysis, etc). Those tools could be employed in future experimental works.

- Additional experimental works have been done to investigate many other ORC components (volumetric expanders and pumps as well as heat exchangers) developing knowledge on those devices, their operation and the practice rules to carry on experimentation on each of them.

- Steady-state physics-based models of the components have developed in the Matlab environment. For each device a tool devoted to the calibration of the model parameters based on available experimental data has also been built. Combining those tools can be powerful in any future work involving this kind of components (heat exchangers, pumps and expanders).

- A 3-step optimization tool has been proposed for the design, performance evaluation and optimization of the ORC candidates for the investigated application. A first optimization tool is devoted to the selection of the design conditions. The second part is dedicated to the design process through a thermo-economic optimization. Moreover, economic models of the ORC components have been achieved and the results and/or the proposed approaches can be employed in other research fields. The last part of the tool is dedicated to the optimization of the system performance in off-design conditions for the selected operating points. The tool itself is dedicated to WHR ORC systems but can nonetheless be used for many other applications involving the ORC technology. On the other hand the 3-step approach can be generalized to other fields of investigation.

- Sensitivity and exergetic analysis tools proposed in this work can be employed outside the scope of this thesis.

- A set of dynamic models have also been developed for the ORC components in AMESim environment. Complete models of different ORC architectures have been built combining the latter models. A methodology for the dynamic validation of the heat exchanger

model is described. Those models and methods can be used outside the field of investigation of this work.

- A methodology, based on the gain scheduling method, has been proposed to automatically design PID controllers devoted to the regulation of the speeds of the expander and pump. It includes the excitation of the non linear system to control and the evaluation of the system response, a linear identification process, the tuning of the controller gains for various operating conditions. This approach can be extended to many other applications requiring the development of PID controllers.

- An interface has been developed to link the steady-state and dynamic models. It enables the automatic population of the dynamic model parameters based on the steady-state results. It also enables to compare the steady-state response of the dynamic models to the steady-state results obtained for various operating conditions. The design of the controller is also achieved through this script.

- Finally this thesis, combining all the contributions can be seen as the generalized tool for the design, optimization and performance evaluation of ORC systems for mobile applications. The only inputs required by this tool are the boundary conditions of the ORC unit.

7.3 Perspectives

From the work achieved, there is still a long way to go before considering the development of the waste heat recovery unit for the truck application. Obviously many other working fluids, components and heat source configurations could be investigated. The use of the engine coolant is for instance a solution commonly investigated by truck manufacturers [23]. Innovative solutions could also be imagined to reject the thermal energy from the condenser otherwise than using a front end radiator. The higher is the number of investigated configurations, the better will probably be the confidence in the results of the identification of the most promising architecture. On the other hand, additional selection criteria should also be considered in the selection process. In particular, the compatibility of the working fluids with material commonly used for the application should be ensured. Moreover, because no unique solution can be identified regarding the fluid selection, the use of mixtures (e;g. water-ethanol) coupling the advantages of the involved pure fluids could be investigated.

Regarding the experiments, the first perspective concerns the evaluation of the heat transfer between the expanded and the lubrication fluids. Because this heat transfer has a large impact on the performance, it would be worth investigating the bearing system more into details based on a reliable geometry description. On test rig, experiments could be achieved to evaluate the heat loss in the turbine without production of work, feeding the turbine and bearings with fluid while the rotor is kept at rest for instance. Those experiments could also be performed to ensure heat transfer is the only phenomenon to consider or if there is an

additional mass transfer from one component to another. Once the phenomenon clearly identified, solutions should be proposed to reduced the heat transfer. Indeed, this issue is not only reducing the power available at the turbine shaft but is also increasing the temperature of the bearing lubrication fluid thus limiting the inlet temperature and pressure and the rotational speed that can be reached by the turbine. Dynamic experiments on the turbine could also be achieved to evaluate the response of this system and its performance to transient modification of the rotational speed and mass flow rate. On the other hand because ethanol is identified as the most promising working fluid for the application, a test rig using this working fluid could be investigated and eventually coupled to a truck engine.

Based on the proposed experiments, the model of the turbine-generator set could be improved. A more advanced model of the bearings and of the heat transfer and eventual mass transfer could be implemented. Concerning the turbine design, a more detailed approach would require a CFD approach.

Moreover, additional work could be performed during the design of the ORC system. Based on the pressure drops in the high pressure heat exchangers, the engine back pressure can be evaluated and its impact on the engine performance and breathing could be quantified. In addition the approach proposed for the design procedure rely on experimental data gathered for each component of the system. Obviously the number of devices that could be tested in laboratory are limited. To increase the size of the data base, including new devices, and validate the scaling method proposed for the design of the components, bringing together experimental data and component models from other institutions, academic or not, would be valuable. The economic analysis should also take the cost of the envisaged generator, batteries and electric motor involved in the regulation of the speeds of the expander and consume the power produced by the WHRS. The electrification of the truck auxiliaries and its economic viability could also be considered. Finally, a key element in the introduction of the technology in the truck field will probably concern the reductions of the component costs.

Finally, during the evaluation of the system performance in transient regime, along driving cycles of the truck, the impact of the ORC system on the engine cooling loop and the fan activation should be further investigated. In this regard a mean value engine model has been developed but specifications of the cooling system are missing. For an even more complete study, a complete vehicle model could be developed so to, among others, evaluate the real benefit in fuel consumption thanks to the WHR system. The dynamic validation of the heat exchanger model, to be complete, should also evaluate the transient response of the system to modifications of the heat sources conditions. The dynamic behavior of the pump and expander could also be taken into account. A more advanced control strategy could also be implemented so to optimize the performance of the ORC units, ensure a safe operation of the system and the constraint inherent to the truck application are observed at all time. Finally additional numeric experiments could be performed to investigate the performance of the WHR unit for other driving cycle conditions. The thermal insulation of the exhaust pipe and its influence on the heat recovery could also be evaluated. More advanced ORC architectures

could finally be considered. For instance, the efficiency loss in the pump system is mainly coming from the electric motor and VFD losses. In this regards, solutions removing the motor and VFD, such as the coupling of the expander and pump shafts, or of the pump and engine shafts, through a gear have already been proposed. However, based on those solutions, a degree of freedom is taken off. Another possibility could be, for instance, to extract a part of the vapor during the expansion and carry on the expansion of the extracted fluid in an additional expander, of reduced size and driving the pump.

Bibliography

[1] ESA. Space in images: Liege, belgium. *http://www.esa.int/spaceinimages/Images/2013/12/Liege_Belgium.*

[2] KOKIC P, CRIMP S, HOWDEN M. A probabilistic analysis of human influence on recent record global mean temperature changes. *Climate Risk Management 2014; 3:1-12.*

[3] IEA. Key world energy statistics. *http://www.iea.org/publications/ freepublications//publication/KeyWorld2014.pdf 2014.*

[4] UNFCCC. Kyoto protocol to the united nations framework convention on climate change. *http://unfccc.int/resource/docs/convkp/kpeng.html 1992.*

[5] EUROPEAN COMISSION. Climate action. *http://europa.eu/pol/pdf/flipbook/fr/climate_action_fr.pdf,* .

[6] EUROPEAN COMISSION. Towards a strategy to address co2 emissions from hdv. *http://ec.europa.eu/clima/policies/transport/vehicles/heavy/index.htm 2013,* .

[7] EUROPEAN COMISSION. Greenhouse gas emissions, analysis by source sector. *2017; http://ec.europa.eu/eurostat/statistics-explained/index.php/Greenhouse_gas_emission_statistics,* .

[8] IPCC. Intergouvernemntal panel on climate change. *http://www.ipcc.ch/; 2017.*

[9] NASA, NOAA. Nasa, noaa data show 2016 warmest year on record globally. *https://www.nasa.gov/press-release/nasa-noaa-data-show-2016-warmest-year-on-record-globally.*

[10] RAFTERY AE, ZIMMER A, FRIERSON DMW, STARTZ R, LIU P. Less than 2 k warming by 2100 unlikely. *Nature Climate Change 2017; 7; 637-641.*

[11] EUROPEAN COMISSION. Climate action. *https://ec.europa.eu/clima/policies/strategies/2050_fr,* .

[12] ESPINOSA N, TILMAN L, LEMORT V, QUOILIN S, LOMBARD B. Rankine cycle for waste heat recovery on commercial trucks: approach, constraints and modelling. *SIA, Diesel International Conference and Exhibition, 2010.*

Bibliography

[13] MACCHI E, ASTOLFI M. Organic rankine cycle (orc) power systems technologies and applications. *Elsevier Edition 2016, Woodhead Publishing Series in Energy.*

[14] OEFELDT F. Naphta boats. *1887; http://www.google.com/patents/US356420;US Patent 356,420.*

[15] KCORC. History of the orc. *http://www.kcorc.org/en/science-technology/history/.*

[16] PATEL P, DOYLE E. Compounding the truck diesel engine with an organic rankine-cycle system. *SAE Technical Paper 1976; no. 760343, SAE International.*

[17] DOYLE E, DINANNO L, KRAMER S. Installation of a diesel-organic rankine compound engine in a class 8 truck for a single-vehicle test. *SAE Technical Paper 1979; no. 790646. SAE International.*

[18] KITSON AND COMPANY. The kitson-still steam-diesel locomotive. *1926; http://www.douglas-self.com/MUSEUM/LOCOLOCO/kitson/kitsonst.htm.*

[19] FREYMANN R, STROBL W, OBIEGLO A. The turbosteamer: A system introducing the principle of cogeneration in automotive applications. *MTZ worldwide 2008; 69(5): 20–27.*

[20] FREYMANN R, RINGLER J, SEIFER M, HORST T. The second generation turbosteamer. *MTZ worldwide 2012; 73: 18-23.*

[21] IBARAKI S, ENDO T, KOJIMA Y, TAKAHASHI K, BABA T, KAWAJIRI S. Study of efficient on-board waste heat recovery system using rankine cycle. *Review of automotive engineering 2007; 28(3):307–313.*

[22] ESPINOSA N. Contribution to the study of waste heat recovery systems on commercial truck diesel engines. *Institut National Polytechnique de Lorraine, Ecole doctorale EMMA, 2011.*

[23] FALCON PROJECT. http://www.fr.renault-trucks.ch/actualites/projet-falcon-k3j.html. *2017.*

[24] DICKSON J, ELLIS M, ROUSSEAU T, SMITH J. Validation and design of heavy vehicle cooling system with waste heat recovery condenser. *SAE International Journal of Commercial Vehicles, 7:458–467.*

[25] SALEH B, KOGLBAUER G, WENDLAND M, FISCHER J. Working fluids for low-temperature organic rankine cycles. *Energy 2007; 32(7):1210–1221.*

[26] HEBERLE F, BRÜGGEMANN D. Exergy based fluid selection for a geothermal organic rankine cycle for combined heat and power generation. *Applied Thermal Engineering 2010; 30(11-12):1326–1332.*

[27] ANDREASEN JG, LARSEN U, KNUDSEN T, PIEROBON L, HAGLIND F. Selection and optimization of pure and mixed working fluids for low grade heat utilization using organic rankine cycles. *Energy 2014; 73:204–213.*

[28] LINKE P, PAPADOPOULOS A, SEFERELIS P. Systematicmethods for working fluid selection and the design, integration and control of organic rankine cycles—a review. *Energies 2015; 8(6): 4755–4801.*

[29] FRANCE INFLATION. Evolution des prix des carburants. *http://france-inflation.com/prix-carburants.php.*

[30] ASHLEY S. Cummins aims to boost heavy-duty diesel efficiency to 55 *SAE Article 2015; 14388.*

[31] ECKERLE W. Engine technologies for ghg and low nox. *ARB Symposium on Phase 2 GHG 2015.*

[32] NOWASTE PROJECT. http://nowasteproject.eu.

[33] EXOES. L'avnir du moteur thermique. *http://www.exoes.com.*

[34] SERMENO S, BIDEAUX E, MORGAN T, NGUYEN D. Heavy duty vehicle cooling system auxiliary load management control: Evaluating the maximum gain of implementing an advanced control strategy. *In SAE Technical Paper 2014; SAE International.*

[35] MAMMETTI M, GALLEGOS D, FREIXAS A, MUNOZ J. The influence of rolling resistance on fuel consumption in heavy-duty vehicles. *In SAE Technical Paper 2013; SAE International.*

[36] BACHMAN LJ, ERB A, SELLERS J. Quantitative estimate of the relation between rolling resistance on fuel consumption of class 8 tractor trailers using both new and retreaded tires. *In SAE Technical Paper 2014; SAE International.*

[37] SUHRMANN JF, PEITSCH D. Daimler's freigthliner supertruck. *http://www.freightlinersupertruck.com, .*

[38] PATTERSON DJ, KRUISWYK RW. An engine system approach to exhaust waste heat recovery. *in DEER Conference, 2007.*

[39] HEAT2POWER. http://www.heat2power.net/. *2017.*

[40] TOOM R. The potential of the co2 emission reduction with a downsized engine and waste heat regeneration system. *in Engine expo 2008; Stutgart.*

[41] LEGROS A. *Conception d'un expanseur scroll adapté à la récupération d'énergie à l'échappement pour une application automobile : Aspects thermodynamiques et tribologiques.* PhD thesis.

Bibliography

[42] Lemort V. Contribution to the characterization of scroll machines in compressor and expander modes. *Universite de Liege, Liege, Belgique, 2008.*

[43] Quoilin S. *Sustainable energy conversion through the use of organic Rankine cycles for waste heat recovery and solar applications.* PhD thesis, University of Liege, Liege, Belgium, 2011.

[44] Declaye S. *Improving the performance of micro-ORC systems.* PhD thesis, University of Liege, Liege, Belgium, 2015.

[45] Oudkerk JF. *Contribution to the Characterization of Piston Expanders for their Use in Small-Scale Power Production Systems.* PhD thesis.

[46] Gunnar L. Waste heat recovery from combustion engines based on the rankine cycle. *Chalmers university of Technology 2016, Gothenburg, Sweden.*

[47] Stanzel N, Streule T, Preissinger M, Bruggemann D. Comparison of cooling system designs for an exhaust heat recovery system using an organic rankine cycle on a heavy duty truck. *Energies 2016; 9(11): 928.*

[48] Cippollone R, Bianchi G, Gualtieri A, Di Battista D, Mauriello M, Fatigati F. Development of an organic rankine cycle system for exhaust energy recovery in internal combustion engines. *Journal of Physics: Conference Series 2015; 655.*

[49] Pascual L. *Study of Organic Rankine Cycles for Waste Heat Recovery in Transportation Vehicles.* PhD thesis.

[50] Di Battista D, Cipollone R. Experimental analysis of an organic rankine cycle plant bottoming a heavy-duty engine using axial turbine as prime mover. *SAE Int. J. Engines 2017; 10(4).*

[51] Peralez J. Rankine cycle for waste heat recovery on board vehicles: control and energy management. *PhD thesis, Université Claude Bernard Lyon 1.*

[52] Feru E, Willems F, de Jager B, Steinbuch M. Modeling and control of a parallel waste heat recovery system for euro-6 heavy-duty diesel engines. *Energies 2014; 7(10):6571-6592.*

[53] Grelet V. *Rankine cycle based waste heat recovery system applied to heavy duty vehicles: topological optimization and model based control.* PhD thesis, University of Lyon, Lyon, France, 2016.

[54] Hernandez NJA, Inoescu C, Gusev S, Desideri A, van den Broek M, Lemort V, De Keyser R. Performance evaluation of mpc for waste heat recovery applications using organic rankine cycle systems. *Latin American control conference 2016, Medellin, Colombia.*

[55] Teng H, Regner G, Cowland C. Waste heat recovery of heavy-duty diesel engines by organic rankine cycle part i: Hybrid energy system of diesel and rankine engines. *SAE Technical Paper 2007-01-0537, 2007, doi:10.4271/2007-01-0537.*

[56] Edwards S, Eitel J, Pantow E., Geskes P, Lutz R, Tepas J. Waste heat recovery: The next challenge for commercial vehicle thermomanagement. *SAE International Journal of commercial vehicles 5(1):395-406, 2012, doi:10.4271/2012-01-1205.*

[57] Amicabile S, Leeb JI, Kum D. A comprehensive design methodology of organic rankine cycles for the waste heat recovery of automotive heavy-duty diesel engines. *Applied Thermal Engineering 2015; 87:574-585.*

[58] Grelet V, Dufour P, Nadri M, Reiche T, Lemort V. Modeling and control of rankine based waste heat recovery systems for heavy duty. *9th IFAC Symposium on Advanced Control of Chemical Processes 2015; 48-8:568–573.*

[59] Grelet V, Reiche T, Lemort V, Nadri M, Dufour P. Transient performance evaluation of waste heat recovery rankine cycle based system for heavy duty trucks. *Applied Energy 2016; 165:878–892.*

[60] Macian V, Serrano JR, Dolz V, Sanchez J. Methodology to design a bottoming rankine cycle, as a waste energy recovering system in vehicles. study in a hdd engine. *Applied Energy 2013; 104:758-771.*

[61] Yamaguchi T, Aoyagi Y, Uchida N, Fukunaga A, Kobayashi M, Adachi T, Hashimoto M. Fundamental study of waste heat recovery in the high boosted 6-cylinder heavy duty diesel engine. *SAE Int. J. Mater. Manf. 2015; 8(2): 209-226.*

[62] Zheng N, Zhao L, Wang XD, Tan YT. Experimental verification of a rolling-piston expander that applied for low-temperature organic rankine cycle. *Applied Energy 2012; 112: 1265-1274.*

[63] Refprop. Nist reference fluid thermodynamic and transport properties database. *https://www.nist.gov/refprop.*

[64] Coolprop. The coolprop fluid library. *http://www.coolprop.org/.*

[65] Zanelli R, Favrat D. Experimental investigation of a hermetic scroll expander-generator. *In Proceedings of the 12th Internnational Compressor Engineering Conference at Purdue 1994; 459-464.*

[66] Daccord R, Melis J, Kientz T, Darmedru A, Pireyre R, Brisseau N, Fonteneau E. Exhaust heat recovery with rankine piston expander. *8th International MTZ Conference 2013.*

[67] Demler RL. The application of the positive displacement reciprocating steam expander to the passenger car. *SAE 1976; Paper 760342.*

[68] ENDO T, KAWAJIRI S, KOJIMA Y, TAKAHASHI, K. Study on maximizing exergy in automotive engines. *SAE Technical Paper 2007; SAE International.*

[69] GLAVATSKAYA Y, PODEVIN P, LEMORT V, SHONDA O, DESCOMBES G. Reciprocating expander for an exhaust heat recovery rankine cycle for a passenger car application. *Energies 2012;5(6):1751-1765.*

[70] JIA X, ZHANG B, PU L, GUO B, PENG, X. Improved rotary vane expander for transcritical co2 cycle by introducing high-pressure gas into the vane slots. *International Journal of Refrigeration 2011; 34: 732-741.*

[71] PARTHOENS A. Study of a roots expander in an organic rankine cycle:semi-empirical model. *Master thesis 2017, University of Liege.*

[72] BOYCE MP. gas turbine engineering handbook. *Fourth Edition 2012, .*

[73] RAHBAR K, MAHMOUD S, AL-DADAH R.K, MOAZAMI N. Modelling and optimization of organic rankine cycle based on a small-scale radial inflow turbine. *Energy Conversion and Management 2015; 91:186-198, .*

[74] STOSIC N, SMITH IK, KOVACEVIC A, MUJIC, E. Review of mathematical models in performance calculation of screw compressors. *International Journal of Fluid Machinery and Systems 2011; 4(2): 271-288.*

[75] KITAGAWA K, HIRAO Y, YANAGI Y, IKEDA Y. Development of hlium oil-free screw compressor. *Proceedings of the Sixteenth International Cryogenic Engineering Conference/ International Cryogenic Materials Conference 1996.*

[76] BADR O, PROBERT SD, O CALLAGHAN PW. Selecting a working fluid for a rankine cycle engine. *Applied Energy 1985; 21:1-42.*

[77] VLAMINCK MD. Turbines axiales, turbines radiales et machines de détente à vis. *Rev. Gen. Therm. Fr. 313.*

[78] LEMORT V, TEODORESE IV, LEBRUN J. Experimental study of the integration of a scroll expander into a heat recovery rankine cycle. *18th International Compressor Engineering Conference 2006, Purdue, USA.*

[79] KANE M CRETEGNY D, FAVRAT D, MAQUET J. Projet htscroll, nouveau système de cogénération à turbine spirale haute température. *Rapport final 2009, Département fédéral de l'environnement, des transports, de l'énergie et de la communication DETEC, Office fédéral de l'énergie OFEN.*

[80] BRUMMER A. Energy efficiency – waste heat utilization with screw expanders. *Pumps, Compressors and Process Components 2012;120-126.*

[81] NIKOLOV A, HUCK C, BRUMMER A. Influence of thermal deformation on the characteristic diagram of a screw expander in automotive application of exhaust heat recovery. *International Compressor Engineering Conference at Purdue 2012.*

[82] JONES AC. Design and test of a small, high pressure ratio radial turbine. *International Gas Turbine and Aeroengine Congress and Exposition 1994.*

[83] HUTKER J, BRUMMER A. Thermodynamic design of screw motors for constant waste heat flow at medium temperature level. *Proceedings of the In the International Compressor Engineering Conference at Purdue 2012; Paper 1478.*

[84] ECKARD SE, BROOKS RD. Design of reciprocating single cylinder expanders for steam. *Final report 1973, Prepared for U.S. Environmental Protection Agency, Office of Air Pollution Control, Alternative Automotive Power Systems Division, Ann Arbor, Michigan.*

[85] AGHAALI H, ANGSTROM H. Temperature estimation of turbocharger working fluids and walls under different engine loads and heat transfer conditions. *SAE Technical Paper 2013; SAE International.*

[86] KANE M, LARRAIN D, FAVRAT D, ALLANI Y. Small hybrid solar power system. *Energy 2003;28:1427-1443.*

[87] MATHIAS JA, JOHNSTON JJR, CAO J, PRIEDEMAN DK, CHRISTENSEN RN . Experimental testing of gerotor and scroll expanders used in, and energetic and exergetic modeling of, an organic rankine cycle. *Journal of Energy Resources Technology 2009;31:1-9.*

[88] LEMORT V, GUILLAUME L, LEGROS A, DECLAYE S, QUOILIN S. A comparison of piston, screw and scroll expanders for small scale rankine cycle systems. *Proceedings of the 3rd International Conference on Microgeneration and Related Technologies 2013.*

[89] BRACCO R, CLEMENTE S, MICHELI D, REINI M. Experimental tests and modelization of a domestic-scale orc (organic rankine cycle). *Energy 2013;5:107-116.*

[90] BRATZ J, SMITH I, STOSIC N. Development of a twin screw expressor as a throttle valve replacement for water-cooled chillers. *proceedings of the International Compressor Engineering Conference, Purdue 200.*

[91] DESIDERI A, VAN DEN BROEK M, GUSEY S, LEMORT V. Experimental campaign and modeling of a low capacity waste heat recovery system based on a single screw expander. *In proceedings of the International Compressor Engineering Conference 2014.*

[92] ZHANG Y, WU Y, XIA G, MA C, JI W, LIU S, YANG K, YANG F. Development and experimental study on organic rankine cycle system with single-screw expander for waste heat recovery from exhaust of diesel engine. *Energy 2014; 77: 499-508.*

[93] HSU S, CHIANG H, YEN C. Experimental investigation of the performance of a hermetic screw expander organic rankine cycle. *Energies 2014; 7: 6172-6185.*

Bibliography

[94] XIA GD, ZHANG Y, WU Y, MA Y, JI W, LIU S, GUO H. Experimental study on the performance of single-screw expander with different inlet vapor dryness. *Applied Thermal Engineering 2015; 87(5): 34–40.*

[95] SEHER D, LENGENFELDER T, GERHARDT J, EISENMENGER N, HACKNER M, KRINN L. Waste heat recovery for commercial vehicles with a rankine process. *In Proceedings of the 21st Aachen Colloquium Automobile and Engine Technology 2012; 7-9.*

[96] COLLETTA DANIELE. *Analisi sperimentale delle prestazioni di espansori volumetrici a palette integrati in un organic Rankine cycle (ORC).* PhD thesis.

[97] VODICKA V, GUILLAUME L, MASCUCH J, LEMORT V. Testing and modeling a vane expander used in an orc working with hexamethyldisiloxane (mm).

[98] BAO J, ZHAO L. A review of working fluid and expander selections for organic rankine cycle. *Renewable and Sustainable Energy Reviews 2013; 24:325-342.*

[99] TOFFOLO A, LAZZARETTO A, MANENTE G, PACI M. A multi-criteria approach for the optimal selection of working fluid and design parameters in organic rankine cycle systems. *Applied Energy 2014; 121: 219-232.*

[100] SHU G, LIU L, TIAN H, WEI H, YU G. Parametric and working fluid analysis of a dual-loop organic rankine cycle (dorc) used in engine waste heat recovery. *Applied Energy 2014; 113:1188-1198.*

[101] LATZ G, ANDERSSON S, MUNCH K. Selecting an expansion machine for vehicle waste-heat recovery systems based on the rankine cycle. *SAE Technical Paper 2013-01-0552, 2013, doi:10.4271/2013-01-0552.*

[102] QUOILIN S, VAN DEN BROEK M, DECLAYE S, DEWALLEF P, LEMORT V. Techno-economic survey of organic rankine cycle (orc) systems. *Renewable and Sustainable Energy Reviews 2013; 22:168-186.*

[103] PERSON JG. Performance mapping vs design parameters for screw compressors and other displacement compressor types. *Verein Deutscher Ingenieure Berichte 1990; 859:15-31.*

[104] DESIDERI A. *Dynamic Modeling of Organic Rankine Cycle Power Systems.* PhD thesis, University of Liege, Liege, Belgium, 2016.

[105] COSTALL AW, GONZALEZ HERNANDEZ A, NEWTON PJ, MARTINEZ-BOTAS RF. Design methodology for radial turbo expanders in mobile organic rankine cycle applications. *Applied Energy 2015; Article in press.*

[106] SONG J, GU CW. Performance analysis of a dual-loop organic rankine cycle (orc) system with wet steam expansion for engine waste heat recovery. *Applied Energy 2015; 156:280-289.*

[107] DI BATTISTA D, MAURIELLO M, CIPOLLONE R. Waste heat recovery of an orc-based power unit in a turbocharged diesel engine propelling a light duty vehicle. *Applied Energy 2015; 152:109-120.*

[108] ARUNACHALAM P, SHEN M, TUNER M, TUNESTAL P, THERN M. Waste heat recovery from multiple heat sources in a hd truck diesel engine using a rankine cycle - a theoretical evaluation. *SAE Technical Paper 2012-01-1602, 2012, doi:10.4271/2012-01-1602.*

[109] ALLOUACHE A, LEGGETT S, HALL M, TU M, BAKER C, FATEH H. Simulation of organic rankine cycle power generation with exhaust heat recovery from a 15 liter diesel engine. *SAE Int. J. Mater. Manf. 8(2):227-238, 2015, doi:10.4271/2015-01-0339.*

[110] XIE H, YANG C. Dynamic behavior of rankine cycle system for waste heat recovery of heavy duty diesel engines under driving cycle. *Applied Energy 2013; 112: 130-141.*

[111] FURUKAWA T, NAKAMURA M, MACHIDA K, SHIMOKAWA K. Rankine cycle based waste heat recovery system applied to heavy duty vehicles: topological optimization and model based control. *SAE Technical Paper 2014-01-0678, 2014, doi:10.4271/2014-01-0678.*

[112] PARK T, TENG H, HUNTER G, VAN DER VELDE B, KLAVER J. A rankine cycle system for recovering waste heat from hd diesel engines - experimental results. *SAE Technical Paper 2011-01-1337, 2011, doi:10.4271/2011-01-1337.*

[113] LEMORT V, DECLAYE S, QUOILIN S. Experimental characterization of a hermetic scroll expander for use in a micro-scale rankine cycle. *Proccedings of the Institution of Mechanical Engineers 2011, Part A: Journal of Power and Energy, 226(1).*

[114] DECLAYE S, QUOILIN S, GUILLAUME L, LEMORT V. Experimental study on an open-drive scroll expander integrated into an orc (organic rankine cycle) system with r245fa as working fluid. *Energy 2013; 55:173-183.*

[115] KANG SH. Design and experimental study of orc (organic rankine cycle) and radial turbine using r245fa working fluid. *Energy 2012; 41:514-524, .*

[116] PEI G, LI YZ, LI J, JI J. Performance evaluation of a micro turbo-expander for application in low-temperature solar electricity generation. *Journal of Zhejiang University-science A (Applied Physics and Engineering) 2011; 12(3):207-213.*

[117] BELL I, WRONSKI J, QUOILIN S, LEMORT V. Pure and pseudo-pure fluid thermophysical property evaluation and the open-source thermophysical property library coolprop. *Industrial and Engineering Chemistry Research 2014; 53:2498-2508.*

[118] BOYCE MP. Radial inflow turbines. *Gas Turbine Engineering Handbook (Fourth Edition) 2012; 8:357–383, .*

[119] KORPELA SA. Radial inflow turbines. *Principles of Turbomachinery 2011; 9:313-358.*

Bibliography

[120] BAINES NC. Radial turbines - an integrated design approach. *6th European conference on turbomachinery-fluid dynamics and thermodynamics 2005, Lille, France (Concepts NREC)*, .

[121] KANG SH. Design and preliminary tests of orc (organic rankine cycle) with two-stage radial turbine. *Energy 2016; 96:142-154*, .

[122] AUNGIER RH. Axial-flow and radial inflow turbine design and analysis. *Turbine aerodynamics 2006*.

[123] EARL L JR, RAMENDRA R. Handbook of turbomachinary. *Second edition revised and expanded 2003*.

[124] SAURET E, ROWLANDS AS. Candidate radial-inflow turbines and high-density working fluids for geothermal power systems. *Energy 2011; 36(7):4460-4467*.

[125] ZHU S, DENG K, LIU S. Modeling and extrapolating mass flow characteristics of a radial turbocharger turbine. *Energy 2015; 87: 628-637*.

[126] POURFARZANEH H, HAJILOUY-BENISI ALI. A new analytical model of a radial turbine and validation by experiments. *Verein Deutscher Ingenieure Berichte 1990; 859:15-31*.

[127] PAYRI F, BENAJES J, REYES M. Modelling of supercharger turbines in internal-combustion engines. *International Journal of Mechanical Sciences 1996; 38(8,9):853-869*.

[128] MARTINS G, MENDOZA OSH, TUMIALAN JA. Semi-empirical modeling of small size radial turbines for refrigeration purpose. *International Compressor Engineering Conference of Purdue 2006*.

[129] SERRANO JR, ARNAU FJ, DOLZ V, TISEIRA A, CERVELLO C,. A model of turbocharger radial turbines appropriate to be used in zero- and one-dimensional gas dynamics codes for internal combustion engines modelling. *Energy Conversion and Management 2008; 49:3729–3745*.

[130] VILIM RB. Development and validation of a radial inflow turbine model for simulation of the snl s-co2 split-flow loop. *Argonne National Laboratory 2011, Nuclear Engineering Division*.

[131] SAKELLARIDIS N, HOUNTALAS D. Meanline modeling of radial turbine performance for turbocharger simulation and diagnostic applications. *SAE 2013; Technical Paper 2013-01-0924*.

[132] RAHBAR K, MAHMOUD S, AL-DADAH R.K. Mean-line modelling and cfd analysis of a miniature radial turbine for distributed power generation systems. *Int J Low-Carbon Tech 2016; 11(2):157-168*.

[133] RAHBAR K, MAHMOUD S, AL-DADAH R.K, MOAZAMI N. Parametric analysis and optimization of a small-scale radial turbine for organic rankine cycle. *Energy 2015; 83:696-711, .*

[134] HENDRICKS E. The analysis of mean value engine models. *SAE 1989; Technical Paper 890563.*

[135] KARMIGGELT R. Mean value modelling of a si engine. *DCT rapporten 1998; Vol. 1998.041; Eindhoven:Technische Universiteit Eindhoven.*

[136] JOULE JP. On the heat evolved by metallic conductors of electricity. *Philosophical Magazine, 19, 260; Scientific Papers 65.*

[137] MAYER JR. Die organische bewegung in ihren zusammenhang mit dem stoffwechsel. *Ein Beitrag zur Naturkunde, Heilbronn, Verlag der Drechslerschen Buchhandlung 1845.*

[138] THOMPSON WE. Aerodynamics of turbine. *Proceedings of the first turbomachinary symposium.*

[139] EULER L. More complete theory of machines that are set in motion by reaction with water. *Memoirs of the Royal Academy of Sciences and Belles Lettres in Berlin, 10: 227-295. An analysis of Segner's wheel.*

[140] CARNOT S. Reflexions sur la puissance motrice du feu et sur les machines propres a developper cette puissance. *Paris: Bachelier 1824.*

[141] THOMPSON W. On the dynamical theory of heat, with numerical results deduced from mr joule's equivalent of a thermal unit, and m. regnault's observations on steam. *Transactions of the Royal Society of Edinburgh 1851; XX (part II): 261–268; 289–298.*

[142] CLAUSIUS R. Über eine veränderte form des zweiten hauptsatzes der mechanischen wärmetheorie. *Annalen der Physik 1854; Poggendoff. xciii: 481–506.*

[143] BALJE OE. A study on design criteria and matching of turbomachines: Part a - similarity relations and design criteria of turbines. *Engineering for Power 1962; ASME Transactions 84A:83-102.*

[144] BALJE OE, BINSLEY RL. Turbine performance prediction: Optimization using fluid dynamic criteria. *North America Aviation, Inc 1966; Rocketdyne Division; Report R-6805; NTIS AD-642767.*

[145] SODERBERG . Unpublished report. *Gas turbine laboratory (MIT) 1949.*

[146] TRAUPEL W, SMITH CW. New general theory of multistage axial flow turbomachines. *1942; United States; Navy Department.*

[147] AINLEY DG, MATHIESON GCR. Method of performance estimation fo axial flow turbines. *Aeronautical Research Council 1957, R and M 2974.*

Bibliography

[148] SMITH SF. A simple correlation of turbine efficiency. *Journal of Royal Aeronautical Society 1965.*

[149] HIETT GF, JOHNSTON IH. Experiments concerning the aerodynamic performance of inwardflow radial turbines. *Proceedings of institution of Mechanical Engineers 1963;178(3I):28-42.*

[150] MIZUMACHI N. A study of radial turbines. *Institute of Industrial Science, University of Tokyo 1958.*

[151] WATANABE I, ARIGA I, MASHIMO T. Effect of dimensional parameters of impellers on performance characteristic of a radial inflow turbine. *Journal Engineering for Power 1971, ASME Transactions; 93A:81-102.*

[152] FUTURAL SM, WASSERBAUER CA. Off-design performance prediction with experimental verification for a radial-inflow turbine. *NASA 1965; Report TND-2621.*

[153] BENSON RS. A review of methods for assessing loss coefficients in radial gas turbines. *International journal of mechanical Sciences 1970; 12:905-932.*

[154] WHITFIELD A, WALLACE FJ. Study of incidence loss models in radial and mixed-flow turbomachinery. *IMechE Conference 1973; 3; C55-73.*

[155] SUHRMANN JF, PEITSCH D. Validation and development of loss models for small size radial turbines. *in Proceedings of ASME Turbo Expo 2010;Power for Land, Sea and Air; GT2010-22666, .*

[156] DEMIERRE J, RUBINE A, SCHIFFMANN Y. Modeling and experimental investigation of an oil-free microcompressor-turbine unit for an organic rankine cycle driven heat pump. *J. Eng. Gas Turbines Power. 2014; 137(3):032602-032602-10 GTP-14-1347.*

[157] RODGERS C. Mainline performance prediction for radial inflow turbines. *Small High Pressure Ratio Turbines 1987 (VKI Lecture Series No. 1987-07); Von Karman Institute; Rhode-St-Genese; Belgium, .*

[158] MUSGRAVE DS. The prediction of design and offdesign efficiency for centrifugal compressor impellers. *ASME 1980; 22nd fluids engineering conference.*

[159] KRYLOV EP; SPUNDE YA. About the influence of the clearance between the working blades and housing of a radial turbine on its exponent. *USAF 1967; Foreign Technology Division; translation FTD-MT-67-15.*

[160] JANSEN W. A method for calculating the flow in a centrifugal impeller when entropy gradients are present. *Royal Society Conference on Internal Aerodynamics 1967; Turbomachinery.*

[161] MOUSTAPHA H, ZELESKY MF, BAINES NC, JAPIKSE D. Axial and radial turbines. *2003; 1st ed. White River Junction: Concepts NREC.*

[162] DAILY JW, NECE RE. Chamber dimension effects on induced flow and frictional resistance of enclosed rotating disks. *ASME Journal of Basic Engineering 1960;82(1):217–230.*

[163] BAINES NC. Radial turbines (courses notes). *Concepts ETI Inc 2006; White River Junction; VT, .*

[164] WHITFIELD A, BAINES NC. Design of radial turbomachines. *1990; 1st edition New York: Longman.*

[165] CHURCHILL SW. Friction-factor equation spans all fluid-flow regimes. *Chem Eng 1977;84:91–2.*

[166] WASSERBAUER CA, GLASSMAN AJ. Fortran program for predicting the off-design performance of radial inflow turbines. *NASA 1975; Lewis Research Center; Cleveland; OH; Paper No. TN-8063.*

[167] CHLICHTING H, GERSTEN K. Boundary layer theory. *8th Edition, Springer-Verlag Berlin Heidelberg.*

[168] COLEBROOK CF. Turbulent flow in pipes. *Journal of the Inst. Civil Eng. 1938;11.*

[169] COPPAGE JE, DALLENBACH F, EICHENBERGER HP, HLAVAKA GE, KNOEPERNSCHILD EM, VAN LEE N. Study of supersonic radial compressor for refrigeration and pressurization systems. *WADC 1956; report 55-257.*

[170] RODGERS C. Performance of high-efficiency radial/axial turbine. *Journal of Turbomachinery 1987, ASME, New York, .*

[171] RODGERS C. A cycle analysis technique for small gas turbines. *in Proceedings IME 1968; 183; part 3N, .*

[172] XIAOYANG G, RUI C. Total pressure loss mechanism of centrifugal compressors. *Mechanical Engineering Research 2014; 4(2).*

[173] WALTZ RA, MORALES JL, NOCEDAL J, ORBAN D. An interior algorithm for nonlinear optimization that combines line search and trust region steps. *Math. Program. 2006; Ser. A 107: 391–408.*

[174] POULY F, CHANGENET C, VILLE F, VELEX P, DAMIENS B. Echauffements et pertes de puissance dans les paliers à roulements fonctionnant à haute vitesse. *19ème Congrès Français de Mécanique 2009.*

[175] HEYWOOD JB. Internal combustion engines fundamentals. *1988.*

[176] CIPOLLONE R, DI BATTISTA D, PEROSINO A, BETTOJA F. Waste heat recovery by an organic rankine cycle for heavy duty vehicles. *SAE Technical Paper 2016; SAE International.*

Bibliography

[177] LECOMPTE S, HUISSEUNE H, VAN DEN BROEK M, SCHAMPHELEIRE SD, DE PAEPE M. Part load based thermo-economic optimization of the organic rankine cycle (orc) applied to a combined heat and power (chp) system. *Applied Energy 2013; 111: 871–881.*

[178] MATHWORKS. Matlab: The language of technical computing. *2017; https://nl.mathworks.com/.*

[179] INCROPERA FP, DEWITT DP, BERGMAN TL, LAVINE AS. Chapter 8. *Fundamentals of Heat and Mass Transfer 6th Edition 2007, John Wiley and Sons Inc.*

[180] AYUB ZH. Plate heat exchanger literature survey and new heat transfer and pressure drop correlations for refrigerant evaporators. *Heat Transfer Engineering 2003; 24(5):3-16.*

[181] SWEP WEBSITE. Bphe construction and denomination. *http://www.swep.net/refrigerant-handbook/8.-practical-advice/qw7/.*

[182] MARTIN H. A theoretical approach to predict the performance of chevron-type plate heat exchangers. *Chemical Engineering and Processing 1996; 35:301-310.*

[183] KHAN TS, KHAN MS, CHYU MC, AYUB ZH. Experimental investigation of evaporation heat transfer and pressure drop of ammonia in a 60 chevron plate heat exchanger. *International Journal of Refrigeration 2012;35(2):336-348.*

[184] DICKES R, DUMONT O, GUILLAUME L, QUOILIN S, LEMORT V. Charge-sensitive modelling of organic rankine cycle power systems for off-design performance simulation. *Applied Energy 2017, In Press, Accepted Manuscript.*

[185] HAN DH, LEE KJ, KIM YH. Experiments on the characteristics of evaporation of r410a in brazed plate heat exchangers with different geometric configurations. *Applied Thermal Engineering 2003; 23:1209-1225, .*

[186] HAN DH, LEE KJ, KIM YH. The characteristics of condensation in brazed plate heat exchangers with different chevron angles. *Journal of the Korean Physical Society 2003;43,1;66-73, .*

[187] ELDEEB R, AUTE V, RADERMACHER R. A survey of correlations for heat transfer and pressure drop for evaporation and condensation in plate heat exchangers. *international journal of refrigeration 2016; 16:12-26.*

[188] ALMALFI RL, VAKILI-FARAHANI F, THOME JR. Flow boiling and frictional pressure gradients in plate heat exchangers. part 2: Comparison of literature methods to database and new prediction methods. *International Journal of Refrigeration 2016; 61:185-203.*

[189] SHAH MM,. A general correlation for heat transfer during
lm condensation inside pipes. *International Journal of Heat and Mass Transfer 1979; 22(4):547-556.*

[190] LONGO GA, RIGHETTI G, ZILIO C. A new computational procedure for refrigerant condensation inside herringbone-type brazed plate heat exchangers. *International Journal of Heat and Mass Transfer 2015; 82:530-536.*

[191] NELLIS G, KLEIN S. Chapter 8. *Heat Transfer 2009, Cambridge University Press.*

[192] DUMONT O. Experimental investigation of the valorization of the waste heat of a gasoline engine based on a rankine cycle. .

[193] ZIVIANI D, BEYENE A, VENTURINI M. Design, analysis and optimization of a micro-chp system based on organic rankine cycle for ultralow grade thermal energy recovery. *Journal of Energy Resources Technology;136:1.*

[194] QIU G, LIU H, AND RIFFAT S. Expanders for micro-chp systems with organic rankine cycle. *Applied Thermal Engineering 2011; 31:3301-3307.*

[195] MIKIELEWICSZ D, MIKIELEWICSZ J, WAJS J. Experiences from operation of different expansion devices for application in domestic micro chp. *Archives of Thermodynamics 31, 4.*

[196] DUMONT O. Experimental investigation of four volumetric expanders. .

[197] DICKES R, DUMONT O, DECLAYE S, QUOILIN S, BELL I, LEMORT V. Experimental investigation of an orc system for a micro-solar power plant. *In poceedings of the 22nd International Compressor Engineering Conference at Purdue 2014.*

[198] NIKOLOV A, BRUMMER A. Investigating a small oil-flooded twin-screw expander for waste-heat utilisation in organic rankine cycle systems. *Energies 2017;10:869.*

[199] OUDKERK JF, DICKES R, DUMONT O, LEMORT V. Experimental performance of a piston expander in small-scale organic rankine cycle. *in Proceedings of the International Conference on Compressors and their Systems 2015.*

[200] DICKES R, DUMONT O, DACCORD R, QUOILIN S, LEMORT V. Modelling of organic rankine cycle power systems in off-design conditions: An experimentally-validated comparative study. *Energy 2017, In Press, Accepted Manuscript, doi:10.1016/j.energy.2017.01.130.*

[201] LEMORT V, QUOILIN S, CUEVAS C, LEBRUN J. Testing and modeling a scroll expander integrated into an organic rankine cycle. *Applied Thermal Engineering 2009; 29:3094-3102.*

[202] TAYLOR CF. Internal combustion engine in theory and practice. *International Texbook Company 1961; Scranton Pensylvania.*

[203] LIN C. Feasibility of using power steering pumps in small-scale solar thermal electric power systems. *Bachelor Thesis 2008, Massachusetts Institute of Technology, Dept. of Mechanical Engineering.*

Bibliography

[204] PIEROBON L, NGUYEN TV, LARSEN U, HAGDLIND F, ELMEGAARD B. Multi-objective optimization of organic rankine cycles for waste heat recovery: Application in an offshore platform. *Energy 2013; 58:538-549.*

[205] WANG J, YAN Z, WANG M, LI M, DAI Y . Multi-objective optimization of an organic rankine cycle (orc) for low grade waste heat recovery using evolutionary algorithm. *Energy Conversion and Management 2013; 71: 146–158.*

[206] SOLIDWORKS. 3d cad solutions. *2017; http://www.solidworks.fr/.*

[207] WIKIPEDIA. Net present value - npv. *URL http://www.investopedia.com/terms/n/npv.asp; 2017, .*

[208] SADASHIVA S. Mms simulation of rsg/fwtrain of a nuclear power plant for developing a rsg level control system. *Technical report 1990; B & W Nuclear Service Company.*

[209] PHERSON PKM, COLLINS GB, GUPPY CB, SUMNER A. Dynamics analysis of a nuclear boiler. *In Institution ofMechanical Engineers 1965; 180: 417–449.*

[210] MAGER DE. Target-mediated drug disposition and dynamics. *Biochemical Pharmacology 2005; 72(1): 1-10.*

[211] WIKIPEDIA. Comparison of systemdynamics software. *URL https://en.wikipedia.org/wiki/Comparison_of_system_dynamics_software; 2017, .*

[212] BONILLA J, YEBRA IJ, DORMIDO S. Chattering in dynamic mathematical two-phase flow models. *Applied Mathematical Modelling 2012; 36(5):2067–2081, .*

[213] SIEMENS PLM SOFTWARES. Lms imagine lab amesim. *https://www.plm.automation.siemens.com/fr/products/lms/imagine-lab/amesim/ 2017.*

[214] MODELON. Modelon dymola. *http://www.modelon.com/products/dymola 2017.*

[215] MODELICA. Modelica association. *https://www.modelica.org 2017.*

[216] SIMULATIONX. Simulation software simulationx. *https://www.simulationx.com/ 2017.*

[217] THERMOCYCLE. The modelica library. *http://www.thermocycle.net/ 2017.*

[218] BENDAPUDI S, BRAUN JE, GROLL EA. Dynamicmodel of a centrifugal chiller system–model development, numerical study and validation. *ASHRAE 2005, .*

[219] BENDAPUDI S, BRAUN JE, GROLL EA. A comparison of moving boundary and finite-volume formulations for transients in centrifugal chillers. *nternational Journal of Refrigeration 2008; 31(8):1437–1452, .*

210

[220] BENDAPUDI S. A literature review of dynamicmodels of vapor compression equipment. *Technical report 2002, Herrick Laboratories, Purdue University.*

[221] GNIELINSKI V. On heat transfer in tubes. *International Journal of Heat and Mass Transfer 63:134-140.*

[222] VDI HEAT ATLAS. 2nd edition. *Springer-Verlag Berlin Heidelberg.*

[223] CASELLA E, MATHIJSSEN T, COLONNA P, VAN BUIJTENEN J. Dynamic modeling of organic rankine cycle power systems. *Journal of Engineering for Gas Turbines and Power 2013; 135(4):042310.*

[224] JENSEN JM. Dynamic modeling of thermo-fluid systems: With focus on evaporators for refrigeration. *Ph.D. Thesis 2003, Energy Engineering, Department of Mechanical Engineering, Technical University of Denmark, Kongens Lyngby, Denmark.*

[225] QUOILIN S, BELL I, DESIDERI A, DEWALLEF P, LEMORT V. Methods to increase the robustness of finite-volume flow models in thermodynamic systems. *Energies 2014;7:1621-1640.*

[226] CASELLA E. Object-oriented modelling of two-phase fluid flows by the finite volume method. *Proceedings 5th Mathmod Vienna 2006, Austria.*

[227] BONILLA J, YEBRA IJ, DORMIDO S. Mean densities in dynamicmathematical two-phase flow models. *Computer Modeling in Engineering and Sciences (CMES) 2010; 67(1):13, .*

[228] QUOILIN S, AUMANN R, GRILL A, SCHUSTER A, LEMORT V, SPLIETHOFF H. Dynamic modeling and optimal control strategy of waste heat recovery organic rankine cycles. *Applied Energy; 88(6): 2183–2190.*

[229] HOU G, SUN R, ZHANG J. Supervisory predictive control of evaporator in organic rankine cycle (orc) system for waste heat recovery. *International Conference on Advanced Mechatronic Systems (ICAMechS) 2011; 306–311.*

[230] ZHANG J, ZHANG W, HOU G, FANG F. Dynamic modeling and multivariable control of organic rankine cycles in waste heat utilizing processes. *Computers & Mathematics with Applications 2012; 64(5): 908-921.*

[231] ZHANG J, ZHOU Y, GAO S, HOU G. Constrained predictive control based on state space model of organic rankine cycle system for waste heat recovery. *In 24th Chinese Control and Decision Conference (CCDC) 2012; 230–234.*

[232] ZHANG J, ZHOU Y LI Y, HOU G, FANG F. Generalized predictive control applied in waste heat recovery power plants. *Applied Energy 2013; 102 :320–326.*

[233] STOBART R, HOUNSHAM S, WEERASINGHE R. The controllability of vapour based thermal recovery systems in vehicles. *SAE Technical Paper 2007; SAE International.*

Bibliography

[234] WILLEMS F, KUPPER F, CLOUDT R. Integrated powertrain control for optimal co2-nox tradeoff in an euro-vi diesel engine with waste heat recovery system. *In American Control Conference (ACC) 2012; 1296–1301.*

[235] LUONG D, TSAO TC. Model predictive control of organic rankine cycle for waste heat recovery in heavy-duty diesel powertrain. *In ASME 2014 Dynamic Systems and Control Conference.*

[236] ZIEGLER JG, NICHOLS NB. Optimum settings for automatic controllers. *Transactionsof ASME 1942; 64: 759–768.*

[237] SKOGESTAD S. Simple analytic rules for model reduction and pid controller tuning. *Journal of Process Control 2003; 13(4): 291–309.*

[238] SMITH CA, CORRIPIO AB. rinciples and practice of automatic process control. *volume 2 1985; Wiley New York.*

[239] RIVERA DE, MORARI M, SKOGESTAD S. Internal model control: Pid controller design. *Industrial & engineering chemistry process design and development 1986; 25(1): 252–265.*

[240] MADHURANTHAKAM C, ELKAMEL A, BUDMAN H. Optimal tuning of pid controllers for foptd, soptd and soptd with lead processes. *Chemical Engineering and Processing: Process Intensification 2008; 47(2): 251-264.*

A Appendix A

A.1 Thermophysical and safety properties of the 122 pure and pseudo pure working fluids available in the CoolProp fluid library

Fluid	Industrial designation	Chemical name	Chemical Formula	CAS number	GWP100(ar4)	ODP(Montreal)	Lifetime	Reference Price [€ or $ /kg]	source prix
1-Butene	1-Butene	1-Butene	C4H8	106-98-9	0	0	0.001	1.0582176	icis $
Acetone	Acetone	Propanone	C3H6O	67-64-1	0.5	0	N.A.	0.7275246	platts $
Air (R729)	Air	Air	-	N.A.			N.A.	2.121	Air liquide €
Ammonia (R717)	Ammonia	Ammonia	NH3	7664-41-7	0	0	0.02	1.212541	molbase $
Argon (R740)	Argon	Argon	Ar	7440-37-1	-1	0	N.A.	1.364	Air liquide €
Benzene	Benzene	Benzene	C6H6	71-43-2	0	0	N.A.	1.201982839	icis $
CarbonDioxide (R744)	CarbonDioxide	CarbonDioxide	CO2	124-38-9	1	0	N.A.	0.5486	molbase €
CarbonMonoxide	CarbonMonoxide	CarbonMonoxide	CO	630-08-0	0	0	0.25	N.A.	N.A.
CarbonylSulfide	CarbonylSulfide	CarbonylSulfide	COS	463-58-1	27	0	N.A.	290	molbase $
CycloHexane	CycloHexane	CycloHexane	C6H12	110-82-7	5	0	N.A.	1.038	molbase $
CycloPropane (C270)	CycloPropane	CycloPropane	C3H6	75-19-4	5	0	0.44	851	molbase $
Cyclopentane	Cyclopentane	Cyclopentane	C5H10	287-92-3	5	0	0.007	38.2	molbase $
D4	Octamethylcyclotetrasiloxane	Octamethylcyclotetrasiloxane	C8H24O4Si4	556-67-2	-1	0	N.A.	3.378	molbase $
D5	Decamethylcyclopentasiloxane	Decamethylcyclopentasiloxane	C10H30O5Si5	541-02-6	-1	0	N.A.	2.993	molbase $
D6	Dodecamethylcyclohexasiloxane	Dodecamethylcyclohexasiloxane	C12H36O6Si6	540-97-6	-1	0	N.A.	3.219	molbase $
Deuterium (D2)	Deuterium	Deuterium	H2	7782-39-0	-1	0	N.A.	N.A.	N.A.
Dichloroethane	Dichloroethane	Dichloroethane	C2H4Cl2	107-06-2	-1	0	0.145	0.484	molbase $
DiethylEther	DiethylEther	DiethylEther	C4H10O	60-29-7	-1	0	N.A.	N.A.	N.A.
DimethylCarbonate	DimethylCarbonate	DimethylCarbonate	C3H6O3	616-38-6	-1	0	N.A.	0.806	molbase $
DimethylEther	DimethylEther	DimethylEther	CH3OCH3	115-10-6	1	0	0.015	0.806	molbase $
Ethane (R170)	Ethane	Ethane	C2H6	74-84-0	6	0	0.21	0.618	molbase $
Ethanol	Ethanol	Ethanol	C2H6O	64-17-5	-1	0	N.A.	1.056	molbase $
EthylBenzene	EthylBenzene	EthylBenzene	C8H10	100-41-4	-1	0	N.A.	1.076	molbase $
Ethylene (R1150)	Ethylene	Ethylene	C2H4	74-85-1	4	0	N.A.	1.371	molbase €
EthyleneOxide	EthyleneOxide	EthyleneOxide	C0H4O	75-21-8	-1	0	N.A.	1.645	molbase $
Fluorine	Fluorine	Fluorine	F2	7782-41-4	-1	0	N.A.	N.A.	N.A.
HFE143m	Trifluoromethoxymethane	Trifluoromethoxymethane	C2F3H3O	421-14-7	680	0	4.4	2.152	molbase $
HeavyWater	Deuterium Oxyde	Deuterium Oxyde	D2O	7789-20-0	-1	0	N.A.	493	molbase $
Helium (R704)	Helium	Helium	He	7440-59-7	-1	0	N.A.	0.806	molbase $
Hydrogen (R702)	Hydrogen	Hydrogen	H2	1333-74-0	6	0	N.A.	0.323	molbase $
HydrogenChloride	HydrogenChloride	HydrogenChloride	HCl	7647-01-0	-1	0	N.A.	0.13	icis $
HydrogenSulfide	HydrogenSulfide	HydrogenSulfide	H2S	7783-06-4	6	0	N.A.	16	alibaba $
IsoButane (R600a)	IsoButane	IsoButane	C4H10	75-28-5	3	0	0.016	1.29	molbase $
IsoButene	IsoButene	IsoButene	C4H8	115-11-7	-1	0	N.A.	401	molbase $
Isohexane	Isohexane	Isohexane	C6H14	107-83-5	-1	0	N.A.	1.849	molbase $
Isopentane (R601a)	Isopentane	Isopentane	C5H12	78-78-4	-1	0	0.009	1.742	molbase $
Krypton (R784)	Krypton	Krypton	Kr	7439-90-9	-1	0	N.A.	1.975	sigma-aldrich
MD2M	Decamethyltetrasiloxane	Decamethyltetrasiloxane	C10H30O3Si4	141-62-8	-1	0	N.A.	447	molbase $
MD3M	Dodecamethylpentasiloxane	Dodecamethylpentasiloxane	C12H36O4Si5	141-63-9	-1	0	N.A.	715	molbase $
MD4M	Tetradecamethylhexasiloxane	Tetradecamethylhexasiloxane	C14H42O5Si6	107-52-8	-1	0	N.A.	1260	molbase $
MDM	Octamethyltrisiloxane	Octamethyltrisiloxane	C8H24O2Si3	107-51-7	-1	0	N.A.	611	molbase $
MM	Hexamethyldisiloxane	Hexamethyldisiloxane	C6H18OSi2	107-46-0	-1	0	N.A.	2.742	molbase $
Methane (R50)	Methane	Methane	CH4	74-82-8	25	0	12	N.A.	molbase $
Methanol	Methanol	Methanol	CH4O	67-56-1	2.8	0	N.A.	0.275	molbase $
MethylLinoleate	MethylLinoleate	MethylLinoleate	C19H34O2	112-63-0	-1	0	N.A.	2027	molbase $
MethylLinolenate	MethylLinolenate	MethylLinolenate	C19H32O2	301-00-8	-1	0	N.A.	1069	molbase $
MethylOleate	MethylOleate	MethylOleate	C19H36O2	112-62-9	-1	0	N.A.	2097	molbase $
MethylPalmitate	MethylPalmitate	MethylPalmitate	C17H34O2	112-39-0	-1	0	N.A.	125	molbase $
MethylStearate	MethylStearate	MethylStearate	C19H38O2	112-61-8	-1	0	N.A.	100	molbase $
Neon (R720)	Neon	Neon	Ne	7440-01-9	-1	0	N.A.	330	chemicool $
Neopentane	Neopentane	Neopentane	C5H12	463-82-1	-1	0	N.A.	1012	molbase $
Nitrogen (R728)	Nitrogen	Nitrogen	N2	7727-37-9	-1	0	N.A.	0.657	Air liquide €
NitrousOxide	Nitrous Oxyde	Nitrous Oxyde	N2O	10024-97-2	298	0.017	N.A.	6.022	Air liquide €
Novec649 (Novec1230)	Novec649	Novec649	C6F12O	756-13-8	1	0	N.A.	1392 (50 IFP)	molbase $
OrthoDeuterium	OrthoDeuterium	OrthoDeuterium	H2	7782-39-0	-1	0	N.A.	N.A.	N.A.
OrthoHydrogen (R702)	OrthoHydrogen	OrthoHydrogen	H2	1333-74-0o	-1	0	N.A.	N.A.	N.A.
Oxygen	Oxygen	Oxygen	O2	7782-44-7	-1	0	N.A.	2.7	Airliquide €
ParaDeuterium	ParaDeuterium	ParaDeuterium	H2	7782-39-0p	-1	0	N.A.	N.A.	N.A.
ParaHydrogen	ParaHydrogen	ParaHydrogen	H2	1333-74-0p	-1	0	N.A.	N.A.	N.A.
Propylene (R1270)	Propylene	Propylene	C3H6	115-07-1	2	0	0.001	1.37	molbase $
Propyne	Methyl Acetylene	Propyne	C3H4	74-99-7	-1	0	N.A.	506	molbase $
R11	CFC-11	Trichlorofluoromethane	CCl3F	75-69-4	4750	1	45	2.577	molbase $
R113	CFC-113	1,1,2-Trichlorotrifluoroethane	CCl2FCClF2	76-13-1	6130	0.8	85	4.767	molbase $
R114	CFC-114	Dichlorotetrafluoroethane	CClF2CClF2	76-14-2	10000	1	190	2199	molbase $
R115	CFC-115	Chloropentafluoroethane	CClF2CF3	76-15-3	7370	0.6	1020	2199	molbase $
R116	PFC-116	Hexafluoroethane	C2F6	76-16-4	12200	0	10000	1380	molbase $
R12	CFC-12	Dichlorodifluoromethane	CCl2F2	75-71-8	10900	1	100	1184	molbase $
R123	HCFC-123	1,1-Dichloro-2,2,2,-Trifluoroethane	CHCl2CF3	306-83-2	77	0.02	1.3	9.355	molbase $
R1233zd(E)	HCFO-1233zd	trans-1-Chloro-3,3,3-trifluoropropylene	C3H2ClF3	102687-65-0	4.5	0	N.A.	840	molbase $
R1234yf	HFO-1234yf	2,3,3,3-Tetrafluoropropene	C3H2F4	754-12-1	4	0	0.029	40.323	molbase $
R1234ze(E)	HFO-1234ze	trans-1,3,3,3-Tetrafluoroprop-1-ene	C3H2F4	29118-24-9	7	0	0.045	3200	molbase $
R1234ze(Z)	HFO-1234ze	trans-1,3,3,3-Tetrafluoroprop-1-ene	C3H2F4	29118-25-0	7	0	0.045	3200	molbase $
R124	HCFC-124	Chlorotetrafluoroethane	CHClFCF3	2837-89-0	609	0.022	5.9	423	molbase $
R125	HFC-125	Pentafluoroethane	CHF2CF3	354-33-6	3500	0	32.6	3.092	molbase $
R13	CFC-13	Chlorotrifluoromethane	CClF3	75-72-9	14400	1	640	1038	molbase $
R134a	HFC-134a	1,1,1,2-tetrafluoroethane	CH2FCF3	811-97-2	1430	0	14.6	3.167	molbase $
R13I1 (CF3I)	CFI-13	Trifluoromethyliodide	CF3I	2314-97-8	0	0	N.A.	481	molbase $
R14	PFC-14	Tetrafluoromethane	CF4	75-73-0	7390	0	50000	1.613	molbase $
R141b	HCFC-141b	1,1-dichloro-1-fluoroéthane	CH3CCl2F	1717-00-6	725	0.11	9.2	2.42	molbase $
R142b	HCFC-142b	1-chloro-1,1-difluoroéthane	CH3CClF2	75-68-3	2310	0.065	17.2	2.581	molbase $
R143a	HFC-143a	1,1,1-trifluoroethane	CH3CF3	420-46-2	4470	0	48.3	5.484	molbase $
R152a	HFC-152a	1,1-difluoroethane	CH3CHF2	75-37-6	124	0	1.5	4.113	molbase $
R161	HFC-161	fluoroethane	CH3CH2F	353-36-6	12	0	0.18	940	molbase $
R21	HCFC-21	Dichlorofluorométhane	CHCl2F	75-43-4	151	0.04	1.7	2.58	molbase $
R218	PFC-218	Octafluoropropane	C3F8	76-19-7	8830	0	2600	973	molbase $
R22	HCFC-22	Chlorodifluorométhane	CHClF2	75-45-6	1810	0.055	11.9	2.183	molbase $
R227EA	HFC-227ea	1,1,1,2,3,3,3-heptafluoropropane	CF3CHFCF3	431-89-0	3220	0	38.9	4.742	molbase $
R23	HFC-23	trifluoromethane	CHF3	75-46-7	14800	0	222	3.118	molbase $
R236EA	HFC-236ea	1,1,1,2,3,3-hexafluoropropane	CHF2CHFCF3	431-63-0	1370	0	11	N.A.	molbase $
R236FA	HFC-236fa	1,1,1,3,3,3-hexafluoropropane	CF3CH2CF3	690-39-1	9810	0	242	530	molbase $
R245ca	HFC-245ca	1,1,2,2,3-pentafluoropropane	CH2FCF2CHF2	679-86-7	693	0.0025	6.5	1809	molbase $
R245fa	HFC-245fa	1,1,1,3,3-pentafluoropropane	CHF2CH2CF3	460-73-1	1030	0	7.7	25	honeywell €
R32	HFC-32	difluoromethane	CH2F2	75-10-5	675	0	5.2	3.387	molbase $
R365mfc	HFC-365mfc	1,1,1,3,3-pentafluorobutane	CF3CH2CF2CH3	406-58-6	794	0	N.A.	868	molbase $
R40	HFC-40	chloromethane	CH3Cl	74-87-3	13	0.02		96.4	molbase $
R404a	R125/R143a/R134a (44/52/4)	N.A.	N.A.	N.A.	3922	0	N.A.	4.33884	mixing
R407c	R32/R125/R134a (23/25/52)	N.A.	N.A.	N.A.	1774	0	N.A.	3.19885	mixing
R41	HFC-41	fluoromethane	CH3F	593-53-3	92	0	2.8	794	molbase $
R410a	R32/R125 (50/50)	N.A.	N.A.	N.A.	2100	0	N.A.	3.2395	mixing
R507a	R125/R143a (50/50)	N.A.	N.A.	N.A.	4000	0	N.A.	4.288	mixing
RC318	CF18	Octafluorocyclobutane	C4F8	115-25-3	10300	0	3200	20.43	molbase $
SES36	Solkatherm	1,1,1,3,3-Pentafluorobutane (= HFC-365mfc)	N.A.	N.A.	3.71	0	N.A.	535	mixing
SulfurDioxide	SulfurDioxide	SulfurDioxide	SO2	7446-09-5	-1	0	N.A.	0.29	molbase $
SulfurHexafluoride	SulfurHexafluoride	SulfurHexafluoride	SF6	2551-62-4	22800	0	3200	9.167	molbase $
Toluene	Toluene	Toluene	C7H8	108-88-3	2.7	0	N.A.	1.1	icis $
Water (R718)	Water	Water	H2O	7732-18-5	0	0	N.A.	0.124	molbase $
Xenon	Xenon	Xenon	Xe	7440-63-3	-1	0	N.A.	1005	molbase $
cis-2-Butene	cis-2-Butene	cis-2-Butene	C4H8	590-18-1	-1	0	N.A.	1273	molbase $
m-Xylene	m-Xylene	m-Xylene	C8H10	108-38-3	-1	0	N.A.	2.63	molbase $
n-Butane (R600)	n-Butane (R600)	n-Butane (R600)	C4H10	106-97-8	4	0	0.018	0.751	molbase $
n-Decane	n-Decane	n-Decane	C10H22	124-18-5	5	0	N.A.	2.42	molbase $
n-Dodecane	n-Dodecane	n-Dodecane	C12H26	112-40-3	5	0	N.A.	2.42	molbase $
n-Heptane	n-Heptane	n-Heptane	C7H16	142-82-5	5	0	N.A.	1.624	molbase $
n-Hexane	n-Hexane	n-Hexane	C6H14	110-54-3	5	0	N.A.	1.177	molbase $
n-Nonane	n-Nonane	n-Nonane	C9H20	111-84-2	5	0	N.A.	217	molbase $
n-Octane	n-Octane	n-Octane	C8H18	111-65-9	5	0	N.A.	2.369	molbase $
n-Pentane (R601)	n-Pentane (R601)	n-Pentane (R601)	C5H12	109-66-0	5	0	0.009	1.452	molbase $
n-Propane (R290)	n-Propane (R290)	n-Propane (R290)	C3H8	74-98-6	3	0	0.041	1.17	molbase $
n-Undecane	n-Undecane	n-Undecane	C11H24	1120-21-4	5	0	N.A.	44	molbase $
o-Xylene	o-Xylene	o-Xylene	C8H10	95-47-6	-1	0	N.A.	0.785	molbase $
p-Xylene	p-Xylene	p-Xylene	C8H11	106-42-3	-1	0	N.A.	1.038	molbase $
trans-2-Butene	trans-2-Butene	trans-2-Butene	C4H8	624-64-6	-1	0	0.018	1238	molbase $

gamme de prix	Application	ASHRAE class	Expansion	Boiling Point [K]	Boiling Point [C]	AF	MM[kg/mol]	TMax[K]	PMax[K]	T3[K]	P3[Pa]
1-547 $ (molbase)	Plastic industry (packaging in food, pharmaceutical and industr	N.A.	dry	266.5067758	-6.643224205	0.19186065	0.05610632	525	50000000	87.8	7.56E-07
1-42 $ (sigma aldrich)	Solvent, intermediate, labs, medical and cosmetics	N.A.	isentropic	328.8404278	55.6904278	0.3071	0.05807914	550	700000000	178.5	2.326486886
N.A.	Climatisation, Refrigeration	N.A.	wet	78.78771092	-194.3622891	0.0335	0.02896546	2000	2000000000	59.75	5264.181069
1-34 $ (molbase)	Fertilizer, Precuresor to nitrogenous compounds, cleaner, ferm	B2	wet	239.5616593	-33.58834071	0.25601	0.01703026	700	1000000000	195.495	6091.223108
N.A.	non reactive substance in high temperature indutrial processes	A1	wet	87.17768777	-185.9723122	-0.00219	0.039948	700	1000000000	83.806	68892.47708
0.737 - 1.25 (molbase-icis)	intermediate to other chemicals	N.A.	dry	352.7894777	79.63947768	0.21083697	0.0781118	725	500000000	278.674	4783.772582
N.A.	Precuresor to chemicals (urea), foods, inert gaas, fire extinguish	A1	wet	0	-273.15	0.22394	0.0440098	1100	800000000	216.592	517964.3434
N.A.	Chemical industry, meat coloring, medicine	N.A.	wet	81.52269414	-191.6273059	0.0497	0.0280101	500	100000000	68.16	15536.87665
290 - 5200	chemical labs	N.A.	wet	222.704972	-50.44502801	0.0978	0.0600751	650	50000000	134.3	64.43457801
1.572-1.572 (icis)	industry (nylon)	N.A.	dry	353.4275829	80.27758286	0.20926	0.08415948	700	250000000	279.47	5240.204369
N.A.	chemical labs	N.A.	wet	0	-273.15	0.13054957	0.042081	473	28000000	273	342702.2037
1-830 (alibaba)	industry (synthetic resins, rubber adhesives)	N.A.	dry	322.0049949	48.85494494	0.20111257	0.0701329	550	250000000	179.7	8.854271413
1.8-690 (sigma-aldrich)	intermediate, non-metal surface treatment, electronics, textile	N.A.	dry	447.990414	174.840414	0.59812483	0.29661576	673	30000000	290.25	69.60923768
2.9-554 (sigma-aldrich)	intermediate, electronic, textiles, cosmetic products, househol	N.A.	dry	483.4950518	210.3450518	0.658	0.3707697	673	30000000	300	27.51166526
3.2-200 (sigma-aldrich)	monomere in the production of silicone polymers, intermediat	N.A.	dry	517.5183171	244.3683171	0.736	0.444924	673	30000000	270.2	0.159752999
465-1076 (sigma aldrich)	heavy water, nuclear fusion, solvent	N.A.	wet	23.61585144	-249.5341486	-0.1362903	0.0040282	600	2000000000	18.724	17189.10197
N.A.	VCM	N.A.		0	-273.15	0.2685785	0	0	0	0	0
N.A.	Medicine (anesthetic), Fuel, Solvent	A3		0	-273.15	0.28192933	0	0	0	0	0
0.8-9.5 (sigma-aldrich)	Solvent, intermediate, fuel additive	N.A.	dry	362.8435571	89.69355712	0.346	0.0900779	600	60000000	277.06	2226.523727
0.9-131 (sigma-aldrich)	solvent, labs, research (fuel)	A3	wet	248.0658313	-25.08416874	0.196	0.04606844	550	50000000	131.66	2.210728141
0.6-645 (sigma-aldrich)	intermediate (ethene), cryogenic refrigeration	A3	wet	184.3250314	-88.82496859	0.099	0.03006904	675	900000000	90.368	1.142108848
1-30 (sigma-aldrich)	medical (antiseptic), recreational, fuel, solvent	N.A.	wet	351.2371426	78.08714262	0.644	0.04606844	650	280000000	159.1	0.000735393
<194 (sigma-aldrich)	intermediate (polystyrene), fuel additive (anti knock agent)	N.A.	dry/wet	408.8247112	135.6747112	0.304	0.106165	700	60000000	178.2	0.000403621
<6.747 (Airliquide)	intermediate	A3	wet	169.1554983	-103.9945017	0.0866	0.02805376	450	300000000	103.989	122.0267632
<960 (icis)	intermediate	N.A.		0	-273.15	0.21019549	0	0	0	0	0
N.A.	preparation of UF6 (nuclear) and SF6 (inert dielectric)	N.A.	wet	84.92209301	-188.227907	0.0449	0.03799681	300	20000000	53.4811	238.8103316
N.A.	Replace R-12 in refrigeration	N.A.	isentropic	249.2701364	-23.87986363	0.28887137	0.10004	420	7200000	240	65359.39301
<987 (sigma-aldrich)	Nulcear magnetique resonance, neutron moderator	N.A.	dry	374.183961	101.033961	0.36430057	0.020027508	825	1000000000	276.969	662.04
<83.16 (Airliquide)	controlled atmosphere, welding	A1	wet	4.208613796	-268.9413862	-0.385	0.004002602	2000	1000000000	2.1768	5033.548897
<115 (Airliquide)	petroleum and chemical industries, coolant, autmotive, nucela	A3	wet	20.32439254	-252.8256075	-0.219	0.00201588	1000	2000000000	13.957	7357.828142
<106 (sigma-aldrich)	chemical industry (hydrochloric acid), semiconductor industry	N.A.		0	-273.15	0.12818922	0	0	0	0	0
<2206 (sigma-aldrich)	analytical chemistry	N.A.	wet	212.5956428	-60.55435719	0.1005	0.03408088	760	170000000	187.7	23258.85584
<282 (alibaba)	refrigeration	N.A.	dry	261.0652436	-12.08475636	0.18353178	0.0581222	575	35000000	113.73	0.022890839
191-401 (molbase sigma-aldrich)	intermediate	N.A.	dry	265.8099761	-7.340023853	0.19259345	0.05610632	525	50000000	132.4	0.676189276
<710.2 (sigma-aldrich)	solvent	N.A.	dry	332.9492021	59.79902011	0.2797	0.08617536	500	1000000000	119.1	7.58E-06
<11.2 (sigma-aldrich)	solvent	A3	dry	300.5961611	27.44616108	0.2274	0.07214878	500	1000000000	112.65	8.93E-05
NA.	Electrical applications, photography, nuclar applications	N.A.	wet	119.5666553	-153.5833447	-0.00089	0.083798	750	200000000	115.77	73502.83741
<2250 (sigma-aldrich)	cosmetic products, electronics, non-metal surface treatment	N.A.	dry	466.9702504	193.8202504	0.668	0.310685	673	30000000	205.2	0.000479684
<4577 (sigma-aldrich)	cosmetic products, polymer preparation, non-metal surface tre	N.A.	dry	502.45069	229.30069	0.722	0.384839	673	30000000	192	5.92E-07
<10000 (lookchem)	cosmetic products, non-metal surface treatment	N.A.	dry	532.1307004	258.9807004	0.82464715	0.45899328	673	30000000	300	1.093376696
<1657 (sigma-aldrich)	cosmetic products, non-metal surface treatment	N.A.	dry	425.1740956	152.0240956	0.52806585	0.23653146	673	30000000	187.2	0.000799034
<205.9 (sigma-aldrich)	cosmetics	N.A.	dry	373.2050138	100.0550138	0.418	0.16237752	580	30000000	204.93	2.95377013
6-32 (molbase)	Fuel	A3	wet	111.507626	-161.642374	0.01142	0.0160428	625	1000000000	90.6941	11696.06411
<33 (sigma-aldrich)	intermediate, fuel	N.A.	wet	337.3633718	64.21337178	0.5720322	0.03204216	580	500000000	175.61	0.186763446
<15840 (sigma-aldrich)	combustible, manufacture of detergents, emulsifiers, lubricant	N.A.	dry	628.1654362	355.0154362	0.80540639	0.29447206	700	50000000	260	1.25E-06
<125200 (sigma-aldrich)	medical research	N.A.	dry	628.5252973	355.3752973	1.14260526	0.29245618	700	50000000	260	7.40E-07
<4180 (sigma-aldrich)	lubricant, cleaning, solvent	N.A.	dry	626.5114216	353.3614216	0.90584936	0.2964794	700	50000000	253.47	4.57E-07
50-11180 (molbase sigma-aldrich)	Food industry	N.A.	dry	601.6382839	328.4882839	0.91031618	0.27045066	700	50000000	302.71	0.016401225
87-25400 (molbase sigma-aldrich)	soap, cosmetics, detergent	N.A.	dry	628.9143501	355.7643501	1.01756	0.29850382	700	50000000	311.84	0.001201007
<15400 (sigma-aldrich)	electrical applications (lighting), cryogenic refrigerant	A1	wet	27.06083462	-246.0891654	-0.0384493	0.020179	723	700000000	24.56	43432.07642
N.A.	rubber manufacture	N.A.	dry	282.2907134	9.140713429	0.1961	0.07214478	550	200000000	256.6	35400.94733
0.074-43 (wiki-sigma-aldrich)	pneumatic industry, welding, food industry	A1	wet	77.24349973	-195.9065003	0.0372	0.02801348	1100	2200000000	63.151	12519.78348
2.6 - 19 (sigma aldrich-molbase)	rocket motors, ICEs, Medicine (anestetic)	N.A.	wet	184.4640642	-88.68593576	0.1613	0.0440128	525	50000000	182.33	87837.43935
N.A.	heat transfer fluid (ORC, electronic cooling)	N.A.		0	-273.15	0.47102359	0	0	0	0	0
N.A.	heavy water, nuclear fusion, solvent	N.A.	wet	23.61585144	-249.5341486	-0.1362903	0.0040282	600	2000000000	18.724	17189.10199
N.A.	petroleum and chemical industries, coolant, autmotive, nucela	N.A.	wet	20.3355392	-252.8144608	-0.219	0.00201594	1000	2000000000	14.008	7559.882381
<8.4 (Air-liquide)	Chemical industry (acids), metal industry (cutting, welding, met	N.A.	wet	90.06210538	-183.0878946	0.0222	0.0319968	300	80000000	54.361	146.2776466
N.A.	heavy water, nuclear fusion, solvent	N.A.	wet	23.61585144	-249.5341486	-0.1362903	0.0040282	600	2000000000	18.724	17189.10198
N.A.	petroleum and chemical industries, coolant, autmotive, nucela	N.A.	wet	20.20290849	-252.9230915	-0.219	0.00201588	1000	2000000000	13.633	7041.086751
1.372250 (sigma-aldrich)	petrochimical industry (intermediate)	A3	wet	225.2418274	-47.90817257	0.146	0.04207974	575	1000000000	87.953	0.000746485
506-5500 (sigma-aldrich)	rocket fuel, organic chemistry	N.A.	wet	0	-273.15	0.204	0.04006	474	31800000	273	263566.906
<110 (sigma-aldrich)	phased out (1996) - exception: hplc in pharmaceutics	A1	isentropic	296.4870693	23.33706932	0.18875065	0.137368	595	100000000	162.68	6.510089436
<102 (sigma-aldrich)	phased out (1996) - exception: hplc in pharmaceutics	A1	dry	320.3384813	47.18848129	0.252535	0.187375	525	200000000	236.93	1871.427544
N.A.	phased out (start in 1996 - complete in 2010)	A1	dry	276.397031	3.247031012	0.2523	0.170921	507	21000000	273.15	88162.38676
N.A.	phased out (start in 1996 - complete in 2010)	N.A.	dry	0	-273.15	0.24843499	0	0	0	0	0
N.A.	phasing out (2020)	A1	isentropic	194.8138273	-78.33617267	0.2566	0.13801182	425	50000000	173.1	26083.73401
N.A.	refrigeration, phased out (start in 1996 - complete in 2010)	A1	wet	243.0888621	-30.06113787	0.17947832	0.120913	525	200000000	116.099	0.242550801
N.A.	refrigeration,phased out (start in 1996 - complete in 2010)	B1	dry	300.6107045	27.46070449	0.2819225	0.152931	523	76000000	166	220233802
<5000 (molbase)	refrigeration,	N.A.	dry	291.1164909	17.96649092	0.30245229	0.13049619	550	100000000	195.15	250.2655778
<4000 (molbase)	refrigeration,	A2L	dry	243.3652786	-29.78472137	0.276	0.114041593	410	30000000	220	31507.55879
<12000 (molbase)	refrigeration,	N.A.	dry	253.8797609	-19.27023911	0.313	0.114041593	420	15000000	168.62	218.5800201
<12000 (molbase)	refrigeration,	N.A.	dry	282.5577786	9.407778555	0.3274	0.114041593	430	6000000	273	67802.93936
<1420 (molbase)	refrigeration,phased out (start in 1996 - complete in 2010)	A1	dry	260.8733643	-12.27663572	0.28809508	0.1364762	470	40000000	120	0.026738624
<800 (molbase)	refrigeration, phasing out (2020)	N.A.	wet	224.7935831	-48.35641695	0.3052	0.1200214	500	60000000	172.52	2914.046038
116-5000 (molbase)	refrigeration,phased out (start in 1996 - complete in 2010)	A1	dry	191.4922705	-81.65772945	0.17458633	0.104459	450	50000000	98.15	0.905572259
<500 (molbase)	refrigeration, phasing out (2020)	A1	wet	246.7888117	-26.36118825	0.32684	0.102032	455	70000000	169.85	389.5637886
<7500 (sigma-aldrich)	refrigeration,	N.A.	wet	0	-273.15	0.17618112	0	0	0	0	0
<1200 (molbase)	refrigeration, phasing out (2020)	N.A.	wet	144.9180419	-128.2319581	0.1785	0.0880046	623	51000000	120	11294.329
<1200 (molbase)	refrigeration,phased out (start in 1996 - complete in 2010)	N.A.	isentropic	304.8212562	31.67125616	0.2195	0.11694962	500	400000000	169.68	6.492735334
<1200 (molbase)	refrigeration, phasing out (2020)	A2	isentropic	263.7025091	-9.447490894	0.2321	0.10049503	470	60000000	142.72	3.63265187
<1200 (molbase)	refrigeration, phasing out (2020)	A2	dry	225.6321461	-47.51784388	0.26148965	0.084041	450	150000000	161.34	1074.945442
<1200 (molbase)	not commonly used,phasing down (2050)	A2	wet	248.8310111	-24.31898889	0.27521711	0.066051	471	58000000	154.56	64.13864974
<4000 (molbase)	not commonly used,phasing down (2050)	N.A.	dry	235.3105856	-37.83941444	0.21624284	0.0480595	450	50000000	130	5.512269533
N.A.	refrigeration,phased out (start in 1996 - complete in 2010)	B1	wet	281.6730899	8.523089905	0.2061	0.1029227	473	138000000	200	872.8349802
<2000 (molbase)	refrigeration,phased out (start in 1996 - complete in 2010)	A1	dry	236.0705718	-37.07942817	0.3172	0.18801933	440	20000000	125.45	2.018573582
<900 (molbase)	refrigeration,phased out (start in 1996 - complete in 2010)	A1	wet	232.0590213	-41.09097867	0.22082	0.086468	550	60000000	115.73	0.379363285
<395 (molbase)	refrigeration, phasing out (2020)	A1	dry	256.5408366	-16.64516343	0.35764124	0.17002886	475	60000000	146.35	7.331566948
<600 (molbase)	refrigeration, phasing out (2020)	A1	isentropic	190.9047845	-82.24521549	0.26296489	0.07001385	425	120000000	118.02	58.04099395
800 - 1400 - 3028 (molbase sigma-aldrich molbase	refrigeration, phasing out (2020)	N.A.	dry	279.0005077	5.850507657	0.36878238	0.1520384	412	6000000	243	17498.1884
<1700 (sigma-aldrich)	refrigeration, phasing out (2020)	A1	dry	271.3458417	-1.804158287	0.3769118	0.1520384	400	700000000	179.6	160.3267788
<7000 (molbase)	refrigeration, phasing out (2020)	N.A.		0	-273.15	0.35456542	0	0	0	0	0
7 - 25 - 134 - (alibaba - honeywell - molbase - sigm	refrigeration, phasing out (2020)	B1	dry	287.8701412	14.72014119	0.3776	0.13404794	440	200000000	171.05	13.75743391
<158 (molbase)	refrigeration, phasing out (2020)	A2	wet	221.2407128	-51.90928715	0.2769	0.052024	435	70000000	136.34	47.99989388
<3000 (molbase)	refrigeration, phasing out (2020)	N.A.	dry	312.9773861	39.82738609	0.3774451	0.14807452	500	35000000	239	2478.418202
0.666 - 1250 (molbase)	refrigeration, phasing out (2020)	N.A.		0	-273.15	0.1500685	0	0	0	0	0
N.A.	refrigeration, phasing out (2020)	A1	wet	226.6539541	-46.49604586	0.293	0.0976038	450	50000000	200	22649.18748
N.A.	refrigeration, phasing out (2020)	A1	wet	229.2508507	-43.89914935	0.363	0.0862036	450	50000000	200	19158.054452
<3200 (molbase)	Semiconductor manufacturing	N.A.	wet	194.5555218	-78.59447825	0.2004	0.03403292	425	70000000	129.82	344.1990638
N.A.	refrigeration, phasing out (2020)	A1	wet	221.4497299	-51.70027009	0.296	0.0725854	450	50000000	200	29160.33537
N.A.	refrigeration, phasing out (2020)	A1	wet	226.1353213	-47.01467868	0.286	0.0988592	450	50000000	200	23232.99282
<1200 (sigma-aldrich)	refrigeration, phasing out (2020)	A1	dry	266.8578021	-6.292197921	0.355345	0.2000312	623	60000000	233.35	19461.05596
N.A.	heat transfer medium, solvent, refrigeration,phasing down (20	N.A.	dry	308.4933821	35.34338205	0.352	0.18845	725	500000000	200	573.2898712
<160 (sigma-aldrich)	chemical industry(sulfuric acid)	B1	wet	262.8381577	-10.31184228	0.25612994	0.0640636	525	35000000	197.7	1660.220188
<238 (molbase)	dielectric medium, medicine, tracer compound, phasing out (20	N.A.	wet	0	-273.15	0.21	0.146055419	650	150000000	223.555	231424.4772
<70 (sigma-aldrich)	chemical industry (intermediate), solvent, fuel (octane booster)	N.A.	dry	383.2828762	110.1328762	0.2657	0.09213842	700	50000000	178	0.039393353
<40 (sigma-aldrich)	agriculture, drinking, transportation, chemical industry, heat ex	A1	wet	372.7559289	99.6059289	0.34429208	0.018051268	1273	1000000000	273.16	611.654667
<10000 (sigma-aldrich)	illumination and optics, lasers, medicine (anestetic)	N.A.	wet	164.8222878	-108.3277122	0.00363	0.131293	750	700000000	161.4	81747.79907
N.A.	intermediate (gasoline, butadiene)	N.A.	isentropic	276.5291207	3.379120717	0.20235593	0.05610632	525	50000000	134.3	0.263649892
0.86 - 8.8 - (molbase - icis - sigma-aldrich)	chemical industry (isophtalic acid)	N.A.	dry/wet	411.7240608	138.5740608	0.326	0.106165	700	200000000	225.3	3.123267556
<1600 (sigma aldrich)	fuel (octane number enhancement)	A3	dry	272.3139334	-0.836066564	0.20081009	0.0581222	575	12000000	134.895	0.665658104
<90 (sigma-aldrich)	fuel (component of gasoline and kerosene)	N.A.	dry	446.7531956	173.6031956	0.4884	0.14228168	675	800000000	243.5	1.404183981
<175 (sigma-aldrich)	solvent, distillation chaser, scintillator component	N.A.	wet	488.8890965	215.7390965	0.57418222	0.17033484	800	200000000	263.6	0.626210864
<112 (sigma-aldrich)	test fuel component in anti-knock test engines, non-polar solve	N.A.	dry	371.0859354	97.93593545	0.349	0.100202	600	100000000	182.55	0.17549029
<110 (sigma-aldrich)	industry (glues), oil extraction, non polar solvent,	N.A.	dry	341.4459554	68.29595539	0.299	0.08617536	548	92000000	177.83	1.277140271
<384 (molbase)	fuel (kerosene), solvent, fuel additive	N.A.	dry	423.416494	150.266494	0.4433	0.1282551	600	800000000	219.7	0.444485529
<210 (sigma-aldrich)	fuel (gasoline)	N.A.	dry	398.3012714	125.1512714	0.395	0.1142285	548	96000000	216.37	1.988916126
1.45 - 9.8 - (molbase - fiers - sigma-aldrich)	industry(blowing polystyrene foam, refrigerant, pesticide), solv	N.A.	dry	308.828438	35.67843801	0.251	0.07214878	573	69000000	143.47	0.076322083
N.A.	fuel (domestic and indutrial), refrigeration, soldering and brazi	A3	wet	230.7382284	-42.4117716	0.1521	0.04409562	650	1000000000	85.525	0.000171651
16 - 100 (molbase)	internal standard in gas chromatography	N.A.	dry	468.3976027	195.2476027	0.5390371	0.15630826	700	500000000	247.541	0.446056045
0.785-8.8 - (molbase - icis - sigma-aldrich)	production of phthalic anhydride	N.A.	dry/wet	417.0244118	143.8744118	0.312	0.106165	700	70000000	247.985	22.80577634
1.038 - 8.8 - (molbase - icis - sigma-aldrich)	synthesis of various polymers,	N.A.	dry/wet	410.978838	137.828838	0.324	0.106165	700	200000000	286.4	580.0849985
<3000 (sigma-aldrich)	intermediate (gasoline, butadiene)	N.A.	dry	273.685613	0.535612958	0.21007683	0.05610632	525	50000000	167.6	74.81669122

TCrit [K]	TCrit [C]	rhoCrit [kg/m³]	PCrit [Pa]	Flammability	Toxicity	Explosivity	Reactivity	Chemical stability	Possibility of hazardous reactions
419.29	146.14	237.8907968	4005100	H220	Not classified for toxicity	H280	May build up electrostatic charges: risk ...	Unstable on exposure to air	Reacts slowly on exposure to air: peroxida...
508.1	234.95	272.971958	4700000	H225	H319, H336	0	Upon combustion: CO and CO2 are form...	Unstable on exposure to light	Not established.
132.5306	-140.6194	342.6845642	3786000	0	Not classified for toxicity	H280	Not reactive under normal conditions	Stable under normal conditions	None under normal processing.
405.4	132.25	225	11333000	H221	H314, H331, H400	H280	Substance has basic reaction.	Stable under normal conditions	Reacts slowly with water (moisture): relea...
150.687	-122.463	535.6	4863000	0	H380	0	Not reactive under normal conditions	Stable under normal conditions	Under normal conditions of storage and u...
562.02	288.87	304.7922436	4894000	H225	H304, H315, H319, H340, H350, H372, H401	0	Thermal decomposition is highly depend...	Stable under normal conditions	No hazardous reaction is expected when ...
304.1282	30.9782	467.6000013	7377300	0	Not classified for toxicity	H280	Substance has acid reaction	Stable under normal conditions	Violent to explosive reaction with (some)...
132.86	-140.29	303.909585	3494000	H220	H331, H360D, H372	H280	May build up electrostatic charges: risk ...	Stable under normal conditions	Reacts with many compounds e.g.: with (s...
378.77	105.62	445.156491	6370000	H220	H331	0	No specific test data related to reactivity	Stable under normal conditions	Under normal conditions of storage and u...
553.6	280.45	271.3301635	4082400	H225	H304, H315, H319, H335, H336, H361, H371,	0	May react with oxygen and strong oxidiz...	This material is considered stable unde...	May react with oxygen and strong oxidizin...
398.3	125.15	258.5000019	5579700	H220	H332, H336, H380	H280	No specific test data related to reactivity	The product is stable.	Under normal conditions of storage and u...
511.72	238.57	267.907678	4571200	H225	H412	0	May build up electrostatic charges: risk ...	Stable under normal conditions.	Reacts violently with (strong) oxidizers: (i...
586.5	313.35	305.7894922	1332000	H226	H302, H312, H320, H361, H413	0	None known.	Stable in sealed containers in a cool pla...	Bases can cause non-hazardous polymeriz...
619.15	346	304.909285	1160000	0	0	0	None known.	Stable under recommended storage co...	In use, may form flammable/explosive vap...
645.78	372.63	279.0957298	961000	H227	0	0	None known.	Stable in sealed containers in a cool pla...	Bases can cause non-hazardous polymeriz...
38.34	-234.81	69.405886	1679600	H220	H380	H280	No reactivity hazard other than the effe...	Stable under normal conditions	May react violently with oxidants. Can for...
0	-273.15	0	0	H225	H315, H319, H331, H335, H350	0	No specific test data related to reactivity	stable	Under normal conditions of storage and u...
0	-273.15	0	0	H224	H302, H305, H316, H320, H335, H361	0	No reactivity hazard other than the effe...	The product is stable.	N.A.
557	283.85	360.3116	4908800	H225	0	H280	No reactivity hazard other than the effe...	Stable under normal conditions.	Reacts violently with oxydants and potass...
400.378	127.228	273.6465336	5336800	H220	0	H280	May build up electrostatic charges: risk ...	Unstable on exposure to air.	Reacts violently with many compounds e...
305.322	32.172	206.18	4872200	H220	0	H280	May build up electrostatic charges: risk ...	Stable under normal conditions.	Violent to explosive reaction with (some)...
514.71	241.56	273.1858492	6268000	H225	H319	0	No specific test data related to reactivity	Stable under normal temperatures and...	Under normal conditions of storage and u...
617.12	343.97	290.9999636	3622400	H226	H315, H319, H332, H351, H360, H373	0	The product is stable. Vapor is explosive	Stable under normal temperatures and...	Has not been reported.
282.35	9.2	214.24	5041800	H220	H336, H380	H280	May build up electrostatic charges: risk ...	Stable under normal conditions.	May polymerise on exposure to some con...
0	-273.15	0	0	H220	H315, H319, H331, H335, H340, H350	0	May be ignited by sparks. Gas/vapour s...	Unstable on exposure to heat. Unstabl...	Reacts slowly on exposure to water (mois...
144.414	-128.736	592.8642264	5172400	H270	H314, H318, H330, EUH071	H280	No specific test data related to reactivity	The product is stable.	Hazardous reactions or instability may oc...
377.921	104.771	465	3635000	0	EUH018, EUH044	H280	Stable under recommended transport or...	Stable under recommended storage co...	Hazardous reactions will not occur under ...
643.847	370.697	355.9999698	21671000	0	0	0	On mixing with water, heat is evolved.	The product is stable.	None known.
5.1953	-267.9547	72.56717426	227600	0	H380	H280	None known.	Stable under normal conditions.	None under normal processing.
33.145	-240.005	31.26226704	1296400	H220	H380	H280	May be ignited by sparks.	Stable under normal conditions.	Reacts violently with many compounds e...
0	-273.15	0	0	H220	H314, H331	H280	Substance has acid reaction.	Unstable on exposure to moisture.	Reacts exothermically with water (moistu...
373.1	99.95	347.2841672	9000000	H220	H330, H335, H400	0	No reactivity hazard other than the effe...	Stable under normal conditions.	May react violently with oxidants. Can for...
407.817	134.667	225.5	3629000	H220	H380	H280	May build up electrostatic charges: risk ...	Stable under normal conditions.	Reacts with (strong) oxidizers: (increased)...
418.09	144.94	233.9633544	4009800	H220	H380	H280	May build up electrostatic charges: risk ...	Unstable on exposure to air.	Reacts slowly on exposure to air: peroxida...
497.7	224.55	233.9661024	3040000	H225	H304, H315, H336, H361, H402, H411	0	Reacts violently with strong oxidizers. In...	Extremely flammable liquid and vapor.	Hazardous polymerization will not occur.
460.35	187.2	235.9986594	3378000	H224	H336, H411	0	No specific test data related to reactivity	The product is stable.	Under normal conditions of storage and u...
209.48	-63.67	909.2083	5525000	0	H380	H280	None known.	Stable	None known.
599.4	326.25	284.1716397	1227000	H227	H302	0	No additional information available	Stable	No additional information available
628.36	355.21	263.9218791	945000	0	H315, H319, H335	0	No additional information available	Stable	No additional information available
653.2	380.05	278.1777427	877000	H227	H315, H319, H335	0	No additional information available	Stable	No additional information available
564.09	290.94	256.7399088	1415000	0	H410	0	No data available	Stable under recommended storage co...	No data available
518.75	245.6	258.1518407	1939000	H225	H401, H411	0	No additional information available	Stable in sealed containers in a cool pla...	No additional information available
190.564	-82.586	162.6600027	4599200	H220	H380	H280	May build up electrostatic charges: risk ...	Stable under normal conditions.	Reacts with (strong) oxidizers: (increased)...
512.5	239.35	273	8215850	H225	H301, H311, H331, H370	0	On heating: release of toxic/corrosive/co...	Hygroscopic.	No additional information available
799	525.85	238.0512133	1341000	0	H315	0	N.A.	N.A.	N.A.
772	498.85	247.7981213	1369000	0	0	0	N.A.	Stable under normal conditions.	N.A.
782	508.85	241.000222	1246000	0	0	0	N.A.	Product is considered stable.	N.A.
755	481.85	242.594242	1350000	0	H315	0	Not a self-reactive substance	Stable under normal temperatures and...	N.A.
775	501.85	237.1015842	1239000	0	H335	0	N.A.	Stable under normal temperatures and...	N.A.
44.4918	-228.6582	481.914878	2680000	0	H380	H280	No specific test data related to reactivity	The product is stable.	Under normal conditions of storage and u...
433.74	160.59	235.9265106	3196000	H220	H380, H400	H280	No specific test data related to reactivity	The product is stable.	Under normal conditions of storage and u...
126.192	-146.958	313.3	3395800	0	H281	0	No reactivity hazard other than the effe...	Stable under normal conditions	None.
309.52	36.37	452.011456	7245000	H270	0	H280	May cause or intensify fire; oxidiser. Sub...	Stable under normal conditions.	Decomposes slowly on exposure to (some...
0	-273.15	0	0		H305	0	This material may be reactive with certa...	Stable.	Hazardous polymerization will not occur...
38.34	-234.81	69.405886	1679600	H220	H380	H280	No reactivity hazard other than the effe...	Stable under normal conditions.	May react violently with oxidants. Can for...
33.22	-239.93	31.1352666	1310650	H220	H380	H280	May be ignited by sparks.	Stable under normal conditions.	Reacts violently with many compounds e...
154.581	-118.569	436.143644	5043000	H270	0	H280	No specific test data related to reactivity	The product is stable.	Hazardous reactions or instability may oc...
38.34	-234.81	69.405886	1679600	H220	H380	H280	No reactivity hazard other than the effe...	Stable under normal conditions.	May react with oxidants. Can for...
32.938	-240.212	31.32274344	1285800	H220	H380	H280	May be ignited by sparks.	Stable under normal conditions.	Reacts violently with many compounds e...
364.211	91.061	229.6291412	4555000	H220	H380	H280	May build up electrostatic charges: risk ...	Unstable on exposur to air.	Oxidizes on exposure to air: peroxidation...
402.38	129.23	244.8999998	5626000	0	H280	H280	No specific test data related to reactivity	The product is stable.	Under normal conditions of storage and u...
471.06	197.91	565	4394000	0	H380, H420	0	No specific test data related to reactivity	Stable	Under normal conditions of storage and u...
487.21	214.06	560	3392200	0	H319, H411, H420	0	No specific test data related to reactivity	Stable under normal conditions.	Hazardous polymerisation does not occur...
418.83	145.68	579.9691372	3257000	0	H380, H420	H280	No specific test data related to reactivity	Stable under normal conditions.	Hazardous polymerisation does not occur...
0	-273.15	0	0	0	EUH059	H280	The product is stable.	Stable under normal conditions.	Hazardous polymerisation does not occur...
293.03	19.88	613.3245281	3048000	0	H380	H280	No specific test data related to reactivity	Material is stable.	Under normal conditions of storage and u...
385.12	111.97	565	4136100	0	H380, H420	H280	No reactivity hazard	Stable under normal conditions.	Under normal conditions of storage and u...
456.831	183.681	550.0036482	3672000	0	H320, H371, H373, H420	0	No specific test data related to reactivity	The product is normally stable.	Under normal conditions of storage and u...
438.75	165.6	478.9210158	3570900	0	H380	H280	N.A.	The product is stable at normal handlin...	May polymerize.
367.85	94.7	475.553442	3382200	H220	H380	H280	Reactions with alkali metals. Reactions w...	The product is stable.	Hazardous reactions or instability may oc...
382.52	109.37	489.2384331	3636250	0	H380	H280	Reactions with alkali metals.	Stable under normal conditions.	None.
423.27	150.12	470	3533000	0	H380	H280	Reactions with alkali metals.	Stable under normal conditions.	None.
395.425	122.275	560	3624295	0	H380, H420	H280	No specific test data related to reactivity	The product is stable.	Under normal conditions of storage and u...
339.173	66.023	573.5822706	3617700	0	H380	H280	No specific test data related to reactivity	The product is stable.	Under normal conditions of storage and u...
301.88	28.73	582.88122	3879000	0	H420	H280	No specific test data related to reactivity	The product is stable.	Under normal conditions of storage and u...
374.21	101.06	511.8999517	4059280	0	0	H280	No specific test data related to reactivity	The product is stable.	Under normal conditions of storage and u...
0	-273.15	0	0	0	H317, H319, H341	H280	Stable at normal temperatures and pres...	Stable	N.A.
227.51	-45.64	625.6616105	3750000	0	H380	H280	No specific test data related to reactivity	The product is stable.	Under normal conditions of storage and u...
477.5	204.35	458.55946	4212000	0	H380, H420	H280	No specific test data related to reactivity	The product is stable.	Under normal conditions of storage and u...
410.26	137.11	445.9969431	4055000	H220	H336, H380, H420	H280	Not reactive under normal conditions	The product is stable.	Under normal conditions of storage and u...
345.857	72.707	431.0000664	3761000	H220	H380	H280	No specific test data related to reactivity	The product is stable.	Under normal conditions of storage and u...
386.411	113.261	368	4520000	H220	0	H280	No specific test data related to reactivity	Material is stable	Under normal conditions of storage and u...
375.25	102.1	301.81366	5010000	0	H315, H319, H335, H336, H380	H280	Stable under recommended transport or...	Stable under normal conditions.	Hazardous reactions will not occur under ...
451.48	178.33	526.0137946	5181200	0	H302, H312, H315, H319, H332, H335, H420	H280	Stable at normal temperatures and pres...	Stable under normal temperatures and...	Under normal conditions of storage and u...
345.02	71.87	627.9845622	2640000	0	H380	H280	No specific test data related to reactivity	The product is stable.	Under normal conditions of storage and u...
369.295	96.145	523.842167	4990000	0	H380, H420	H280	The product decomposes on heating.	The product is chemically stable	Stable at normal temperatures and storag...
374.9	101.75	594.2508657	2925000	0	H380	H280	Decomposes on heating.	The product is stable.	Under normal conditions of storage and u...
299.293	26.143	526.504152	4832000	0	H380	H280	May react with aluminium	Stable under normal conditions.	Under normal conditions of storage and u...
412.44	139.29	564.9746944	3420000	0	H315, H319, H380	H280	No specific test data related to reactivity	The product is stable.	Under normal conditions of storage and u...
398.07	124.92	551.2912384	3200000	0	H380	H280	No specific test data related to reactivity	The product is stable.	Under normal conditions of storage and u...
0	-273.15	0	0	H224	H301, H311, H331	H280	N.A.	Stable under recommended storage co...	N.A.
427.01	153.86	519.4357675	3651000	0	H315, H319, H335, H380	H280	N.A.	Stable under normal conditions.	N.A.
351.255	78.105	424.0000012	5782000	H220	H380	H280	No specific test data related to reactivity	Stable under normal conditions.	Under normal conditions of storage and u...
460	186.85	473.838464	3266000	H220	H380	0	No specific test data related to reactivity	Stable under normal conditions.	Under normal conditions of storage and u...
0	-273.15	0	0	H220	H351, H373, H420	H280	May be ignited by sparks. Gas/vapour s...	Stable under normal conditions.	Reacts violently with (strong) oxidizers: (i...
345.27	72.12	482.162772	3734800	0	H380	H280	Decomposes on heating.	Stable under normal conditions.	Under normal conditions of storage and u...
359.345	86.195	453.43094	4631700	0	H380	H280	Decomposes on heating.	Stable under normal conditions.	Under normal conditions of storage and u...
317.28	44.13	316.506156	5897000	H220	H380	H280	Not reactive under normal conditions	Stable under normal conditions.	May form explosive mixtures with air.
344.494	71.344	459.0300696	4901200	0	H380	H280	Stable under recommended storage and...	The product is stable.	Hazardous reactions will not occur under ...
343.765	70.615	490.74	3704900	0	H336, H380	H280	This material is chemically stable under...	The product is stable	Hazardous reactions will not occure unde...
388.38	115.23	619.9727007	2777500	0	H380	H280	No reactivity hazard	Stable under normal conditions.	None.
450.7	177.55	517.58	2849000	N.A	N.A.	N.A.	Risk of violent reaction. Risk of explosio...	Stable under recommended storage co...	Strong oxidizers, alkali metals and alkaline...
430.64	157.49	525.002841	7884000	0	H314, H318, H331	H280	Substance has acid reaction	Unstable on exposure to moisture.	Reacts with water (moisture): release of c...
318.7232	45.5732	742.3	3754983	0	0	H280	Substance has neutral reaction.	Stable under normal conditions.	N.A.
591.75	318.6	291.986653	4126000	H225	H304, H315, H336, H361, H373	0	Upon combustion: CO and CO2 are form...	Stable under normal conditions.	Under normal conditions of storage and u...
647.096	373.946	322	22064000	N.A.	N.A.	N.A.	N.A.	Stable	N.A.
289.733	16.583	1102.8612	5842000	0	H380	H280	No reactivity hazard	Stable under normal conditions.	none
435.75	162.6	238.1152221	4225500	H220	H380	H280	No reactivity hazard	Stable under normal conditions.	May occur. Hazardous polymerization ma...
616.89	343.74	282.929725	3534600	H226	H304, H312, H315, H319, H332, H335, H412	0	N.A.	Stable under recommended storage an...	Stable under normal conditions of use.
425.125	151.975	228	3796000	H220	H380	H280	May build up electrostatic charges: risk ...	Stable under normal conditions.	Reacts with (strong) oxidizers: (increased)...
617.7	344.55	233.3419552	2103000	H226	H304	0	May build up electrostatic charges: risk ...	Stable under normal conditions.	Reacts with (strong) oxidizers: (increased)...
658.1	384.95	226.5453372	1817000	H226	H304	0	May build up electrostatic charges: risk ...	Stable under normal conditions.	Reacts with (strong) oxidizers: (increased)...
540.13	266.98	232	2736000	H226	H304, H315, H336, H410	0	May build up electrostatic charges: risk ...	Stable under normal conditions.	Can form potentially explosive atmosphe...
507.82	234.67	233.18	3034000	H225	H304, H315, H336, H361f, H373, H411	0	May build up electrostatic charges: risk ...	Stable under normal conditions.	Hexane can react vigorously with strong o...
594.55	321.4	232.141731	2281000	H226	H304, H315, H336, H410	0	May build up electrostatic charges: risk ...	Stable under normal conditions.	Reacts with (strong) oxidizers: (increased)...
569.32	296.17	234.8994874	2497000	H225	H304, H336, H411	0	May build up electrostatic charges: risk ...	Stable under normal conditions.	Reacts with (strong) oxidizers: (increased)...
469.7	196.55	232	3370000	H225	H304, H336, H411	0	May build up electrostatic charges: risk ...	Stable under normal conditions.	Reacts with (strong) oxidizers: (increased)...
369.89	96.74	220.4781	4251200	H220	0	H280	May build up electrostatic charges: risk ...	Stable under normal conditions.	Reacts violently with many compounds e...
638.8	365.65	236.794019	1990400	H227	H304, H315, H319, H335, H336	0	May build up electrostatic charges: risk ...	Stable under normal conditions.	Slightly reactive to reactive with oxidizing...
630.259	357.109	284.9999425	3737500	H226	H304, H312, H315, H319, H332, H335, H412	0	Photochemically reactive.	Stable under recommended storage an...	Stable under normal conditions of use.
616.168	343.018	286.0000168	3531500	H226	H303, H304, H312, H315, H319, H332	0	Reacts violently with strong oxidising ag...	Stable under recommended storage an...	Stable under normal conditions of use.
428.61	155.46	236.3759262	4027300	H220	H380	H280	N.A.	Stable under normal conditions.	Hazardous polymerization may occur if no...

Conditions to avoid	Incompatible materials	Hazardous decomposition products	NFPA Health	NFPA Fire	NFPA Reactivity	NFPA Specific	HMIS Health	HMIS Fire	HMIS Physical	HMIS Protective
Use spark-/explosionproof appliances and l	Combustible materials, oxidizing ager	Upon combustion: CO and CO2 are fo	1	4	0	N.A.	0	4	1	N.A.
Direct sunlight. Extremely high or low temp	Strong acids, Strong bases	fume. Carbon monoxide. Carbon diox	1	3	0	N.A.	1	3	0	C
None known.	None known.	None known.	0	0	0	N.A.	0	0	0	N.A.
Use spark-/explosionproof appliances and l	Oxidizing materials, (strong) acids, halog	On heating: release of toxic/combusti	3	1	0	N.A.	3	1	2	N.A.
No specific data	No known incompatible products	Under normal conditions of storage a	0	0	0	SA	0	0	3	N.A.
Avoid heat, sparks, open flames and other i	Strong oxidising agents	Thermal decomposition is highly depe	2	3	0	N.A.	2	3	0	N.A.
Keep away from naked flames/heat.	(strong) bases, metal powders	No data available.	2	0	0	SA	1	0	3	N.A.
Use spark-/explosionproof appliances and l	Combustible materials, oxidizing ager	No data available.	2	4	0	N.A.	1	4	3	N.A.
Avoid all possible sources of ignition (spark	Extremely reactive or incompatible w	Under normal conditions of storage a	3	4	0	N.A.	3	4	2	N.A.
Heat, flames and sparks.	Oxidizing solids. Oxidizing liquids.	Carbon Dioxide, Carbon oxides	1	3	0	N.A.	1	3	0	H
Avoid all possible sources of ignition (spark	Highly reactive or incompatible with t	Under normal conditions of storage a	1	4	0	N.A.	1	4	3	N.A.
Use spark-/explosionproof appliances and l	Oxidizing agents, highly flammable m	Upon combustion: CO and CO2 are fo	2	3	0	N.A.	2	3	0	H
Heat. Open flame. Sparks.	Oxidizing agent. Peroxides.	Organic acid vapors.	2	2	0	N.A.	2	2	0	N.A.
Avoid excessive heat and light.	Oxidizing agents	None known.	0	2	0	N.A.	0	2	0	N.A.
Heat. Open flame. Sparks.	Oxidizing agent. Peroxides.	Formaldehyde, Organic acid vapors.	0	1	0	N.A.	0	1	0	N.A.
Keep away from heat/sparks/open flames/	Oxidizing agent, Halogens, Alkaline ea	Under normal conditions of storage a	0	4	0	N.A.	0	4	3	N.A.
Avoid all possible sources of ignition (spark	N.A.		2	3	0	N.A.	2	3	0	H
heat, ignition sources, incompatible materi	Strong oxidizing agents, halogens, sul	Under fire conditions this product ma		4	0	N.A.	1	4	0	N.A.
Heat, ignition sources, incompatible materi	Highly reactive with oxidizing agents.	Under fire conditions this product ma	1	3	0	N.A.	2	3	0	j
Use spark-/explosionproof appliances and l	Highly flammable materials, oxidizing	Upon combustion: CO and CO2 are fo	1	4	1	N.A.	2	4	0	H
Use spark-/explosionproof appliances and l	Oxidizing agents, (strong) acids, halog	Upon combustion: CO and CO2 are fo	2	4	0	N.A.	1	4	3	N.A.
Incompatible materials, ignition sources, ex	Strong oxidizing agents, acids, alkali m	Under normal conditions of storage a	2	3	0	N.A.	2	3	0	E
Incompatible materials, ignition sources, ex	Oxidizing agents.	Carbon dioxide and carbon monoxide	2	3	0	N.A.	2	3	0	H
Use spark-/explosionproof appliance and lig	Combustible materials, oxidizing ager	Upon combustion: CO and CO2 are fo	2	4	2	N.A.	1	4	3	N.A.
Use spark-/explosionproof appliances and l	Combustible materials, oxidizing ager	Upon combustion: CO and CO2 are fo	2	4	2	N.A.	1	4	3	N.A.
No specific data.	Extremely reactive or incompatible w	Under normal conditions of storage a	4	0	4	N.A.	3	0	3	N.A.
Do not pierce or burn, even after use. Do no	Strong oxidizing agents, Strong acids	carbon monoxide, carbon dioxide, hy	N.A.	N.A.	N.A.	N.A.	N.A.	N.A.	N.A.	N.A.
None known.	None known.	None known.	1	0	0	N.A.	1	0	0	A
None under recommended storage and han	None known.	None known.	0	0	0	SA	0	0	3	N.A.
Use spark-/explosionproof appliances and l	Combustible materials, oxidizing ager	N.A.	0	4	0	N.A.	0	4	3	N.A.
Keep away from naked flames/heat. Take p	Oxidizing agents, reducing agents, (str	On exposure to air: release of corrosi	3	0	1	N.A.	3	0	3	N.A.
Avoid moisture in installation systems. Keep	Ammonia. Bases. Bromine pentafluor	Thermal decomposition may produce	4	4	0	N.A.	4	4	0	N.A.
Use spark-/explosionproof appliances and l	Combustible materials, oxidizing ager	Upon combustion: CO and CO2 are fo	1	4	0	N.A.	1	4	2	N.A.
Use spark-/explosionproof appliances and l	Combustible materials, oxidizing ager	Upon combustion: CO and CO2 are fo	1	4	0	N.A.	1	4	2	N.A.
Direct sunlight, extremely high or low temp	Strong acids, strong bases, strong oxid	None known.	2	3	0	N.A.	1	1	4	N.A.
Avoid all possible sources of ignition (spark	Reactive or incompatible with the foll	Under normal conditions of storage a	1	3	0	N.A.	1	3	0	H
None known.	None known.	None known based on information su	0	0	0	SA	0	0	0	N.A.
Heat. Open flame. Sparks	Oxidizing agent.	Formaldehyde. Organic acid vapors. S	0	2	0	N.A.	1	2	0	N.A.
Heat. Open flame. Sparks	Oxidizing agent.	Formaldehyde. Organic acid vapors. S	2	2	0	N.A.	1	2	0	N.A.
Heat. Open flame. Sparks	Oxidizing agent.	Formaldehyde. Organic acid vapors. S	N.A.	N.A.	N.A.	N.A.	1	2	0	N.A.
Keep away from open flames, hot surfaces a	Strong oxidizing agents, Strong acids	Carbon monoxide (CO), Carbon dioxid	0	3	0	N.A.	0	3	0	N.A.
Heat. Open flame. Sparks.	Oxidizing agent. Peroxides.	Organic acid vapors.	2	3	2	N.A.	2	3	1	H
Use spark-/explosionproof appliances and l	Combustible materials, oxidizing ager	Upon combustion: CO and CO2 are fo	0	4	0	N.A.	0	4	3	N.A.
Direct sunlight. High temperature. Incompa	Strong oxidizers. Strong bases. Strong	Carbon dioxide. Carbon monoxide.	1	3	0	N.A.	2	3	0	H
N.A.	Strong oxidizing agents	N.A.	0	1	0	N.A.	0	1	1	N.A.
Incompatible products. Excess heat. Exposu	Strong oxidizing agents	Carbon monoxide (CO), Carbon dioxid	N.A.	N.A.	N.A.	N.A.	N.A.	N.A.	N.A.	N.A.
N.A.	Strong oxidizing agents	N.A.	0	1	0	N.A.	N.A.	N.A.	N.A.	N.A.
Heat, flames, sparks and other sources of ig	Oxidizing agents and strong bases	Thermal decomposition will evolve irr	N.A.	N.A.	N.A.	N.A.	1	1	1	N.A.
Incompatible materials, dust generation, str	Strong oxidizing agents.	Carbon monoxide, carbon dioxide, ac	1	2	0	N.A.	1	2	0	N.A.
No specific data.	No specific data.	Under normal conditions of storage a	0	0	0	SA	0	0	3	N.A.
Avoid all possible sources of ignition (spark	Under normal conditions of storage a	Under normal conditions of storage a	1	4	0	N.A.	1	4	2	N.A.
Avoid high temperatures, exposure to Lithiu	None.	Under certain conditions, nitrogen ca	3	0	0	SA	3	0	2	N.A.
Keep away from naked flames/heat.	Combustible materials, reducing ager	On burning: release of toxic and corro	0	0	0	OX	1	0	3	N.A.
Light.	Strong bases, Amines, Alcohols	Carbon oxides and Hydrogen Fluoride	3	0	1	0	1	0	1	X
Keep away from heat/sparks/open flames/	Oxidizing agent, Halogens, Alkaline ea	Under normal conditions of storage a	0	4	0	N.A.	0	4	3	N.A.
Use spark-/explosionproof appliances and l	Combustible materials, oxidizing ager	N.A.	0	4	0	N.A.	0	4	3	N.A.
No specific data.	Highly reactive or incompatible with t	Under normal conditions of storage a	0	0	0	OX	0	0	3	N.A.
Keep away from heat/sparks/open flames/	Oxidizing agent, Halogens, Alkaline ea	Under normal conditions of storage a	0	4	0	N.A.	0	4	3	N.A.
Use spark-/explosionproof appliances and l	Combustible materials, oxidizing ager	N.A.	0	4	0	N.A.	0	4	3	N.A.
Use spark-/explosionproof appliances and l	Oxidizing agents, (strong) acids, halog	Upon combustion CO and CO2 are fo	2	4	1	N.A.	1	4	2	N.A.
Avoid all possible sources of ignition (spark	Highly reactive or incompatible with t	Under normal conditions of storage a	2	4	2	N.A.	1	4	2	N.A.
No specific data.	Highly reactive or incompatible with t	Under normal conditions of storage a	1	0	0	N.A.	1	0	1	N.A.
Protect from heat/overheating. Keep away	Calcium, Potassium, Powdered metals	Under normal conditions of storage a	1	0	0	N.A.	1	0	0	N.A.
Pressurized container. Protect from sunlight	Potassium, Calcium, Powdered metals	In case of fire hazardous decompositi	2	1	0	N.A.	1	1	0	N.A.
Heat	N.A.	Thermal decomposition yields toxic	0	0	0	N.A.	1	0	1	N.A.
Heat, flames and sparks.	Incompatible with alkali or alkaline ea	Decomposition products are hazardou	2	0	0	N.A.	2	0	0	N.A.
Do not mix with oxygen or air above atmos	(Under specific conditions: e.g. very h	Halogens, halogen acids and possibly	2	0	1	N.A.	1	0	2	N.A.
Avoid sources of ignition such as sparks, hot	Freshly abraded aluminum surfaces (r	Hydrochloric and hydrofluoric acids; a	1	1	0	N.A.	2	1	0	N.A.
Protect from sunlight. Do not expose to tem	Finely divided metals (Al, Mg, Zn). Str	Under normal conditions of storage a	2	0	0	N.A.	2	0	0	N.A.
Avoid all possible sources of ignition (spark	Extremely reactive or incompatible w	Risk of formation of toxic pyrolysis pr	1	4	0	N.A.	1	4	0	N.A.
Some risk may be expected of corrosive and	Reactions with alkali metals.	Under normal conditions of storage a	2	1	0	N.A.	1	1	0	N.A.
Some risk may be expected of corrosive and	Reactions with alkali metals.	Under normal conditions of storage a	2	1	0	N.A.	1	1	0	N.A.
Do not mix with oxygen or air above atmos	Highly reactive or incompatible with	Halogens, halogen acids and possibly	2	0	0	N.A.	1	0	0	N.A.
Do not mix with oxygen or air above atmos	(Under specific conditions: e.g. very h	Halogens, halogen acids and possibly	2	0	0	N.A.	1	0	0	N.A.
Flames, extremely hot metal surfaces, heati	Avoid contact with strong alkali and a	Hydrogen Fluoride, Hydrogen Chlorid	2	0	0	N.A.	1	0	1	N.A.
Heat, hot surfaces, flames.	Alkali metals, alkaline earth metals, p	Under normal conditions of storage a	2	1	0	N.A.	1	1	0	N.A.
from physical damage and heat. Containers	Active metals, fires of metal hydrides.	will decompose to Iodine, Hydrogen f	2	0	1	N.A.	N.A.	N.A.	N.A.	N.A.
Heat, flames and sparks.	May react violently with chemically ac	Under normal conditions of storage a	1	0	0	N.A.	0	0	3	N.A.
se, hazardous reactions will not occur.	Freshly abraded aluminium surfaces (	Under normal conditions of storage a	2	1	0	N.A.	2	1	0	N.A.
Avoid heat, sparks, flames, and other igniti	Strong oxidizing agents. Alkali or alkal	Under normal conditions of storage a	2	4	0	N.A.	1	4	2	N.A.
Avoid all possible sources of ignition (spark	Highly reactive or incompatible with t	Under normal conditions of storage a	2	4	0	N.A.	1	4	0	N.A.
Avoid all possible sources of ignition (spark	Incompatible with alkali or alkaline ea	Decomposition products are hazardou	2	4	0	N.A.	1	4	2	N.A.
Keep away from heat/sparks/open flames/	Air, Strong oxidising agents, Strong ac	Thermal decomposition toxic gas	3	3	0	N.A.	2	3	0	N.A.
Heat, Flame, Sparks, Other ignition sources	Strong oxidizing agents	Carbon oxides, Hydrogen chloride gas	1	0	0	N.A.	1	0	0	N.A.
Heat, flames and sparks.	May react violently with chemically ac	Under normal conditions of storage a	2	0	0	N.A.	1	0	2	N.A.
Heat, hot surfaces, flames. Do not mix with	Alkali metals, alkaline earth metals, p	Thermal decomposition yields toxic pr	1	1	0	N.A.	1	1	0	N.A.
Avoid sources of heat or open flame. Expos	Incompatible with strong reducing ag	Under normal conditions of storage a	1	0	1	N.A.	1	0	0	N.A.
Heat, hot surfaces, flames. The product is n	(Under specific conditions: e.g. very h	Thermal decomposition yields toxic p	1	1	0	N.A.	1	1	0	N.A.
Protect from sunlight. Do not expose to tem	Alkali metals. Finely divided metals (A	Under normal conditions of storage a	3	0	0	N.A.	2	0	0	N.A.
Protect from sunlight. Do not expose to tem	bases, alkali metals, oxidizing materia	Thermal decomposition or combustio	1	0	0	N.A.	1	0	1	N.A.
Heat, flames. Extremes of tempe	Strong oxidizing agents	In case of fire: Carbon oxides, Hydrog	N.A.	N.A.	N.A.	N.A.	N.A.	N.A.	N.A.	N.A.
Protect from heat/overheating. Protect from	Alkali metals. Finely divided metals (A	Thermal decomposition generates: Ca	1	0	0	N.A.	2	0	0	N.A.
Keep away from heat, sparks, and flame. Av	Reacts with finely divided metals such	Hydrogen fluoride by thermal decom	2	4	0	N.A.	1	4	1	N.A.
Heat/Sources of heat.	Oxidizing agents, Metallic powders, A	Hydrogen fluoride, Fluorophosgene.	0	4	1	N.A.	0	4	1	N.A.
Use spark-/explosionproof appliances and l	Combustible materials, oxidizing ager	Decomposes on exposure to tempera	2	4	0	N.A.	2	4	2	N.A.
Do not mix with oxygen or air above atmos	Under specific conditions: e.g. very hi	Decomposition products are hazardou	1	0	1	N.A.	1	0	1	N.A.
Do not mix with oxygen or air above atmos	(Under specific conditions: e.g. very hi	Decomposition products are hazardou	2	1	0	N.A.	1	1	0	N.A.
Heat, flames and sparks.	Oxidizing agents.	Hydrogen fluoride. Carbonyl fluoride.	2	4	0	N.A.	1	4	0	N.A.
Heat, hot surfaces, flames. The product is n	Alkali metals, alkaline earth metals, p	Thermal decomposition yields toxic p	1	1	0	N.A.	1	1	0	N.A.
Do not mix with oxygen or air above atmos	(Under specific conditions: e.g. very h	Thermal decomposition giving toxic a	2	1	0	N.A.	1	1	0	N.A.
None under recommended storage and han	Polystyrene. Alloys with >2% magnesi	Thermal decomposition may produce	2	0	0	N.A.	1	0	2	N.A.
Heat, flames and sparks.	Strong oxidizers, alkali metals, Light a	Gaseous hydrogen fluoride (HF). Fluo	0	3	1	N.A.	0	3	1	N.A.
Keep away from naked flames/heat. Avoid	combustible materials, oxidizing agen	In moist air: release of corrosive mist	3	0	0	N.A.	3	0	2	N.A.
Keep away from naked flames/heat	Reactive or incompatible with the foll	On burning: release of toxic and corro	0	0	0	N.A.	0	0	0	B
Heat. Direct sunlight. Sparks. Open flame.	Reactive with oxidizing agents. Incom	Thermal decomposition is highly depe	2	3	0	N.A.	2	3	0	H
N.A.	N.A.	N.A.	0	0	0	N.A.	0	0	0	A
None under recommended storage and han	N.A.	Under normal conditions of storage a	0	0	0	SA	0	0	3	N.A.
Avoid heat, flames, sparks and other source	Acids. Halogens. Oxidizing agent.	Under normal conditions of storage a	1	4	0	N.A.	1	4	1	N.A.
Heat, flames and sparks.	Reactive with oxidizing agents.	Thermal decomposition products: oxi	2	3	0	N.A.	2	3	0	H
Use spark-/explosionproof appliances and l	Combustible materials, oxidizing ager	Upon combustion: CO and CO2 are fo	1	4	0	N.A.	0	4	1	N.A.
Heat, ignition sources (flames, sparks, etc.),	oxidizing agents.	Carbon dioxide Carbon monoxide	0	2	0	N.A.	2	2	0	G
Heat, ignition sources (flames, sparks, etc.),	oxidizing agents.	Carbon dioxide Carbon monoxide	1	2	0	N.A.	2	2	0	G
Heat, ignition sources (flames, sparks, etc.),	May react with oxygen and strong oxi	Carbon dioxide Carbon monoxide	1	3	0	N.A.	1	3	0	G
Heat, ignition sources (flames, sparks, etc.),	oxidizing agents.	Carbon dioxide Carbon monoxide	1	3	0	N.A.	2	3	0	G
Heat, ignition sources (flames, sparks, etc.),	Highly reactive with oxidizing agents.	Carbon dioxide Carbon monoxide	2	3	0	N.A.	2	3	0	H
Heat, ignition sources (flames, sparks, etc.),	oxidizing agents.	Carbon dioxide Carbon monoxide	2	3	0	N.A.	2	3	0	H
Heat, ignition sources (flames, sparks, etc.),	oxidizing agents.	Carbon dioxide Carbon monoxide. It v	1	4	0	N.A.	1	4	0	H
Use spark-/explosionproof appliances and l	Combustible materials, oxidizing ager	Carbon dioxide Carbon monoxide	2	4	0	N.A.	1	4	2	N.A.
Heat, ignition sources (flames, sparks, etc.),	oxidizing agents	Carbon dioxide Carbon monoxide	2	0	0	N.A.	2	0	0	J
Avoid heat, sparks, open flames and other i	Reactive with oxidizing agents. Acids.	Thermal decomposition is highly depe	2	3	0	N.A.	2	3	0	H
Avoid heat, sparks, open flames and other i	Reactive with oxidizing agents.	Thermal decomposition is highly depe	2	3	0	N.A.	2	3	0	H
Keep away from heat/sparks/open flames/	Strong oxidizers (e.g., chlorine, bromi	Thermal decomposition may produce	1	4	0	N.A.	0	4	1	N.A.

B Appendix B

In this Appendix, the performance of the turbo generator are detailed in terms of power production and static-to-static isentropic efficiency and according to the condensing pressure and overheating degree investigated during the experimental campaign. This is achieved considering successively fluids R245fa and then R1233zd.
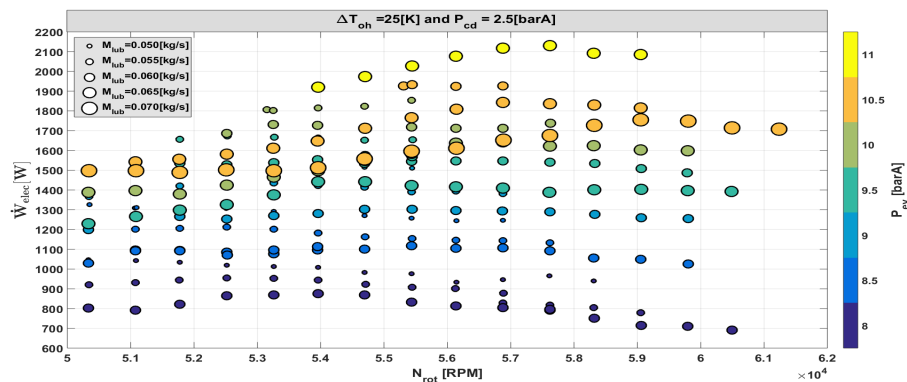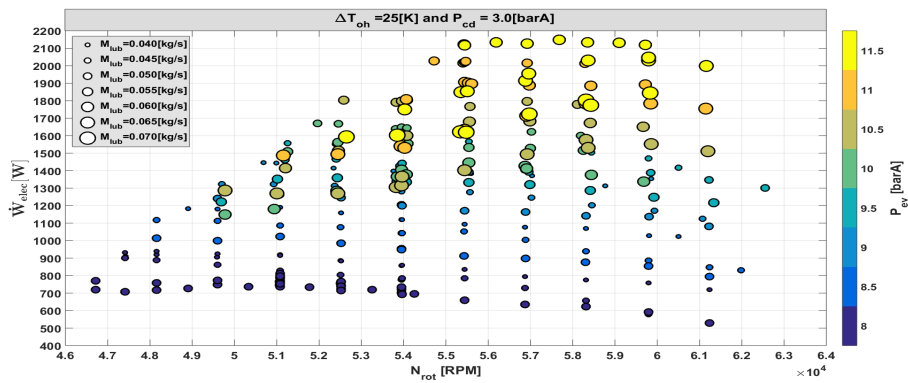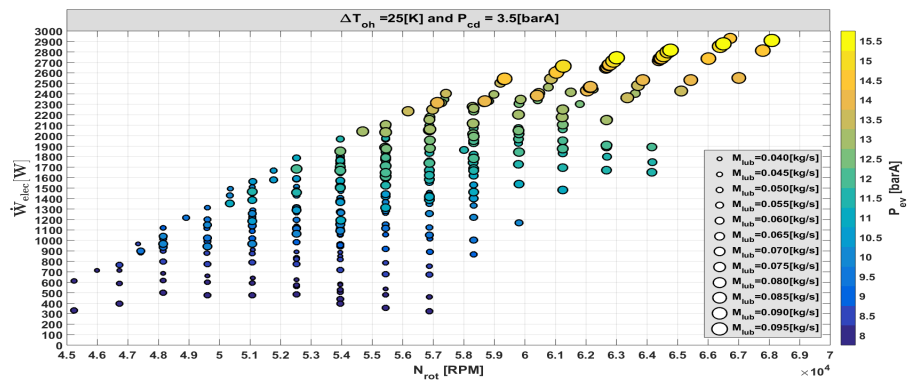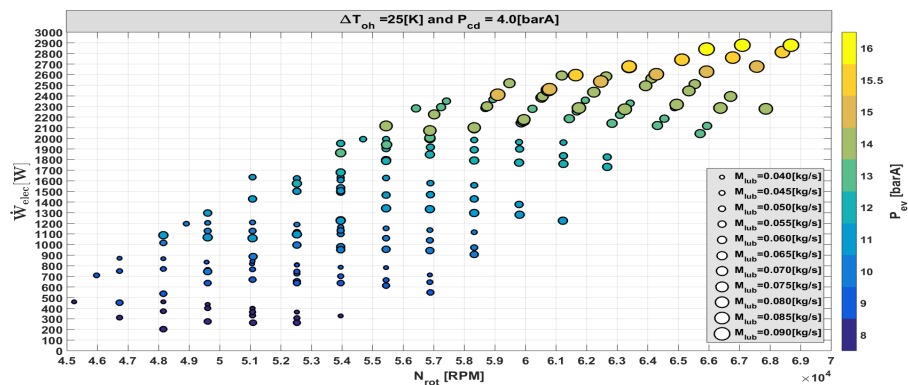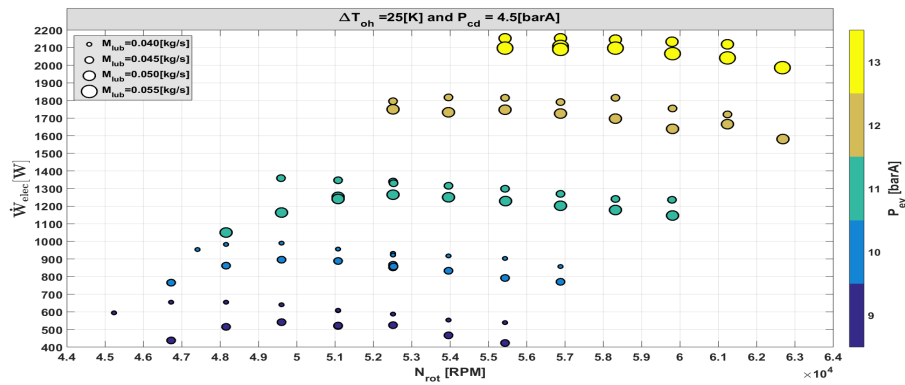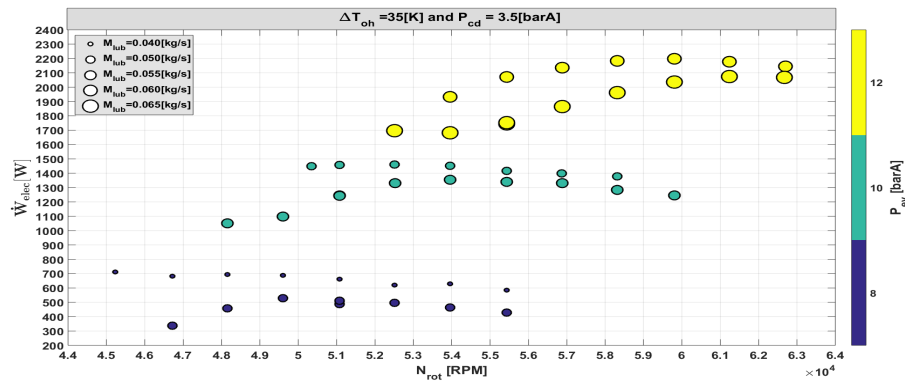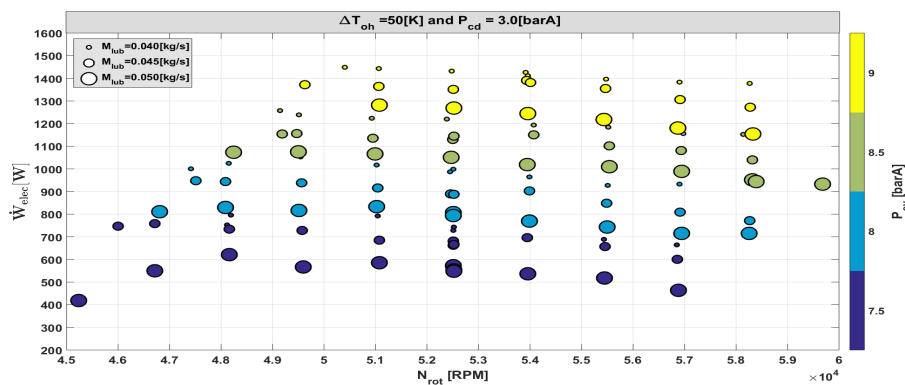

Figure B.1 – Power produced by the turbo generator with R245fa as a function of the rotational speed and inlet pressure (or mass flow rate) for a condensing pressure of 2.5 barA and an overheating degree of 25K
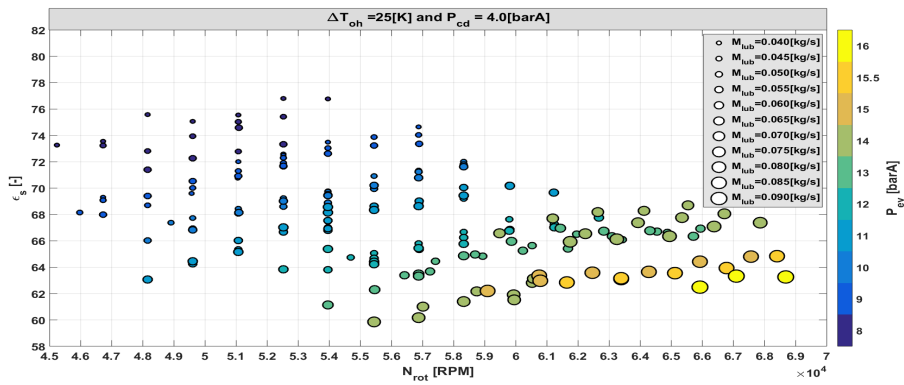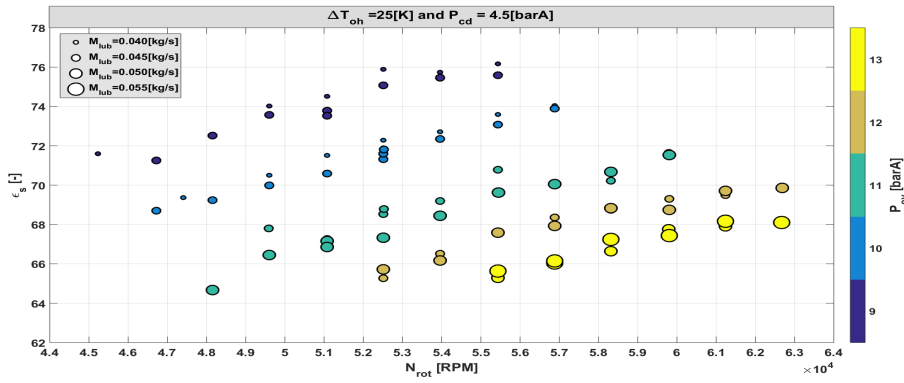
Figure B.2 – Power produced by the turbo generator with R245fa as a function of the rotational speed and inlet pressure (or mass flow rate) for a condensing pressure of 3 barA and an overheating degree of 25K

Figure B.3 – Power produced by the turbo generator with R245fa as a function of the rotational speed and inlet pressure (or mass flow rate) for a condensing pressure of 3.5 barA and an overheating degree of 25K
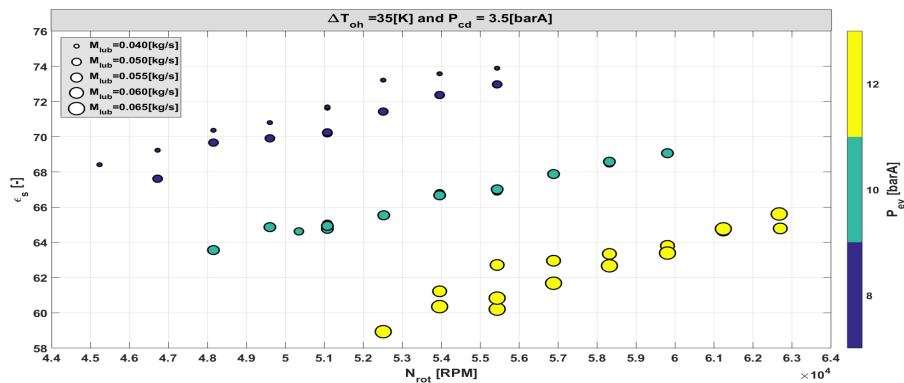

Figure B.4 – Power produced by the turbo generator with R245fa as a function of the rotational speed and inlet pressure (or mass flow rate) for a condensing pressure of 4 barA and an overheating degree of 25K

Figure B.5 – Power produced by the turbo generator with R245fa as a function of the rotational speed and inlet pressure (or mass flow rate) for a condensing pressure of 4.5 barA and an overheating degree of 25K

Figure B.6 – Power produced by the turbo generator with R245fa as a function of the rotational speed and inlet pressure (or mass flow rate) for a condensing pressure of 3.5 barA and an overheating degree of 35K

Figure B.7 – Power produced by the turbo generator with R245fa as a function of the rotational speed and inlet pressure (or mass flow rate) for a condensing pressure of 3 barA and an overheating degree of 50K
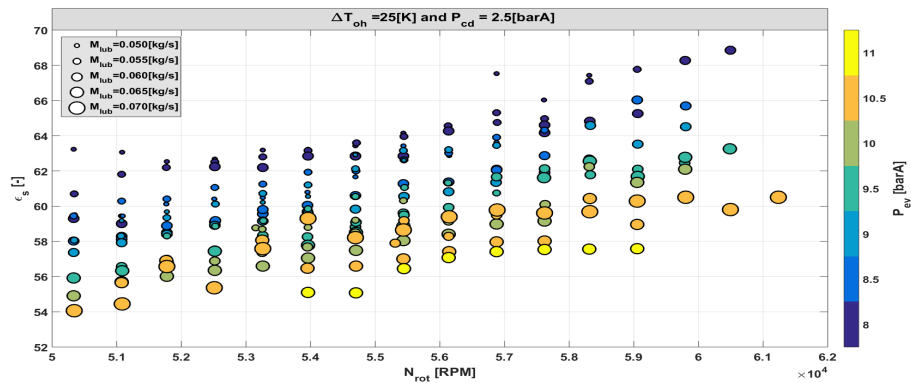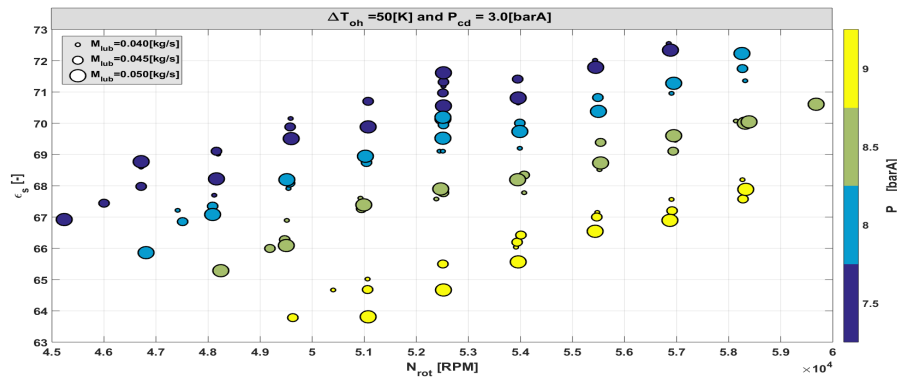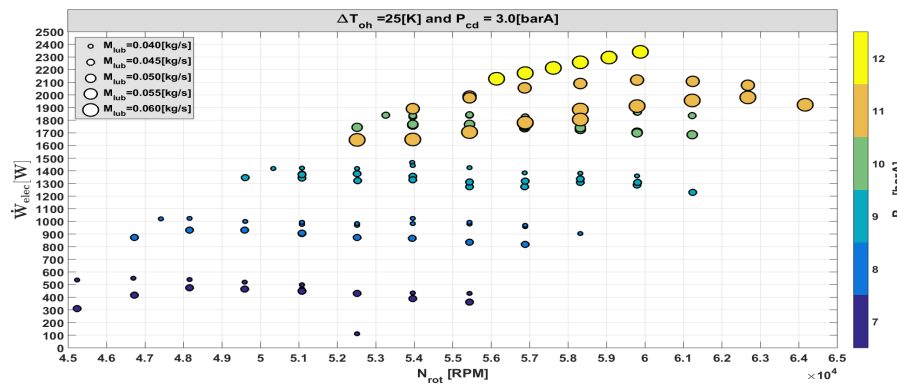
Figure B.8 – Isentropic efficiency reached by the turbine with R245fa as a function of the rotational speed and inlet pressure (or mass flow rate) for a condensing pressure of 2.5 barA and an overheating degree of 25K
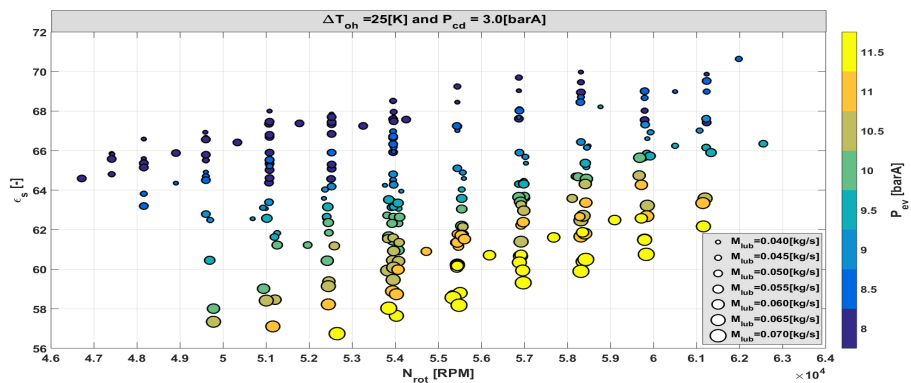
Figure B.9 – Isentropic efficiency reached by the turbine with R245fa as a function of the rotational speed and inlet pressure (or mass flow rate) for a condensing pressure of 3 barA and an overheating degree of 25K
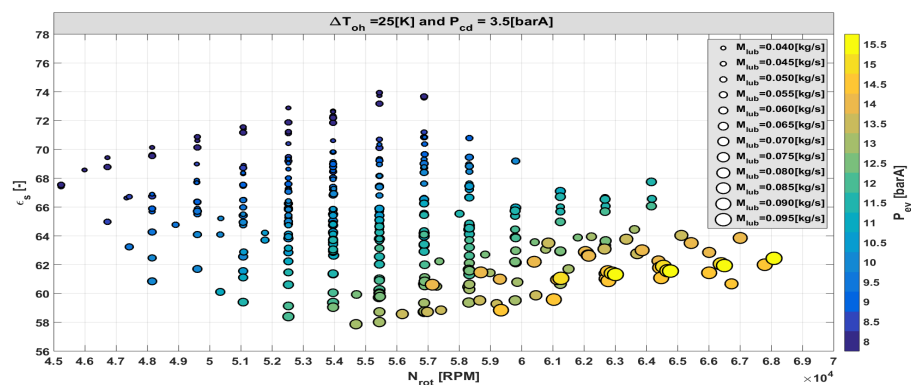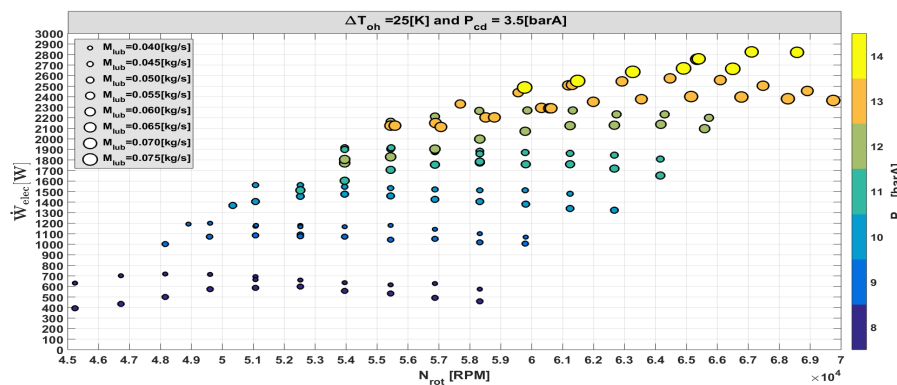

Figure B.10 – Isentropic efficiency reached by the turbine with R245fa as a function of the rotational speed and inlet pressure (or mass flow rate) for a condensing pressure of 3.5 barA and an overheating degree of 25K
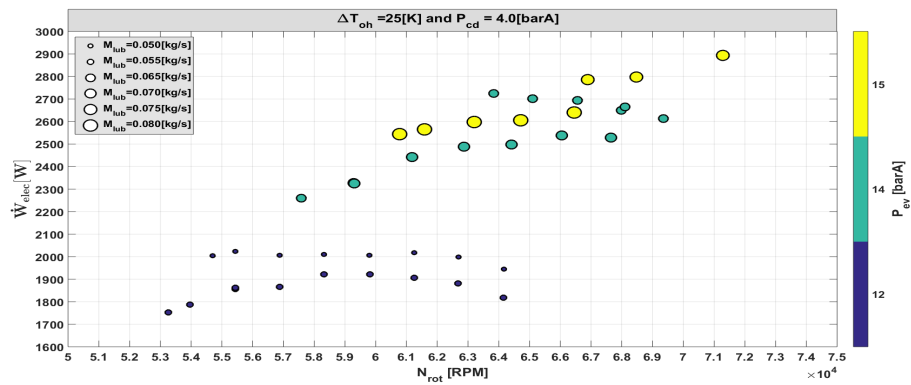
Figure B.11 – Isentropic efficiency reached by the turbine with R245fa as a function of the rotational speed and inlet pressure (or mass flow rate) for a condensing pressure of 4 barA and an overheating degree of 25K

Figure B.12 – Isentropic efficiency reached by the turbine with R245fa as a function of the rotational speed and inlet pressure (or mass flow rate) for a condensing pressure of 4.5 barA and an overheating degree of 25K

Figure B.13 – Isentropic efficiency reached by the turbine with R245fa as a function of the rotational speed and inlet pressure (or mass flow rate) for a condensing pressure of 3.5 barA and an overheating degree of 35K

Figure B.14 – Isentropic efficiency reached by the turbine with R245fa as a function of the rotational speed and inlet pressure (or mass flow rate) for a condensing pressure of 3 barA and an overheating degree of 50K
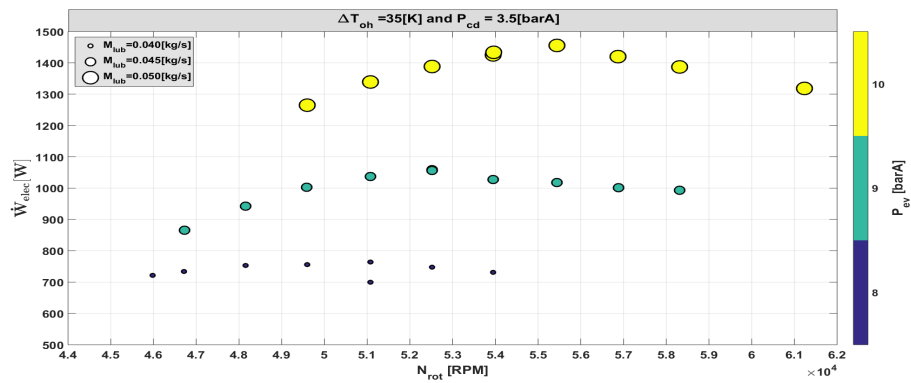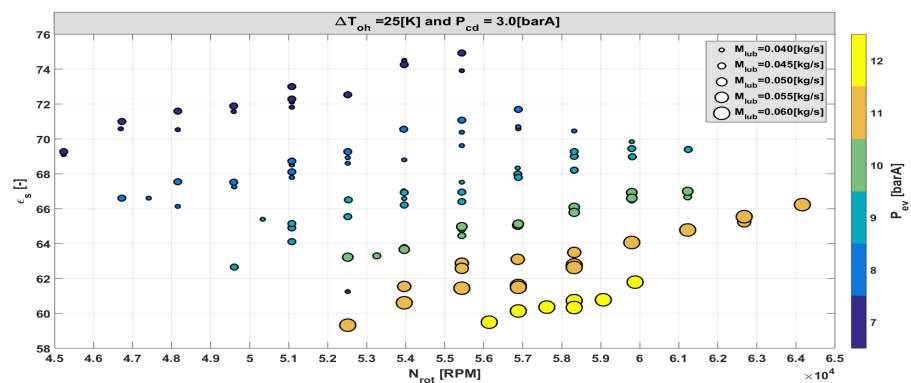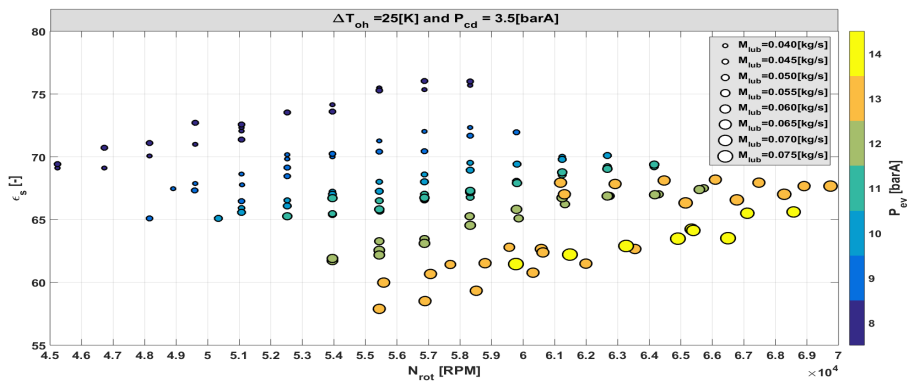

Figure B.15 – Power produced by the turbo generator with R1233zd as a function of the rotational speed and inlet pressure (or mass flow rate) for a condensing pressure of 3 barA and an overheating degree of 25K

Figure B.16 – Power produced by the turbo generator with R1233zd as a function of the rotational speed and inlet pressure (or mass flow rate) for a condensing pressure of 3.5 barA and an overheating degree of 25K

Figure B.17 – Power produced by the turbo generator with R1233zd as a function of the rotational speed and inlet pressure (or mass flow rate) for a condensing pressure of 4 barA and an overheating degree of 25K

Figure B.18 – Power produced by the turbo generator with R1233zd as a function of the rotational speed and inlet pressure (or mass flow rate) for a condensing pressure of 3.5 barA and an overheating degree of 35K
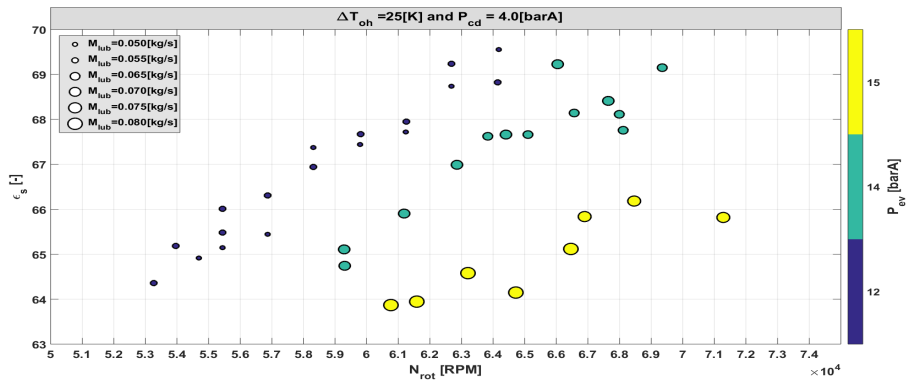

Figure B.19 – Isentropic efficiency reached by the turbine with R1233zd as a function of the rotational speed and inlet pressure (or mass flow rate) for a condensing pressure of 3 barA and an overheating degree of 25K
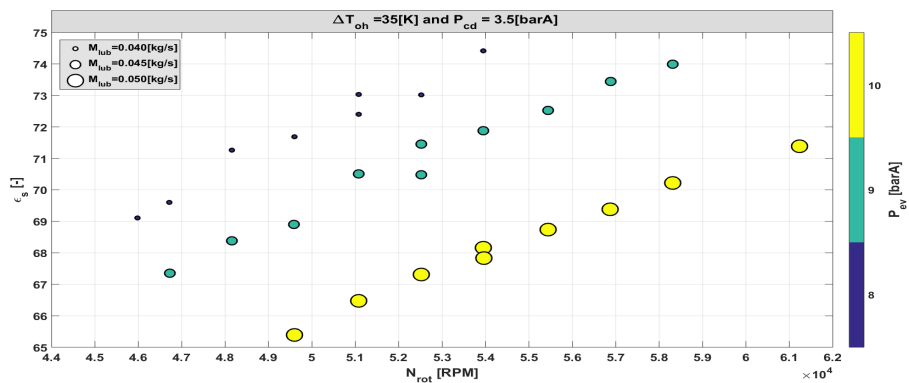
Figure B.20 – Isentropic efficiency reached by the turbine with R1233zd as a function of the rotational speed and inlet pressure (or mass flow rate) for a condensing pressure of 3.5 barA and an overheating degree of 25K

Figure B.21 – Isentropic efficiency reached by the turbine with R1233zd as a function of the rotational speed and inlet pressure (or mass flow rate) for a condensing pressure of 4 barA and an overheating degree of 25K

Figure B.22 – Isentropic efficiency reached by the turbine with R1233zd as a function of the rotational speed and inlet pressure (or mass flow rate) for a condensing pressure of 3.5 barA and an overheating degree of 35K

C Appendix C

In this appendix are shown the distribution of the source of losses in the bearings model assuming there is no heat transfer from the fluid expanded in the turbine to the lubricant in the bearings (Figure C.1). The comparison of the predicted and measured enthalpy flow rate over the lubrication fluid indicates the windage and friction losses alone are not sufficient to represent the enthalpy increase of the lubrication fluid in the bearings (Figure C.2). The maximal relative error on the lubrication enthalpy flow rate is above 40%.
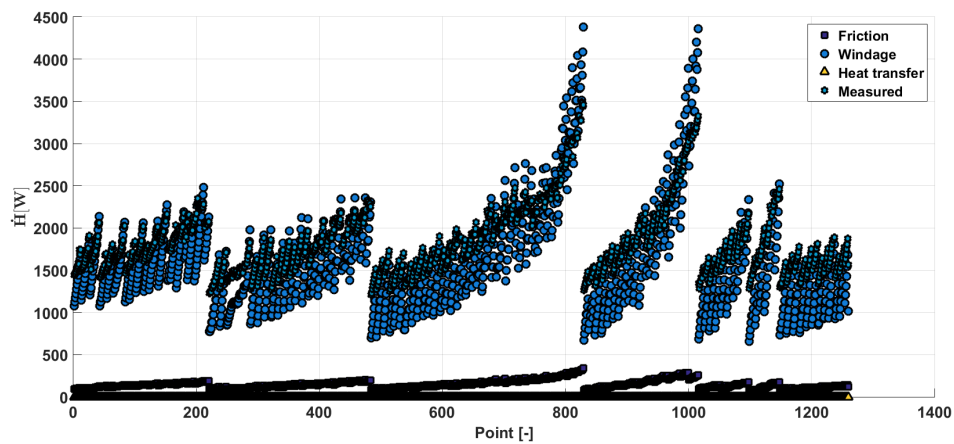

Figure C.1 – Distribution of the sources of losses according to the bearings models for the 1260 measurement points achieved with fluid R245fa
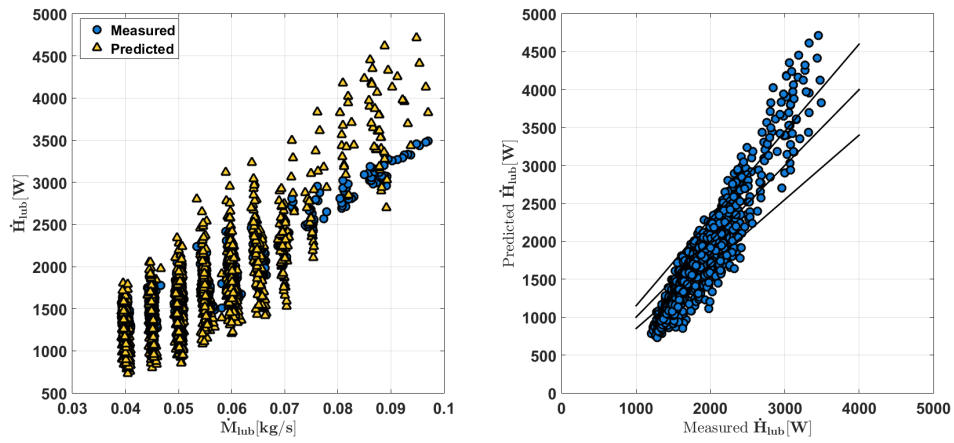
Figure C.2 – Comparison between predicted and measured enthalpy flow rate of the lubrication fluid between the inlet and outlet of the bearings for the 1260 measurement points achieved with fluid R245fa

D Appendix D

In this Appendix are reported the results of the cost estimation achieved for the piston expander. First the 3D sketch achieved in Solidworks is shown in Figure D.1. Then the cost distribution based on the considered parts of the machines are shown in Figure D.2.

In this Appendix are also reported the design results achieved with piston expander assuming the clearance volume and mechanical could be reduced (Figure D.3). As it can be seen the result obtained in terms of SIC and net power outputs are now comparable to those achieved with the scroll and screw expanders.
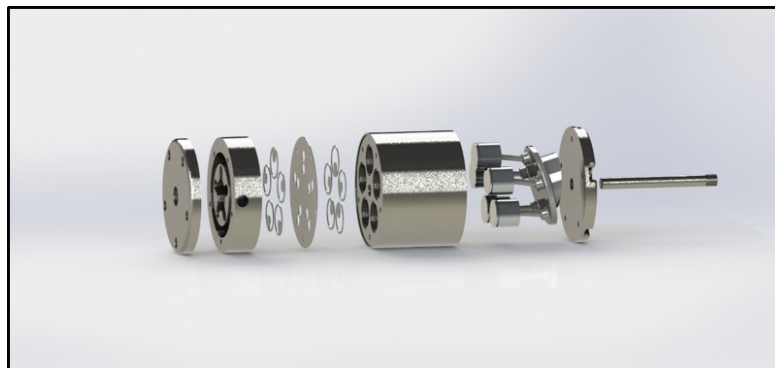

Figure D.1 – 3D scheme with the main components of a 5 cylinders swash-plate piston expander

Part	Material	Weight [kg]	Quantity	All machining			Machining + molding				
				Cost Material [$]	Cost Manufacturing [$]	Total cost [$]	Work type	Cost Material [$]	Cost Manufacturing [$]	Mold cost [$]	Total cost [$]
Back plate	AISI 304	2.01	20000	43.41	15.29	58.7	Molding	43.41	3.38	0.13	46.92
End plate	AISI 304	2.01	20000	43.41	37.53	80.94	Molding	43.41	3.38	0.13	46.92
Front plate	AISI 304	4.69	20000	101.3	29.36	130.66	Molding	101.3	3.38	0.13	104.81
Hole plate	AISI 304	0.12	20000	2.7	6.14	8.84	Machining	2.7	6.14	0	8.84
Main housing	AISI 304	14.6	20000	315.48	1330.07	1645.55	Molding	315.48	3.38	0.13	318.99
Main Shaft	Plain carbon steel	0.24	20000	0.73	9.52	10.25	Machining	0.73	9.52	0	10.25
Piston head	AISI 304	0.25	100000	5.46	6.68	12.14	Molding	5.46	3.38	0.13	8.97
Piston rod	Plain carbon steel	0.03	100000	0.11	2.63	2.74	Machining	0.11	2.63	0	2.74
Swash plate	Plain carbon steel	2.79	20000	8.68	17.86	26.54	Machining	8.68	17.86	0	26.54
Valve plate	AISI 304	0.01	100000	0.22	3.47	3.69	Machining	0.22	3.47	0	3.69
Total cost	/	26.75	20000	521.5	1458.55	1980.05	/	521.5	56.52	0.65	625.51

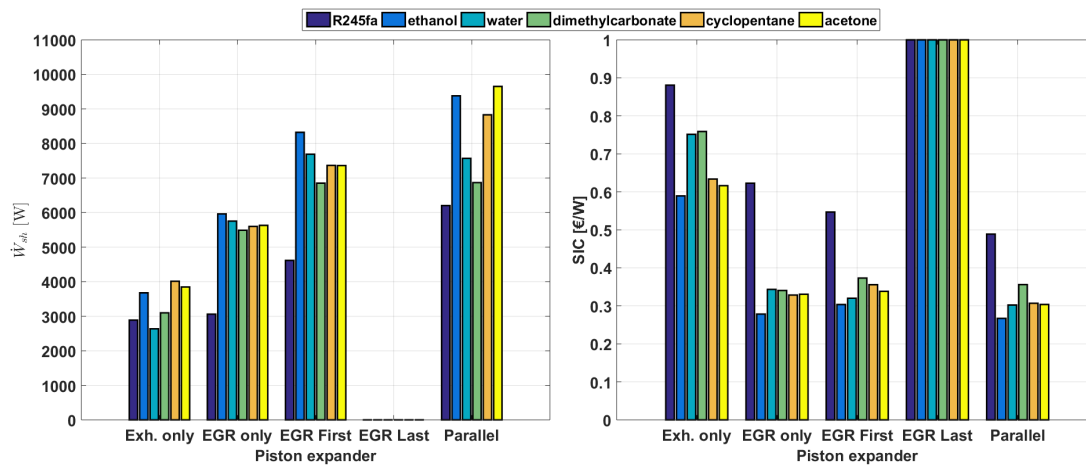Figure D.2 – Cost distribution of the swash piston expander

Figure D.3 – New estimation of the SIC and power output obtained with the piston expander characterized by a clearance volume of 2%, reduced internal leakages and mechanical losses

If I was young, I'd flee this town
I'd bury my dreams underground
As did I, we drink to die, we drink tonight.

— Beirut

Faculty of applied sciences
Department of Aerospace
and Mechanical Engineering
Thermodynamics laboratory
University of Liege

B49 Institut de
Thermodynamique
Quartier Polytech 1
Allée de la Découverte 17
Campus du Sart-Tilman 4000
Liège (BELGIUM)
Phone : +32 4 366 48 23
http://www.labothap.ulg.ac.
be